

3 PETROGRAPHY

The petrographic analysis of the Bafoussam granitoids is based on thin sections that were prepared from specimens of the different granitoid groups encountered in the investigated area. Several thin sections of each lithological group are studied for mineral identification as well as for estimation of the abundance of each mineral expressed as volume percentage of the rock. The locations of the specimens from which the thin sections were made are given and can be visualized in the sample locations map in the Appendix. Modal compositions were determined by visually estimating percentages of minerals in the thin sections and in hand-specimen slabs. Some first information of mineral chemistry are also included. The mineral abbreviations are after Kretz (1983).

3.1 Biotite granitoid

Biotite granitoid is by far the most frequent lithology in the studied area. Twenty-five samples have been investigated in detail: four samples were collected from Badeng locality (BAN-13: BD-1: BD-2: NKJ-1), three samples from Bapi locality (TA-7: BAP-1: SAN-1), seven samples from Baleng quarry (BL-8: BL-13: BL-11: BL-4: BL-5: BG-1: BL-9), eight samples from Sedembong locality (SE-1: SE-2: SE-4: SE-5: PA-1: PA-2: TEN-31: BJD-33), two samples from Lemgo locality (LE-2: NG-3a) and one sample (NG-7) from an enclave within the deformed granitoid from Bafoussam-town.

Petrographically, the biotite granitoid consists of potassium feldspar, quartz, plagioclase, biotite and sometimes amphibole (Fig. 3.1A, B and C). Accessory minerals include titanite and, in small extent, allanite, apatite, zircon and iron-oxides. Chlorite, sericite and saussurite are the most common products of alteration.

Potassium feldspar: Cross-hatched and/or carlsbad twinned potassium feldspar with, in general, embayment at the grain boundaries is the main mineral present (~ 35–55 vol. %). Its structural state varies from orthoclase to microcline ($\text{Or}_{92-97}\text{Ab}_{8-3}$). The crystals are tabular- or lath-shaped and mostly subhedral with an average grain size of 5 mm in length. String and vein perthite exsolutions are common, while myrmekites (Fig. 3.1A) are also frequently observed at

the K-feldspar crystal rims adjacent to plagioclase. Compositional zoning is quite common in K-feldspars (Fig. 3.2A). Apatite, quartz, plagioclase are found as small inclusions. K-feldspar is locally altered and replaced by sericite.

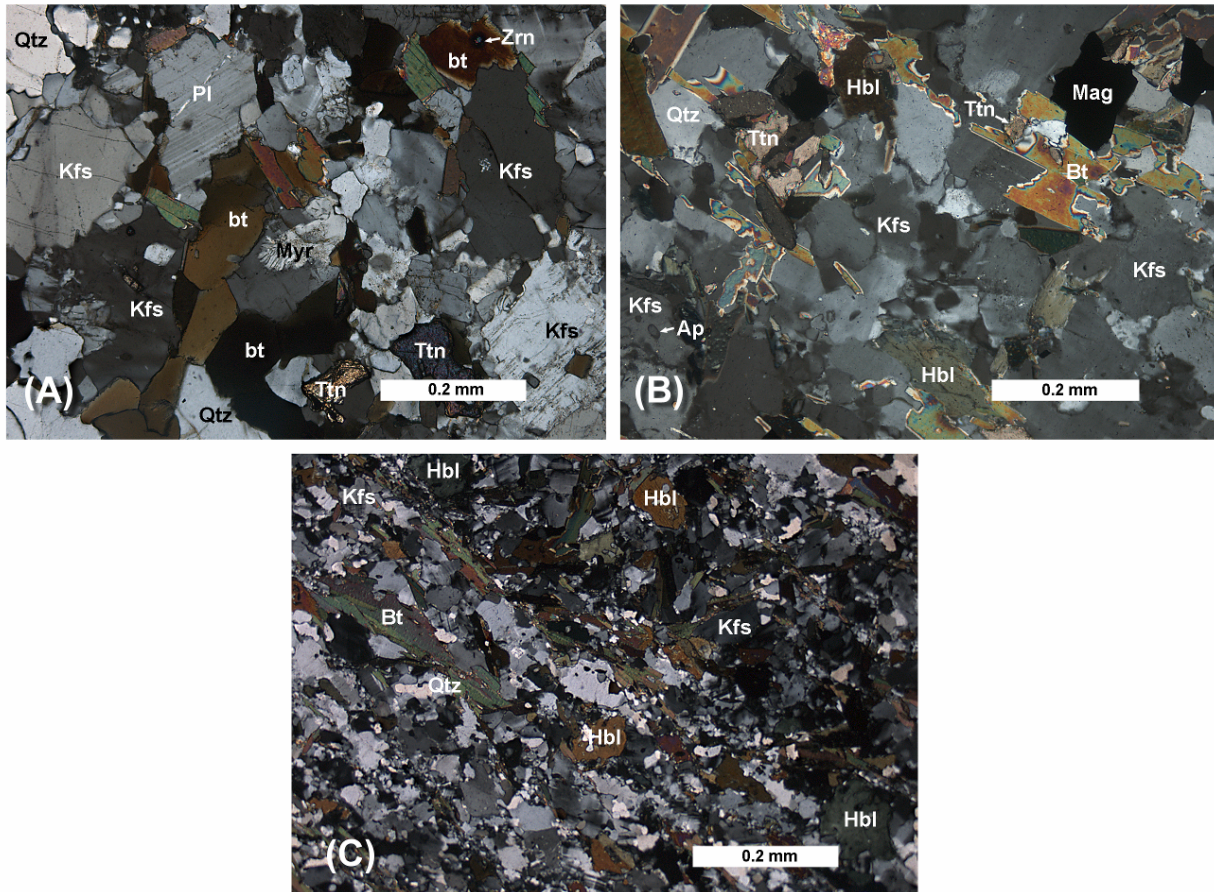


Figure 3.1: Photomicrographs in cross-polarized light, showing the common structures of the biotite granitoid. **(A)** and **(B)** coarse-grained magmatic structure, **(C)** medium-grained structure.

Quartz: Elongated quartz (~ 20–35 vol. %) occurs as anhedral grains which range in size from 0.2 to 3 mm in length and occasionally enclose plagioclase and potassium feldspar crystals. Quartz commonly displays sub-grain domains and undulatory extinction as signs of deformation (Fig. 3.2B). The crystal boundaries often show embayment. Quartz is also found as intergrowths in myrmekites and as inclusions within feldspar crystals.

Plagioclase: Albite and carlsbad twinned plagioclase (~ 20 vol. %) is commonly subhedral with straight or corroded grain outlines (Fig. 3.1A). The crystal grains range in size from 1 to 3 mm in length. The plagioclase is an oligoclase ($An_{17-35}Ab_{64-82}$), often displays

normal zonation with the An-content decreasing from the core ($\text{An}_{35}\text{Ab}_{64}$) towards the rim ($\text{An}_{20}\text{Ab}_{79}$). Antiperthitic texture with patches of microcline is not rare. Irregular synneusis aggregates are locally found. Quartz, apatite, biotite and rarely titanite exist as small inclusions within plagioclase crystals. Some plagioclase cores are clouded, entirely pseudomorphed by a mixture of fine-grained sericite, saussurite and epidote.

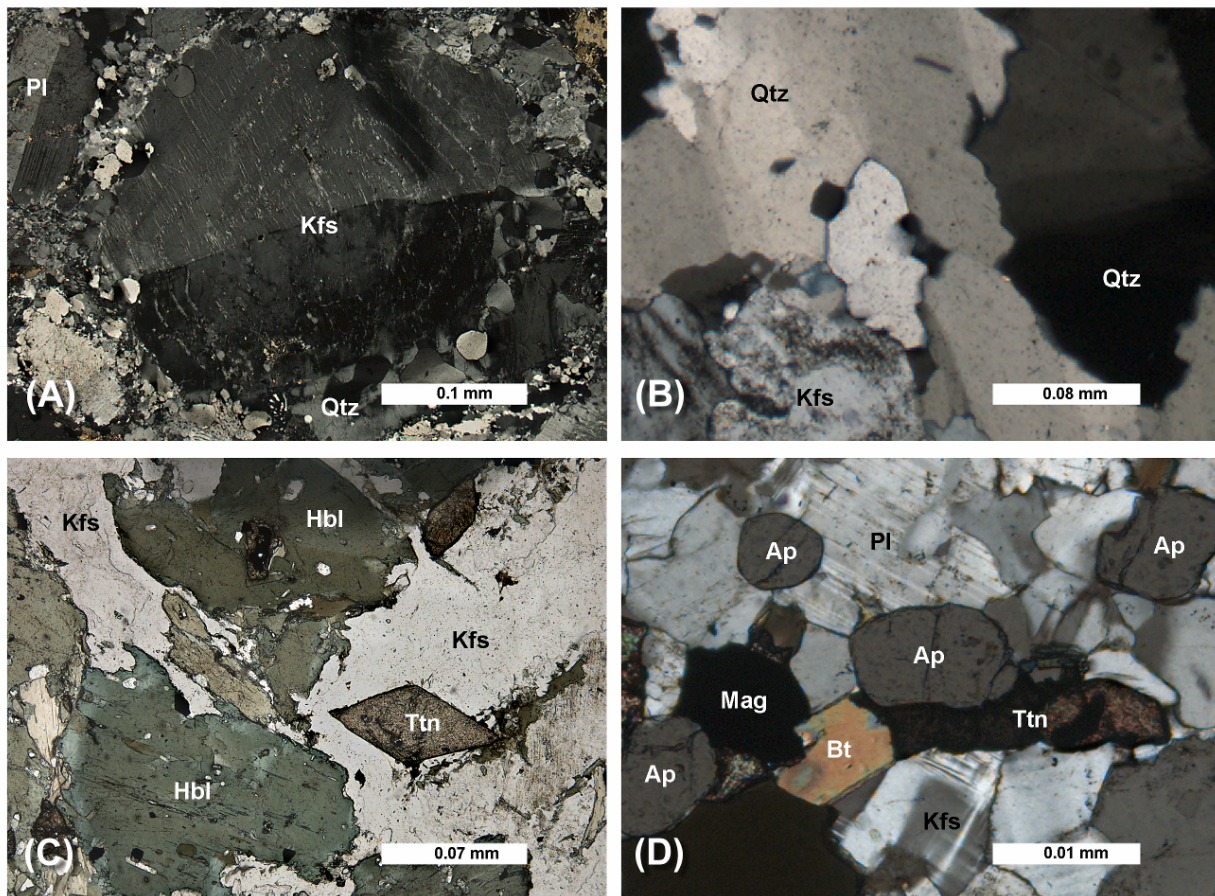


Figure 3.2: Photomicrographs of the biotite granitoid. Cross-polarized light for (A), (B) and (D). Plane-polarized light for (C). (A) Zoned potassium feldspar (Kfs), displaying carlsbad-twinning. (B) Large quartz (Qtz) crystals with undulose extinction. (C) Hornblende (Hbl) minerals showing an optical zoning and lamellar twinning along $\{100\}$ plane. (D) Isolated rounded apatite (Ap) crystals in the biotite granitoid.

Biotite: Strongly pleochroic biotite (z: greenish brown-yellowish brown and x: brown-dark brown) constitutes about 5 vol. % of the analyzed rock components and is a moderate Fe biotite (X_{Fe} : 0.44–0.51). Its grain size reaches 1 mm. Biotite occurs mostly as subhedral individual flakes that display in places shredded ends; however, aggregates are also found particularly associated with iron-oxides and titanite. Some crystals are bent or kinked due to

tectonic overprint. Biotite has abundant inclusions of titanite, zircon and opaque. It is commonly altered to form pale green to grey green chlorite at its rims or along its {001} cleavages.

Hornblende: Hornblende, not omnipresent, is magnesio-hastingsite to edenite (X_{Mg} : 0.50–0.57). Medium prismatic and tabular hornblende (~ 5–10 vol. %) is strongly pleochroic from blue green to yellow green colour. Mineral grains present anhedral to subhedral forms and reach the size of 1.5 mm in length. Locally, they exhibit optical zoning marked by usual pale green rims and dark green cores (Fig. 3.2C). Many crystals show the typical two directions of cleavage, while lamellar twinning along {100} is exhibited by only few crystals. Small anhedral quartz grains and euhedral zircon are common as inclusions in some hornblende crystals. Hornblende is scarcely pseudomorphed by chlorite.

Titanite is found as brown, poorly-shaped crystals usually in corona position around iron-oxides or as subhedral to euhedral crystals measuring up to 3 mm in length, showing flattened diamond shape. When coexisting with hornblende, titanite proportion is significant, reaching up to 5 vol. %. **Allanite** occurs as subhedral tabular crystals reaching up to 2.4 mm in length and displaying weakly yellowish to brown pleochroism and occasionally zoning. **Iron-oxides** (ilmenite and magnetite) usually form anhedral to subhedral crystals that are commonly associated with biotite or titanite; they rarely occur as isolated grains disseminated in the rocks. **Apatite** (average grain size: 0.1 mm) forms tiny hexagonal, rounded or rectangular grains occurring usually as inclusions in feldspars or seldom as isolated mineral (Fig. 3.2D). **Zircon** is observed as minute grains with pleochroic halos hosted frequently by biotite (Fig. 3.1A), but also by hornblende. **Chlorite** is a retrograde product of biotite and hornblende, whereas **sericite** and **saussurite** replace potassium feldspar and plagioclase.

3.2 Deformed biotite granitoid

The twenty-nine studied samples of the deformed biotite granitoid have been taken from Bafoussam-town (NG-5: BA-31a: TK-3a: BFS-4: BFS-1: BFS-2: NG-3a: BFS-7a: NG-1a: TK-2a), Baleng (MD-1: ND-1: ND2a: BAS-25: BAS-26: BAS-27: BAL-2: BAN-5), River Noun bridge (BNF-10a: BNF-14: BNF-7: BNF-24a: BNF-8: BNF-6a: BNF-10a: BNF-3: NO-1a), River Noun bed (NN-1a).

The deformed biotite granitoid commonly shows porphyroclastic texture which is defined, in various proportions, by porphyroclasts of potassium feldspar, plagioclase and additional hornblende in the hornblende-bearing variety. The porphyroclasts disturbed the foliation which is characterized by aligned biotite streaks and multi-grain quartz aggregates forming the matrix (Fig. 3.3A, B). The term *porphyroblast* describes remnants of pre-existing megacrysts when the size is diminished by syn-deformational recrystallization or by myrmekite replacement. Titanite, allanite, apatite, zircon, ilmenite and magnetite are the most frequent accessory minerals, whereas chlorite, sericite and epidote represent the alteration products.

Several signatures of brittle and ductile deformations are observed. Both deformation behaviours include undulose extinction and different degrees of dynamic recrystallization particularly of quartz and minor feldspars, internal micro-cracking in porphyroclasts, sometimes accompanied by dislocation glides, and mechanical kinking and bending in the plagioclase grains. On the other hand, recrystallized new grain aggregates of the matrix commonly flank the porphyroclasts, forming *mantled porphyroblast* structure. They are often deformed into wings that extend on the both sides of the porphyroblast parallel to the foliation; wing shape can be used as a shear sense indicator. Two mantled porphyroblast types are recognized, Θ -type without wings and Φ -type possessing wings without stair-stepping (difference in elevation on the both sides). The material behaviour of quartz and feldspars indicates that deformation occurred under a temperature above 500°C (Tullis, 1990; Passchier and Trouw, 1998).

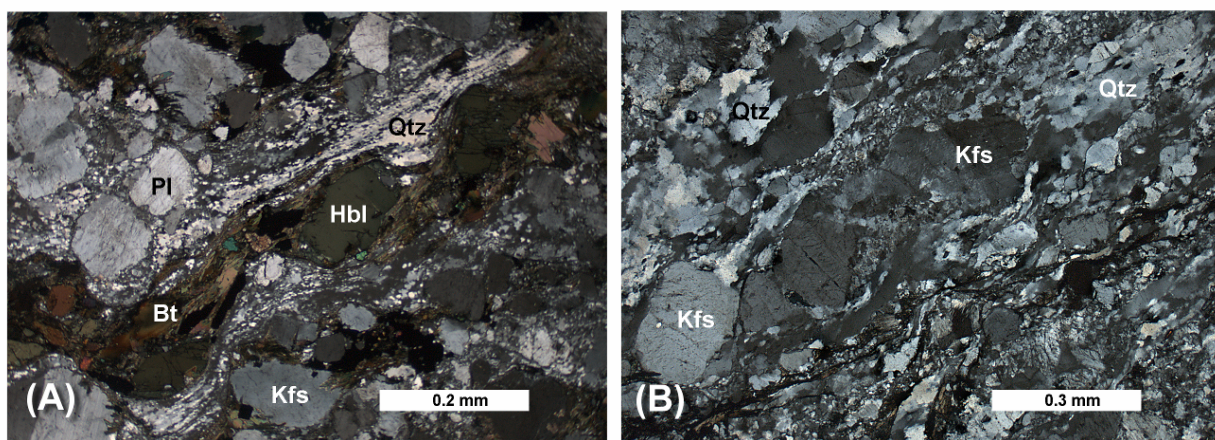


Figure 3.3: (A) and (B) photomicrographs in cross-polarized light, displaying the structure of the deformed biotite granitoid. Note the mylonitic fabric.

Potassium feldspar: Subhedral lath shaped potassium feldspar (5–40 vol. %) occurs as porphyroclasts with a maximum length of 3 mm (Fig. 4A). Cross-hatched microcline twinning and rarely orthoclase twinning are easily distinguishable, adopting the deformation of the crystals. K-feldspar is microcline and rarely orthoclase ($\text{Or}_{91-96}\text{Ab}_{9-4}$) and occasionally exhibits regular compositional zoning and wavy extinction. String- and rarely flame-shaped perthitic exsolutions of albite are observed. The replacement of K-feldspar by a plagioclase-vermicular quartz symplectite forming myrmekites is not scarce. Particularly, the myrmekites grow along the K-feldspar grain boundaries parallel to the foliation (Fig. 3.4B), interpreted as deformation related (Simpson and Wintsch, 1989; Vernon, 1991). Simpson and Wintsch (1989) show, that myrmekites in deformed granitic rocks develop only on sides of K-feldspar porphyroblast facing the shortening direction. The crystals are corroded and wrapped around by fine-grained recrystallized feldspars, quartz or in some cases thin trails of biotite. Plagioclase, apatite, biotite, allanite and titanite are found as inclusions, while sericite represents a secondary product.

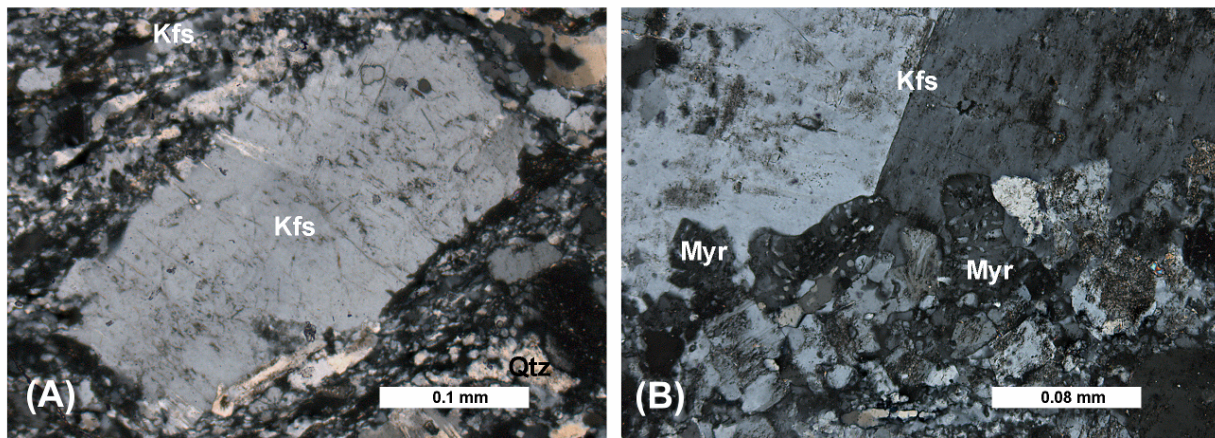


Figure 3.4: Photomicrographs in cross-polarized light of the deformed biotite granitoid. (A) Potassium feldspar (Kfs) wrapped by fine-grained matrix. (B) Growth of the myrmekites (Myr) along a K-feldspar (Kfs) grain boundary parallel to the foliation. Note the carlsbad-twinning of the K-feldspar.

Quartz: In contrast, quartz (10–35 vol. %) generally shows complete recrystallization. Quartz grains are mostly anhedral, their size varies from less than 0.05 to 1 mm. Quartz occurs elongated (quartz-I) or newly formed and fine-grained (quartz-II) (Fig. 3.5A and B) around porphyroclasts. The elongated crystals often exhibit ribbon-like shape with strong crystal-plastic deformation, sub-grain patterns and undulatory extinction related to high-temperature, solid-stage deformation (Kruhl, 1996). Their long direction is parallel to the foliation. The boundaries

of quartz crystals are irregular, due to grain boundary migration recrystallization. Locally, quartz shows dynamic recrystallization to form small grains (up to 0.5 mm in length) which are in some places in equilibrium with straight grain boundaries joining in a triple junction to produce annealed texture. Quartz usually fills intragranular cracks in feldspars.

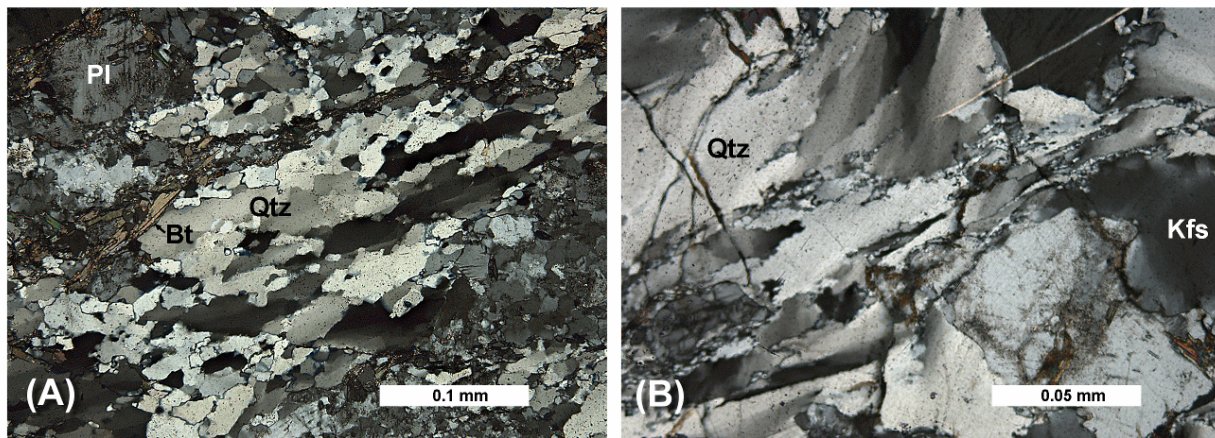


Figure 3.5: Photomicrographs in cross-polarized light of the deformed biotite granitoid. (A) Quartz grains displaying dynamic recrystallization fabric. Note the elongated shape of old quartz (*Qtz*: quartz-I) with undulose extinction and subgrains which are recrystallized into small quartz grains (*Qtz*: quartz-II). (B) Quartz (*Qtz*) crystals with irregular grain boundaries due to grain boundary migration recrystallization. Note the undulose extinction and the elongate subgrains in quartz.

Plagioclase: Porphyroclasts of plagioclase (20–45 vol. %) are tabular-shaped with rounded corners and ranging in size from 0.4 to 2 mm. They are albite to oligoclase ($An_{9-28}Ab_{71-90}$) and exhibit locally a weak reverse zonation (core: $An_9Ab_{90} \rightarrow$ rim: $An_{17}Ab_{82}$) (Fig. 3.6A). The majority of twins in the plagioclase obey the albite twin law. However, the association with pericline-law twins is locally observed. Twin lamellas are often bent. Some crystals of plagioclase display deformational kink-bands (Fig. 3.6B), wavy extinction and sets of micro-cracks sometimes accompanied by slightly dislocation and displacement forming *bookshelf* structure (Fig. 3.6 C and D). There are local synneusis aggregates of plagioclase. Quartz, apatite and titanite inclusions are frequent. The plagioclase alteration into both sericite and epidote is ubiquitous, but the extent of the alteration varies between the samples.

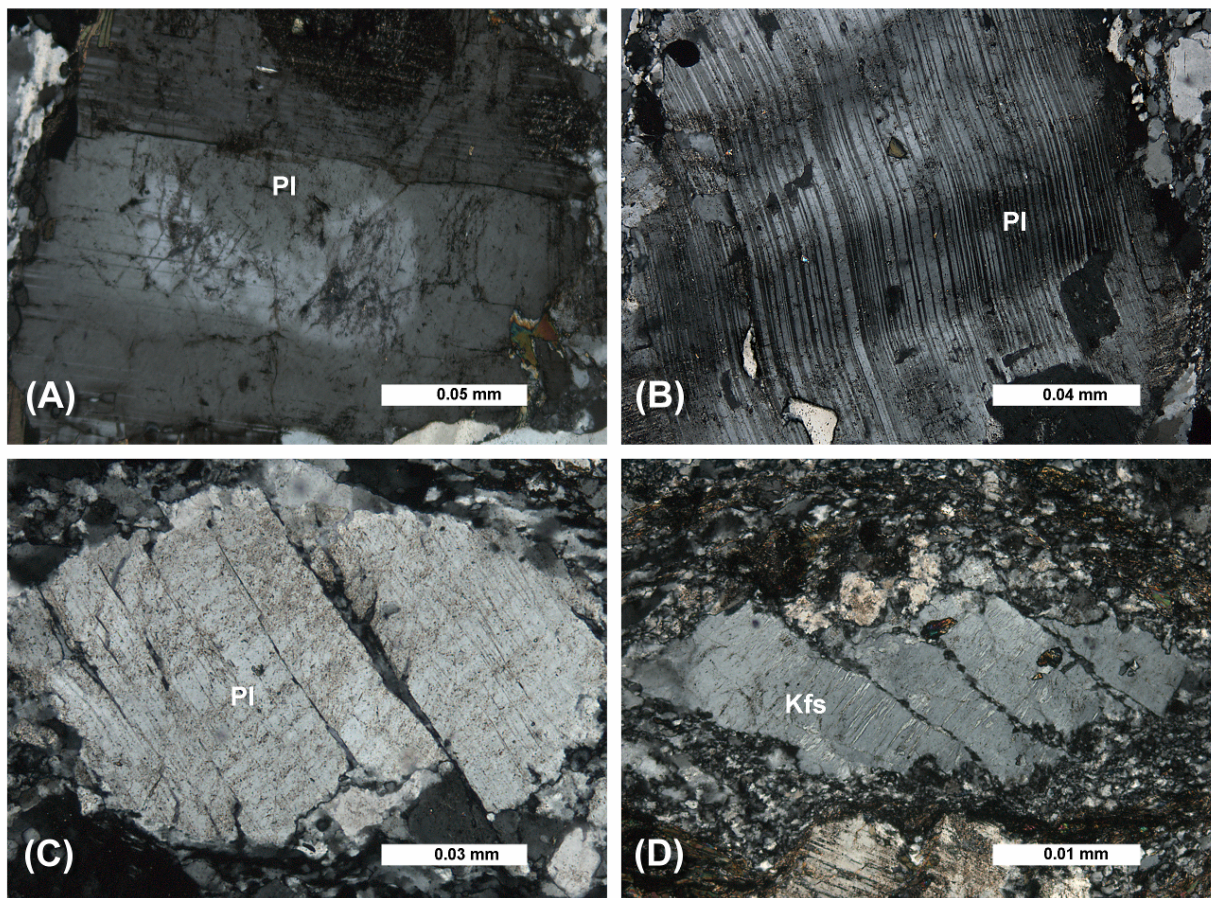


Figure 3.6: Photomicrographs in cross-polarized light of the deformed biotite granitoid. **(A)** Subhedral, tabular and zoned plagioclase (*Pl*), displaying combined albite and carlsbad twining. **(B)** Kink-band deformation of twin lamellas in plagioclase (*Pl*). **(C)** and **(D)** typical "Bookshelf" fracturing structure in plagioclase (*Pl*) and potassium feldspar (*Kfs*), respectively. Note the flame perthite in K-feldspar.

Hornblende: Strongly pleochroic hornblende (0–20 vol. %) is coloured from yellowish green to bluish green. It is represented by magnesio-hastingsite and edenite (X_{Mg} : 0.52–0.62) which form tabular or irregular-shaped porphyroclasts, measuring up to 2 mm in length. Some porphyroclasts have simple and lamellar {100} twinning or cleavage {110} in two directions that intersect at approximately 60° and 124° . Zoned hornblende crystals, with pale-green cores (edenite) and bluish-green edges (magnesio-hornblende) are found. They often show a poikilitic texture, commonly with inclusions of quartz, biotite, titanite and opaques (Fig. 3.7A). The hornblende is in part replaced by chlorite and epidote, particularly along the rims.

Biotite: Flakes of biotite (X_{Fe} : 0.40–0.67; ~5 vol. %) are pleochroic from yellowish to green- or dark-brown. The size of the crystals reaches up to 0.5 mm. Biotite is commonly bent

with irregular grain boundaries. Its flakes are distributed along the foliation in between the interstices of porphyroclasts and often associated with titanite, allanite and opaque minerals. There are local thin trails of dusty biotite. Inclusions of zircon and patches of retrograde chlorite are frequent.

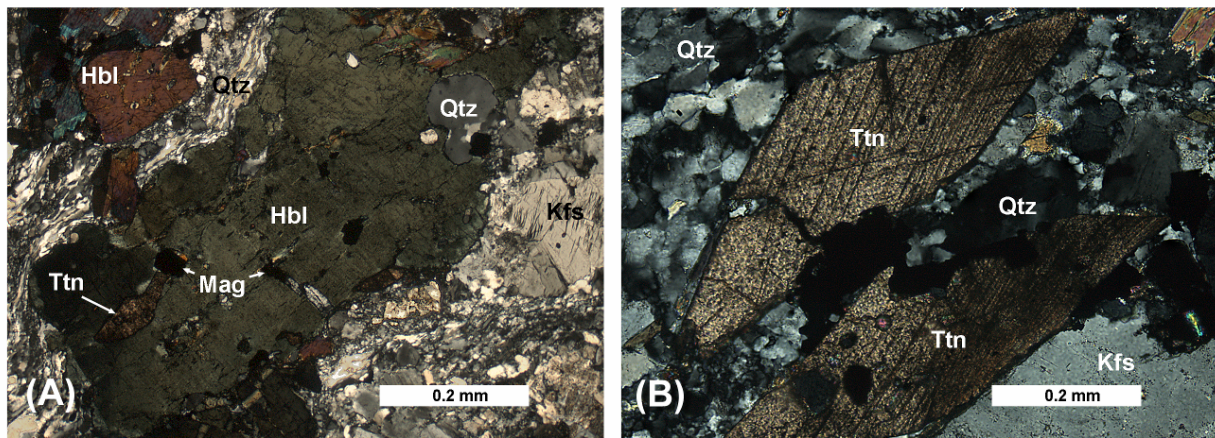


Figure 3.7: Photomicrographs in cross-polarized light of the deformed biotite granitoid. (A) Poikilitic hornblende (*hbl*) with titanite (*Ttn*), magnetite (*Mag*) and quartz (*Qtz*) inclusions. (B) Diamond-shaped euhedral titanite (*Ttn*) crystals, displaying prismatic cleavage on $\{110\}$.

Pale brown **titanite** has a size up to 2 mm in length. In general, it is euhedral, characterized by tabular and diamond-like morphology and elongated according to the foliation. Some crystals show a mildly pleochroism and are twinned. Locally, distinct prismatic cleavage on $\{110\}$ (Fig. 3.7B) and twins on $\{100\}$ are observed. **Allanite** grains are euhedral and ranging in size between 0.2 and 1 mm. They are light to dark-brown coloured, often zoned and twinned. Short prismatic and acicular crystals of **apatite** (up to 0.4 mm) appear either as inclusion within amphibole and feldspars or as isolated minerals distributed in the matrix. Euhedral crystals of **zircon** (less than 0.2 mm) are found as inclusions, producing pleochroic halos in biotite and amphibole. **Hematite** is the dominant oxide, with minor **ilmenite**. Both have been re-equilibrated below the solidus and often wrapped by a corona of titanite. Weakly pleochroic **epidote** is colourless to pale-yellow. Epidote crystals are poorly-shaped and their size ranges from 0.2 to 0.7 mm. They commonly rim allanite and replaced plagioclase and hornblende. Grey-green **chlorite** forms at the expense of biotite.

3.3 Mega feldspar granitoid

Sixteen samples of mega-feldspar granitoid are analyzed, eight collected from Bamoungoum locality (BM-1: BM-1a: BM-2: HO-1: KE-1: KO-12: DML-1: DML-1a: DML-2), three from Kobikong locality (BNF-27: BN-1: BN-2), two from Tesse locality (TE-2: TE-6) and two from Tsêla locality (TS-1: TS-2).

The mega feldspar granitoid shows a porphyritic granular structure. Its characteristic feature is the presence of large white or light pink potassium feldspar crystals (2 to 8 cm in length) with respectable twinning and zonation, which are suspended in a groundmass of finer grains of quartz, K-feldspar, plagioclase, biotite, with titanite, allanite, apatite, iron-oxides, zircon and monazite as accessory phases (Fig. 3.8A). Secondary minerals such as chlorite, sericite and epidote are also present.

Commonly, cracks and recrystallization in the course of brittle deformation influence can be observed, with in some cases K-feldspar and plagioclase being fractured, quartz being elongated and biotite aligned along shear planes. Cracks in the feldspars are frequent, filled by epidote.

Potassium feldspar: Subhedral potassium feldspar (24–40 vol. %) occurs as megacrysts ($\text{Or}_{92-95}\text{Ab}_{8-5}$), but scarce interstitial crystals are also found in the groundmass. There is no difference in composition between megacrysts and matrix K-feldspar. It is frequently lath-shaped or tabular microcline showing straight or embayed grain borders, association of cross-hatched and carlsbad twin patterns, and locally compositional zoning. Irregular distributed tiny strings of perthite exsolutions are in some places observed (Fig. 3.8B). At the crystal rims adjacent to plagioclase, quartz vermicules are sporadically found in plagioclase, forming myrmekite texture. K-feldspar often encloses euhedral tabular plagioclase, quartz and apatite. Varying extents of replacement of the potassium feldspar by patches of sericite that tend to be concentrated in the core are observed.

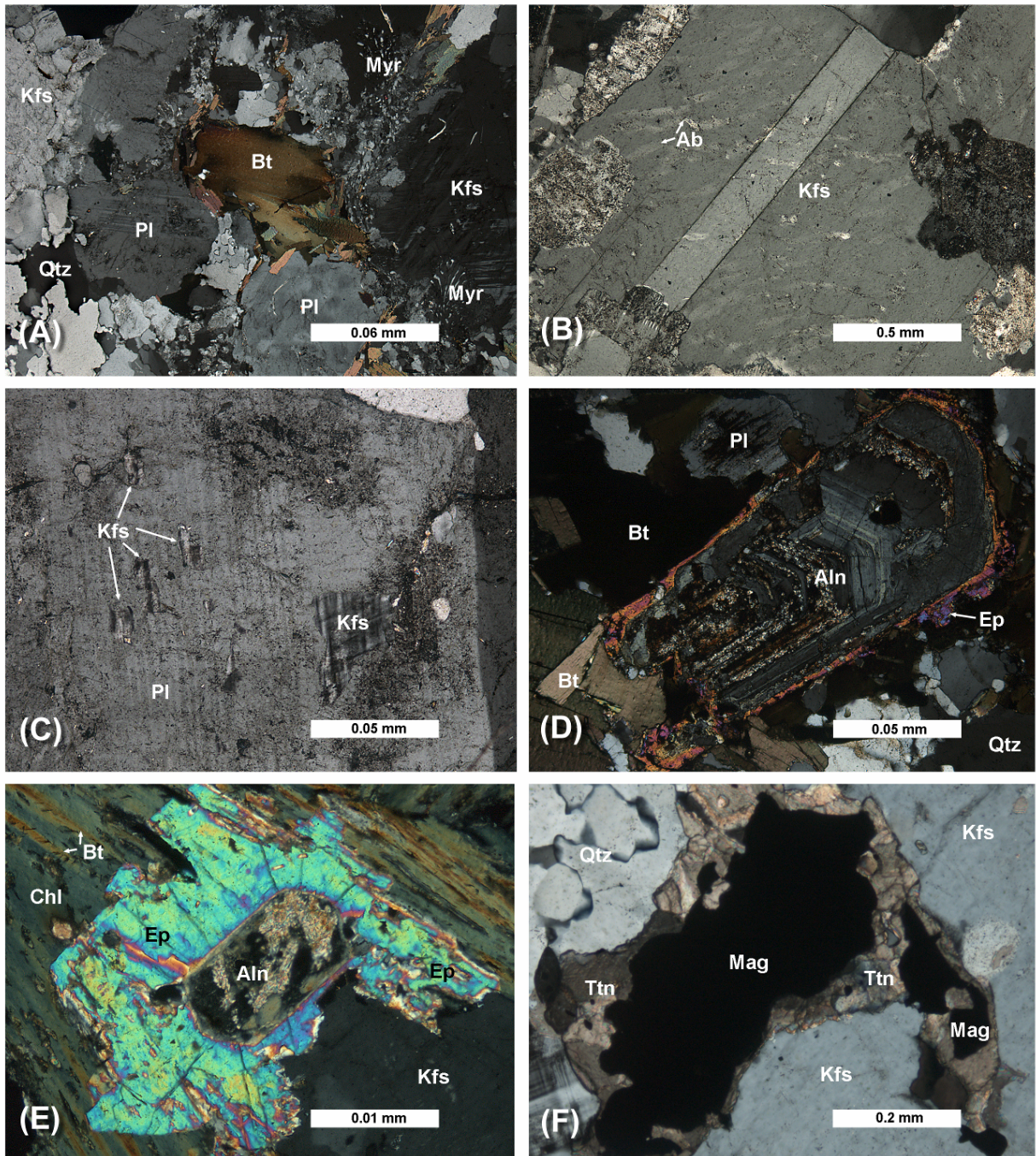


Figure 3.8: Photomicrographs in cross-polarized light of the mega feldspar granitoid. **(A)** Porphyritic granular structure. **(B)** Lath-shaped potassium feldspar (*Kfs*) displaying string perthite (*Ab*). **(C)** Lath-shaped plagioclase (*Pl*) with patches of K-feldspar (microcline). **(D)** Zoned allanite (*Aln*) rimmed by epidote (*Ep*). **(E)** Retrograde development corona of epidote (*Ep*) around allanite (*Aln*), both surrounded by chlorite (*Chl*). **(F)** Magnetite (*Mag*) rimmed by retrograde titanite (*Ttn*).

Quartz: Inequigranular quartz (15–25 vol. %) appears rarely isolated. It forms elongated crystals which measure from 0.2 to 2.5 mm in length, displaying undulose extinction and in some cases chessboard pattern subgrains as common features. The grain boundaries are irregular.

Along the zones of intensive shearing, low-temperature marginal recrystallization of quartz forming fine-grained aggregates is observed in the narrow rims. These fine-grained quartz grains often corrode feldspar crystals.

Plagioclase: Tabular plagioclase crystals (22–25 vol. %) are chiefly oligoclase along with subordinate albite ($An_{9-28}Ab_{90-61}$), showing distinct albite twin lamellas that are frequently combined with carlsbad twins. Locally, pericline-law twins formed over the pre-existing albite twinning are discretely concentrated along crystal rims. The plagioclase has subhedral to euhedral forms with embayed or straight outlines. The grain size is varying from 0.6 mm up to 2.5 cm in length. Zoned plagioclase with strong increase of the An-contents from core (An_4Ab_{95}) to rim ($An_{17}Ab_{82}$) is not rare. There are patches of microcline as exsolutions (Fig. 3.8C). Small amounts of earlier-formed of biotite, quartz, and apatite are found as inclusions. Several degrees of sericitization and saussuritization are observed in the course of alteration processes, and in some cases the plagioclase crystals are completely dusted, due to the alteration.

Biotite: Subhedral flakes of biotite (~ 5 vol. %) between 0.4 and 1.5 mm in length are often corroded at their border, except when they are hosted by K-feldspar and plagioclase. Biotite crystals show intensive pleochroism (X_{Fe} : 0.53–0.82; z: dark brown-yellow brown and x: brown-pale brown). Commonly, biotite in the groundmass forms aggregates, mantling crystals of K-feldspars and plagioclase. In some places, biotite is recrystallized in fine grains which are associated with fine-grained quartz along shear planes. The biotite crystals are rich in pleochroic halos revealing inclusions of zircon and/or monazite. In addition, apatite inclusions are not rare. Biotite flakes are often partially or totally chloritized with concentration of opaques along the cleavages.

Zoned and twinned **allanite** is characterized by yellowish brown to brown pleochroism and commonly rimmed by an epidote phase (Fig. 3.8D and E). Its grains are euhedral, elongated or short prismatic and reach the dimension of 1.7 mm in length. **Titanite** occurs either as subhedral to euhedral crystals which range in size from 0.3 to 1.2 mm in length or as poorly-shaped crystals mantling opaques (Fig. 3.8F). In most cases, the occurrence of **apatite** crystals reaching the size of 0.3 mm in length is confined to inclusion within feldspars, biotite and titanite. **Zircon** is found as small well-defined crystal inclusions accompanied by pleochroic

halos mainly in biotite. **Magnetite** and **ilmenite** are the iron-oxide minerals. They occur as distinct isolated crystals (up to 2.2 mm in length) in the groundmass or as aggregates together with biotite, titanite and rare hornblende. They are often observed as inclusions in the feldspar megacrysts. Owing to the later alteration overprint, biotite is locally replaced by **chlorite**, whereas **sericite** and **epidote** are developed from former feldspars and allanite, and additionally fill narrow fissures in feldspar crystals.

3.4 Two-mica granitoid

A total of nine samples of the two-mica granitoid is examined here, of which three samples come from Bamoungoum locality (BM-3: BM-4: BM-5), five samples from Bapi locality (BP-1: TA-9: BAN-6: BF1: BF2) and one sample from Kobikong locality (NO-30).

The two-mica granitoid is light greyish colored and in general fine- to medium-grained. It has a granular magmatic texture and consists of potassium feldspar, quartz, plagioclase, with subordinate amounts of muscovite, biotite and occasionally garnet (Fig. 3.9). Zircon, monazite, apatite and ilmenite are accessories, while sericite and chlorite are alteration products.

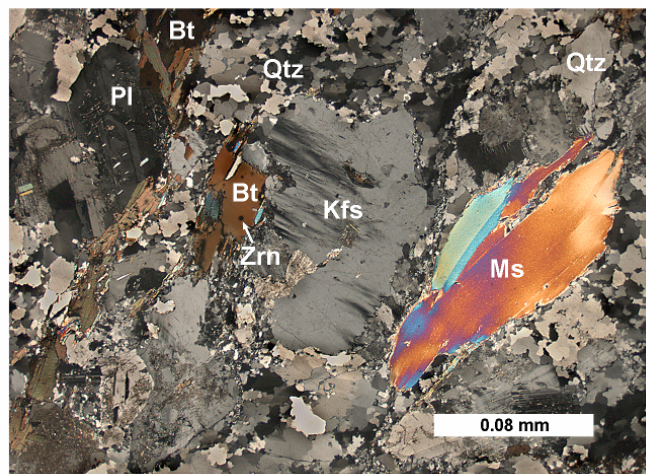


Figure 3.9: Photomicrograph in cross-polarized light of the two-mica granitoid, showing a medium-grained magmatic structure.

Potassium feldspar: Subhedral to anhedral potassium feldspar (~41 vol. %), either microcline or occasionally orthoclase ($\text{Or}_{81-96}\text{Ab}_{19-4}$) is the major component. It occurs as medium-grained laths or scarcely tabular grains of 1–4 mm in length and usually has embayed

outlines. The K-feldspar exhibits distinct cross-hatched and carlsbad twins. Some crystals show film, flame and patchy perthitic albite intergrowths (Fig. 3.10 A, B and C). Occasionally, the contact between K-feldspar and plagioclase crystals is characterized by myrmekitic texture. Besides small euhedral inclusions of plagioclase, quartz and apatite inclusions are also observed. Potassium feldspar alteration to sericite is common, but the extent of replacement varies, with K-feldspar cores showing a high concentration of sericite.

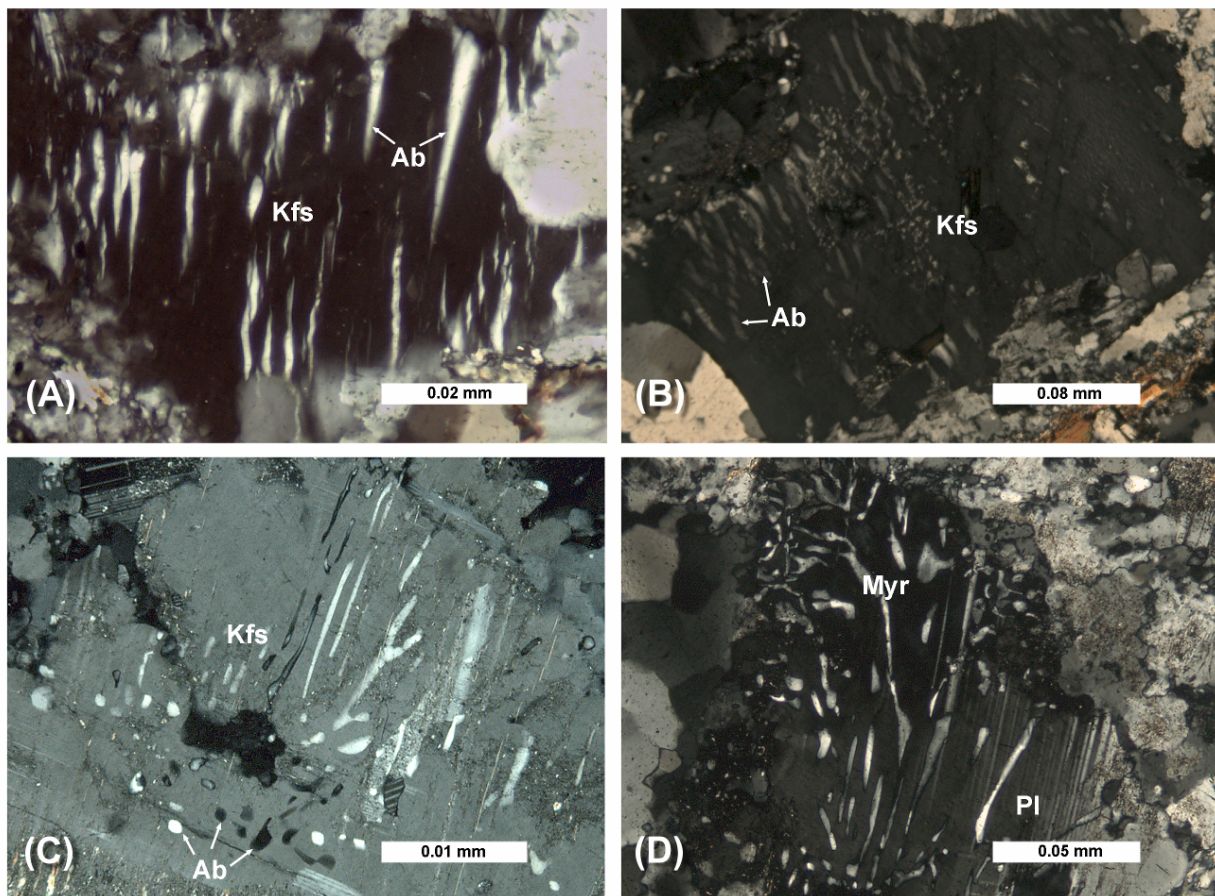


Figure 3.10: Photomicrographs in cross-polarized light of the two-mica granitoid. (A) Potassium feldspar (*Kfs*) flame perthite (albite: *Ab*). (B) K-feldspar (*Kfs*) film perthite (*Ab*). (C) K-feldspar (*Kfs*) with patches of perthite (albite: *Ab*). (D) Myrmekitic intergrowth (*Myr*) within a plagioclase (*Pl*).

Quartz: Ubiquitous quartz (~ 32 vol. %) usually occurs as separate crystals (0.1–3 mm) or as irregular aggregates with very variable sizes, filling interstices between the feldspar crystals. Some large crystals of quartz display lamellas with subgrain patterns and undulatory extinction as a result of strain processes. On the other hand, subhedral earlier-formed quartz grains appear as small inclusion in feldspars. Quartz intergrowths are observed forming

myrmekites with plagioclase which is preferentially in contact with adjacent K-feldspar (Fig. 3.10D).

Plagioclase: Flattened tabular plagioclase (~ 22 vol. %) is present in subhedral to euhedral forms and measures from 1 to 3 mm in length. Albite polysynthetic twinning is common. Sporadically, pericline twins are also observed along the rim of some crystals. Plagioclase is albite to oligoclase ($An_{3-22}Ab_{96-77}$), commonly antiperthitic showing patches of microcline. It often shows reverse zonation (core: $An_{3-5}Ab_{96-94}$ \rightarrow rim: $An_{12-14}Ab_{87-85}$). Fine-grained plagioclase crystals (about 0.3 mm long) are frequently associated with fine-grained quartz. Locally, plagioclase crystals suffer marginal corrosion from fine-grained quartz, yet others are mantled by small muscovite flakes. Sericitization of plagioclase is common, frequently at the core of the crystal.

Muscovite: Subhedral to anhedral Muscovite (X_{Fe} : 0.52–0.82; ~ 3 vol. %) shows typical flaky grains either scattered or hosted by plagioclase and biotite. Its grains are colourless with irregular to straight margins and range from 0.6 to 2 mm in length. Individual muscovite lamellas are rare (Fig. 3.11); they form aggregates that are in some cases accompanied by biotite. Fine grained muscovite commonly surrounds K-feldspar and plagioclase. Apatite inclusions are often in muscovite.

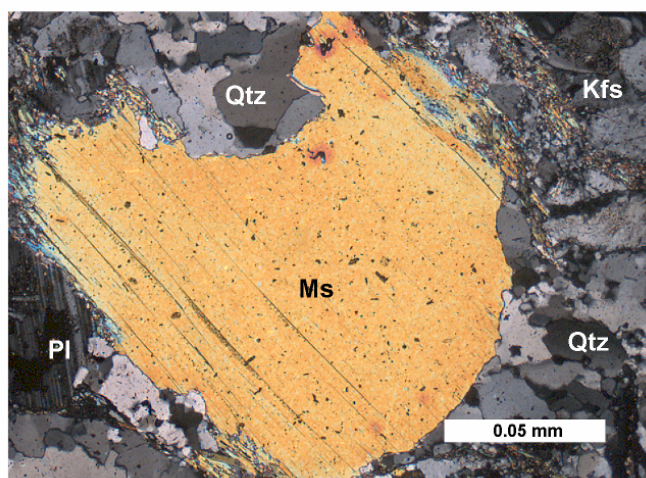


Figure 3.11: Photomicrograph in cross-polarized light of the two-mica granitoid, displaying a flaky muscovite (Ms) corroded by quartz (Qtz).

Biotite: subhedral to anhedral Fe-rich biotite (X_{Fe} : 0.64–0.80; ~2 vol. %) has a varying grain size of up to 2 mm and occurs as separate crystals or as intergranular aggregates. The lamellas are perfectly pleochroic, changing the colour from light green to yellowish green along z axis and yellowish brown to dark brown along x axis. Biotite flakes often contain inclusions of zircon and/or monazite and apatite. Occasionally, biotite is partially replaced by chlorite with concentration of magnetite and ilmenite along cleavages.

Garnet: euhedral garnet (~1 vol. %) is almandine–spessartine (X_{Fe} : 0.99; X_{Mn} : 0.46–0.56) and is sparsely distributed. It is found only in small proportion in sample TA-9. Garnet occurs as colourless to whitish, small and rounded grains and has a diameter of 1–5 mm. Garnet crystals are often fractured with muscovite and chlorite developing along the fractures, and are almost free of inclusions (Fig. 3.12A).

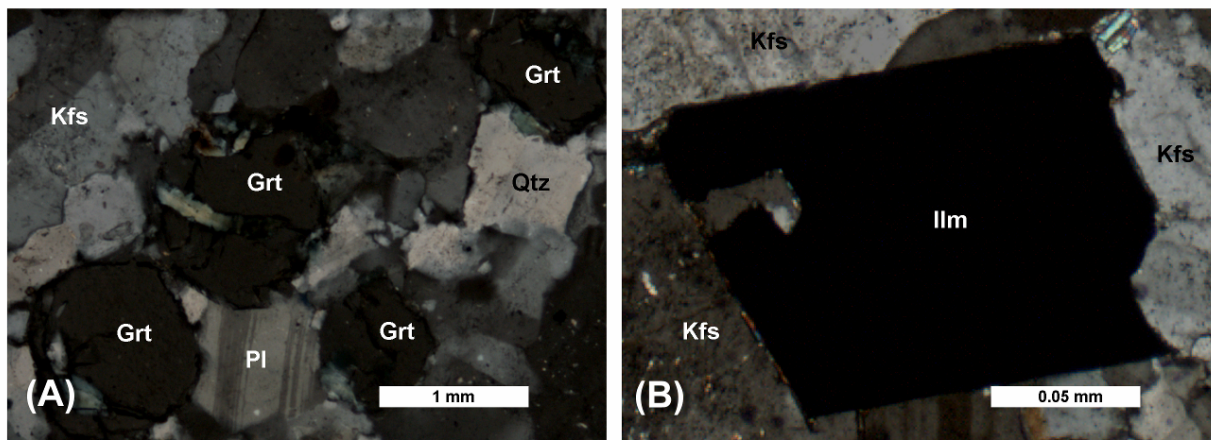


Figure 3.12: Photomicrographs in cross-polarized light of the two-mica granitoid. **(A)** Rounded garnet (*Grt*) grains. **(B)** Euhedral isolated ilmenite (*Ilm*).

Zircon and **monazite** are found as euhedral crystals usually confined to inclusions in biotite and producing typical brownish or purplish pleochroic halos (Fig. 3.9A). **Apatite** occurs as stubby prisms commonly included in feldspars and muscovite, while **ilmenite** crystals occur isolated (Fig. 3.12B), as inclusion within feldspars and muscovite or alteration product of biotite. The common minerals of retrograde origin include **chlorite** which replaces former biotite and **sericite**, formed at the expense of feldspars.

To conclude, the main petrographic and mineralogical characteristics of the Bafoussam granitoids are summarized in Table 3.1. These granitoids display quite similar minerals composition, with exception of the two-mica granitoid which additionally has primary muscovite and rare igneous garnet. In each granitoid group, minerals have been crystallized during two phases of the evolution: (1) a magmatic phase during which the main minerals, potassium feldspar, quartz, plagioclase, biotite, hornblende, muscovite, garnet and the accessory minerals have been formed; and (2) a late-magmatic phase that resulted in a transformation of minerals present (e.g., oxide mineral → titanite, biotite → oxide mineral). The transformation of the primarily crystallized minerals through alteration is moreover observed and the minerals such as chlorite, sericite and epidote have formed at the expense of biotite, feldspars, hornblende and allanite, respectively.

The sequence of crystallization deduced from the petrographical observations is summarized in Figure 3.13. Liquidus minerals are oxides (magnetite and/or ilmenite), and apatite as they are included in the other minerals. Quartz and feldspar are commonly the last minerals to crystallize.

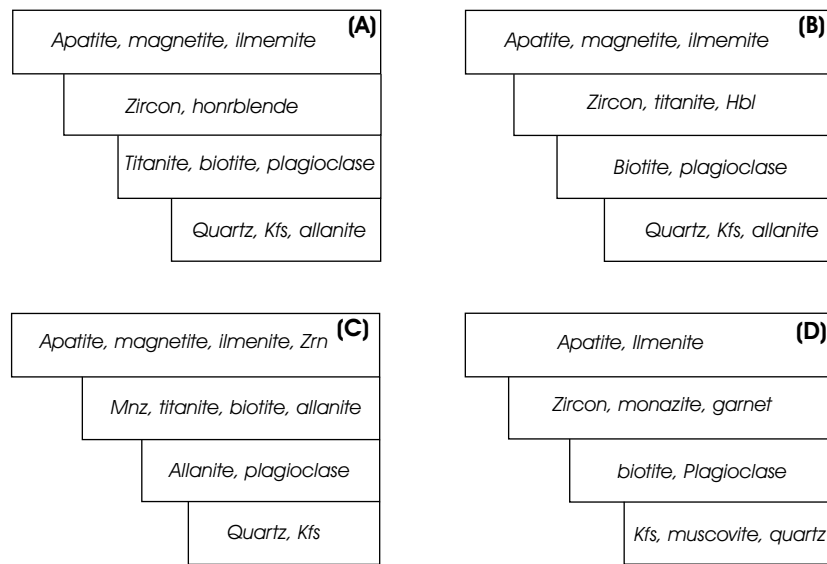


Figure 3.13: Sequence of crystallization in the different Bafoussam granitoid groups as deduced from the petrographical observations. **(A)** Biotite granitoid, **(B)** deformed biotite granitoid, **(C)** mega feldspar granitoid, **(D)** two-mica granitoid. Mineral abbreviations: *Zrn*: zircon; *Mnz*: Monazite; *Hbl*: hornblende; *Kfs*: potassium feldspar.

Table 3.1: Summary of petrographic characteristics and modes of the Bafoussam granitoids

Notes: -: absent; x: present; xx: common; s: secondary; Kfs: orthoclase and/or microcline; Or: orthoclase; Ab: albite

$X_{Mg} = Mg/(Mg + Fe^{2+})$ and $X_{Fe} = Fe^{2+}/(Mg + Fe^{2+})$, both calculated in molar ratios from microprobe analyses

	Biotite granitoid	Deformed biotite granitoid	Mega feldspar granitoid	Two-mica granitoid
Texture and structure	Medium- to coarse grained (up to 1cm) and heterogranular, but also fine-grained; generally massive; host hornblende-bearing enclaves; presence of late aplite, pegmatite and quartz dykes	Granoblastic, medium- to coarse grained (Kfs up to 2 cm); weakly to strongly tectonic foliation defined by orientation of hornblende, biotite, potassium feldspar, metagabbro and phyllonite? enclaves	Porphyritic (Kfs up to 8cm), strong alignment of megacrysts; magmatic and tectonic foliation locally superimposed; locally augengneiss texture	Typically medium-grained (~4 mm); unfoliated to weakly foliated; presence of biotite-rich (surmicaceous) enclaves
Mineralogy (vol. %)				
Potassium feldspar	35–55 ($Or_{92-97}Ab_{8-3}$)	5–40 ($Or_{91-96}Ab_{9-4}$)	24–40 ($Or_{92-95}Ab_{8-5}$)	~41 ($Or_{81-96}Ab_{19-4}$)
Quartz	20–35	10–35	15–25	~32
Plagioclase	~20 ($An_{17-35}Ab_{82-64}$)	20–40 ($An_{9-28}Ab_{90-71}$)	22–25 ($An_{0-28}Ab_{90-62}$)	~22 ($An_{3-22}Ab_{96-77}$)
Biotite	~5 ($X_{Fe}: 0.44-0.51$)	~5 ($X_{Fe}: 0.40-0.67$)	~5 ($X_{Fe}: 0.53-0.82$)	~2 ($X_{Fe}: 0.64-0.80$)
Hornblende	5–10 ($X_{Mg}: 0.50-0.57$); not ubiquitous, magnesio-hastingsite to edenite	~20 ($X_{Mg}: 0.52-0.62$); not omnipresent, magnesio-hastingsite to edenite	—	—
Primary muscovite	—	—	—	~3 ($X_{Fe}: 0.52-0.82$)
Igneous garnet	—	—	—	1 ($X_{Fe}: 0.99$; $X_{Mn}: 0.46-0.56$), almandine-spessartine
Accessories				
Apatite	xx	xx	xx	x
Titanite	xx	xx	x	—
Allanite	x	x	x	—
Zircon	xx	xx	xx	x
Monazite	—	—	x	x
Ilmenite	x	x	x	x
Magnetite	x	x	x	—
Chlorite	s	s	s	s
Sericite	s	s	s	s
Epidote	s	s	s	—
Classification (using CIPW norm and major element data)	Mostly syenogranite and subsidiary alkali-feldspar granite, monzogranite and quartz-monzonite	Mainly syenogranite and secondary alkali-feldspar granite, monzogranite, granodiorite, quartz-syenite, quartz-monzonite, quartz-monzodiorite	Syenogranite and monzogranite, subordinate granodiorite	Alkali-feldspar granite and syenogranite

4 MINERAL CHEMISTRY

Chemical compositions and structural formulas have been determined for a number of minerals within 27 selected samples of the Bafoussam granitoids using electron microprobe (EMP) analysis. The microprobe analysis has been focussed on biotite, muscovite, garnet, hornblende and feldspars, as these minerals potentially contain information about the magma's chemical evolutionary path. Representative microprobe results are listed in Tables A.2.1–A.2.6b, Appendix A.2 and the analytical procedures are given in the Appendix A.1.2. Mineral formulas have been calculated with the computer software Framework IV (Ashton Tate GmbH).

4.1 Micas: biotite and muscovite

According to their classification (Rieder et al., 1998), micas are phyllosilicates in which the unit structure contains one octahedral sheet between two opposing tetrahedral sheets. The simplified crystal-chemical formula of micas can be written as $IM_{2-3} \square_{1-0} T_4 O_{10} A_2$ (Rieder et al., 1998; Rieder, 2001), where labels represent the following chemical elements: I is generally K, Na, Ca, and rarely Cs, NH₄, Rb, Ba; M is commonly Li, Fe²⁺ or Fe³⁺, Mg, Al, Ti, and rarely Mn²⁺ or Mn³⁺, Zn, Cr, V; \square represents a vacancy; T is usually Al, Fe³⁺, Si, and rarely Be, B; and A is commonly F, OH, and rarely Cl, O (oxy-micas), S.

4.1.1 Biotite

Biotite refers to a series of true trioctahedral dark micas with range of compositions between the annite ($KFe^{2+}_3AlSi_3O_{10}[OH]_2$) – phlogopite ($KMg_3AlSi_3O_{10}[OH]_2$) and siderophyllite ($KFe^{2+}AlAl_2Si_2O_{10}[OH]_2$) – eastonite ($KMg_2AlAl_2Si_2O_{10}[OH]_2$) joints (Rieder et al. 1998).

Biotite is present as a common ferromagnesian silicate in all the granitoid types of the Bafoussam area where it occurs as an early- to late-stage crystallization mineral. It forms euhedral to subhedral discrete flakes, measuring up to 2 mm in length or aggregates of several grains intimately associated with muscovite, hornblende, titanite and Fe-Ti oxides. Biotite often

contains inclusions of zircon, apatite, titanite, ilmenite (magnetite). Biotite flakes are frequently altered, either partially along its {001} cleavages or completely to chlorite. Table A.2.1 in the Appendix A.2 reports the compositions and the structural formulas of the analyzed biotites. The structural formulas of biotite were calculated under anhydrous conditions on the basis of twenty-two oxygens. The total iron is represented as Fe^{2+} .

The chemical composition of biotite from the studied Bafoussam granitoids indicates pronounced variations in total Al contents, Mg contents and $\text{Fe}^{2+}/(\text{Fe}^{2+} + \text{Mg})$ values. For the biotite granitoid, biotite has mean total Al values of 2.476–2.810 atoms per formula unit (a.p.f.u), $\text{Fe}^{2+}/(\text{Fe}^{2+} + \text{Mg})$ ratios of 0.436–0.510 and Mg values of 2.486–2.865 a.p.f.u. In the deformed biotite granitoid, the biotite has total Al, $\text{Fe}^{2+}/(\text{Fe}^{2+} + \text{Mg})$ and Mg values of 2.476–2.987 a.p.f.u, 0.411–0.666 and 1.594–3.001 a.p.f.u, respectively, whereas the biotite from the mega feldspar granitoid contains 2.704–3.404 a.p.f.u of total Al, 0.526–0.820 of $\text{Fe}^{2+}/(\text{Fe}^{2+} + \text{Mg})$ ratios and 0.820–2.393 a.p.f.u of Mg. Finally, the biotite from the two-mica granitoid is characterized by high and variable total Al contents (2.888–3.433 a.p.f.u) as well as moderate $\text{Fe}^{2+}/(\text{Fe}^{2+} + \text{Mg})$ and Mg values in the range of 0.637 to 0.808 and 0.873 to 1.802 a.p.f.u, respectively.

The data of the analyzed biotites are presented in the idealised annite – phogopite – siderophyllite – eastonite quadrilateral (Fig. 4.1A), which shows the $\text{Fe}^{2+}/(\text{Fe}^{2+} + \text{Mg})$ and total Al ($\sum\text{Al}$) compositional relationships of trioctahedral micas from igneous rock suites (Speer, 1984). This quadrilateral diagram also offers, by these two variables, the degree of peraluminosity and the redox state of the mica host rocks. In Figure 4.1A, the biotite samples mostly plot towards the annite – siderophyllite joints of the quadrilateral, indicating general high $\text{Fe}^{2+}/(\text{Fe}^{2+} + \text{Mg})$ values and total Al contents, respectively, of 0.411–0.820 and 2.476–3.433 a.p.f.u of biotites from the Bafoussam granitoids. With $\text{Fe}^{2+}/(\text{Fe}^{2+} + \text{Mg}) \geq 0.33$, all these samples contain biotite (*sensu stricto*) in the sense of Deer et al. (1962) and are classified as meroxenes and lepidomelanes except some mega feldspar granitoid samples which plot in the field of siderophyllite, following the terminology of biotite after Tröger (1982) (Fig. 4.1). Using the nomenclature of Foster (1960), they have compositions of Fe^{2+} -biotites.

The generation of the biotites is obtained using the $(\text{FeO}^* + \text{MnO}) - 10\text{TiO}_2 - \text{MgO}$ ternary diagram (Fig. 4.1B) after Nachit (1986), which distinguishes between primary or magmatic

biotites, re-equilibrated primary or late-magmatic biotites and secondary or post-magmatic biotites. The investigated biotites indicate compositions lying mainly within the re-equilibrated primary biotites field, even if the transformations are not always visible under the optic microscope. However, most samples of the two-mica granitoid and less samples of the mega feldspar granitoid display composition of primary biotites.

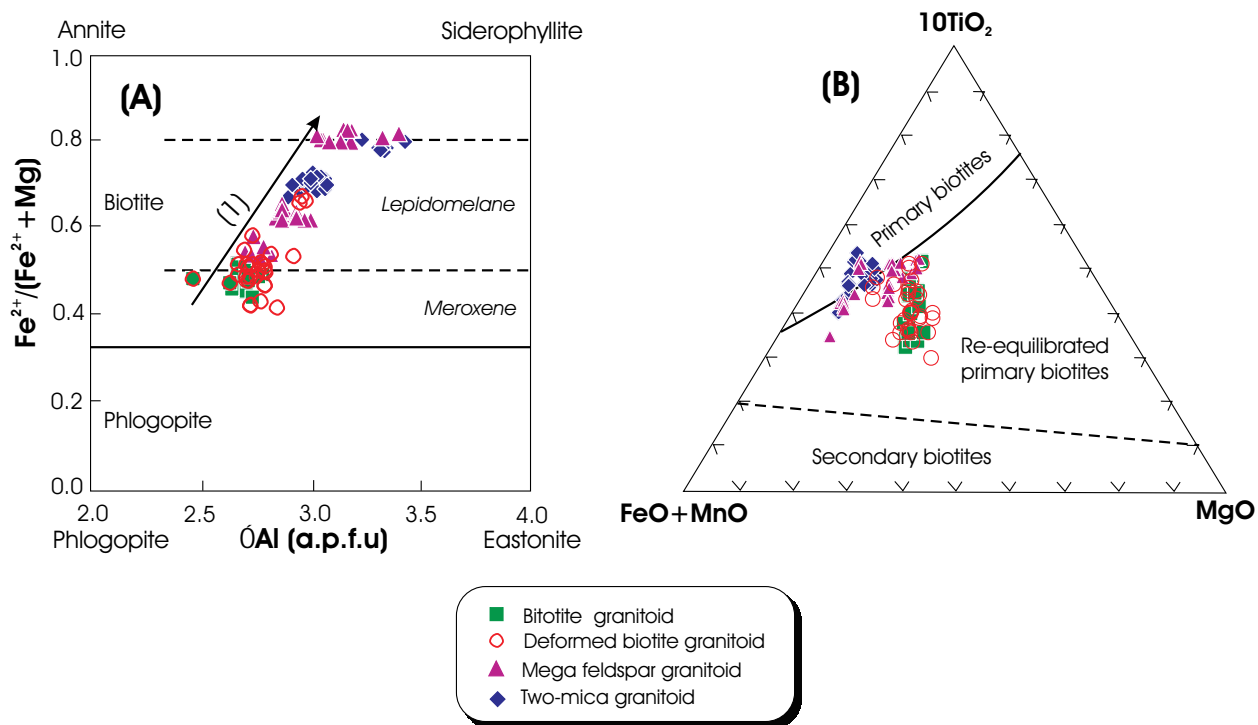


Figure 4.1: (A) Nomenclature of biotite of the Bafoussam granitoids expressed in the $\text{Fe}^{2+}/(\text{Fe}^{2+} + \text{Mg})$ versus ΣAl (a.p.f.u.) diagram also known as the annite – phlogopite – siderophyllite – eastonite quadrilateral. Fe^{2+} : total iron atoms ($\text{Fe}^{2+} + \text{Fe}^{3+}$) and ΣAl : total Al (${}^{[4]}\text{Al} + {}^{[6]}\text{Al}$). The subdivision of tetrahedral micas (heavy line: Deer et al., 1962) and the biotite classification (dashed lines: Tröger, 1982) are shown. (B) Classification based on the $(\text{FeO}^* + \text{MnO})$ – 10TiO_2 – MgO ternary diagram of Nachit (1986), showing the position of the Bafoussam granitoid biotites mostly within the re-equilibrated primary (post-magmatic) biotites field. FeO^* : total iron oxides ($\text{FeO} + \text{Fe}_2\text{O}_3$). Trend (1) reflects the significant contribution of crustal component during the granitoids genesis.

The late- to post-magmatic evolution of primary biotites generally leads to the increase of aluminium (${}^{[6]}\text{Al}$) and magnesium and to the decrease of titanium concentration (Nachit, 1986). The re-equilibration of the investigated biotites may be related to: (1) the late subsolidus reactions associated with chloritisation of biotite; and (2) the plastic deformation that has variably overprinted the studied granitoids hosting the biotites. During this deformation, the biotite occasionally experienced kink banding and was locally recrystallized to small flakes.

Moreover, the Ti of biotite is controlled by the temperature of crystallisation (Guidotti et al., 1977; Guidotti, 1984; Nachit, 1986; Patiño-Douce, 1993) and the titanium saturating phase such as titanite, ilmenite and rutile (Puziewicz and Koepke, 1991). The solubility of Ti increases with an increase in temperature, whereas the presence of a Ti-rich mineral increases the Ti content of biotite. Using this temperature–Ti relationship for the granitoids under study, the biotite granitoid (Ti: 0.176–0.388 a.p.f.u), deformed biotite granitoid (Ti: 0.157–0.390 a.p.f.u), mega feldspar granitoid (Ti: 0.206–0.404 a.p.f.u) and the two-mica granitoid (Ti: 0.216–0.459 a.p.f.u) Ti contents overlap, suggesting that they seem to have been crystallized at quite similar temperatures. Monier and Robert (1986) argued that the Ti content of biotite in granitoid rocks also depends on the Ti content of the magma, the lower Ti-saturation boundary being constrained by the equilibrium with amphibole. The colour of the biotite seems also to be related to the Ti content, as well as the Mg and Fe ones (Deer et al., 1962; Lalonde and Bernard, 1993). The roughly brownish tinge of the studied biotites reflects then the relative high total Fe and Ti contents, hence a poor Mg content.

Numerous studies carried out on igneous biotites have demonstrated that chemical compositions of biotite in igneous rocks can be employed as a tool for the tectonomagmatic and petrogenetic discrimination (Nachit et al., 1985; Ague and Brimhall, 1988; Lalonde and Bernard, 1993; Abdel-Rahman, 1994). Since biotite continuously equilibrates with the host magma, its composition reflects the composition of the magma from which it crystallized and indirectly the nature of the protolith.

Nachit et al. (1985) proposed a classification system on the basis of total Al and Mg in structural formulas to discriminate the biotite samples into different fields, alumino-potassic, calc-alkaline, subalkaline, alkaline and peralkaline, according to the host rocks magma natures. In the total Al against Mg (a.p.f.u) (Fig. 4.2A), the biotites of the Bafoussam granitoids have compositions similar to those of calc-alkaline granites of Nachit et al. (1985) and display a negative correlation between total Al and Mg.

Furthermore, several diagrams based on major elements FeO^* , MgO and Al_2O_3 of biotite minerals have been introduced by Abdel-Rahman (1994) to differentiate the biotite compositions of plutonic rocks that crystallized from three distinct magma types, hence tectonic settings: (1)

anorogenic extension-related peralkaline granites; (2) calc-alkaline I-type orogenic suites; and (3) peraluminous rocks including S-type orogenic granites. Amongst these diagrams, the ternary $\text{FeO}^*-\text{MgO}-\text{Al}_2\text{O}_3$ diagram is chosen here, as it best provides information about the variations in peraluminosity and the oxidation-reduction state of the rock hosting the mica. In the $\text{FeO}^*-\text{MgO}-\text{Al}_2\text{O}_3$ (wt. %) triangular plot (Fig. 4.2B), biotite samples from the investigated granitoids define a linear trend between the fields of peraluminous and calc-alkaline granites with the biotite granitoid and the deformed biotite granitoid being more calc-alkaline and the two-mica granitoids and the mega feldspar granitoid being more peraluminous.

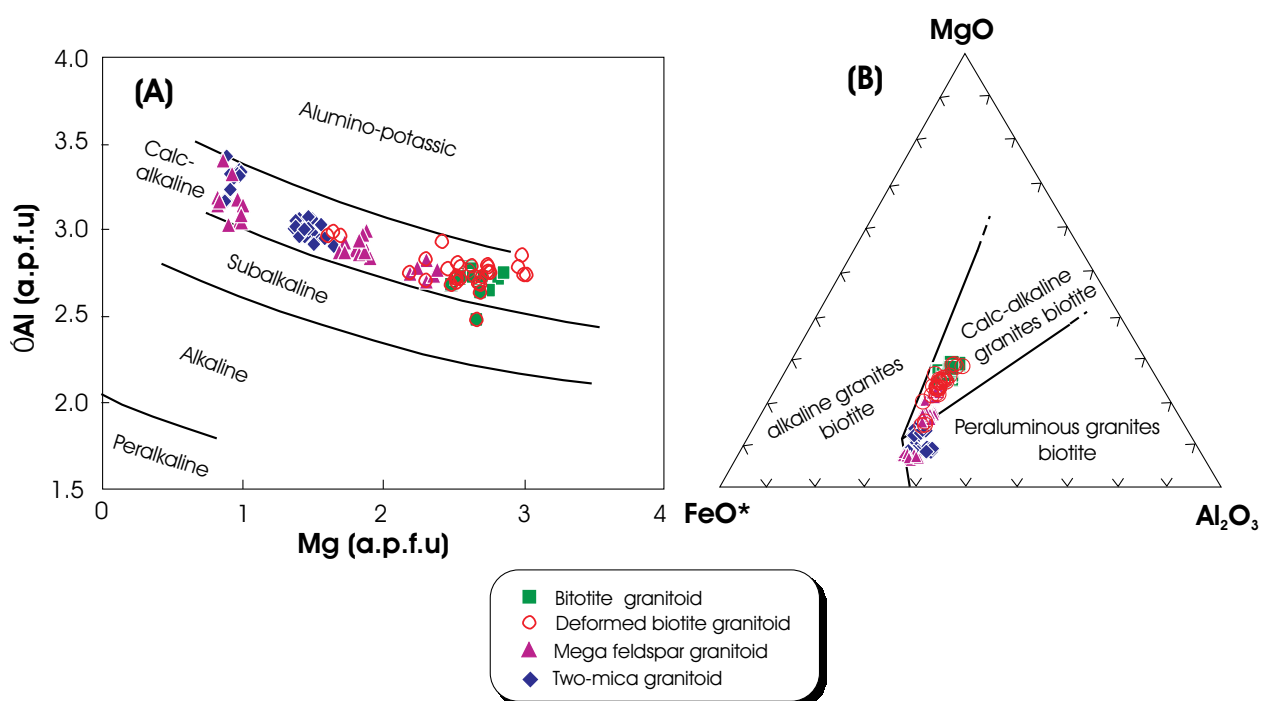


Figure 4.2: Biotite compositions of the Bafoussam granitoids: (A) Classification Mg versus ΣAl (a.p.f.u) diagram after Nachit et al. (1985), demonstrating the calc-alkalic affinity of the rocks hosting the analyzed biotites. ΣAl = total Al ($^{[4]}\text{Al} + ^{[6]}\text{Al}$). (B) $\text{FeO}^*-\text{MgO}-\text{Al}_2\text{O}_3$ (wt. %) biotite discrimination diagram modified after Abdel-Rahman (1994), showing the calc-alkaline and peraluminous characters of the Bafoussam granitoids. FeO^* = total iron ($\text{FeO} + \text{Fe}_2\text{O}_3$).

The Bafoussam biotite compositions in the quadrilateral (Fig. 4.1A) show a progressive increase principal of the total Al contents and of the $\text{Fe}^{2+}/(\text{Fe}^{2+} + \text{Mg})$ ratios of biotites from intermediate to evolved host granitoids, as illustrated by the trend (1). This trend compares closely to those observed in the Canadian Appalachian granites (Shabani et al., 2003), the Japanese ilmenite-series granites (Czamanske et al., 1981) and the Hercynian granite of northern Portugal (Konings et al., 1988). It is interpreted to indicate considerable contributions of crustal

material (metasediments) during the petrogenesis of the Bafoussam granitoid magmas, either by assimilation or anatexis. Moreover, the positive correlation between total Al and $\text{Fe}^{2+}/(\text{Fe}^{2+} + \text{Mg})$ is also consistent with the compositional trend of biotites from continental-collision related granites (Lalonde and Bernard, 1993).

On the other hand, the analyzed biotite samples commonly have higher ASI values [alumina saturation index = $\sum \text{Al}/(\text{Ca} + \text{Na} + \text{K})$] varying from 1.3 to 1.9 with the highest values appearing in biotite from two-mica granitoid. Such high values of ASI in biotite, in particular biotite coexisting with muscovite and other peraluminous minerals, are evident for increased alumina activity in the crystallizing magma (Zen, 1988).

The highest $\text{Fe}^{2+}/(\text{Fe}^{2+} + \text{Mg})$ ratio of the two-mica granitoid and mega feldspar granitoid biotites reflects the Mg-poor nature of the more felsic (or evolved) granitoid magma. The experimental investigations performed by Robert (1981) have shown that the incorporation of Al in a trioctahedral mica structure principally depends on Fe and Mg contents, and on temperature. The Al substitution is as higher as the temperature is lower, and the initial composition of mica more enriched in iron and hence deprived in Mg.

Among biotite compositions, the excellent negative total Al and Mg correlation depicted in Figure 4.2 is usually explained by a number of substitutions operating between four biotite end-members. According to Stussi and Cuney (1996), the calc-alkaline biotite compositions are mainly controlled by the following exchange schemes:

- (1) $\text{Mg} \leftrightarrow \text{Fe}$ (phlogopite – annite substitution: Speer, 1984)
- (2) $2^{2+}[6]\text{M}, 2^{[4]}\text{Al} \leftrightarrow [4]\square, 2^{[4]}\text{Si}$ along annite / phlogopite – MTS (tetrasilicic mica) join (Robert, 1981; Monier and Robert, 1986)
- (3) $3^{2+}[6]\text{M} \leftrightarrow 2^{[4]}\text{Al}, [6]\square$ along the annite / phlogopite–muscovite join (Robert, 1981; Monier and Robert, 1986).

4.1.2 Muscovite

The term muscovite or “white mica” broadly describes dioctahedral mica (Rieder et al., 1998), having muscovite (*sensu stricto*: $\text{KAl}_2\text{AlSi}_3\text{O}_{10}[\text{OH}]_2$), paragonite ($\text{NaAl}_2\text{AlSi}_3\text{O}_{10}$

[OH]₂), margarite ($\text{CaAl}_2\text{Al}_2\text{Si}_2\text{O}_{10} \text{[OH]}_2$) and celadonite ($\text{K}[\text{Mg}, \text{Fe}^{2+}][\text{Fe}^{3+}, \text{Al}]\text{Si}_4\text{O}_{10} \text{[OH]}_2$) as principal end-members.

The muscovite occurrence is restricted to the two-mica granitoid of the Bafoussam area. It forms large subhedral or euhedral crystals, having grain sizes of up to 2 mm in length and containing inclusions of accessory magmatic minerals. Muscovite crystals are generally isolated or imbricated, and parallel growths of muscovite and biotite are rarely encountered. Selected oxide components and atom concentrations of the examined muscovites are portrayed in Table A.2.2 in the Appendix A.2. The structural formulas were calculated on a dry condition basis assuming twenty-two oxygens and all the iron was considered as Fe^{2+} . End-member compositions in molecular proportions are presented respecting the margarite, paragonite, celadonite, and muscovite (*sensu stricto*) succession.

The analyzed white mica samples exhibit the following distinguished chemical contents, including Ti: 0.013–0.149 a.p.f.u, total Al: 4.744–5.724 a.p.f.u, Na: 0.049–0.149 a.p.f.u, Si: 6.099–6.378 a.p.f.u; the elements, Ca, Ba and Mn are present, but in negligible amounts. The white micas are dominated by the muscovite end-member in the range 77–90 mol. % followed by moderate celadonite (5–19 mol. %) and paragonite (3–9 mol. %) portions, and a negligible share of margarite (up to 0.1 mol. %).

In plutonic rocks, the magmatic or non-magmatic provenance of muscovite is a problem. Different criteria that distinguish between primary or magmatic, secondary or late- to post-magmatic and hydrothermal generations of muscovite have been established (Miller et al., 1981; Monier et al., 1984; Speer, 1984). Using these criteria together, the investigated muscovites have compositional ambiguities, displaying primary, secondary and hydrothermal compositions (Table 4.1). However, plotted in the Mg–Ti–Na (a.p.f.u) triangular diagram from Miller et al. (1981) that discriminates between primary and secondary muscovites, the Bafoussam two-mica granitoid muscovites fall within the primary muscovites field (Fig. 4.3A). Furthermore, in the $\text{FeO}^*-\text{TiO}_2-\text{MgO}$ (wt. %) compositional triangle modified after Monier et al. (1984), the analyzed muscovites occupy the magmatic muscovites field and follow the compositional trend described by the leucogranite magmatic muscovites of the Millevaches Massif in France (Fig. 4.3B).

Table 4.1: Comparison of the chemical compositions of the analyzed two-mica granitoid muscovites of the Bafoussam area with data of primary, secondary and hydrothermal muscovites compiled from Miller et al. (1981), Monier et al. (1984) and Speer (1984).

* Fe^{2+} = total Fe ($\text{Fe}^{2+} + \text{Fe}^{3+}$)

** Fe^{3+} values

Atoms (a.p.f.u)	Bafoussam two-mica granitoid muscovites	Primary muscovites	Secondary muscovites	Hydrothermal muscovites
Ti	0.013 – 0.149	0.078	0.016	0.004 – 0.010
ΣAl (${}^{[4]}\text{Al} + {}^{[6]}\text{Al}$)	4.744 – 5.724	5.198	4.748	4.300 – 5.080
Na	0.049 – 0.165	0.198 – 1.974	0.050 – 1.998	0.000 – 0.010
Mg	0.101 – 0.329	0.152 – 4.118	0.338 – 4.194	0.270 – 0.530
Si	6.099 – 6.378	6.210	6.410	6.500 – 7.000
Fe^{2+*}	0.238 – 0.692	0.470	0.641	0.055 – 0.100**
Na/(Na + K)	0.030 – 0.090	0.060 – 0.120	0.010 – 0.070	< 0.040

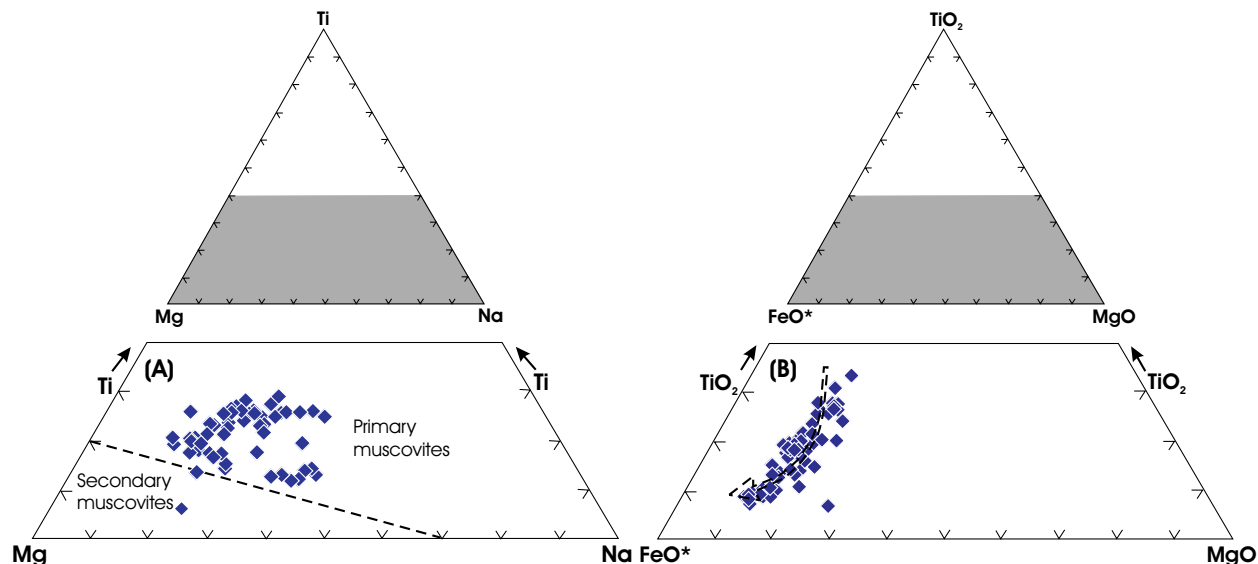


Figure 4.3: Composition of two-mica granitoid muscovites of the Bafoussam area. **(A)** Primary (magmatic) origin of the analyzed muscovites onto Mg–Ti–Na (a.p.f.u) triangular diagram from Miller et al. (1981). **(B)** FeO^* – TiO_2 – MgO (wt. %) ternary diagram modified after Monier et al. (1984). The arrow illustrates the compositional evolution of the magmatic muscovites. FeO^* : total iron oxides ($\text{FeO} + \text{Fe}_2\text{O}_3$). Coloured parts in the insets (above) are the areas shown in the main figures.

The magmatic origin is also consistent with the textural characteristics exhibited by the investigated muscovites, as well-developed large tabular crystals locally with irregular termination and often showing mica twinning. Miller et al. (1981) and Speer (1984) conclude from their studies that primary magmatic muscovite contains higher Ti content than muscovite of

secondary origin. Accordingly, because of the resistance of Ti to subsolidus reaction compared to Mg, Fe, Na and K in muscovite, Zen (1988) has emphasized Ti enrichment in muscovite as an indicator of magmatic origin. The ambiguities noticed in the analyzed muscovite compositions (Table 4.1) may indicate the dependence of the plutonic muscovite chemistry also from the individual environment in which the muscovite crystallized.

The studied muscovites have chemical compositions different to the ideal end-member muscovite ($KAl_2AlSi_3O_{10}[OH]_2$), as defined by Miller et al. (1981). This deviation in composition is explained by the variable extents of the celadonite and the paragonite substitutions that took place during the crystallisation of the granitic rocks. These substitutions can be quantitatively estimated.

The substitution toward celadonite is measured by the following parameters introduced by Guidotti and Sassi (1976): $s = (Si - 6) > 0$, $Fm = (Fe^{2+} + Mg) \geq 0$ and $a = (6 - Al) > 0$. Within the investigated muscovites, s varies between 0.112 and 0.378 a.p.f.u., Fm between 0.381–1.020 a.p.f.u. and a between 0.276 and 1.256 a.p.f.u. Plotted into the $(Fe^{2+} + Mg)$ versus $Si - 6$ (a.p.f.u.) diagram (Fig. 4.4A), the studied muscovites show a rapid increase in $(Fe^{2+} + Mg)$ ratios with $Si - 6$ being relatively constant, and fall above the muscovite–phengite solid solutions line, in between the two end-members. They are then qualified as celadonitic muscovite, mildly phengitic in nature. The classic celadonite substitutional mechanism is identified as the reverse Tschermak exchange, $(Fe^{2+} + Mg)^{[6]} \leftrightarrow ([^6]Al + [^4]Al)$. Velde (1972) suggested that celadonitic primary muscovite crystallizes at low temperature or high pressure conditions.

The paragonite substitution is also expressed in the Bafoussam muscovites as it is demonstrated in the Na versus K (a.p.f.u.) diagram (Fig. 4.4B). In this diagram, the analyzed muscovite samples plot between 3 and 9 % of $Na^* = 100 \text{ Na}/(\text{Na} + \text{K})$ values which give the extent of paragonite substitution.

Muscovite Ti contents are related to the crystallization temperature (Guidotti et al., 1977; Monier and Robert, 1986) and apparently also to the presence/absence of the Ti-mineral (ilmenite) in the two-mica granite (Puziewicz and Koepke, 1991). Based on experimental data, the typical primary or magmatic muscovite crystallization has to be generally assumed to high-temperature (650 °C–700 °C) and low-pressure (2–5 kbar) conditions that correspond to a depth

of 7–18 km (Anderson and Rowley, 1981; Miller et al., 1981; Monier and Robert, 1986). According to the thermodynamic considerations of Anderson and Rowley (1981), the magmatic muscovites having celadonite component (thus the muscovite of the Bafoussam two-mica granitoid) crystallize from tonalitic to granodioritic melt.

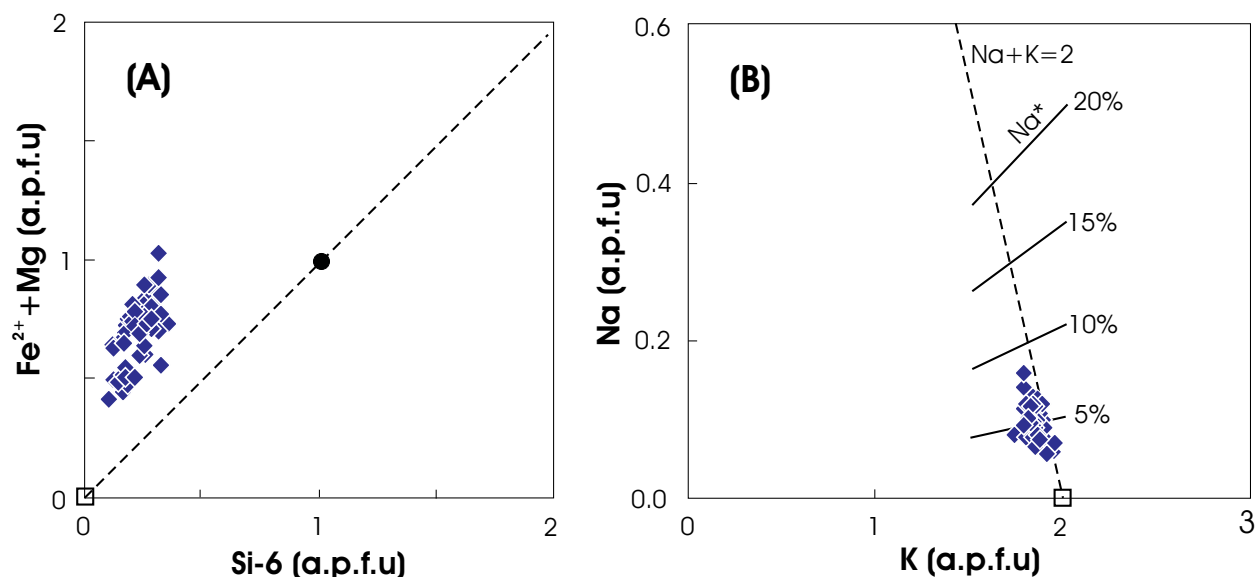


Figure 4.4: Compositional variation within two-mica granitoid muscovites from the Bafoussam area. (A) $(\text{Fe}^{2+} + \text{Mg})$ versus $\text{Si} - 6$ (a.p.f.u) diagram, illustrating the extent of the celadonitic substitution. Fe^{2+} : total Fe ($\text{Fe}^{2+} + \text{Fe}^{3+}$), the filled circle is the phengite position whereas the open square represents the ideal muscovite one. (B) Degree of paragonite substitution expressed in the Na against K (a.p.f.u) diagram. $\text{Na}^* = 100 \text{Na}/(\text{Na} + \text{K})$. The open square shows the ideal muscovite composition.

4.2 Garnet

Garnet is the general name of a group of minerals, with standard formula: $X^{2+}_3 Y^{3+}_2 \text{Si}_3 \text{O}_{12}$, mainly with $X = \text{Ca}, \text{Fe}, \text{Mn}$, or Mg and $Y = \text{Al}, \text{Cr}$, or Fe . The common garnet end-members are pyrope ($\text{Mg}_3\text{Al}_2\text{Si}_3\text{O}_{12}$), almandine ($\text{Fe}^{2+}_3\text{Al}_2\text{Si}_3\text{O}_{12}$), spessartine ($\text{Mn}_3\text{Al}_2\text{Si}_3\text{O}_{12}$), grossular ($\text{Ca}_3\text{Al}_2\text{Si}_3\text{O}_{12}$), andradite ($\text{Ca}_3\text{Fe}^{3+}_2\text{SiO}_{12}$) and uvarovite ($\text{Ca}_3\text{Cr}_2\text{Si}_3\text{O}_{12}$).

Like muscovite, garnet is not omnipresent in the Bafoussam granitoids. It was identified in the two-mica granitoid in sample TA-9, where it occurs as typical euhedral grains that measure less than 0.5 mm in diameter. Garnet crystals are free of inclusions. Representative chemical analyses are compiled in Table A.3.3 in the Appendix A.2, where they have been calculated on the basis of twenty-four oxygens. Molecular proportions of their end-member

components are given in the following sequence: uvarovite, andradite, grossular, almandine, spessartine and pyrope. Calculation of Fe^{3+} was carried out assuming an ideal occupancy of the mineral formula.

The mineralogical composition of the investigated garnets displays only moderate variation as shown in Figure 4.5. The garnet solid solutions may be regarded as members of the almandine–spessartine series which have nearly equal proportions of almandine and spessartine, respectively, 44.1 to 54.5 mol. % and 43.4 to 55.5 mol. %. The total of the remaining components is less than 3 mol. % with pyrope (0.2–0.7 mol. %), andradite (0.3–1.8 mol. %), uvarovite (up to 0.2 mol. %) and grossular (up to 1.2 mol. %). The almandine–spessartine composition of the analyzed garnets is expressed in the $\text{Mg}-\text{Mn}-\text{Fe}^{2+}$ (a.p.f.u) triangular diagram of garnet (Fig. 4.5). The garnets are compositionally similar to igneous garnets reported from highly peraluminous granites elsewhere (e.g., Clarke, 1981; Miller and Stoddard, 1981; Du Bray, 1988; Nalini et al., 2000; Jung et al., 2001); some garnets with significant proportion of the grossular component have been likewise recognized to be also igneous in composition (Anderson and Rowley, 1981).

The garnets of the two-mica granitoid from Bafoussam area with their almandine–spessartine composition are then considered to be purely igneous phases. The euhedral grain shapes of garnet crystals and the paucity of inclusions coupled with the high Mn and Fe^{2+} contents (2.609–3.317 a.p.f.u and 2.646–3.277 a.p.f.u, respectively) and low Mg contents (0.012–0.038 a.p.f.u) support this interpretation. This also suggests equilibrium with melt during crystallization (Zen, 1988). Moreover, Clemens and Wall (1981) have demonstrated by experimental investigations of phase relation in the peraluminous system that garnet is a common product of the crystallization of peraluminous melts.

Exceptionally, some studied garnet crystals appear to be weakly zoned. There is a tendency for almandine and pyrope components to increase and the spessartine component to decrease from core to rim (Fe^{2+} , core: 2.646–2.919 a.p.f.u → rim: 3.069–3.180 a.p.f.u; Mg, core: 0.012–0.013 a.p.f.u → rim: 0.023–0.031 a.p.f.u; Mn, core: 3.02–3.317 → rim: 2.697–2.878 a.p.f.u, respectively). The zonation with decrease in Mn from core to rim is a salient feature in

igneous garnets and has been noted for garnet from other two-mica granitoid rocks (Anderson and Rowley, 1981; Jung et al., 2001).

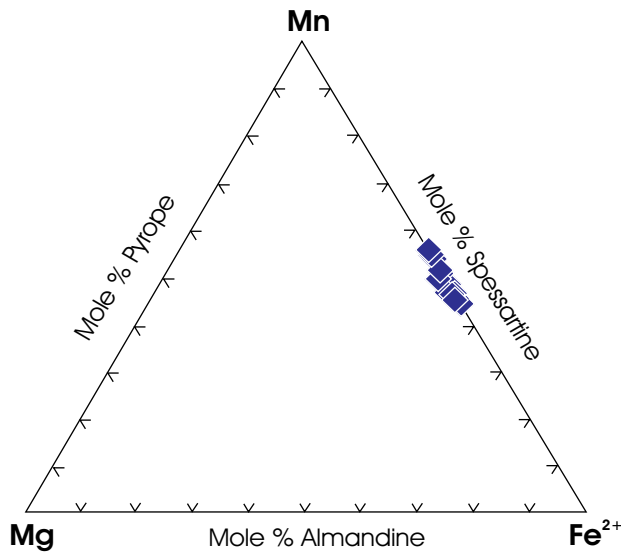


Figure 4.5: Almandine–spessartine composition of two-mica granitoid garnets of the Bafoussam area projected onto the Mg–Mn–Fe²⁺ (a.p.f.u) triangular diagram.

Several mechanisms for the formation of plutonic garnets have been suggested (see review by Miller and Stoddard, 1981). Garnets in granitic rocks are considered to be a late-stage liquidus mineral that crystallized in differentiated magmas in response to the increase of the Mn content. The corresponding reaction is:



The enrichment of Mn in garnets of strongly peraluminous magma has been explained by Miller and Stoddard (1981) with the absence of ferromagnesian minerals such as hornblende, which has higher affinity for Mn than biotite. Moreover, du Bray (1988) argued that the presence of excess alumina in the magma is an additional requirement for the garnet occurrence in granitic rocks. Since the core-rim decrease in Mn is observed in the studied garnets, a depletion crystallization model is suggested for their origin, i.e. initial crystallization of garnet induces early decrease of Mn in the parent magma.

In an experimental study carried out at high pressure, Green (1977) has underlined the importance of the role played by the MnO in the genesis of garnets of magmatic origin. Mn increases the field of garnet stability and allows its crystallization at very low pressures.

According to Green's experimental data, garnets with > 10 mol. % of spessartine (thus the garnets of the Bafoussam two-mica granitoid) can crystallize in liquids of granitic composition at minimum pressure of 5 kbar, which corresponds to a depth of 18 km.

4.3 Amphibole

Ideally, the amphibole structure has a general formula unit of $A_{0-1} B_2 C_5 T_8 O_{22} (\text{OH})_2$ (Leake et al., 1997: 2004). The recommended allotment of ions to crystallographic sites is as follows:

- (1) Sum T to 8.00 a.p.f.u using Si, then Al, then Ti.
- (2) Sum C to 5.00 a.p.f.u using any excess Al and Ti from (1) and then successively Fe^{3+} , V, Cr, Mn^{3+} , Zr, Mg, Zn, Ni, Co, Fe^{2+} , Mn^{2+} , and Li.
- (3) Sum B to 2.00 a.p.f.u using first any excess above 5.00 a.p.f.u from C , in the reverse order of (2), starting with Li and then Mn^{2+} , etc., and then following with Ca, Ba and Na.
- (4) Any excess above 2.00 a.p.f.u in B is assigned to A in the reverse order of (3), starting with Na, and finally all the K is allocated to A . Total A should be 0 to 1.00.

Within the investigated granitoids, amphibole crystallized, like biotite, during and early stage of the magma evolution (Fig. 3.13). Although amphibole is not omnipresent in the Bafoussam granitoids, it has been observed in the biotite granitoid and the deformed biotite granitoid. Amphibole has subhedral forms with a grain size ranging between 1 and 2 mm in length and frequently associated with biotite and titanite. It is green to green-brown coloured, locally displays a compositional zoning (brown-green cores to pale green rims) and the characteristic double cleavages and $h_1\{100\}$ twinning. Zircon, apatite and opaques are frequently found as inclusion in amphibole. The chemical analyses are recorded in Table A.2.4 in the Appendix A.2. The structural formula of amphibole was calculated on twenty-three oxygens anhydrous basis. Because the electron microprobe cannot distinguish between Fe^{2+} and Fe^{3+} , the amounts of these cations were calculated by the midpoint method, when the mean value for Fe^{3+} between the minimum and the maximum possible Fe^{3+} value to reach a satisfying formula occupancy is taken.

The amphibole compositions of the biotite granitoid and the deformed biotite granitoid of the Bafoussam area are, in general, characterised by high Ca (1.836–1.946 a.p.f.u and 1.758–1.923 a.p.f.u), Mg (1.993–2.302 a.p.f.u and 2.005–3.121 a.p.f.u) and Al (1.354–1.785 a.p.f.u and 1.275–1.790 a.p.f.u). They are calcic amphiboles, commonly referred to as *hornblende* (Hawthorne, 1983). This group is characterized by an occupancy of the *B* position with $^{[B]}(\text{Mg}+\text{Fe}^{2+}+\text{Mn}^{2+}+\text{Li}) \leq 0.50$, $^{[B]}(\text{Ca}+\text{Na}) \geq 1.00$ and $0.50 \leq ^{[B]}\text{Na} < 1.50$ (Leake et al., 2004).

In the International Mineralogical Association (I.M.A) approved classification and nomenclature (Leake et al., 1997), the composition of the studied amphiboles varies between magnesio-hastingsite to edenite, with high Mg/(Mg + Fe²⁺) ratios ranging from 0.50–0.62 and Si contents of 6.457–6.868 a.p.f.u (Fig. 4.6). Generally, the amphiboles are not zoned. However, zonation occurs in some crystals of the deformed biotite granitoid and displays two characteristics (Fig. 4.7): (1) variation of the Mg-number, increasing as well as decreasing from the core to the rim; and (2) increase of the Si content and decrease of the $^{[A]}(\text{Na} + \text{K})$ towards the rim that indicate the formation of magnesio-hornblende.

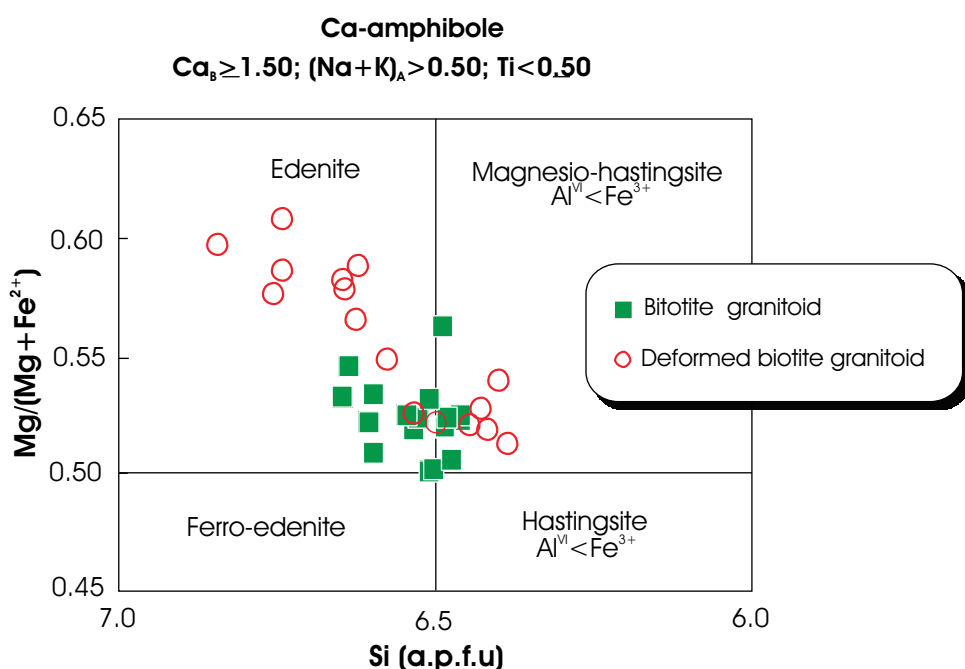


Figure 4.6: Classification diagram of calcic amphiboles using the variation of $\text{Mg}/(\text{Mg} + \text{Fe}^{2+})$ with Si (a.p.f.u) following the terminology of amphiboles after Leake et al. (1997).

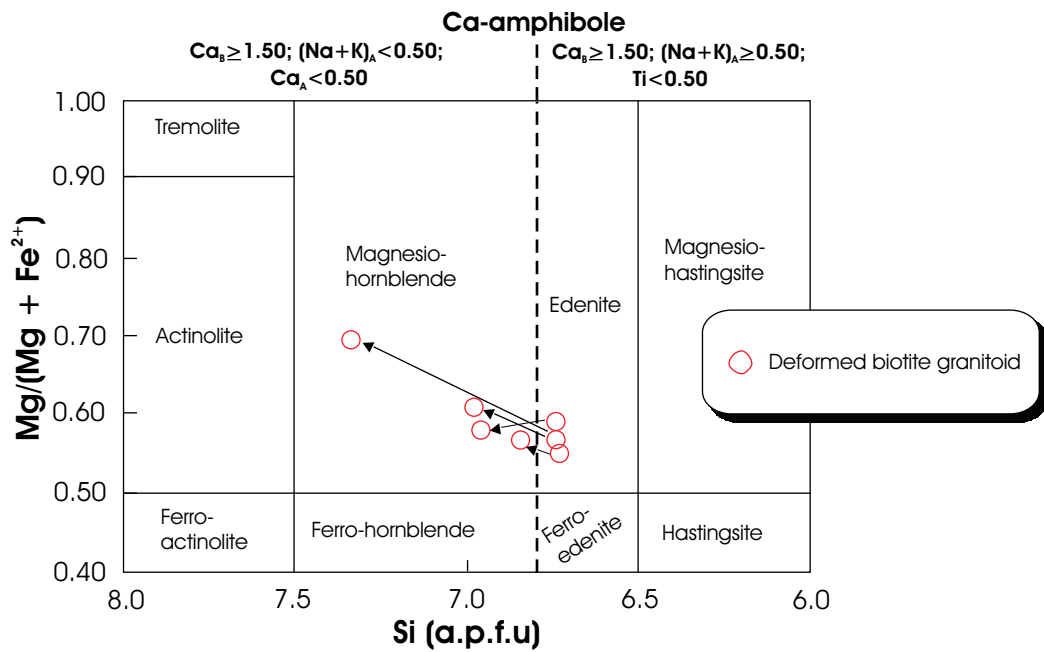


Figure 4.7: Classification diagram of calcic amphiboles using the variation of $Mg/(Mg + Fe^{2+})$ with $Si \text{ (a.p.f.u)}$ according to the classification of Leake et al. (1997). The diagram combines the two groups of calcic amphiboles with the parameters $(Na + K)_A \geq 0.50; Ti < 0.50$ and $(Na + K)_A < 0.50; Ca_A < 0.50$. The two groups are separated by broken line. Arrows join zoned crystals and point towards the rim.

The investigated amphiboles do not exceed Si values of 7.500 (a.p.f.u) that represents the limit given by Leake (1971) for the true igneous amphiboles silica contents. Furthermore, the magmatic origin of the amphiboles of the Bafoussam granitoids is indicated on the $(Ca + Na + K) - Si \text{ (a.p.f.u)}$ (Fig. 4.8A) and the $[^6]Al - \sum Al \text{ (a.p.f.u)}$ plots (Fig. 4.8B), where they fall inside the field of igneous amphibole crystallization defined by Leake (1971).

The relationship between tetrahedral $Al (^4Al)$ and total $Al (\sum Al)$ in the amphiboles of the Bafoussam granitoids is also portrayed in Figure 4.8B, where an excellent positive trend is observed as also reported by Hammarstrom and Zen (1986) in their mineralogic study of hornblendes from calc-alkaline plutons. This positive trend reveals the great variation of the Al contents of the amphiboles of the biotite granitoid and the deformed biotite granitoid. The two amphibole populations define a linear correlation just under the 1:1 slope in the same plot, demonstrating that there is a slight excess of total Al over $[^4]Al$ which represents more than 90 % of the total aluminium. The $[^4]Al/Al[^6]$ ratios range between 4.66 and 15.15 and are consistent with the igneous origin of the investigated amphiboles (Fleet and Barnett, 1978).

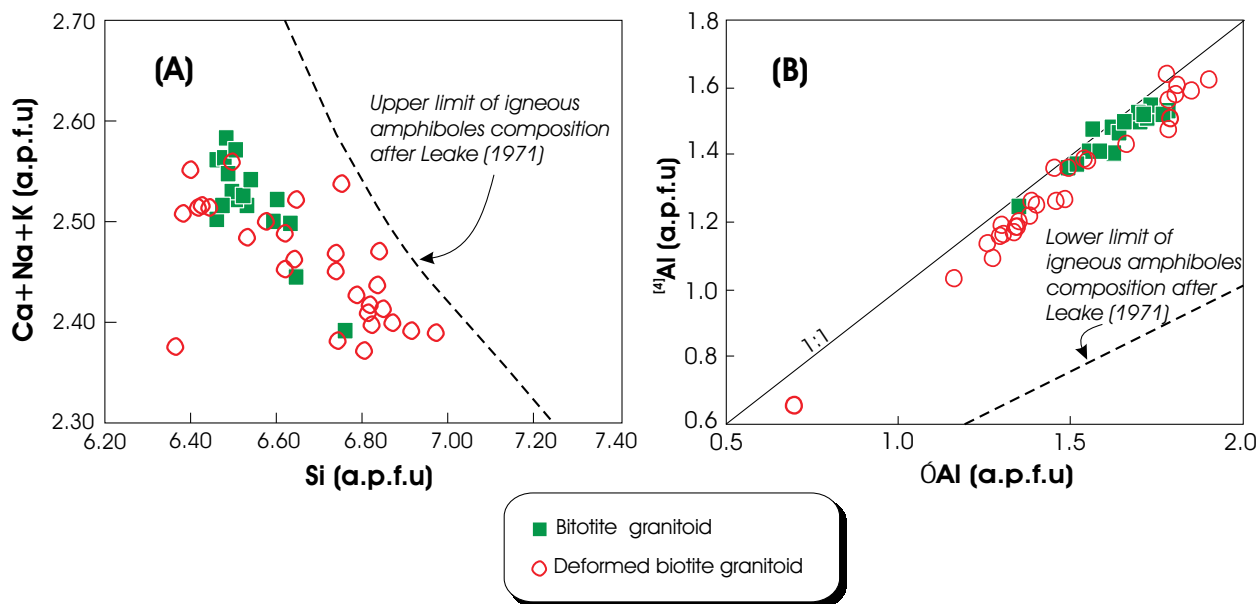


Figure 4.8: Discrimination diagrams for amphiboles after Leake (1971) portraying a magmatic origin of amphiboles of the Bafoussam granitoids. **(A)** Plot of $(\text{Ca} + \text{Na} + \text{K})$ versus Si (a.p.f.u). **(B)** Relationship between $[{}^4\text{Al}]$ and $\sum \text{Al}$ (a.p.f.u) in the analyzed amphiboles. $\sum \text{Al}$ = total Al ($[{}^4\text{Al}] + [{}^6\text{Al}]$).

The variations in hornblende compositions observed in the classification diagram (Fig. 4.6) are principally governed by the substitution schemes acting during its evolution. Two types of substitution mechanisms, simple isovalent and coupled heterovalent, control the variations in the chemistry of amphibole (Czamanske and Wones, 1973; Hawthorne, 1983; Vyhnař et al., 1991).

(1) ***The simple isovalent substitution*** concerns single cations with the same valence states such as $\text{Fe}^{2+} \leftrightarrow \text{Mg}^{2+}$, $[{}^A\text{K}] \leftrightarrow [{}^A\text{Na}$, $\text{Mn}^{2+} \leftrightarrow \text{Mg}^{2+}$ and $[{}^6\text{Al}] \leftrightarrow \text{Fe}^{3+}$; the most common of these exchanges in igneous hornblendes being $\text{Fe}^{2+} \leftrightarrow \text{Mg}^{2+}$ and $[{}^A\text{K}] \leftrightarrow [{}^A\text{Na}$ (Gilbert et al., 1982). An example of simple substitution is shown in Figure 4.9, plotting Fe^{2+} against Mg. The fair linear and negative correlation between Fe^{2+} and Mg indicates that this simple substitution is operative in the Bafoussam granitoid hornblende samples. This trend is typical of the calcic amphiboles.

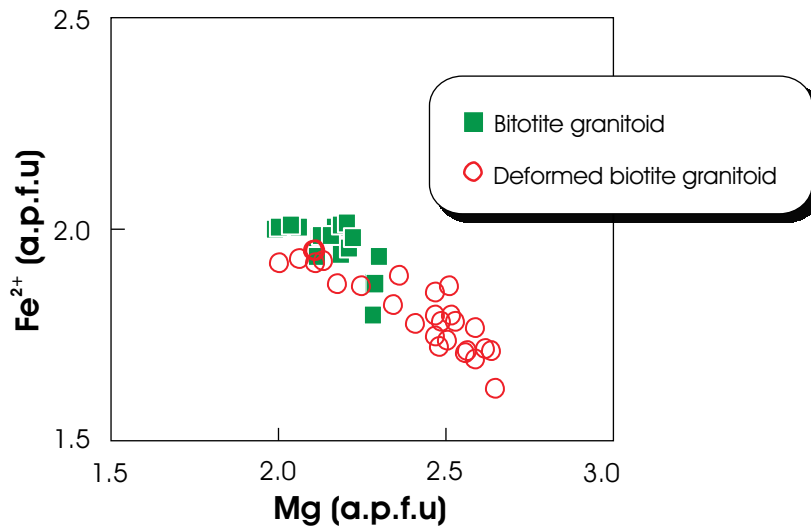


Figure 4.9: Simple substitution of Fe^{2+} for Mg in the Bafoussam granitoid hornblendes.

(2) **The coupled heterovalent substitution** involves cations with different valences to conserve charge balance. For these exchange reactions, tremolite, $\square\text{Ca}_2\text{Mg}_5\text{Si}_8\text{O}_{22}(\text{OH})_2$, is commonly assumed to be the idealized starting end-member. The principal heterovalent substitutions that result in other end-members (whose names are used to designate a given cation exchange scheme) are listed in Table 4.2.

Table 4.2: Main types of heterovalent substitutions in amphiboles on the basis of the idealized tremolite formula $\square\text{Ca}_2\text{Mg}_5\text{Si}_8\text{O}_{22}(\text{OH})_2$ (Czamanske and Wones, 1973; Vyhnař et al., 1991). ${}^{[\text{A}]}\square$ indicates vacancy in the site A.

Substitution mechanism		End member
${}^{[\text{A}]}\square + {}^{[4]}\text{Si} = {}^{[\text{A}]}\text{Na} + {}^{[4]}\text{Al}$	Edenite	$\text{NaCa}_2\text{Mg}_7\text{AlO}_{22}(\text{OH})_2$
$2{}^{[4]}\text{Si} + 2{}^{[6]}\text{Mg} = 2{}^{[4]}\text{Al} + 2{}^{[6]}\text{Al}$	Al-Tschermakite	$\square\text{Ca}_2(\text{Mg}_3\text{Al}_2)\text{Si}_6\text{Al}_2\text{O}_{22}(\text{OH})_2$
$2{}^{[4]}\text{Si} + 2{}^{[6]}\text{Mg} = 2{}^{[4]}\text{Al} + 2{}^{[6]}\text{Fe}^{3+}$	Fe-Tschermakite	$\square\text{Ca}_2(\text{Mg}_3\text{Fe}_2^{3+})\text{Si}_6\text{Al}_2\text{O}_{22}(\text{OH})_2$
$2{}^{[4]}\text{Si} + {}^{[6]}\text{Mg} = 2{}^{[4]}\text{Al} + {}^{[6]}\text{Ti}$	Ti-Tschermatikite	$\square\text{Ca}_2(\text{Mg}_4\text{Ti})\text{Si}_6\text{Al}_2\text{O}_{22}(\text{OH})_2$
${}^{[\text{A}]}\square + {}^{[\text{M}4]}\text{Ca} = {}^{[\text{A}]}\text{Na} + {}^{[\text{M}4]}\text{Na}$	Richterite	$\text{Na}(\text{CaNa})\text{Mg}_5\text{Si}_8\text{O}_{22}(\text{OH})_2$
$2{}^{[\text{M}4]}\text{Ca} + 2{}^{[6]}\text{Mg} = 2{}^{[\text{M}4]}\text{Na} + 2{}^{[6]}\text{Fe}^{3+}$	Riebeckite	$\square\text{Na}_2(\text{Fe}_3^{2+}\text{Fe}_2^{3+})\text{Si}_8\text{Al}_2\text{O}_{22}(\text{OH})_2$
$2{}^{[\text{M}4]}\text{Ca} + 2{}^{[6]}\text{Mg} = 2{}^{[\text{M}4]}\text{Na} + 2{}^{[6]}\text{Al}$	Glaucomphane	$\square\text{Na}_2(\text{Mg}_3\text{Al}_2)\text{Si}_8\text{O}_{22}(\text{OH})_2$
${}^{[\text{A}]}\square + {}^{[6]}\text{Mg} + 2{}^{[4]}\text{Si} = {}^{[\text{A}]}\text{Na} + 2{}^{[4]}\text{Al} + {}^{[6]}\text{Al}$	Hastingsite	$\text{NaCa}_2(\text{Fe}_4^{2+}\text{Fe}^{3+})\text{Si}_6\text{Al}_2\text{O}_{22}(\text{OH})_2$
${}^{[\text{A}]}\square + {}^{[6]}\text{Mg} + 2{}^{[4]}\text{Si} = {}^{[\text{A}]}\text{Na} + 2{}^{[4]}\text{Al} + {}^{[6]}\text{Fe}^{3+}$	Pargasite	$\text{NaCa}_2(\text{Mg}_4\text{Al})\text{Si}_6\text{Al}_2\text{O}_{22}(\text{OH})_2$

The linear correlations observed between Si and $[^4]\text{Al} + [^{\text{A}}](\text{Na} + \text{K})$ (Fig. 10A), and Si + $(\text{Fe}, \text{Mg})^{2+}$ and $[^4]\text{Al} + [^6]\text{Al}$ (Fig. 10B) demonstrate that edenitic and tschermakitic substitution mechanisms are active in the Bafoussam granitoid hornblendes. In a plot of $[^{\text{A}}](\text{Na} + \text{K})$ versus $[^4]\text{Al}$ (Fig. 10C), the compositions of the analyzed hornblende define a trend parallel to a line joining the pargasitic and the edenitic substitutions. This trend substantiates the combined and the compensatory operation of both edenitic and tschermakitic substitution schemes. In diagrams Fe^{3+} versus $[^4]\text{Al}$, $[^6]\text{Al}$ versus $[^4]\text{Al}$ and Ti versus $[^4]\text{Al}$ (Fig. 10D, E, F), the hornblende compositions did not show any clear correlations, revealing the simultaneous expressions of all tschermakitic substitution types.

The lack of correlation observed between $[^{\text{A}}](\text{Na} + \text{K})$ versus $[^{\text{M}4}]\text{Na}$ (Fig. 4.11A), Fe^{3+} versus $[^{\text{M}4}]\text{Na}$ (Fig. 4.11B) and Ti versus $[^4]\text{Al}$ (Fig. 4.11D) indicates that the richterite, riebeckite and glaucophane types of substitutions, respectively, are not operative in the Bafoussam granitoids hornblendes. This emphasizes that the edenitic and tschermakitic substitution types dominate over the other types of substitution during the evolution of the analyzed hornblendes, as it is confirmed in Figure 4.11D after Robinson et al. (1971). The Figure 4.11D shows a good linear correlation along the line 1:1 between $[^{\text{A}}](\text{Na} + \text{K}) + 2\text{Ti} + \text{Fe}^{3+} + [^6]\text{Al}$ and $[^4]\text{Al}$. Following Vyhnař et al. (1991), the deviation of the trend from the slope of 1:1 (Fig. 4.11D) and the cluster of the analyzed amphiboles above the tremolite–Ti-glaucophane substitution line within the $[^6]\text{Ti}$ versus $[^{\text{M}4}]\text{Na}$ diagram (Fig. 4.11E) suggest that the tschermakitic substitution may be coupled with glaucophane type substitution of the form $[^{\text{M}4}]\text{Ca} + [^{\text{M}4}]\text{Al} = [^{\text{M}4}]\text{Na} + [^{\text{M}4}]\text{Ti}$.

The edenitic, tschermakitic, pargasitic and hastingsitic mechanism substitution types observed in hornblendes of the granitoids described in this study have been recognized to be typical in calcic amphiboles from calc-alkaline granitoids plutons (Fabriès et al., 1984; Vyhnař et al., 1991). Because these amphiboles contain more than 1.5 Ca (a.p.f.u), the glaucophanic, riebeckitic and richteritic exchange schemes (substitution of Ca for Na in [M4]) are of little importance or completely absent. From several experimental studies, Fabriès et al. (1984) have deduced that the substitutions active in igneous hornblendes are determined by variations in the crystallization parameters (temperature, pressure, oxygen and water fugacity) during crystallization processes.

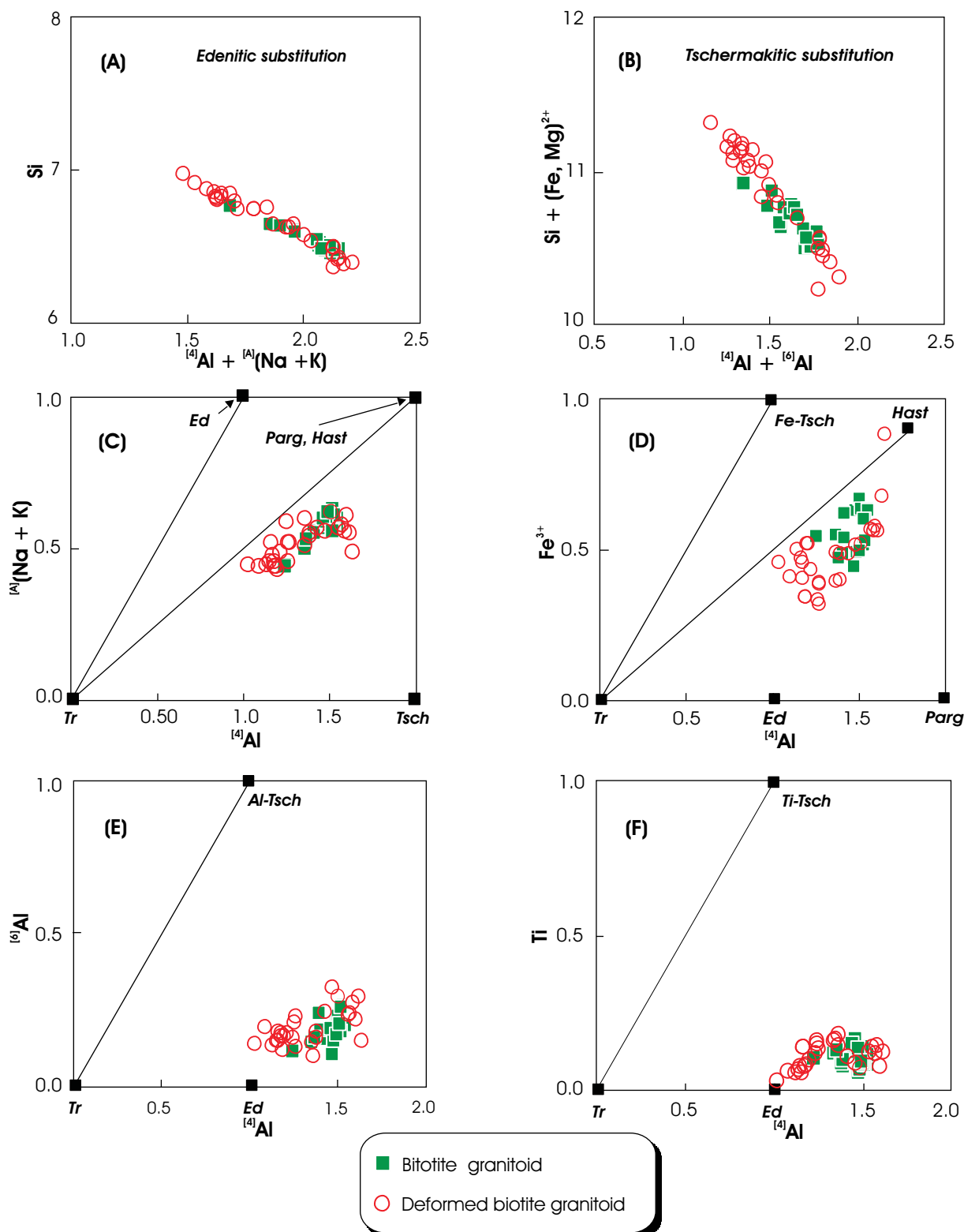


Figure 4.10: Plots illustrating edenitic and tschermarkitic substitution mechanisms in hornblendes of the Bafoussam granitoids: (A) Si versus $[{}^4\text{Al}] + [{}^{\text{A}}(\text{Na} + \text{K})]$ (a.p.f.u), (B) $\text{Si} + (\text{Fe}, \text{Mg})^{2+}$ versus $[{}^4\text{Al}] + [{}^6\text{Al}]$ (a.p.f.u), (C) $[{}^{\text{A}}(\text{Na} + \text{K})]$ versus $[{}^4\text{Al}]$ (a.p.f.u), (D) Fe^{3+} versus $[{}^4\text{Al}]$ (a.p.f.u), (E) $[{}^6\text{Al}]$ versus $[{}^4\text{Al}]$ (a.p.f.u), and (F) Ti versus $[{}^4\text{Al}]$. End-member amphibole compositions are: edenite (*Ed*), hastingsite (*Hast*), Pargasite (*Parg*), Tremolite (*Tr*), aluminum tschermarkite (*Al-Tsch*), iron tschermarkite (*Fe-Tsch*), and titanium tschermarkite (*Ti-Tsch*).

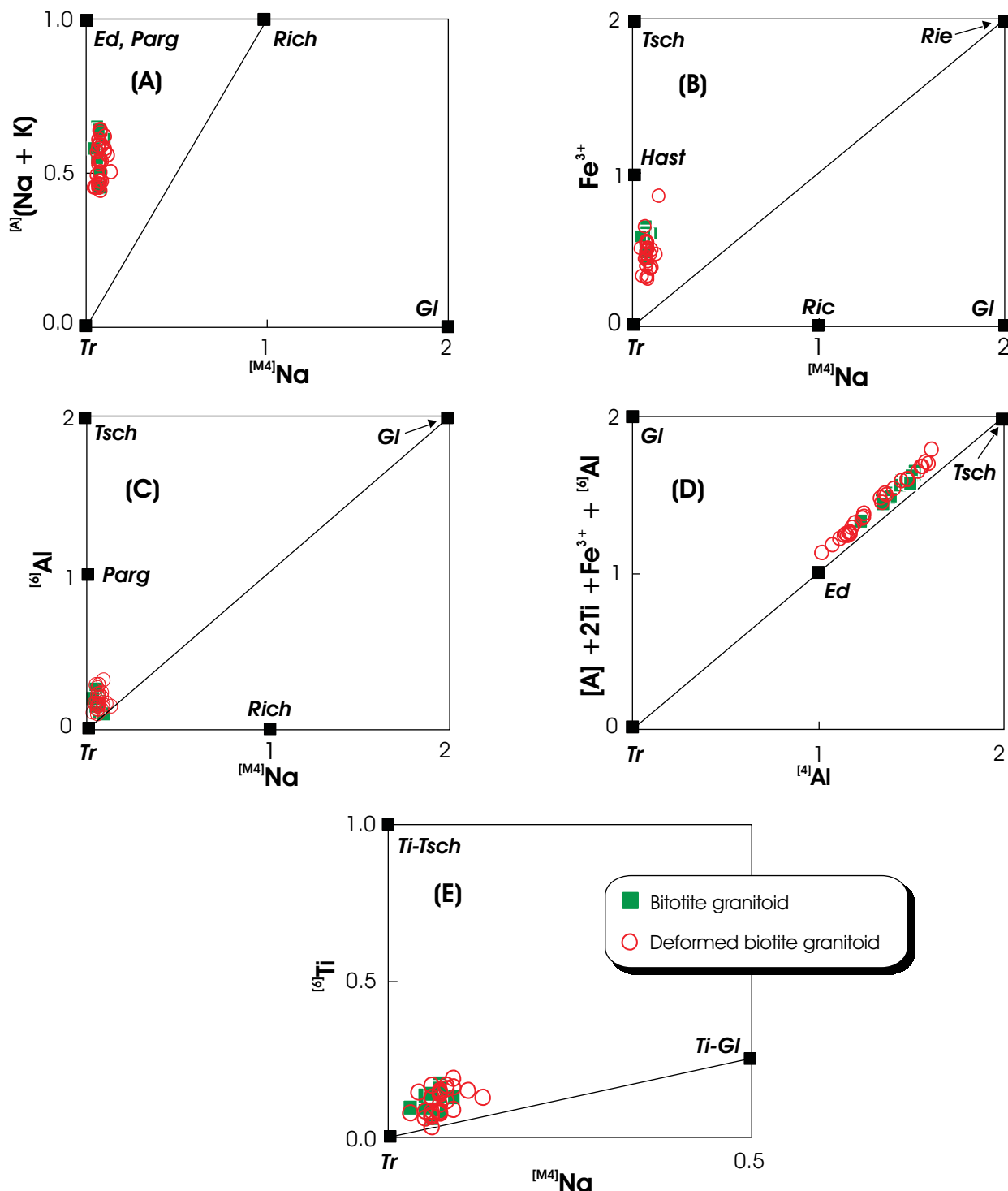


Figure 4.11: Variation diagrams, showing the substitution mechanisms in hornblendes of the Bafoussam granitoids. (A) $[\text{A}](\text{Na} + \text{K})$ versus $[\text{M}^4]\text{Na}$ (a.p.f.u.), (B) Fe^{3+} versus $[\text{M}^4]\text{Na}$ (a.p.f.u.), (C) ${}^6\text{Al}$ versus $[\text{M}^4]\text{Na}$ (a.p.f.u.), (D) $[\text{A}] + 2\text{Ti} + \text{Fe}^{3+} + {}^6\text{Al}$ versus ${}^4\text{Al}$ (a.p.f.u.), and (E) ${}^6\text{Ti}$ versus $[\text{M}^4]\text{Na}$ (a.p.f.u.). End-member amphibole compositions are: edenite (Ed), glaucophane (Gl), hastingsite (Hast), Pargasite (Parg), richterite (Rich), riebeckite (Rie), Tremolite (Tr); Tsch refers to all tschermarkite-type substitutions.

4.4. Feldspars: potassium feldspar and plagioclase feldspar

The feldspar minerals are aluminum silicates whose crystalline structure is composed of an infinite network of SiO_4 and AlO_4 tetrahedral (Ribbe, 1975). The standard chemical formula of feldspars can be written as $MT_4\text{O}_8$, where T represents Al and Si, and M is monovalent Na and/or K for AlSi_3O_8 and divalent Ca or Ba for $\text{Al}_2\text{Si}_2\text{O}_8$.

The feldspar minerals are the most abundant components in all of the Bafoussam granitoids. They are represented by potassium feldspar, microcline and orthoclase, with development of perthite in both category, and plagioclase feldspar. Both feldspar group crystals are frequently euhedral laths and subhedral grains and commonly occur individually in a matrix, but also in compact groupings. All feldspar typical twins are somewhat common. Representative analyses of alkali feldspar and plagioclase feldspar, and their calculated formulas based on eight oxygens, are presented in Tables A.2.5a: b, respectively in the Appendix A.2.

4.4.1 Potassium feldspar

The potassium feldspar from all the Bafoussam granitoids has remarkably constant chemical composition, despite the great difference in size from one granitoid group to another and within each granitoid group. Phenocrysts and matrix potassium feldspar roughly have similar compositions. The analyzed potassium feldspars have generally a restricted range of composition between $\text{Or}_{92}\text{Ab}_8\text{An}_0$ and $\text{Or}_{97}\text{Ab}_3\text{An}_0$ in the biotite granitoid (Fig. 4.6A), $\text{Or}_{91}\text{Ab}_9\text{An}_0$ and $\text{Or}_{96}\text{Ab}_4\text{An}_0$ in the deformed biotite granitoid (Fig. 4.6B), $\text{Or}_{92}\text{Ab}_8\text{An}_0$ and $\text{Or}_{95}\text{Ab}_5\text{An}_0$ in the mega feldspar granitoid (Fig. 4.6C) and finally, $\text{Or}_{81}\text{Ab}_{19}\text{An}_0$ and $\text{Or}_{96}\text{Ab}_4\text{An}_0$ in the two-mica granitoid (Fig. 4.6D). The investigated potassium feldspar falls solely within the orthoclase field, reflecting low temperature stabilities, according to King (1989).

In the granitoids under study, potassium feldspars are generally weakly zoned. However, pronounced zonation is noticed in some K-feldspars, with cores richer in potassium relative to the rims ($\text{Or}_{93}\text{Ab}_7\text{An}_0$ and $\text{Or}_{85}\text{Ab}_{15}\text{An}_0$, respectively) in the two-mica granitoid. The opposite is the case in the mega feldspar granitoid: the rims are richer in potassium relative to the cores ($\text{Or}_{95-92}\text{Ab}_{5-8}\text{An}_0$ and $\text{Or}_{90-76}\text{Ab}_{10-24}\text{An}_0$, respectively). According to Parsons and Boyd (1971),

the increase of magma fractionation results in an increasing degree of ordering in potassium feldspar, so that microcline predominates over orthoclase with progressive fractionation. This is corroborated in the investigated granitoids, where orthoclase predominates over microcline in the intermediate phases, while it becomes subordinate in amount relative to microcline in the more involved granitoids.

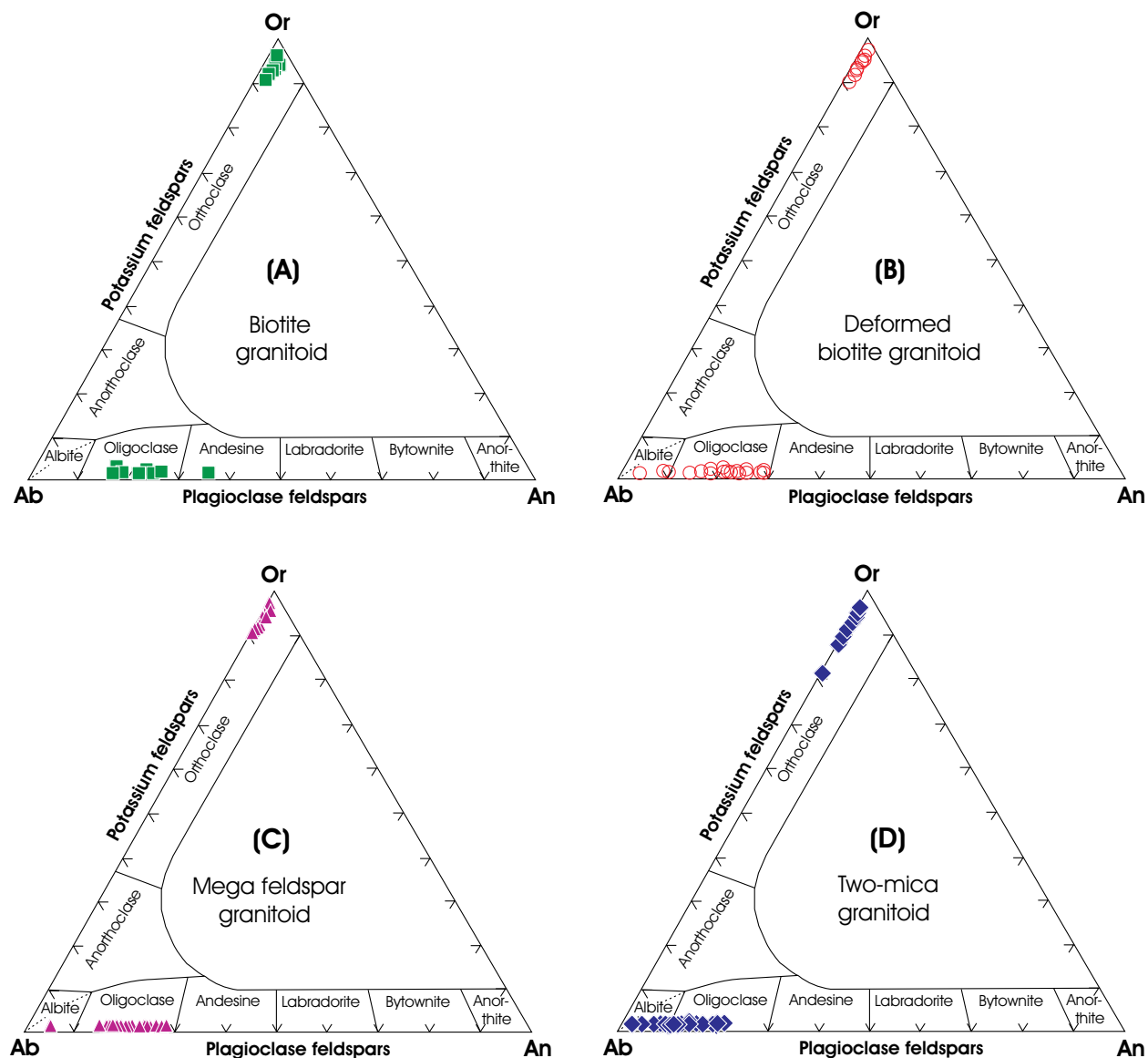


Figure 4.6: Nomenclature and composition of the feldspars (Alkali feldspar and plagioclase feldspar) of the Bafoussam granitoids onto the albite (Ab)–orthoclase (Or)–anorthite (An) triangular diagram.

4.4.2 Plagioclase feldspar

The studied plagioclases are essentially sodium-rich, characterized by low to moderate anorthite contents. In the biotite granitoid, plagioclases are more calcic and range from oligoclase to andesine with compositions between $\text{Ab}_{82}\text{An}_{17}\text{Or}_1$ and $\text{Ab}_{64}\text{An}_{35}\text{Or}_1$, respectively (Fig. 4.6A). Plagioclase compositions of the deformed biotite granitoid (Fig. 4.6B) and of the mega feldspar granitoid (Fig. 4.6C) are mainly oligoclase with $\text{Ab}_{90}\text{An}_9\text{Or}_1$ – $\text{Ab}_{71}\text{An}_{28}\text{Or}_1$ and $\text{Ab}_{85}\text{An}_{14}\text{Or}_1$ – $\text{Ab}_{72}\text{An}_{25}\text{Or}_2$, respectively. In the two-mica granitoid (Fig. 4.6D), plagioclases are classified as albite and oligoclase with compositions ranging from $\text{Ab}_{96}\text{An}_3\text{Or}_1$ to $\text{Ab}_{77}\text{An}_{22}\text{Or}_1$.

Two types of plagioclase zoning have been observed within the Bafoussam granitoids:

(1) **Reverse zoning** with the increase of An-content from the core towards the rim as in the deformed biotite granitoid (core: $\text{Ab}_{90}\text{An}_9\text{Or}_1$ → rim: $\text{Ab}_{82}\text{An}_{17}\text{Or}_1$), the mega feldspar granitoid (core: $\text{Ab}_{95}\text{An}_4\text{Or}_1$ → rim: $\text{Ab}_{82}\text{An}_{17}\text{Or}_1$) and the two-mica granitoid (core: $\text{Ab}_{96-94}\text{An}_{3-5}\text{Or}_1$ → rim: $\text{Ab}_{87-85}\text{An}_{12-14}\text{Or}_1$) samples.

(2) **Normal zoning** with increasing Ab content from the core towards the rim as in the biotite granitoid samples (core: $\text{Ab}_{64}\text{An}_{35}\text{Or}_1$ → rim: $\text{Ab}_{79}\text{An}_{20}\text{Or}_1$).

4.5 Iron-titanium oxides: magnetite and ilmenite

Opaque oxides are omnipresent in all Bafoussam granitoid rocks, but only as accessory constituents. They are magnetite and ilmenite. The both minerals mostly occur as small grains in inclusions within the main mineral phases. However, some magnetite and ilmenite samples with the size comparable to other minerals appear isolated in the matrix. Moreover, some hematite crystals in the matrix are rimmed by titanite. The magnetite and ilmenite formula was calculated based on four and six oxygens, respectively. A calculation method on the basis of three and four cations, respectively, was chosen to determinate the Fe^{3+} contents of magnetite and ilmenite. The selected analyses of magnetite and ilmenite are given in Tables A.2.6a: b in the Appendix A.2.

In spite of their different textural positions, the analyzed **magnetite** shows homogeneous chemical composition. The magnetite composition of the Bafoussam granitoids is characterized

by negligible amounts of TiO_2 (0.00–0.17 wt. %), Al_2O_3 (0.00–0.06 wt. %) and MnO (0.00–0.17 wt. %), and compares to the ideal magnetite end-member composition.

The Bafoussam granitoid **ilmenite** samples display only a small compositional variation and can be taken as a pure ilmenite. They have Fe_2O_3 content ranging between 0.03–0.22 wt. % and accessory amounts of MgO (0.00–0.17 wt. %) and MnO (0.00–0.17 wt. %).

4.6 Mineral chemistry of igneous phases

In conclusion, microprobe data of the analyzed minerals display in general minor or no variation in mineral composition between the granitoid types:

- Biotite is Fe-rich (X_{Fe} : 0.41–0.82) and has a composition of biotite (*sensus stricto*). The $\text{Fe}^{2+}/(\text{Fe}^{2+} + \text{Mg})$ ratios increase with increasing $\sum \text{Al}$ values. This trend is typical for continental collision-related granites and indicates an important contribution of crustal material during the petrogenesis of the investigated granitoids. Biotite is generally of re-equilibrated primary composition, likely caused by the deformation that variably affected their host rocks. Its chemical composition is typical calc-alkaline and characterizes the granitoids described in this study as being calc-alkaline and peraluminous granitoids.

- Muscovite (X_{Fe} : 0.52–0.82) is primary in composition and has experienced celadonite substitution and up to 9 % paragonite substitution. The celadonitic composition of primary muscovite suggests the crystallization of the studied granitoid from tonalitic to granodioritic melt.

- Garnet is a purely igneous phase, having almandine–spessartine composition (X_{Fe} : 0.99 and X_{Mn} : 0.46–0.56). Some garnet crystals exhibit core-rim decrease in Mn that points to the depletion crystallization model, i.e. initial crystallization of garnet causes early decrease of Mn in the original melt.

- Amphibole belongs to the calcic-group and is thus termed hornblende. It has magnesio-hastingsite and edenite compositions (X_{Mg} : 0.50–0.62) and typical igneous amphibole characteristics. The edenitic and tschermakitic substitutions have mainly played an important role during the evolution of hornblende in the investigated granitoids.

- Feldspars are represented by exclusively orthoclase (microcline and orthoclase: $\text{Or}_{81}\text{Ab}_{19}\text{An}_0$ – $\text{Or}_{97}\text{Ab}_3\text{An}_0$) for potassium feldspar, while plagioclase is mostly oligoclase, with less albite and andesine ($\text{Ab}_{96}\text{An}_3\text{Or}_1$ – $\text{Ab}_{71}\text{An}_{28}\text{Or}_1$). Zonation is common within the feldspars, the plagioclase shows weakly reverse zonation, but zoning in normal way is also observed.

- The iron-titanium oxides, magnetite and ilmenite have, respectively, nearly pure end-member composition.

5 ESTIMATES OF CRYSTALLIZATION CONDITIONS

It has been demonstrated that mineral chemistry and mineral assemblages are recorders of variations of physical conditions (P , T , X , fluids) in the crust. An attempt to quantify these physical conditions has been made, using several calibrations for each. Nevertheless, the mega feldspar granitoid and some samples of the biotite granitoid and the deformed granitoid have no suitable mineral assemblage to obtain quantitative pressure estimations. Textural information such as fine to coarse grain-size and local plastic and/or brittle deformation, however, indicate emplacement of these granitoids at a medium level of the continental crust (< 10 kbar).

5.1 Temperature estimates

5.1.1 Zircon and apatite saturation thermometry

The approach of estimating magmatic temperatures through zircon and apatite saturation has been proposed by Watson and Harrison (1983) and Harrison and Watson (1984). These thermometers were calculated using P_2O_5 and Zr concentrations in the granitoids and have a reported uncertainty of $\sim \pm 25^\circ\text{C}$. The basic assumptions for these thermometer models are as follows (Watson and Copobianco, 1981; Watson and Harrison, 1984):

- Neither zircon nor apatite crystals are pre-magmatic, entrained from wall-rock through late-stage contamination, or inherited, derived at a deeper level from a contributing source material.
- The granitoid whole-rock data approach the composition of the melt from which zircon and apatite were derived. This implies that there is no provision of zircon and apatite in the original melt through cumulate, restite and country rock assimilation.

These models allow the estimation of liquidus conditions, where one or both phases are early in the crystallisation sequence, or solidus conditions, where one or both phases are late. The resulted temperature may be indicative: (1) either of the temperature at which the zircon or apatite last equilibrated with the melt, this can be the temperature of extraction of the granitic magma from the source in the case that no fractional crystallization occurred between the source

region and the emplacement level (Miller et al., 1988); (2) or in the case of fractional crystallisation, the temperature of differentiation from parental magma (Scaillet et al., 1990).

- Zircon saturation temperatures

Hanchar and Watson (2003) reviewed the zircon saturation thermometry studies and summarized the main applications of the zircon saturation thermometry to igneous rocks and metamorphic rocks. The temperature from the zircon saturation model (T_{Zr}) was calculated according to the equation in Watson and Harrison (1983), representing the relationship between zircon solubility, temperature and major element composition of the melt:

$$\ln D_{\text{Zr}}^{\text{zircon/melt}} = \{-3.8 - [0.85(M - 1)]\} + 12900/T_{\text{Zr}} \quad (5.1)$$

where:

$D_{\text{Zr}}^{\text{zircon/melt}}$ = concentration ratio of Zr (ppm) in zircon to that in the saturated melt, i.e. bulk-rock concentration of Zr in rock sample; all Zr is assumed to be in zircon

M = compositional factor that accounts for the dependence of zircon solubility on SiO_2 and peraluminosity of the melt $[(\text{Na} + \text{K} + 2\text{Ca})/(\text{Al} \times \text{Si})$, all in cation fraction]

T_{Zr} = temperature in Kelvin (however, T_{Zr} referred to this study has been converted to °C)

The results of temperatures from the zircon saturated model (T_{Zr}) are presented in Table 5.1 and are presented graphically on the Zr (ppm) versus the cation ratio $(\text{Na} + \text{K} + 2\text{Ca})/(\text{Al} \times \text{Si})$ plot of the granitoid whole-rock compositions (Fig. 5.1A: Watson and Harrison, 1983). The Figure 5.1A illustrates the proportions of Zr that can be dissolved in granitoid melts of various compositions at different temperatures. The studied granitoids display high Zr concentrations (43–524 ppm), arguing for relative high temperatures of emplacement. The calculated zircon saturation temperatures range between 757–858 °C (average $n = 22$: 808 ± 34 °C, 1σ) for the biotite granitoid, 679–866 °C (average $n = 22$: 797 ± 48 °C, 1σ) for the deformed biotite granitoid, 788–837 °C (average $n = 11$: 815 ± 17 °C, 1σ) for the mega feldspar granitoid and 700–824 °C (average $n = 8$: 772 ± 41 °C, 1σ) for the two-mica granitoid.

The high zirconium concentration in the studied granitoids (43–524 ppm, with just two values below 110 ppm) implies that they contain non-xenocrystic zircon. This is also reflected by the temperatures obtained above having mean average range of 772 ± 41 to 815 ± 17 °C which is

close to 837 ± 48 °C, as reported for the genesis of granitoids with no or negligible inherited zircon (Miller et al., 2003). Since the investigated granitoids did not show any excess of alkalis over alumina [$(\text{Na}_2\text{O} + \text{K}_2\text{O})/\text{Al}_2\text{O}_3 < 1.0$: Fig. 7.5] and have roughly $\text{Zr} > 100$ ppm, the melts involved in the production of these rocks were saturated in zircon (Watson, 1979), despite of their slight felsic nature with 57–75 wt. % SiO_2 . This is corroborated by the decreasing trend observed in the Zr versus SiO_2 diagram (see Fig. 7.10) that points to zircon saturation at 62 wt. % SiO_2 .

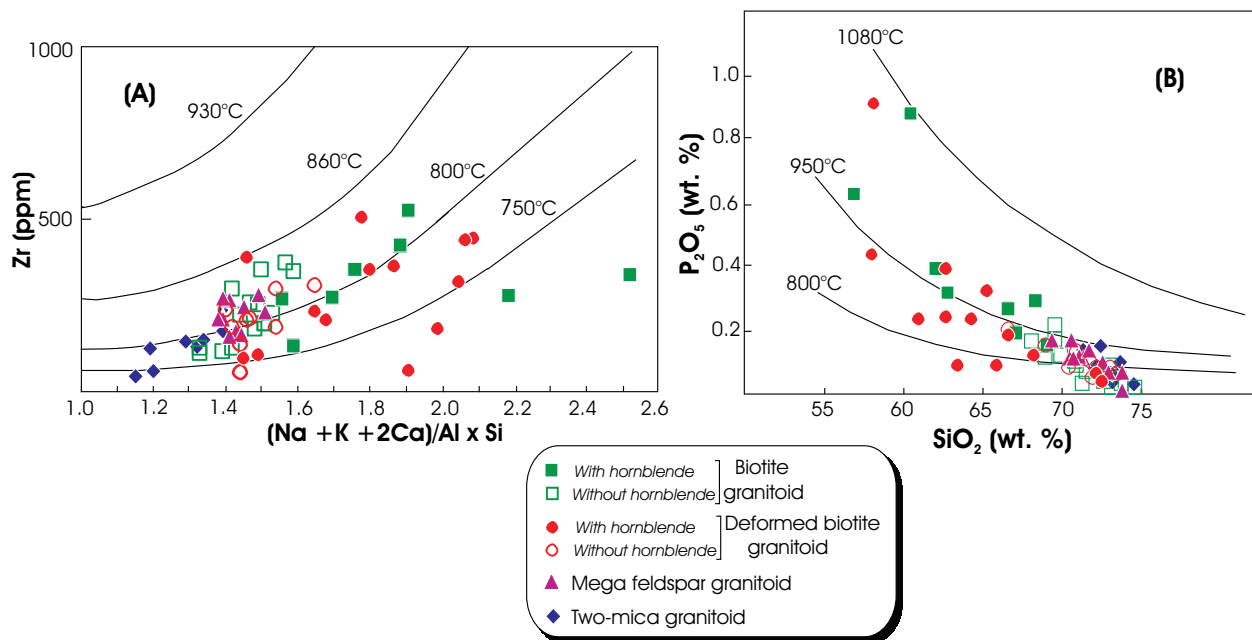


Figure 5.1: Temperature estimates in degree Celsius (°C) of the Bafoussam granitoids based on proportions of P_2O_5 and Zr (wt. %) that can be dissolved in granitoids melts of various compositions at different temperatures. **(A)** Zircon saturation temperature estimates (Watson and Harrison, 1983). **(B)** Apatite saturation estimates (Green and Watson, 1982). Zircon and apatite saturation isotherms are indicated, labelled with their respective temperatures.

- Apatite saturation temperatures

From their experimental study, Harrison and Watson (1984) established the following expression for the relation between apatite solubility, temperature and melt major element composition:

$$\ln D_{\text{P}}^{\text{apatite/melt}} = [(8400 + ((\text{SiO}_2 - 0.5)2.64 \times 10^4))/T_{\text{P}}] - [3.1 + (12.4(\text{SiO}_2 - 0.5))] \quad (5.2)$$

where:

$D_{\text{P}}^{\text{apatite/melt}}$ = ratio of the P_2O_5 concentration (wt. %) in apatite to that in the saturated melt, i.e. bulk-rock concentration of P_2O_5 in rock sample; all P_2O_5 is assumed to be in apatite

$$\begin{aligned} \text{SiO}_2 &= && \text{weight fraction of silica in the melt} \\ T_p &= && \text{temperature in Kelvin (Hereafter, } T_p \text{ have been converted to } ^\circ \text{C)} \end{aligned}$$

The calculated apatite saturated temperatures (T_p) are given in Table 5.1 and by the plot of P_2O_5 versus SiO_2 (wt. %) according to Green and Watson (1982) (Fig. 5.1B). The Figure 5.5B shows the concentration of P_2O_5 in the granitoids under study which are compared to the proportions of P_2O_5 that can be dissolved in granitoid melts of various compositions at different temperatures. The concentrations of P_2O_5 vary widely within the investigated granitoids (up to 0.90 wt. %), suggesting a wide temperatures range of formation. The obtained apatite saturated temperatures are significantly higher than those estimated using the zircon saturation method (T_{Zr}), having mean values of 792–1077 °C (average $n = 22$: 920 ± 71 °C, 1σ) for the biotite granitoid, 822–1055 °C (average $n = 22$: 915 ± 52 °C, 1σ) for the deformed biotite granitoid, 746–966 °C (average $n = 11$: 914 ± 60 °C, 1σ) for the mega feldspar granitoid and 838–952 °C (average $n = 8$: 896 ± 39 °C, 1σ) for the two-mica granitoid.

From petrographic analysis (see Chapter 3) of the investigated granitoids, no signs of the resorption of apatite or compositional zoning have been observed. This supports the idea of a magmatic origin of the apatite. On the other hand, the pattern of P_2O_5 (Fig. 5.1B) exhibits a saturation apatite trend (decreasing of P_2O_5 with increasing SiO_2) and indicates that the magmas of the granitoids under study were saturated in apatite at around 58 wt. % SiO_2 , i.e. at lower SiO_2 values compared to the occurrence of the zircon saturation.

Zircon and apatite within the Bafoussam granitoids appear as euhedral crystals, commonly as inclusions in the major rock-forming phases such as biotite, feldspars and hornblende. Therefore, zircon and apatite might result from an early stage of crystallization (Hoskin et al., 2000) and thus represent a stage at or near the liquidus of the magma. The significant difference in the calculated saturation temperatures between the two thermometer models by ca. 40–160 °C (Figure 5.2 and Table 5.1) could be attributed to the saturation of the investigated granitoids with respect to apatite and zircon at distinct stages of crystallization, the apatite being the earliest crystallizing phase. Moreover, such a discrepancy could also be justified by a small excess component of apatite in the granitoids under study (Evans and Hanson, 1993). It can then be concluded from these data that several phases occurring in a single

sample did not necessarily crystallize simultaneously and the mineral composition may register intervals of equilibrium crystallization.

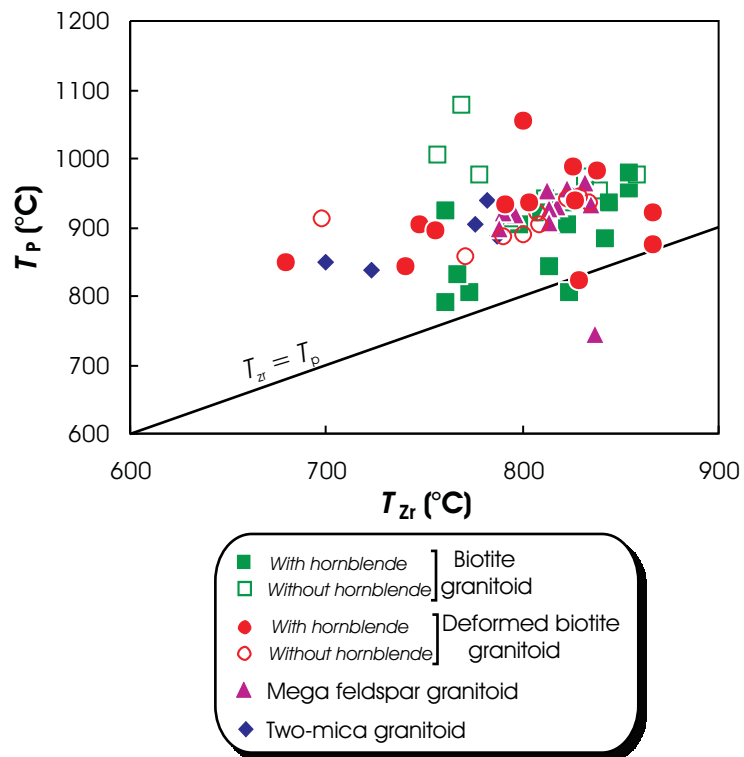


Figure 5.2: Comparison between apatite saturation (T_p) and zircon saturation (T_{Zr}) temperatures of the Bafoussam granitoid, showing the significant excess of the calculated T_p over T_{Zr} .

Pichavant et al. (1992) demonstrated that the apatite saturation is also controlled by the aluminum saturation index [ASI = molar $\text{Al}_2\text{O}_3/(\text{Na}_2\text{O} + \text{K}_2\text{O} + \text{CaO})$], in addition to SiO_2 content of the melt and temperature as suggested by Harrison and Watson (1984). The saturation model of Harrison and Watson (1984) may be then unsuitable for the studied granitoids, since they have increasing ASI and become strongly peraluminous in the two-mica granitoid (Fig. 7.9). Moreover, the presence of monazite in the granitoids indicates that all the P_2O_5 is not fixed by apatite as assuming by Harrison and Watson (1984). Hence, the magmatic temperatures are probably overestimated by the apatite thermometer.

5.1.2 Hornblende–plagioclase thermometry

Within the granitoids discussed in this study, only certain samples of the biotite granitoid and the deformed biotite granitoid contain the mineral pair hornblende and plagioclase, which

can be used to constrain their solidus temperature using hornblende–plagioclase thermometry. Several hornblende–plagioclase thermometers are currently available, but the model of Holland and Blundy (1994) appears to be the most accepted (Ague and Brandon, 1996). The temperature of crystallization of these granitoids was then calculated using the edenite–tremolite equilibrium expression of the hornblende–plagioclase thermometer as advised by Holland and Blundy (1994) for quartz-bearing assemblages or silica-saturated rocks. This calibration has a reported uncertainty of ± 75 °C. The temperatures have been calculated from the chemical analyses of the coexisting amphibole and plagioclase determined by the electron microprobe (Tables A.2.4 and A.2.5b, Appendix A.2) with help of the HbPl 1.2 computer program (supported by Tim Holland and Jon Blundy).

Table 5.1: Estimated crystallization temperatures (°C) of the Bafoussam granitoids after Watson and Harrison (T_{Zr} : 1983), Harrison and Watson (T_p : 1984) and Holland and Blundy (Hbl–Pl thermometry: 1994).

* Samples containing hornblende minerals

Values in brackets are calculated average values with uncertainties (1σ)

n represents the number of values

σ is the standard deviation

Temperature calibrations	Biotite granitoid (n = 14; 8*)	Deformed biotite granitoid (n = 9; 13*)	Mega feldspar granitoid (n = 11)	Two-mica granitoid (n = 8)
T_{Zr} (°C)	761 – 854 (808 ± 34)	698 – 834 (796 ± 42)	790 – 837 (815 ± 17)	700 – 824 (772 ± 41)
	757 – 858* (808 ± 36)*	740 – 866* (798 ± 54)*		
T_p (°C)	792 – 980 (886 ± 60)	857 – 944 (910 ± 29)	746 – 966 (914 ± 60)	838 – 952 (896 ± 39)
	937 – 1077* (981 ± 45)*	822 – 1055* (919 ± 65)*		
Hbl–Pl thermometry (°C)	739 – 790* (764 ± 14)* $n = 17$	699 – 788* (733 ± 30)* $n = 28$	–	–

Hornblende and plagioclase from the biotite granitoid crystallized at temperature of 739–790 °C (average n = 17: 764 ± 14 °C, 1σ); the deformed biotite granitoid yielded slightly lower temperatures, ranging from 699 to 788 °C (average n = 28: 733 ± 30 °C, 1σ). They are consistent with the experimental data on the liquidus for igneous hornblendes (< 950 °C; Gilbert et al.,

1982). These temperatures were estimated for a reasonable pressure of 5 kbar. The average temperatures obtained by hornblende–plagioclase geothermometry are slightly lower than those given by zircon saturation, 808 ± 36 °C and 798 ± 54 °C, respectively, for the biotite granitoid and the deformed biotite granitoid (Table 5.1). This points to the crystallization of hornblende immediately after that of zircon, as suggested by sequence of crystallization in the granitoids (Fig. 3.13A and B).

To conclude, the average temperatures for the various granitoid types given by the different thermometers are overlapped within their uncertainties, strongly suggesting that they do not differ significantly between the four granitoids types. The temperatures estimated using zircon saturation and hornblende–plagioclase calibrations seem to be more likely close to the temperatures of melts that have generated the investigated granitoids. Nzolang (2005) reported similar T_{Zr} temperatures in the neighbouring Bantoum biotite-granites (810–870 °C) and leucogranites (715–745 °C). Moreover, the temperature ranges obtained are close to those inferred for the genesis of other calc-alkaline granitoid rocks with an I- or S-type origin (650–850 °C: Whitney, 1988; 720–820 °C: Jung et al., 2001; 797–880 °C: El Baghdadi et al., 2003). In their study of the I-type granites of the Lachlan fold belt, Chappell et al. (2000) distinguished high- and low-temperature I-type granites based on the patterns of Zr variation and the Al-oversaturation. The high-temperature I-type granites are metaluminous and show two step Zr variations, an increasing followed by decreasing with increasing SiO_2 , while the low-temperature granites are peraluminous and are characterized by a decrease of Zr with increasing SiO_2 . The granitoids under study can be compared to their low-temperature I-type granites. Although they exhibit metaluminous and peraluminous character, their Zr abundances decrease with increasing SiO_2 (Figs. 7.9 and 7.10).

5.2 Pressure estimates

5.2.1 Aluminium-in-hornblende geobarometry

Hammarstrom and Zen (1986) and Hollister et al. (1987) have shown in their empirical and theoretical studies that aluminum content of hornblende in near-liquidus calc-alkaline granitoid rocks varies linearly with pressure of crystallization, thereby providing means of

constraining the depth of granitic pluton emplacement. Since then, the aluminum-in-hornblende geobarometer has evolved and many experimental calibrations have been performed (see Anderson and Smith, 1995 for review). Schmidt (1992) has attributed the increase of the total Al (ΣAl) with pressure to Al-Tschermakitic exchange (see Table 4.2). Although the estimated pressure using this barometer can be affected by temperature, ion substitution in hornblende, oxygen fugacity, volatiles and magma composition, Ague (1997) has proved the reliability of the aluminum-in-hornblende geobarometer in natural systems.

The biotite granitoid and deformed biotite granitoid contain the seven magmatic equilibrium mineral phases (quartz + plagioclase + alkali feldspar + hornblende + biotite + titanite + Fe–Ti oxide) which enable the application of the aluminum-in-hornblende geobarometry. Also, their hornblende $\text{Fe}^{2+}/(\text{Fe}^{2+} + \text{Mg})$ ratios of 0.44–0.50 and 0.31–0.49, respectively, are within the recommended limiting values (< 0.65) of the calibration by Anderson and Smith (1995). Furthermore, the narrow compositional range of the feldspars in these granitoids (mainly oligoclase) provides the additional restriction necessary for Al content in hornblende to be entirely a function of the pressure (Hollister et al., 1987).

The microprobe analysis results (Table A.2.4 in the Appendix A.2) of hornblendes have been used to calculate the pressure. The rim and core of unzoned hornblendes are almost similar in composition and were both used for pressure calculation, although the rim portions of the crystal most likely crystallized in equilibrium with the other mineral phases (Johnson and Rutherford, 1989). The pressure at which the magma crystallized was computed according to the following equation of Schmidt (1992):

$$P (\pm 0.6 \text{ kbar}) = -3.01 + 4.76 \sum\text{Al} \quad r^2 = 0.99, \quad (5.3)$$

where:

- $\sum\text{Al}$ = total number of Al atoms in hornblende per unit formula (based on 23 oxygens)
- r^2 = correlation coefficient in Schmidt's experimental calibration
- P = pressure in kilobars (kbar)

The $\sum\text{Al}$ content of hornblende from the biotite granitoid and deformed biotite granitoid yielded pressures ranging from 3.4–5.5 kbar (average $n = 18$: 4.8 ± 0.5 kbar, 1σ) and 2.5–6.1

kbar (average $n = 27$: 4.2 ± 1.1 kbar, 1σ), respectively. For comparison, these pressures obtained with Schmidt's (1992) calibration are higher than those estimated with the other aluminum-in-hornblende calibrations of Hammarstrom and Zen (1986), Hollister et al. (1987) and Johnson and Rutherford (1989), due to the temperature effects discussed by Anderson and Smith (1995). The pressures calculated from these various aluminum-in-hornblende calibrations decrease in the following sequence: Schmidt (1992) → Hollister et al. (1987) → Hammarstrom and Zen (1986) → Johnson and Rutherford (1989) (Table 5.2).

As expected, only a small difference in the calculated pressures is noticed from core and rim compositions of single hornblende samples. The calculated pressures may likely represent the conditions during final emplacement, as the crystallization of the magma must have been well advanced to produce the entire mineral assemblage required for aluminum-in-hornblende barometry. A similar pressure range as for the biotite granitoid and deformed biotite granitoid (2.5–6.1 kbar) has been yielded by the different aluminum-in-hornblende calibrations for other granitoids plutons in west Cameroon (e.g., 2.0–6.0 kbar, Tetsopgang, 2003; 4.8–5.9 kbar, Nzolang, 2005).

Table 5.2: Comparison of the results from aluminum-in-hornblende geobarometric calibrations applied to the Bafoussam granitoids.

Values in brackets are calculated average values with uncertainties (1σ)

n represents the number of values

σ is the standard deviation

Rock type	Biotite granitoid ($n = 18$)	Deformed biotite granitoid ($n = 27$)
Total Al (a.p.f.u)	1.35 – 1.78	1.16 – 1.90
<hr/>		
Barometer		Pressures (kbar)
Schmidt (1992)	3.4 – 5.5 (4.8 ± 0.5)	2.5 – 6.1 (4.2 ± 1.1)
Hollister et al. (1987)	2.9 – 5.3 (4.5 ± 0.7)	1.9 – 6.0 (3.8 ± 1.2)
Hammarstrom and Zen (1986)	2.8 – 5.1 (4.3 ± 0.6)	1.8 – 5.7 (3.7 ± 1.2)
Johnson and Rutherford (1989)	2.3 – 4.1 (3.4 ± 0.5)	1.5 – 4.6 (2.9 ± 0.9)

5.2.2 Phengite geobarometry

Many studies have demonstrated that the presence of primary muscovite in granitic rocks allows the estimation of a lower limit of pressure (hence minimum depth) of crystallization (e.g., Anderson and Rowley, 1981; Massonne and Schreyer, 1987). Velde (1967) calibrated the phengite geobarometer based on the component of celadonite in muscovite–celadonite mica or phengite ($KAl_2[AlSi_3O_{10}](OH)_2 - K(Mg, Fe^{2+})(Fe^{3+}, Al)[SiO_4](OH)_2$), which raises with the increasing pressure. Afterwards, Massonne and Schreyer (1987) established a new calibration for quartz + biotite + phengite + K-feldspar assemblages. This calibration, illustrated in graphical form, demonstrates that Si content (half formula unit) in phengite increases with increasing pressure by nearly linear function, whereas increasing temperature implies only minor decrease of Si contents. Anderson (1996) has expressed the Massonne and Schreyer (1987) graphical solutions by the following equation:

$$P \text{ (kbar)} = -2.6786\text{Si}^2 + 43.975\text{Si} + 0.01253 T(\text{°C}) - 113.9995 \quad (5.4)$$

where:

Si = Si contents (a.p.f.u., 22 oxygens)

P = pressure in kbar

T = temperature (°C: here the calculated average T_{Zr})

In the two-mica granitoid, the analysed muscovite contains considerable amounts of celadonitic component (see Fig. 4.4A, Table A.2.2, Appendix A.2), which makes it appropriate for phengite barometry. Si-values range between 6.099 and 6.378 a.p.f.u. The calculated pressures of crystallization of the Bafoussam two-mica granitoid range between 4.7–9.0 kbar (average $n = 56$: 6.6 ± 1.0 kbar) corresponding to the average zircon saturation temperature (T_{Zr}) of 772 °C. This average pressure value is interpreted as a reasonable approximation to the crystallization pressure of the Bafoussam two-mica granitoid and it compares well to the range of pressures documented in the Nkambe two-mica granitoid in west Cameroon (5.5–8.0 kbar: Tetsopgang, 2003). It is also consistent with the emplacement pressure of leucogranite from Damara orogen, Namibia (~6.0 kbar: Jung et al., 2001), as well as Himalayan two-mica granites (6.0–8.0 kbar) inferred from experimental data (Patiño-Douce and Harris, 1998).

The crystallization pressures of the Bafoussam granitoids obtained above are assumed to be equivalent to emplacement pressures. They have then been converted to emplacement depths by using the equivalency 1 kbar = 3.7 km, assuming an average crustal density of 2.7 g/cm³ and taking in consideration the limits which these data impose on vertical crustal movements. Estimates of emplacement depths for dated plutons may provide direct evidence for the ascent or descent of the exposed crustal sections through time, thus providing fundamental information about tectonic processes in orogenic belts. The depths were calculated from the average pressure values using Schmidt's (1992) calibration and phengite barometry (Anderson, 1996). The studied granitoids yielded different depths of emplacement: biotite granitoid–depth ~18 km, deformed biotite granitoid– depth ~ 15 km and two-mica granitoid – depth ~ 24 km.

5.3 Oxygen fugacity estimates

The oxygen fugacity ($f\text{O}_2$) is the parameter which controls the redox state of the magma. The intrinsic oxygen fugacity of a magmatic rock reflects its source material (Wones, 1989) as well as its tectonic setting (Carmichael, 1991; Burkhard, 1993). Granites derived from mantle are normally oxidized, while S-type granites are more reduced (Chappell and White, 1992). Granites that are highly oxidized during crystallization occur in compressive tectonic positions, i.e. convergent plate boundaries, whereas granites formed by fractionation from mantle-derived magmas in rift zones are reduced.

In general, the reconstruction of the original oxygen fugacities of primary magmas from granitoid rocks is difficult, as magnetite commonly becomes Ti free during slow cooling and the ilmenite undergoes one or more stages of oxidation–exsolution (Haggerty, 1976). However, roughly qualitative constraint on the oxidation state of a magma can be made based on the rock's mineral assemblage (Czamanske and Wones, 1973) and the mineral chemistry (Burkhard, 1991). The presence of titanite, magnetite and quartz in granitoids implies high oxygen fugacity, at least nickel–nickel oxide (NNO) buffer. The occurrence of euhedral titanite and magnetite as early-crystallizing phases in silicate rocks indicates that the magma was relatively oxidized. High Mg content of the amphibole occurring in the rock indicates somewhat oxidized magma.

Beside the lack of determined ferrous/ferric ratios in biotite of the Bafoussam granitoids at the time of magmatic equilibration, the relative oxygen fugacity can still be quantitatively calibrated using the $\text{Fe}^{2+}/(\text{Fe}^{2+} + \text{Mg})$ value of biotite in $f(\text{O}_2)$ -T diagram for biotite + K-feldspar + magnetite equilibrium at a total pressure of 2070 bar (Fig. 5.3: Wones and Eugster, 1965). Apart from the two-mica granitoid which does not include magnetite, these three phases coexist in the studied granitoids. Based on the presence of ilmenite as sole opaque mineral in the two-mica granitoid, the $f(\text{O}_2)$ at which this granite equilibrated is believed to be in general moderately reduced, at or below the quartz–fayalite–magnetite (QFM) buffer (Chappell and White, 1992; Pichavant et al., 1996). Taking the average zircon saturation temperatures (T_{Zr}) for the other granitoid groups, estimated $f(\text{O}_2)$ values span a range of 10^{-16} to 10^{-11} bars. Values of $f\text{O}_2$ in the Bafoussam granitoids are presented in detail in Table 5.3.

Within the $f(\text{O}_2)$ -T diagram (Fig. 5.3), biotite compositions of the biotite granitoid and the deformed biotite granitoid overlap the NNO line, suggesting oxidation conditions. Their samples that plot above the QFM line have hematite as opaque phase, while the ones falling between the NNO and hematite–magnetite (HM) lines contain additionally Mg-rich hornblende (Fig. 4.6) and titanite. Biotites of the mega feldspar granitoid plot between the nickel–nickel oxide (NNO) and the quartz–fayalite–magnetite (QFM) buffers, indicative of relatively oxidation conditions. The mega feldspar granitoid has ilmenite as a main opaque mineral with additional minor magnetite and titanite.

Wones (1989) introduced an equilibrium expression for the quantitative evaluation of the oxygen fugacity, using the assemblage titanite + magnetite + quartz:

$$\log f(\text{O}_2) = -30930/T + 14.98 + 0.14(P - 1)/T \quad (5.5)$$

where:

$$\begin{aligned} T &= \text{temperature in Kelvin} \\ P &= \text{pressure in kbar} \end{aligned}$$

The oxygen fugacity is calculated for the biotite granitoid and the deformed biotite granitoid using temperatures and pressures obtained from hornblende–plagioclase thermometry and aluminum-in-hornblende barometer (Schmidt, 1992), respectively. The biotite granitoid and

the deformed biotite granitoid show the oxygen fugacity values ranging from 10^{-15} to 10^{-13} and 10^{-17} to 10^{-14} , respectively.

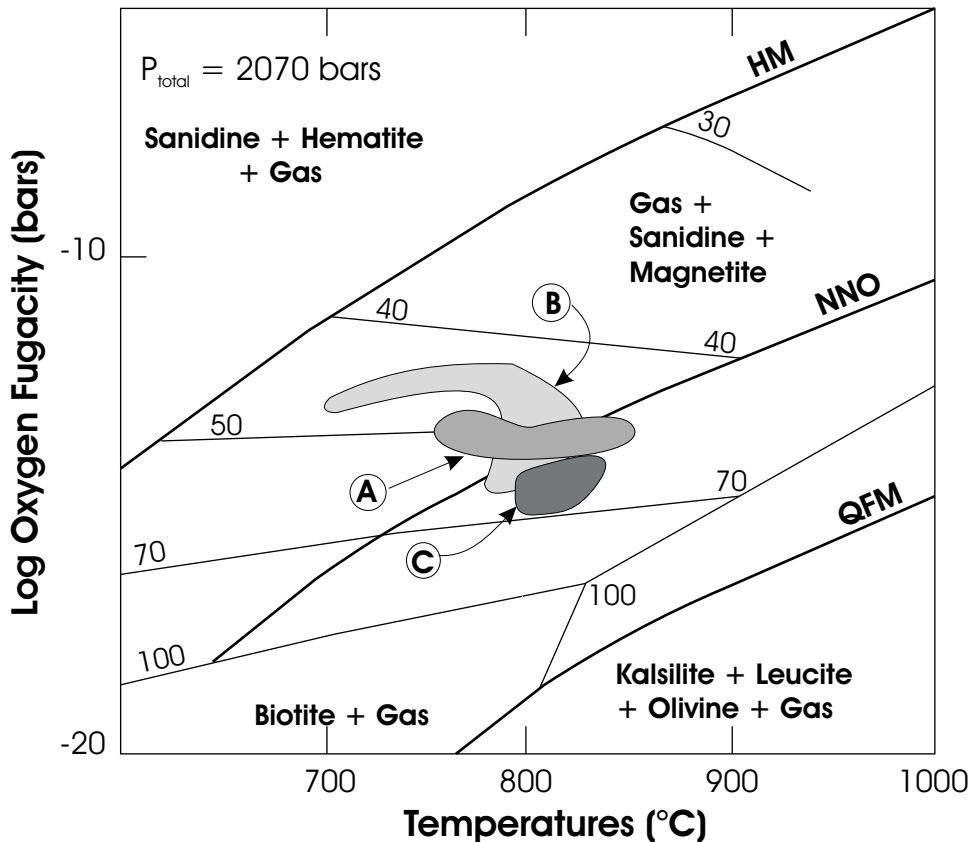


Figure 5.3: $\log f(\text{O}_2)$ versus T diagram for the biotite + magnetite + gas equilibrium at $P_{\text{total}} = 2070$ bars (Wones and Eugster, 1965). Light lines: isopleths $[\text{Fe}^{2+}/(\text{Fe}^{2+} + \text{Mg})] \times 100$; heavy lines: $f(\text{O}_2)$ (oxygen fugacity) buffers: quartz–fayalite–magnetite (QFM), nickel–nickel oxide (NNO), and hematite–magnetite (HM). Labelled fields represent the range of oxygen fugacity for the samples from the Bafoussam granitoids at an equilibrium temperature (T_{Zr}) of 698–866 °C. Symbols are as follows: A = biotite granitoid; B = deformed biotite granitoid; C = mega feldspar granitoid. This diagram represents the Central portion of the original diagram of Wones and Eugster (1965).

Table 5.3: Estimated values of oxygen fugacity during the crystallization of Bafoussam granitoids after Wones and Eugster (1965) and * Wones (1989)

Rock types	$\text{Fe}^{2+}/(\text{Fe}^{2+} + \text{Mg})$	$f(\text{O}_2)$ bars
Biotite granitoid	0.436 – 0.510	$10^{-14} – 10^{-12}$ $10^{-15} – 10^{-13}*$
Deformed biotite granitoid	0.441 – 0.666	$10^{-14} – 10^{-11}$ $10^{-17} – 10^{-14}*$
Mega feldspar granitoid	0.526 – 0.820	$10^{-16} – 10^{-14}$

The results yielded by the equation of Wones (1989) are slightly lower than those obtained from the Wones and Eugster (1965) calibration (Table 5.3). The mineral transformations such as microperthites and flames perthites, and titanite reaction rims around ilmenite and/or magnetite that occurred during the consolidation of the Bafoussam granitoids (Chapter 3) reflect the changing of $f(O_2)$ and temperature conditions (Czamanske and Wones, 1973; Wones, 1989). The granitoid samples containing Mg-rich hornblende as additional ferromagnesian mineral are more oxidized than the ones having only biotite. The oxygen fugacity values suggest mantle-derived magma and a compressive geotectonic setting for the biotite granitoid, the deformed biotite granitoid and the mega feldspar granitoid.

Water content is also an important parameter in the formation of granitic magmas. The experimental studies of Whitney (1988) demonstrated that granitoid rocks require about 4 wt. % water or more for the paragenesis of their mineral crystallization. The water content of magma is reflected by the presence and modal abundance of mafic minerals such as biotite and amphibole which are the only major silicate minerals that admit water in their structure. Generally, melts formed in the middle continental crust are likely to be water-undersaturated (Clemens, 1984; Ebadi and Johannes, 1991).

In conclusion, the granitoids described in this study crystallized under varying pressures (4.2 ± 1.1 to 6.6 ± 1.0 kbar) at temperatures which are not significantly different (772 ± 41 to 808 ± 34 °C), from oxidized magma ($\text{Log}fO_2$ from -17 to -13) with exception of the two-mica granitoid for which the magma was slightly reduced. The pressure data suggest emplacement at different depths ranging between 15 and 24 km. The pressure and temperature range obtained for the Bafoussam granitoids are lower than the culmination of the granulite facies tectono-metamorphic event that has affected the Neoproterozoic belt of Cameroon (Nzenti et al., 1988) and neighbouring provinces of Nigeria (Férré et al., 1998) and Central Africa Republic (Pin and Poidevin, 1987). However, they are comparable to the amphibolite facies metamorphism encountered within the migmatitic gneisses wall-rock in the Bafoussam region (Tagne-Kamga, 2003). This suggests that the crust had either remained at constant depth or that only minor uplift occurred between the peak of the metamorphism and the solidification of the intrusions within the investigated area.

6 FLUID INCLUSION STUDY

Fluid migration is an important process which controls the geochemical and the metamorphic evolution of the continental crust to a significant degree. When flowing through rocks, microscopic samples (micrometer-size) of fluids can be trapped as *fluid inclusions* within growing host minerals (primary inclusion) or during later healing of fluid-filled microcracks and/or fractures (secondary inclusion). Fluid inclusions can contain a wide variety of materials (liquid, gas and solid) and their study has proven to be an important aspect of any fluid-rock interaction research. They are common in geologic samples. Fluid inclusions research is applied in various geological disciplines such as ore deposit geology, sedimentary geology, metamorphic petrology, studies of crustal and mantle magmas, lavas and lunar geology (Roedder, 1984). Fluid inclusions have been widely used in ore deposit geology in order to determine the origin and the evolution of mineralizing fluids and ultimately to better understand ore formation processes (e.g., Wilkinson, 2001), as well as in petroleum geology to identify oil compositional evolution and migration, and possible reservoir rocks (e.g., Burruss, 2003). However, much recent works have been driven in structural geology and have demonstrated that fluid inclusions can be used as thermobarometric, structural and tectonic markers, providing important information on the structural and tectonic history of rocks (e.g., Boullier, 1999).

In this chapter, data are presented resulting from a preliminary fluid inclusion study on hydrothermal quartz veins that are commonly observed within the Bafoussam granitoid outcrops. They are deformed or no and oriented NNE–SSW and NE–SW, with up to 19 cm wide. Quartz veins are direct evidence for the circulation of ancient hydrothermal fluids associated with the fracturing of the rock. Five samples of quartz veins have been selected for fluid inclusion analysis. From petrographic microscopy, all samples chosen contain fluid inclusions. However, only one sample (SE-1) deriving from a quartz vein transecting the deformed biotite granitoid hosts a large number of fluid inclusions of sufficient sizes (greater than 1–2 μm), making them suitable for the application of detailed analytical methods, such as microthermometry. Microthermometric procedures used are described in detail in Appendix A.1.5.

In the following, emphasis is given to: (1) a description of the types of fluid inclusions observed; and (2) their chemical composition as inferred primarily from the microthermometric

data. Furthermore, a possible application of the fluid inclusion data in constraining the conditions (pressure and temperature) of the deformation is discussed.

6.1 Petrography and types of fluid inclusions

Petrographic characterization is a very important part of any fluid inclusion study. The reason for this is that petrography provides information about the chronology of entrapment of fluid inclusions as primary, secondary or pseudosecondary (Roedder, 1984; van den Kerkhof and Hein, 2001; Goldstein, 2003). *Primary* fluid inclusions are entrapped during the crystal growth. They are concentrated in particular growth sectors or associated with the position of particular growth faces. They tend to show typical regular shape, "negative-crystal" shape, bounded by well developed faces. But not all fluid inclusions with negative-crystal shape are primary! *Secondary* denotes fluid inclusions trapped at any time after crystal growth is finished, normally when microcracks or deformation features transect all growth zones of a mineral and heal to trap inclusions. Secondary fluid inclusions normally form planar arrays that cut across growth zones of a crystal. *Pseudosecondary* fluid inclusions are entrapped before the end of crystal growth, but are not necessarily related to the crystal growth. Like secondary fluid inclusions, they are trapped along microfractures, but their entrapment is followed by further crystal growth.

The studied fluid inclusions were observed both in primary igneous quartz and in recrystallized quartz grains. The correlation of the analysed fluid inclusions with growth zones in quartz crystals was possible, since any well developed crystal growth zones was observed. In most cases, however, establishment of the relative chronology of the fluid inclusions within single quartz grains could be achieved based on their spatial relationships. They are generally found occurring either in clusters without any apparent link to fractures, or aligned along well-healed fracture planes (Fig. 6.1A and B). A minor number of solitary inclusions occur arbitrarily distributed within quartz crystals. Most of the fluid inclusions are thus clearly secondary in origin.

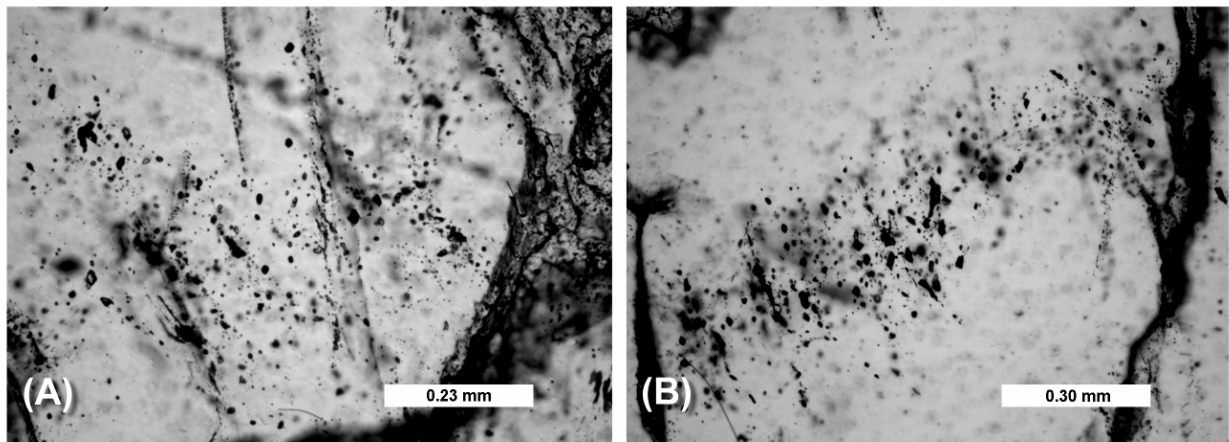


Figure 6.1: (A) and (B) Photomicrographs of typical groups of fluid inclusion (dark spots) trails in quartz crystals. Inclusions oriented diagonally across the field of view represent entrapment along healed micro-fractures.

From the petrographic study, two types of fluid inclusions have been distinguished based on the major phase composition present at room temperature ($\sim 20^{\circ}\text{C}$): (1) Mixed aqueous– non-aqueous volatiles fluid inclusions; and (2) pure aqueous fluid inclusions. The first inclusion type commonly occurs either in groups or along healed fractures internal to a single crystal, constituting short trails; locally, isolated mixed aqueous–non-aqueous volatiles fluid inclusions are found. The second inclusion type is always aligned along healed microfractures cutting across quartz crystal boundaries in several trails. All fluid inclusions are salt-undersaturated as no daughter minerals were observed.

6.1.1 Mixed aqueous–non-aqueous volatile fluid inclusions

According to the proportion of aqueous and non-aqueous volatile (mainly CO_2) ratios at room temperature, the mixed aqueous–non-aqueous volatiles fluid inclusions can be subdivided in: (1) non-aqueous volatiles-rich mixed fluid inclusions and; (2) aqueous-rich mixed fluid inclusions. Commonly, fluids inclusions with clearly different chemical and/or physical features occur within the same quartz crystal, but in separate groups or arranged along separate healed micro-fractures. This inclusion type represents by far the most abundant type.

- Non-aqueous volatile-rich mixed fluid inclusions

At room temperature, non-aqueous volatile-rich mixed fluid inclusions contain one phase (vapour or liquid non-aqueous volatiles), two phases (aqueous liquid + liquid non-aqueous volatiles) or three phases (aqueous liquid + liquid non-aqueous volatiles + vapour non-aqueous volatiles). Their size mostly varies between 15–72 µm (longest axis).

- **Monophase non-aqueous volatile fluid inclusions** are commonly low-density (solely vapour) inclusions and dark in appearance. They are commonly irregular in shapes and elongated, and less commonly display negative crystal form (Fig. 6.2A and B).

- **Two phase non-aqueous volatile-rich fluid inclusions** consist of large volume of liquid non-aqueous volatile with a thin rim of aqueous liquid, with a degree of fill [$F = V_A/(V_A + V_V)$; A, aqueous; V, volatile] lower than 0.1 (Fig. 6.2C). They show irregular, oval or round forms.

- **Three phase non-aqueous volatile-rich fluid inclusions** dominantly consist of liquid + vapour of non-aqueous volatile phase bubbles with a large volume of the liquid phase that envelopes the vapour bubble of varying volumes, and a small aqueous liquid phase (Fig. 6.2D, E and F). The degree of fill of this inclusions type is low and variable along a given trail [$F = V_A/(V_A + V_V) < 0.5$]. These fluid inclusions are sub-rectangular, elongate, round in shape and are comparable in size to the monophase gas inclusions.

- Aqueous-rich mixed fluid inclusions

Like the non-aqueous volatiles-rich fluid inclusions, they are regular shaped (round, elongate or ovoid, and less commonly show negative crystal form) but smaller, mostly 15–30 µm in size (longest axis). In these fluid inclusions, the aqueous liquid phase predominates over an omnipresent small volume of non-aqueous volatiles that usually consists of two bubbles of both liquid and vapour phase (Fig. 6.3A, B, C and D), at room temperature. They are generally characterized by a consistent and variable degree of fill [$F = V_A/(V_A + V_V)$], ranging between 0.6 and 0.8.

6.1.2 Pure aqueous fluid inclusions

Easily recognisable by their bright appearance, pure aqueous fluid inclusions are typically of small size, less than 10 µm, and characterized by oval, round or elongate shapes. However, a few inclusions are large (10–35 µm), having mostly irregular and flattened forms. Their degree

of fill [$F = V_A/(V_A + V_V)$] is near 1.0 (Fig.6.4A and B). Pure aqueous fluid inclusions display two phases, including a dominant aqueous liquid phase and a small bubble of aqueous vapour phase.

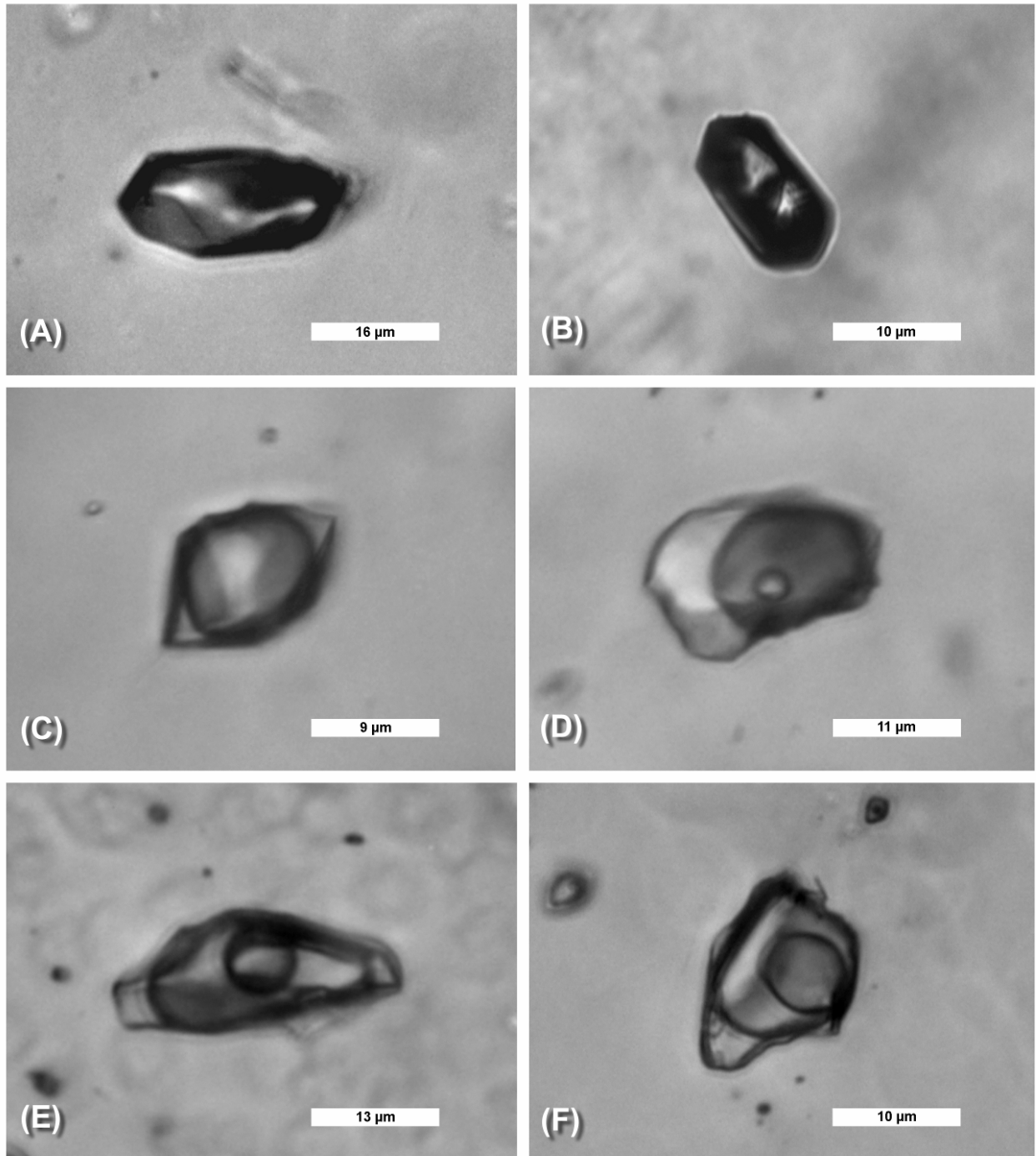


Figure 6.2: Photomicrographs of the different types of non-aqueous volatile-rich mixed fluid inclusions found in the studied quartz veins. (A) and (B) one-phase inclusions consisting of CO₂ vapour. (C) Two-phase inclusion displaying a dominant CO₂ liquid bubble and a thin rim of H₂O liquid. (D), (E) and (F) Three-phase inclusions comprising small CO₂ vapour bubble with increasing size from (D) to (F), large CO₂ liquid bubble and rim of H₂O liquid.

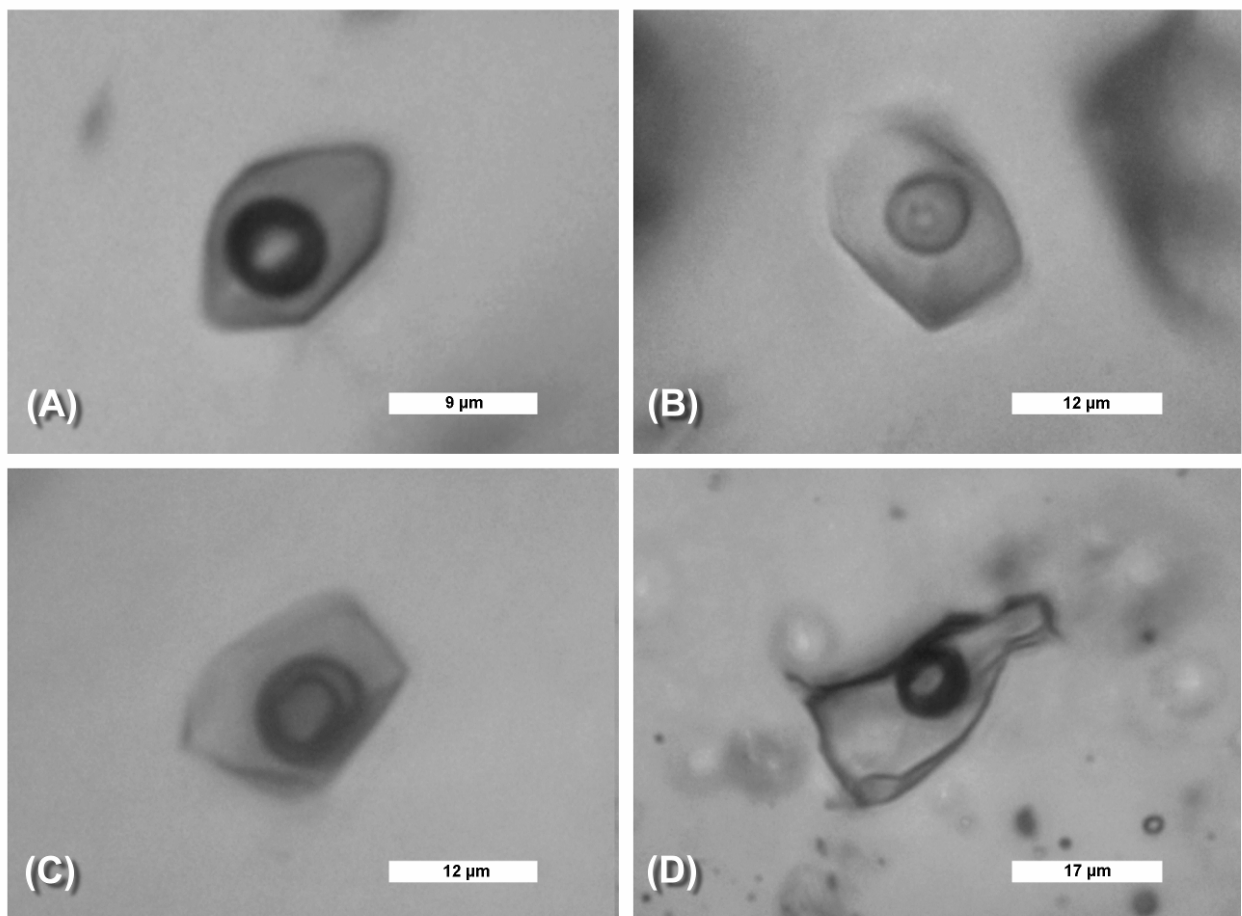


Figure 6.3: Aqueous-rich mixed fluid inclusions photomicrographs. (A), (B), (C) and (D) Various shapes of three-phase inclusions exhibiting a large volume of H₂O liquid and bubbles of CO₂ liquid and CO₂ vapour.

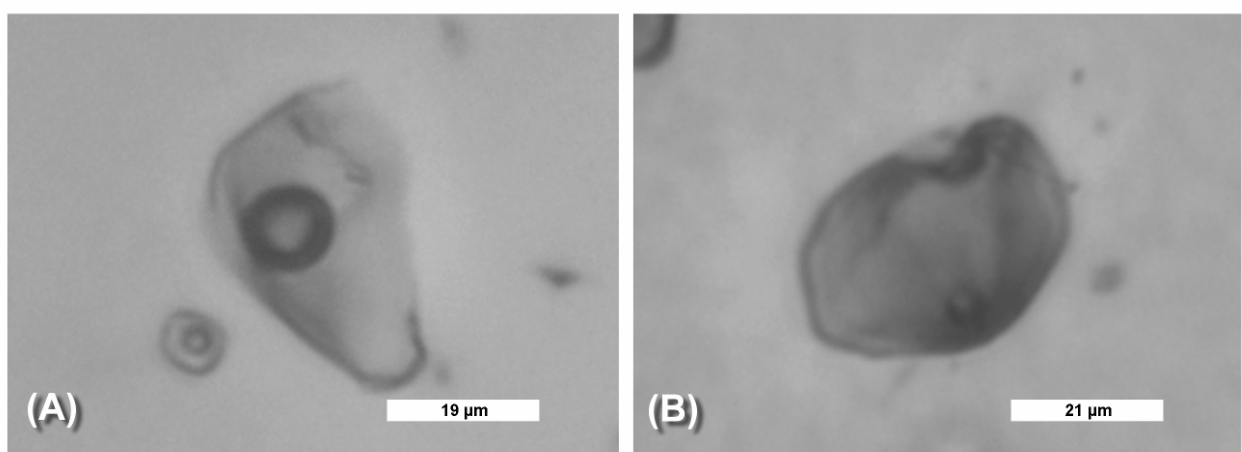


Figure 6.4: Photomicrographs of the pure aqueous fluid inclusions. (A) and (B) Large two-phase inclusion consisting of H₂O liquid and H₂O vapour.

6.2 Microthermometric data

Microthermometry is the most commonly used non-destructive analytical technique for determining temperatures of characteristic phase changes (e.g., melting of CO₂, homogenization of CO₂, ice melting) within the fluid inclusions during freezing/heating runs of rock samples. The microthermometric data help to constrain the compositional properties of the fluid that traversed a rock in its history, based on the fundamental assumption that the inclusions have behaved as closed system since their formation (Roedder, 1984; Goldstein and Reynolds, 1994; Brown, 1998). The FLINCOR computer program (Brown, 1989) was used to calculate the densities and isochores of the fluid inclusions. The results for microthermometric measurements obtained from samples representative of the above three categories of fluid inclusions are listed in Tables A.5.1 to A.5.3 in the Appendix A.5.

- Mixed aqueous–non-aqueous volatile fluid inclusions

After freezing, and during a progressive heating of these fluid inclusions to the temperature of total homogenization, the following phase transitions were observed in the sequence: melting of CO₂ (T_m CO₂), melting of clathrates (T_m cla), homogenization of CO₂ (T_h CO₂), and total homogenization (T_h_{total}) of the fluid inclusion. Clathrate or gas hydrate is crystalline water-gas (i.e. CO₂, CH₄, N₂) compound for which the melting temperature depends on the pressure, gas composition and salinity of the aqueous phase (e.g., Diamond, 1992). The salinity of the aqueous phase in this inclusion type has been calculated from the clathrate melting temperature, using the computer program *Q2* of Bakker (1997).

- Non-aqueous volatile-rich mixed fluid inclusions: the T_m CO₂ of the great majority of these inclusions range between -58.1 °C and -56.9 °C. But small number of non-aqueous volatile-rich fluid inclusions has higher T_m CO₂ between -56.7 and -56.6 °C (Fig. 6.5A). The clathrate was formed exclusively by the three-phase non-aqueous volatile bearing fluid inclusions. It melts generally before reaching T_h CO₂ at T_m cla ranging from +4 to +10 °C (Fig. 6.5C). The overall range of T_m cla corresponds to salinities of 1 to 10 equiv. wt. % NaCl (average: 8 equiv. wt. % NaCl) (Fig. 6.6A). T_h CO₂ ranges from +5 to +30 °C (Fig. 6.5B) and with homogenization to the liquid phase, although homogenization to the vapour phase with T_h CO₂ ranging between +7 and +30 °C was observed in few cases. The average values of T_m cla

and $T_h \text{ CO}_2$ correspond to densities of 0.44 to 0.87 g/cm³ (Brown and Lamb, 1989). The total homogenization of the non-aqueous volatiles-rich fluid inclusions was observed in both the liquid and vapour phase, and T_{total} displays a wide range between 170 °C and 300 °C with a peak at 260 °C (Fig. 6.6A).

- **Aqueous-rich mixed fluid inclusions:** $T_m \text{ CO}_2$ of the aqueous-rich mixed fluid inclusions were determined between –56.9 °C and –56.6 °C with a limited number near –56.6 °C (Fig. 6.5A). $T_m \text{ cla}$ which have been observed only in a few aqueous-rich mixed fluid inclusions, are constantly between +5 and +7 °C (Fig. 6.5C). The salt concentrations calculated from $T_m \text{ cla}$ compare to the non-aqueous volatile-rich fluid inclusions in range, i.e. between 1–10 equiv. wt. % NaCl, but have a lower average of 6 equiv. wt. % NaCl (Fig. 6.6A). This corresponds to an average density of 1.00g/cm³. $T_m \text{ CO}_2$ shows a wide range from +7 to +26 °C (Fig. 6.5B), with the CO₂ homogenization commonly to the liquid phase. Total homogenization of these fluid inclusions was exclusively observed to the liquid phase, with T_{total} in the range of 150 and 250 °C (Fig. 6.6B).

- Pure aqueous fluid inclusions

Pure aqueous fluids inclusions exhibit phase transitions different from the above mixed aqueous–non-aqueous volatiles fluid inclusions, during freezing/heating runs. The phase transitions observed to the temperature of homogenization were in the following order: first melting of H₂O or eutectic temperatures (Te), melting of the last crystal of ice (T_m ice), and total homogenization temperature (T_{total}).

Most Te recorded was between –39.1 and –26.7 °C with an average value of –32.7 °C. T_m ice ranges from –5.0 to –1.0 °C (Fig. 6.5C) and correspond to an average density of 0.96 g/cm³. Salt content of these fluid inclusions, calculated from the final melting temperature of ice (Bodnar, 1993), range from 3 to 8 equiv. wt. % NaCl, with an average of 6 equiv. wt. % NaCl (Fig. 6.6A). The pure aqueous fluid inclusions homogenized to the liquid at lower T_{total} than the mixed aqueous–non-aqueous volatile fluid inclusions, i.e. between 130 and 150 °C (Fig. 6.6B).

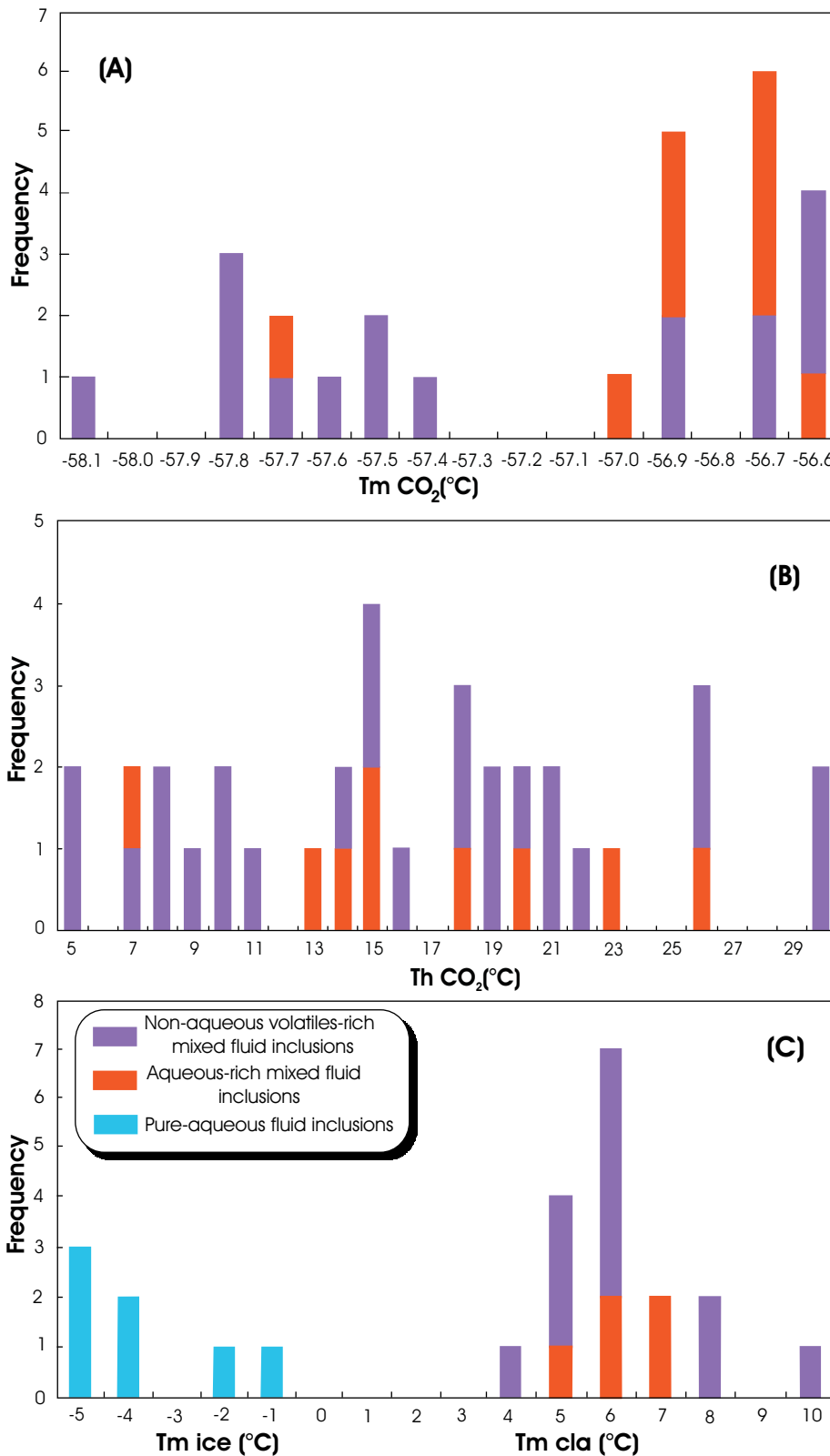


Figure 6.5: Histograms compiling the different microthermometry results of the fluid inclusions. **(A)** Distribution of melting temperatures of CO₂ (Tm CO₂). **(B)** Distribution of the homogenization temperatures of CO₂ (Th CO₂). **(C)** Distributions of the final melting temperatures of ice (Tm ice) in the pure aqueous fluid inclusions and the clathrates melting temperatures (Tm cla) of the non-aqueous volatiles-rich and aqueous-rich mixed fluid inclusions.

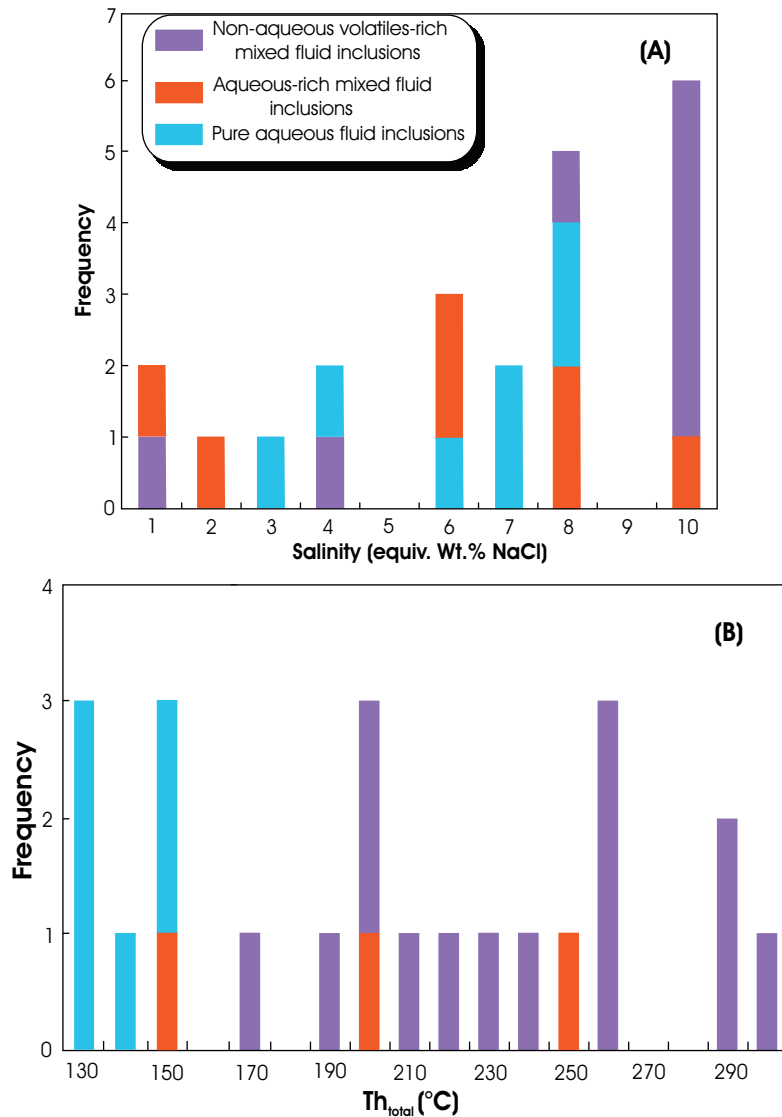


Figure 6.6: (A) Histogram showing the variation of calculated salinity. (B) Histogram of the total homogenization temperatures (Th_{total}) distribution of the analysed fluid inclusions.

6.3 Interpretation and discussion of data

The CO_2 melting temperatures recorded for mixed aqueous–non-aqueous volatiles fluid inclusions indicate two clearly distinct gas compositions (van den Kerkhof, 1990; Murphy and Roberts, 1995): (1) a CO_2 – CH_4 mixture composition for inclusions having $\text{Tm CO}_2 < -56.6 \text{ }^{\circ}\text{C}$. The proportions of CH_4 have been estimated using the diagrams of CO_2 homogenization to liquid and vapour of Heyen et al. (1982), assuming that essentially no N_2 is present. The concentrations of CH_4 are quite variable, ranging from 4.1 to 13.5 mole % and 5.5 to 9.0 mole % in the non-aqueous volatiles-rich mixed and aqueous-rich mixed fluid inclusions, respectively; and (2) a nearly pure CO_2 composition for inclusions having $\sim -56.6 \text{ }^{\circ}\text{C} \text{ Tm CO}_2$.

For pure aqueous fluid inclusions on the other hand, the eutectic temperatures (T_e) indicate that the compositions of these pure aqueous fluids can only be partly described in the pure H_2O -NaCl system (Shepherd et al. 1985). The average T_e value of -32.7 °C being well below the H_2O -NaCl eutectic temperature of -21.2 °C, points to a Na-dominated mixed salt system that contains also significant amounts of divalent cations.

On bivariate plots (Fig. 6.7), the data points roughly define linear arrays. The salinity versus total homogenization (Th_{total}) temperatures diagram (Fig. 6.7A) displays a linear trend which, according to Shepherd et al. (1985), can be interpreted as a mixing of a higher temperature–medium salinity fluid with a lower temperature–low salinity fluid.

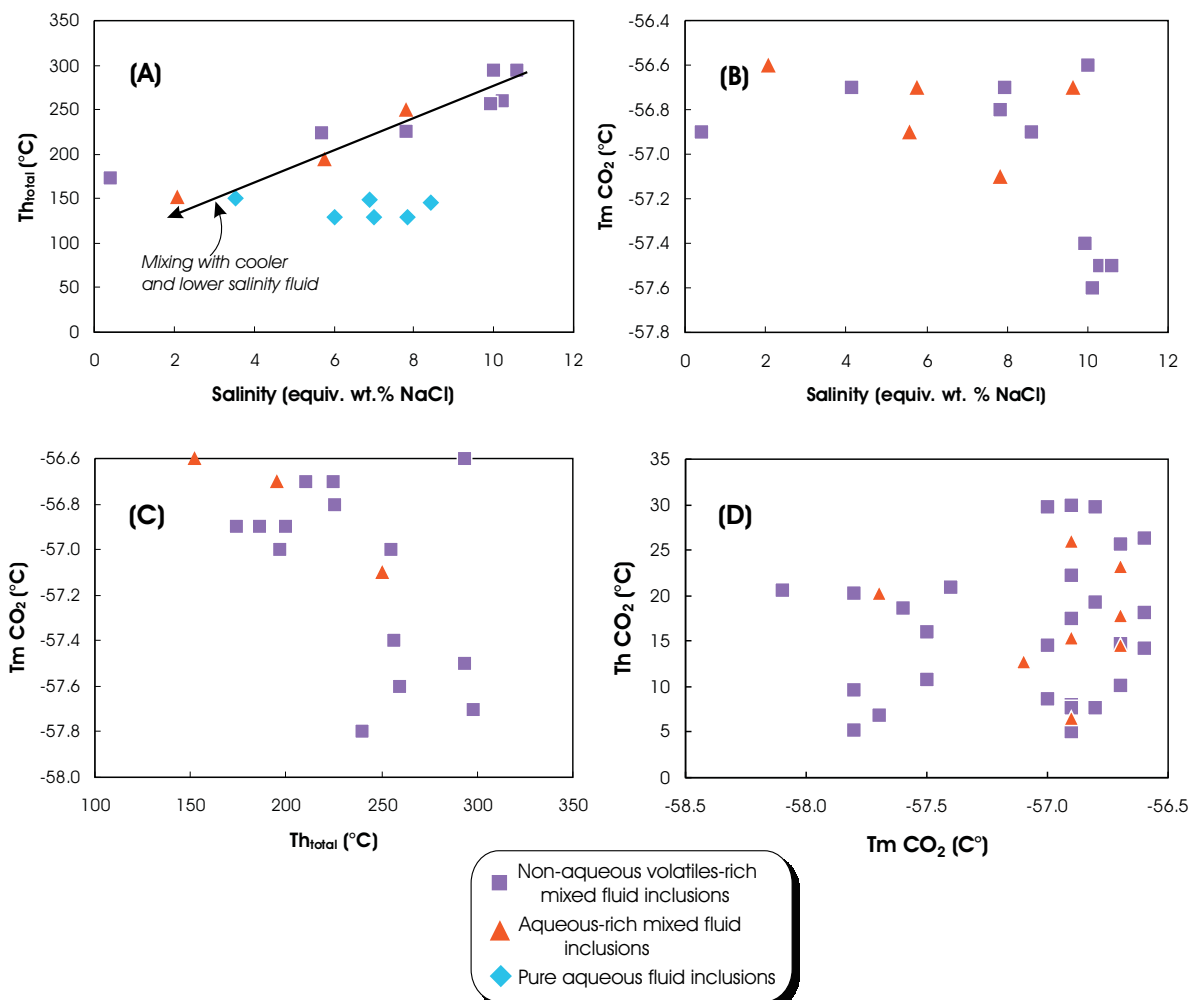


Figure 6.7: Characteristics of the fluid inclusions, showing roughly linear trend. **(A)** Salinity versus total homogenization (Th_{total}) temperatures. **(B)** Salinity versus CO_2 melting temperatures ($Tm\ CO_2$). **(C)** Th_{total} versus $Tm\ CO_2$. **(D)** $Tm\ CO_2$ versus CO_2 homogenization temperatures ($Th\ CO_2$).

The mixing evolution of fluids is also illustrated in plots of salinity versus CO₂ melting temperatures (Fig. 6.7B) and total homogenization temperatures versus CO₂ melting temperatures (Fig. 6.7C). The aqueous–non-aqueous volatile-rich mixed fluid inclusions do not define a clear decrease of T_m CO₂ and T_m CO₂ trend portraying addition of CH₄ to CO₂ (Fig. 6.7D), as suggested by van den Kerkhof (1990).

The densities of the fluid inclusions make it possible to set constraints on the physical conditions of the entrapment of these fluids. The analyzed fluid inclusions are clearly subdivided in two groups, which appear not related to each other (Fig. 6.9): aqueous-rich mixed fluid inclusions and pure aqueous fluid inclusions have similar densities and thus might be of similar genesis, whereas the non-aqueous volatile-rich mixed fluid inclusions have distinctly lower density.

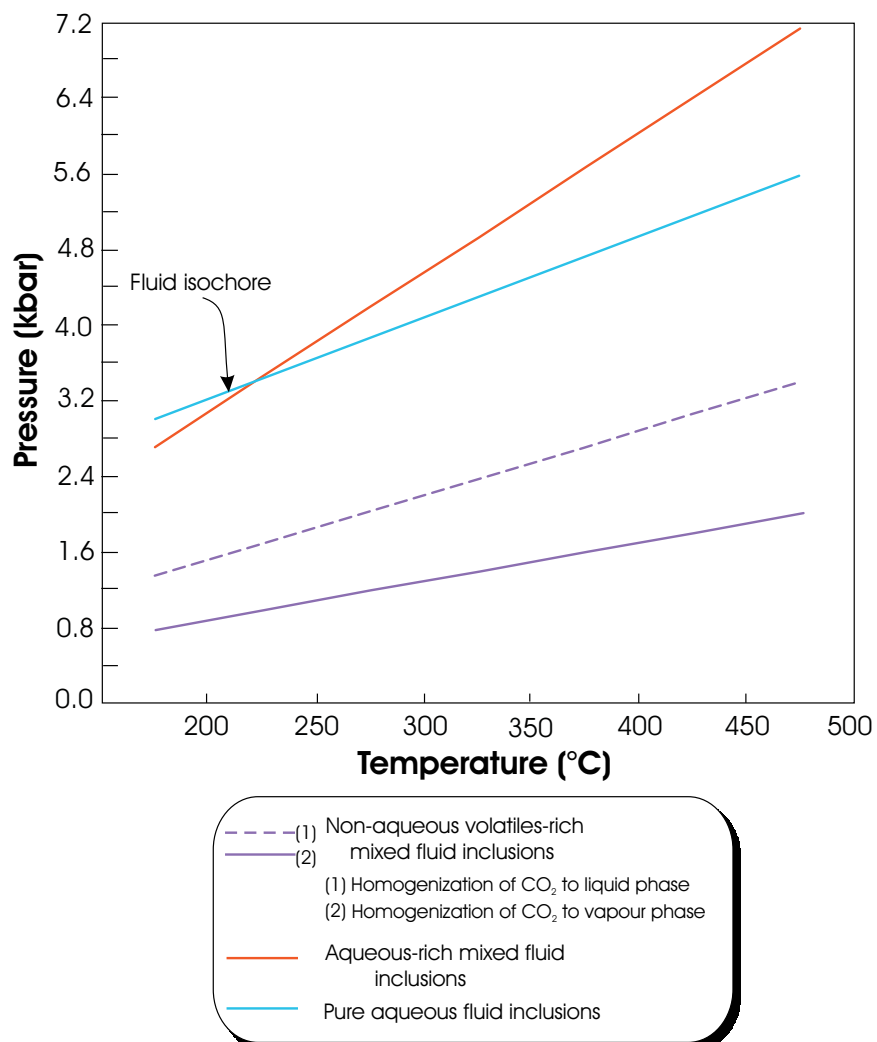


Figure 6.8: P–T traces of isochores for the investigated fluid inclusions.

Although the intersection of the isochores for the aqueous-rich mixed fluid inclusions and the pure aqueous fluid inclusions at 3.4 kbar and 225 °C is subject to large uncertainties due to uncertainties in the calculation of the respective densities and the small angle of intersection, it gives a rough estimate of the likely geothermal gradient, 18 °C/km at the time of fluid entrapment. The non-aqueous volatile-rich mixed fluid inclusions show two distinct isochores, depending on their homogenization to liquid or to vapour (Fig. 6.8). Both correspond to a steep geothermal gradient of 68 °C/km. Considering the well developed negative crystal form, relatively high entrapment temperature is inferred (Goldstein and Reynolds, 1994).

7 GEOCHEMISTRY

7.1 Major and trace element geochemistry

Whole-rock geochemical analysis has been performed on 29 samples of the biotite granitoid, 26 samples of the deformed biotite granitoid, 11 samples of the mega feldspar granitoid and 9 samples of the two-mica granitoid. The obtained major and trace element data are listed in Table A.3.1 in the Appendix A.3 and the analytical process is summarized in the Appendix A.1.3. The investigation of the major and trace elements will allow to place constraints on nomenclature, magmatic affinities, tectonic setting as well as nature of the source rocks and the main evolutionary processes of the studied granitoids.

7.1.1 Major elements

The investigated granitoids span a large compositional range in silica content from 56.9–74.6 wt. %. They have high values of alkali oxides, with $K_2O = 1.73\text{--}7.32$ wt. % and $Na_2O = 1.25\text{--}5.13$ wt. %, and of $Fe_2O_3^*$ (total Fe) = 0.96–7.79 wt. %, but low abundance in MnO (0.01–0.20 wt. %), MgO (0.10–3.97 wt. %), CaO (0.37–4.85 wt. %), P_2O_5 (up to 0.90 wt. %). The TiO_2 contents are low to moderate (0.07–0.91 wt. %). Al_2O_3 ranges between 12.0 and 17.6 wt. %.

Plots of major element abundances against SiO_2 (Harker variation diagrams) as an index of fractionation show a well-defined linear covariation with respect to increasing silica contents, suggesting that mineral fractionation has an appreciable effect on silica content (Fig. 7.1). On the one hand, a clear defined decrease in TiO_2 , Al_2O_3 , Fe_2O_3 , MnO , MgO , CaO , Na_2O and P_2O_5 is shown in Figure 7.1. The trend is diffuse for the least evolved members (SiO_2 up to 66 wt. %) and thereafter, narrow and roughly linear for higher silicic compositions ($SiO_2 > 66$ wt. %) with increasing SiO_2 . On the other hand, a scattered trend is displayed by K_2O , which weakly increases with increasing SiO_2 (Fig. 7.7B). These oxide variations roughly describe the typical calc-alkaline trends on Harker plots (Roger and Greenberg, 1990).

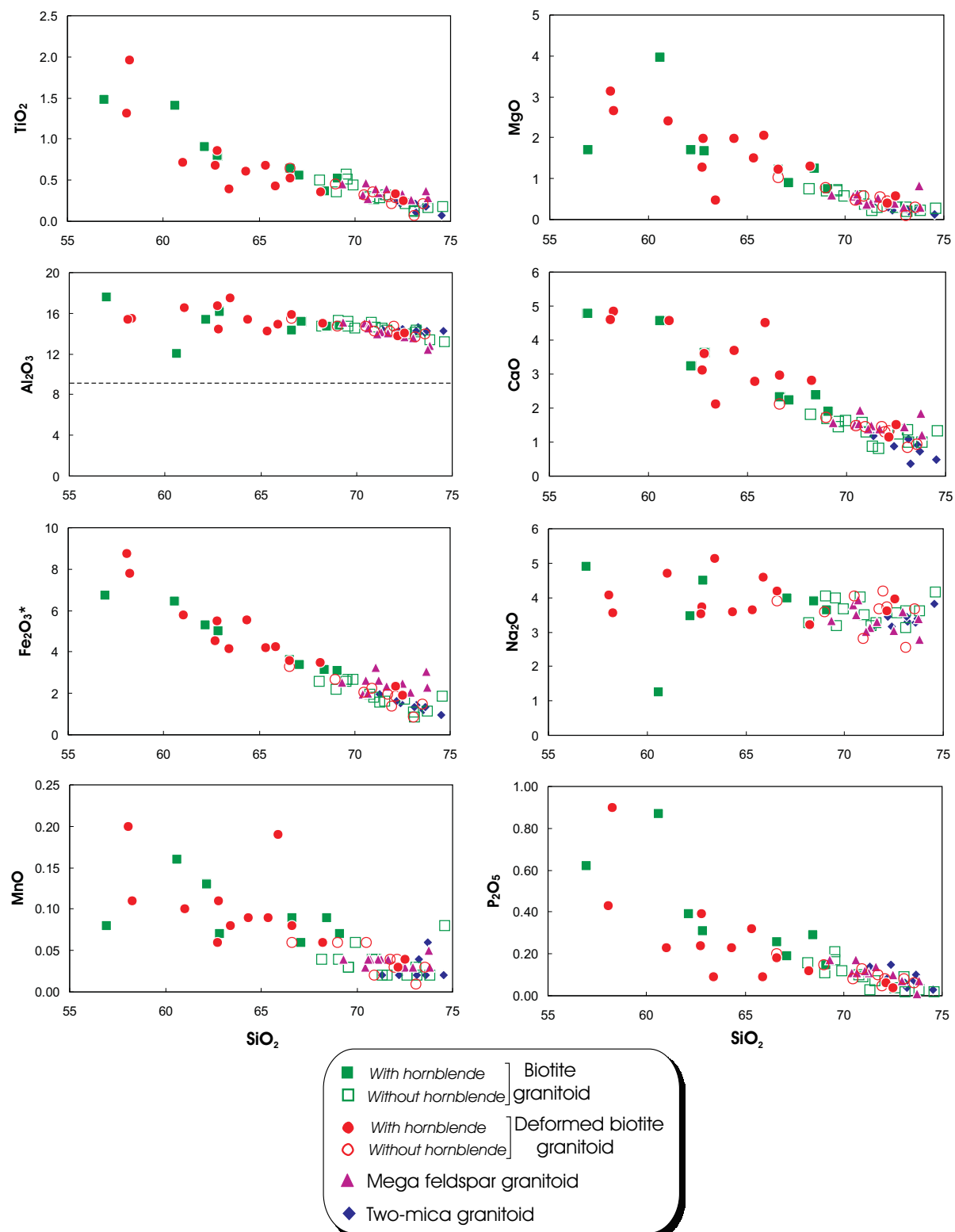


Figure 7.1: Harker variation diagrams for some major elements (wt. %) plotted against SiO_2 (wt. %) content for the Bafoussam granitoids. The trends obtained are broadly along extrapolation of typical calc-alkaline trends and suggest general fractional crystallization.

7.1.1.1 Nomenclature of the granitoids

The Q'-ANOR diagram after Streckeisen and Le Maitre (1979) and the multicationic parameters R_1-R_2 diagram of De La Roche et al. (1980), are employed for geochemical nomenclature purposes of the studied granitoids, taking exclusively into account their normative compositions obtained from the major element data and the main major elements, respectively. The normative compositions, CIPW norm were calculated with help of the computer program NORM (supported by Jake Lowenstern, USGS 2000), applying the calculation scheme of Kelsey (1965).

Following the Q'-ANOR classification (Fig. 7.2), the majority of biotite granitoid samples plot into the field of granite, with syenogranite being most common (Fig. 7.2A). But a few samples plot within the fields of alkali-feldspar granite, quartz-syenite and quartz-monzonite. The deformed biotite granitoid falls into the fields of alkali-feldspar granite, syenogranite, monzogranite, granodiorite, quartz-syenite, quartz-monzonite and quartz-monzdiorite, and therefore shows the broadest chemical variation (Fig. 7.2B). The mega feldspar granitoid is mostly granite (Fig. 7.2C), whereas the two-mica granitoid occupies the alkali-feldspar granite and syenogranite domains (Fig. 7.2D).

The R_1-R_2 diagram (Fig. 7.3A) classifies the biotite granitoid as a syenogranite (major), monzogranite, quartz-monzonite, syenodiorite, and monzdiorite, while the deformed biotite granitoid is distributed within the fields of syenogranite, monzogranite, granodiorite, quartz-monzonite and monzdiorite (Fig. 7.3B). The mega feldspar granitoid plots into the syenogranite and monzogranite fields (Fig. 7.3B), and the two-mica granitoid is a syenogranite (Fig. 7.3A).

This classification using the geochemical data well supports the mineralogy of the granitoids. They are largely of syenogranite composition that is consistent with the broadly predominance of potassium feldspar over the plagioclase in these granitoid rocks. The wide variety in composition of biotite granitoid and deformed biotite granitoid is mostly displayed by the samples containing additional hornblende as a ferromagnesian mineral.

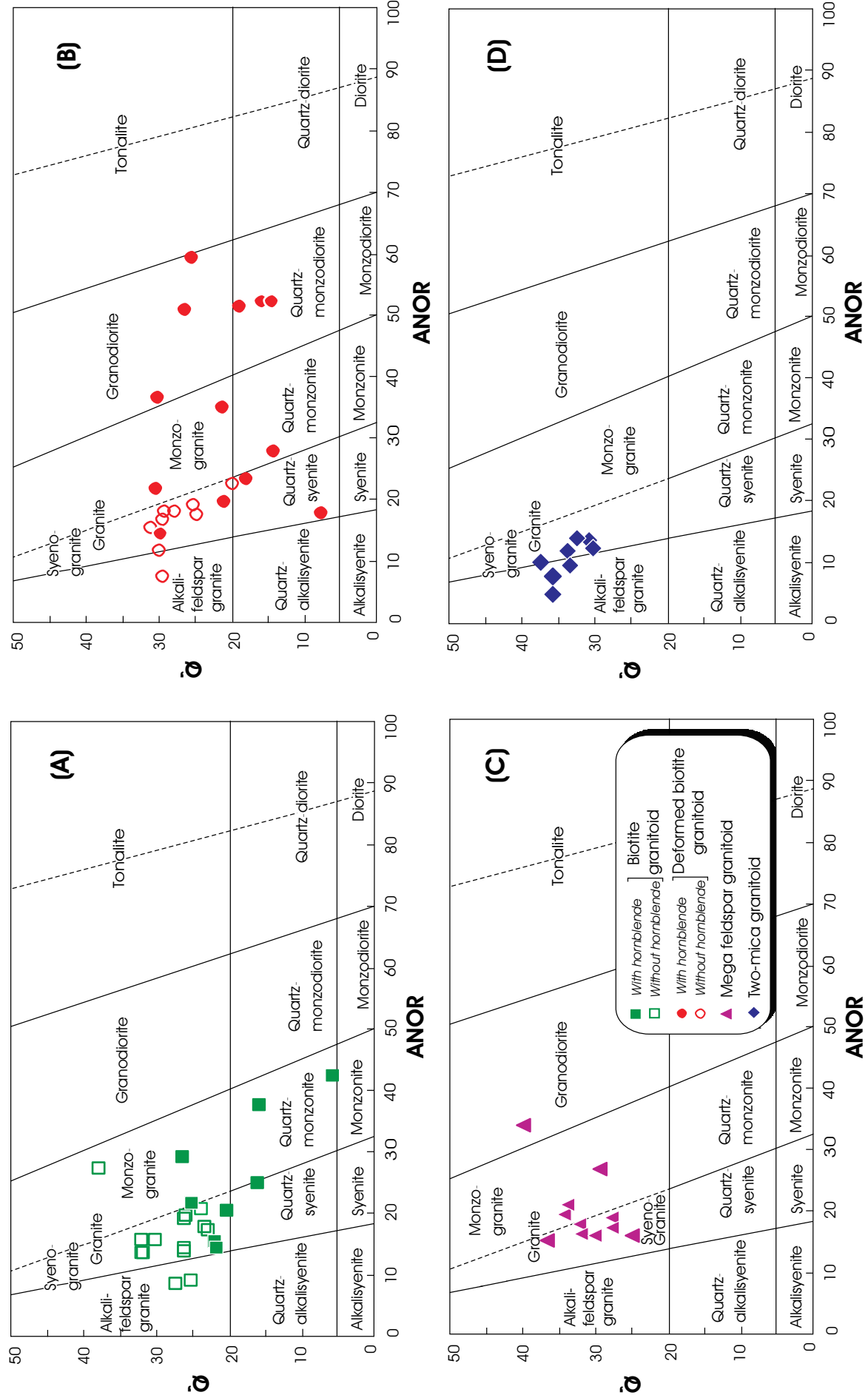


Figure 7.2: Classification of the Bafoussam granitoids using their molecular normative compositions $\text{ANOR} = 100 \times \text{An}/(\text{An} + \text{Or})$ versus $\text{Q}' = 100\text{Q}/(\text{Q} + \text{Or} + \text{Ab} + \text{An})$ after Streckeisen and Le Maitre (1979).

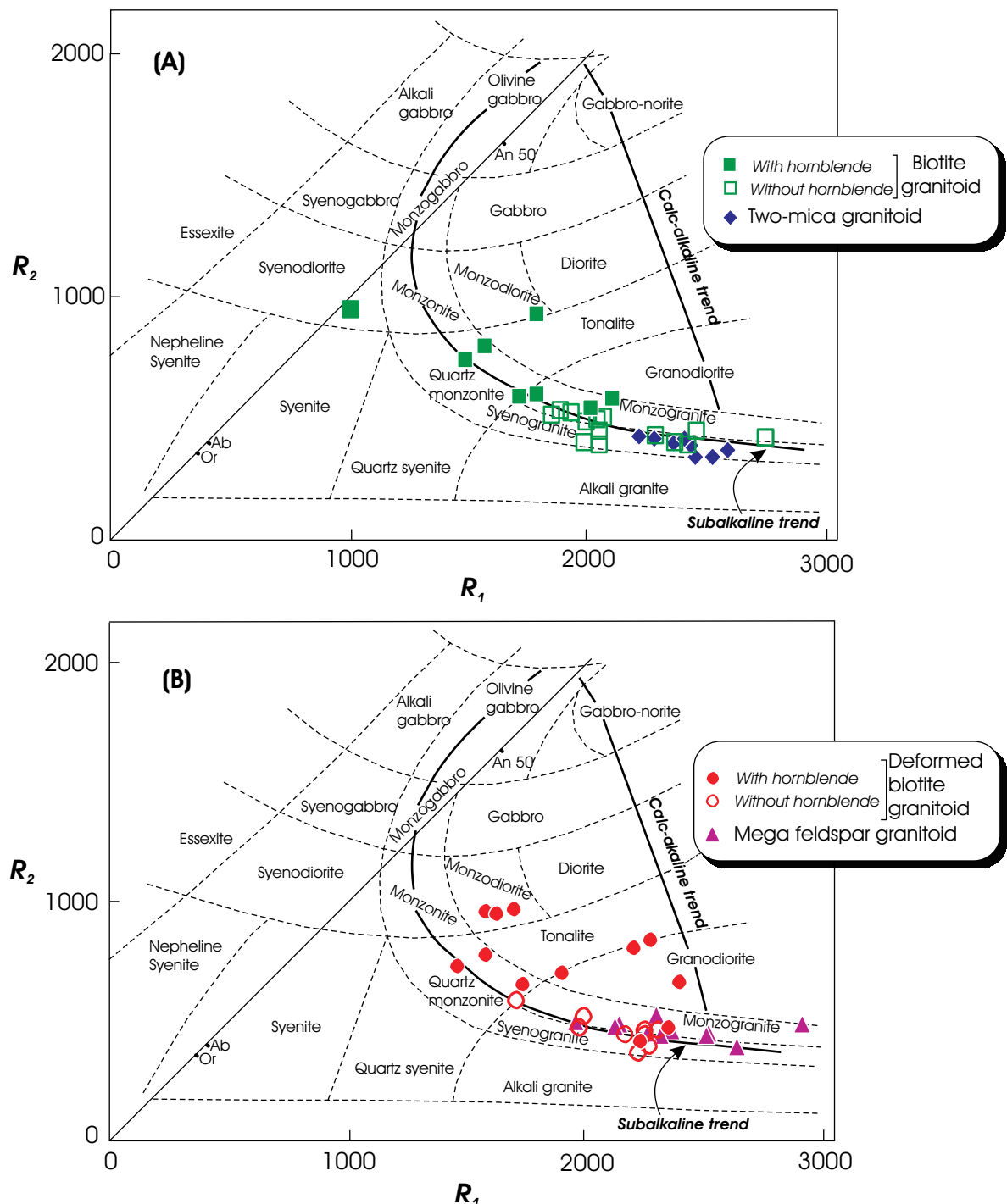


Figure 7.3: Classification of the Bafoussam granitoids using the multicationic parameters $R_1 = 4\text{Si} - 11(\text{Na} + \text{K}) - 2(\text{Fe} + \text{Ti})$ versus $R_2 = 6\text{Ca} + 2\text{Mg} + \text{Al}$ diagram of De La Roche et al. (1980). The continuous line is the "feldspar fraction" line (Ab: albite, An 50: plagioclase An 50, Or: orthoclase). Sub-alkaline and calc-alkaline evolution trends after Debon and Lemmet (1999) are also showed.

7.1.1.2 Magmatic affinities

The total alkali-silica (TAS) diagram is often employed for discriminating the granitoids between alkaline and sub-alkaline series although the boundary between the two series differs according to various authors. Here, the TAS diagram of Middlemost (1997) is chosen as it offers a classification in alkaline, mid-alkaline and sub-alkaline (calc-alkaline + tholeiitic) fields (Fig. 7.4A). For comparison, the separating line between alkaline and sub-alkaline series of Miyashiro (1978) is also applied. In Figure 7.4A, the total alkalis ($\text{Na}_2\text{O} + \text{K}_2\text{O}$) ratio varies little and shows a diffuse flat trend with increasing SiO_2 . The granitoids under study occupy a transitional position between non-alkaline and mid-alkaline series. The biotite granitoid and deformed granitoid plot mainly in the field of mid-alkaline, whereas a few of them are non-alkaline, with respect of the two dividing lines. Most of the mega feldspar granitoid and two-mica granitoid straddle the boundary between the non-alkaline and mid-alkaline rocks of Middlemost (1997) as well as of Miyashiro (1978).

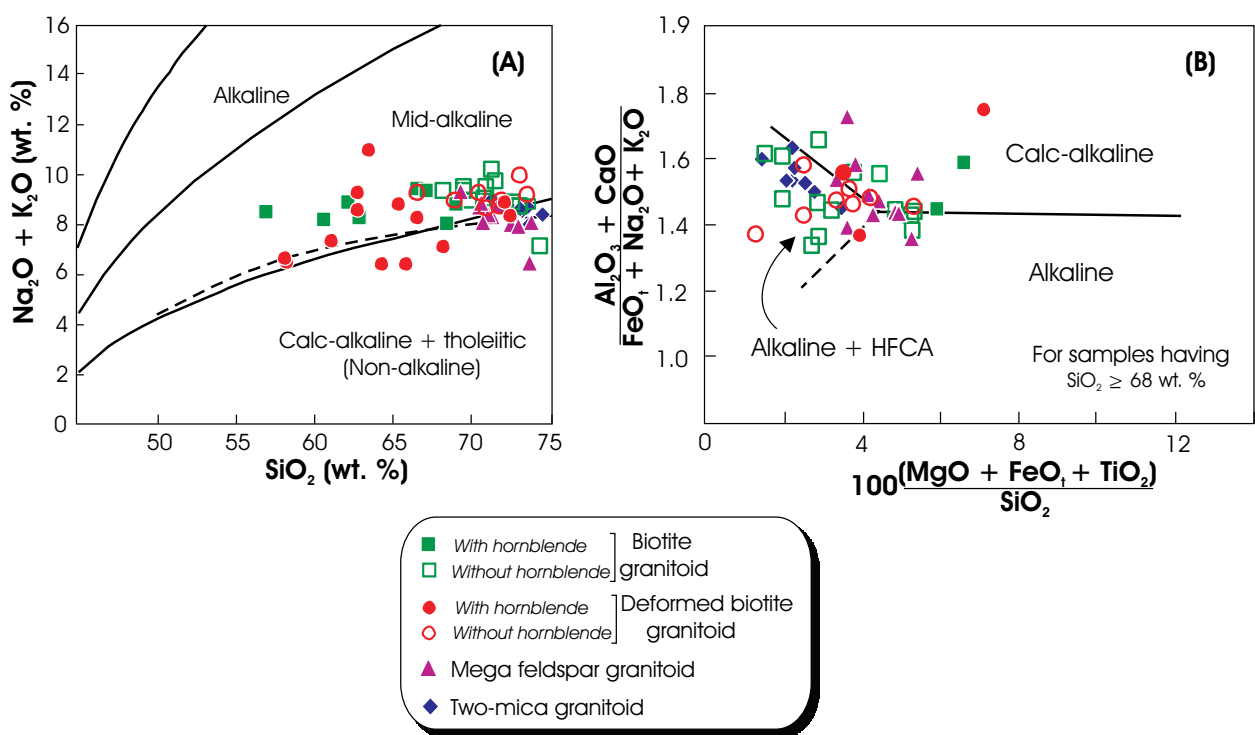


Figure 7.4: Transitional position between sub-alkaline to alkaline affinities of the Bafoussam granitoids. (A) $\text{Na}_2\text{O} + \text{K}_2\text{O}$ versus SiO_2 (wt. %) diagram after Middlemost (1997). The dashed line shown for comparison is the Miyashiro (1978) boundary distinguishing between alkaline – sub-alkaline granitoids. (B) $(\text{Al}_2\text{O}_3 + \text{CaO})/(\text{FeO}_t + \text{Na}_2\text{O} + \text{K}_2\text{O})$ versus $100 \times (\text{MgO} + \text{FeO}_t + \text{TiO}_2)/\text{SiO}_2$ (wt. %) with $\text{SiO}_2 \geq 68$ wt. % from Sylvester (1989). HFCA: highly fractionated calc-alkaline.

Moreover, the transitional character between alkaline and sub-alkaline is also expressed in the discrimination diagram of Sylvester (1989) which, for the rocks with $\text{SiO}_2 \geq 68$ wt. %, distinguishes between alkaline, alkaline + highly fractionated calc-alkaline (HFCA) and calc-alkaline granitoids (Fig. 7.4B). The highly fractionated calc-alkaline granite is believed to be a variety of alkaline granite (Sylvester, 1989) because of close compositional similarity between the two granites types. In the Sylvester's diagram (Fig. 7.4B), the biotite granitoid, the deformed biotite granitoid and the mega feldspar granitoid plot simultaneously within all the defined fields, biotite granitoid more within the alkaline + highly fractionated calc-alkaline and calc-alkaline fields, the deformed biotite granitoid and the mega feldspar granitoid in majority within the fields of calc-alkaline and alkaline + highly fractionated calc-alkaline, respectively. Finally, the two-mica granitoid is classified exclusively in the common field of alkaline + highly fractionated calc-alkaline granites.

The agpaitic index, $A.I = \text{molar } (\text{Na} + \text{K})/\text{Al}$, distinctly separates the alkaline ($A.I > 0.87$; Liégeois et al., 1998) and peralkaline series ($A.I > 1.0$) from the calc-alkaline series, having an $A.I < 0.87$. In the $A.I$ versus SiO_2 diagram (Fig. 7.5), most of the biotite granitoid and deformed granitoid samples as well as the mega-feldspar granitoid and the two-mica granitoid exclusively are classified as calc-alkaline granitoids, although a few evolved samples are moderately alkaline. The fact that most of the granitoid samples do not exceed an agpaitic index $A.I$ of 0.87 can be explained by their slightly low Na_2O content compared to the K_2O concentration. Further investigation of Figure 7.5 displays two different trends of the agpaitic index with increasing silica. The first trend (1) follows an abrupt ascending and exclusively calc-alkaline line of the evolution, where the granitoids having hornblende do not exceed the value of $A.I = 0.87$. The other trend, (2) exhibits a first steep and then more or less flattening line of evolution and slightly ascends into alkaline series and points out the tendency of silica-rich samples to be slightly alkaline.

The sub-alkaline character of the investigated granitoids is confirmed in the multicationic parameters (R_1-R_2) diagram after De La Roche et al., 1980 (Fig. 7.3), showing the sub-alkaline and calc-alkaline trends of Debon and Lemmet (1999). The biotite granitoid, the mega feldspar granitoid and the two-mica granitoid largely follow the sub-alkaline line of evolution, while the deformed biotite granitoid shows sub-alkaline and calc-alkaline trends.

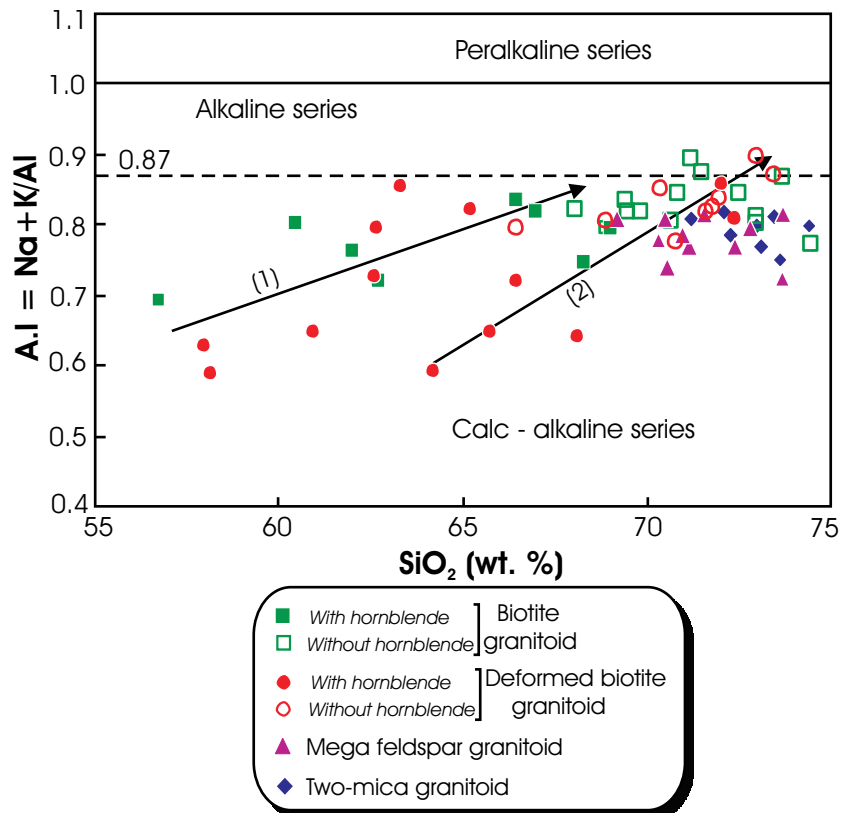


Figure 7.5: Agpaitic index ($\text{Na} + \text{K}$)/Al (at. %) versus SiO_2 diagram, indicating a calc-alkaline character for the Bafoussam granitoids. The dashed line that separates alkaline and calc-alkaline granitoids series corresponds to an A.I of 0.87 (after Liégeois et al., 1998).

According to the modified alkali-lime index (MALI = $\text{NaO}_2 + \text{K}_2\text{O} - \text{CaO}$) after Frost et al. (2001), the Bafoussam granitoids can be divided into alkalic, alkali-calcic, calc-alkalic, and calcic affinities. The MALI classification represents for a suite of igneous rocks the SiO_2 value at which $(\text{Na}_2\text{O} + \text{K}_2\text{O})/\text{CaO}$ are equivalent to 1.0. The MALI is commonly used to interpret the magma source. The MALI of the studied granitoids slightly increases with increasing SiO_2 (wt. %) as showed in Figure 7.6. Their high total alkalis ($\text{Na}_2\text{O} + \text{K}_2\text{O} = 6.31\text{--}10.93$ wt. %) content compared to lime concentration ($\text{CaO} = 0.37\text{--}4.85$ wt. %) classifies the biotite granitoid in part to the alkali-calcic and alkalic series fields, the deformed biotite granitoid mostly to the calc-alkalic and alkali-calcic fields, the mega feldspar granitoid in part to the calc-alkalic and alkali-calcic series fields, whereas the two-mica granitoid fits to the alkali-calcic series field solely (Fig. 7.6).

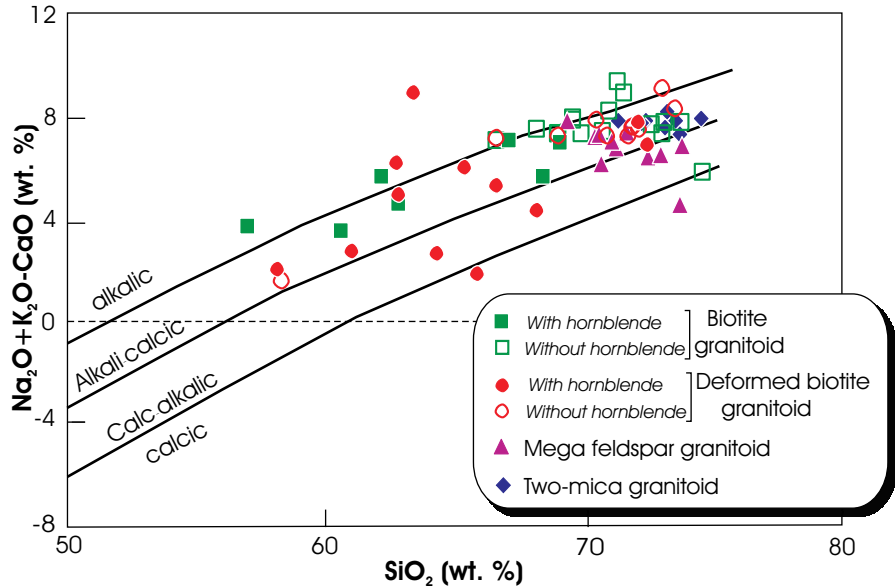


Figure 7.6: Modified alkali-lime index ($\text{Na}_2\text{O} + \text{K}_2\text{O} - \text{CaO}$) against SiO_2 (wt. %) diagram of Frost et al. (2001), demonstrating the dominating alkali-calcic affinity of the Bafoussam granitoids, which follow an alkalic to calcic trend.

Following the classification of Turner et al. (1996) for Tibetan lavas, the investigated granitoids can be considered as "true shoshonites", as they plot within the field for shoshonitic rocks that is restrained to $\text{K}_2\text{O}/\text{Na}_2\text{O}$ ratios between 0.5 and 2.0 (Fig. 7.7A). In addition, Rickwood (1989) and Müller et al. (1992) have already suggested that granitoids with high potassium concentrations can also be classified as belonging to a shoshonitic rock series. In this terminology, the high-potassic character is also exhibited in the standard K_2O versus SiO_2 diagram (Fig. 7.7B), used to subdivide the calc-alkaline suite into high-K and low-K types, as summarized by Rickwood (1989). The biotite granitoid, the mega feldspar granitoid and the two-mica granitoid have high-K calc-alkaline to shoshonitic character, while the deformed biotite granitoid scatters in part within the medium-K calc-alkaline, in part within the high-K calc-alkaline and in part within the shoshonitic fields. The general high-potassic character of the granitoids under study is concordant with their Al_2O_3 content higher than 9 % (dashed line in Al_2O_3 versus SiO_2 diagram, Fig. 7.1: Morrison, 1980; Müller et al., 1992) and with their noticeable abundance of K-feldspar (and hence of K_2O). According to Liégeois et al. (1998), the low Na_2O content at around 3 % counterbalancing the high K_2O content points to a shoshonitic trend rather than to a high-K one.

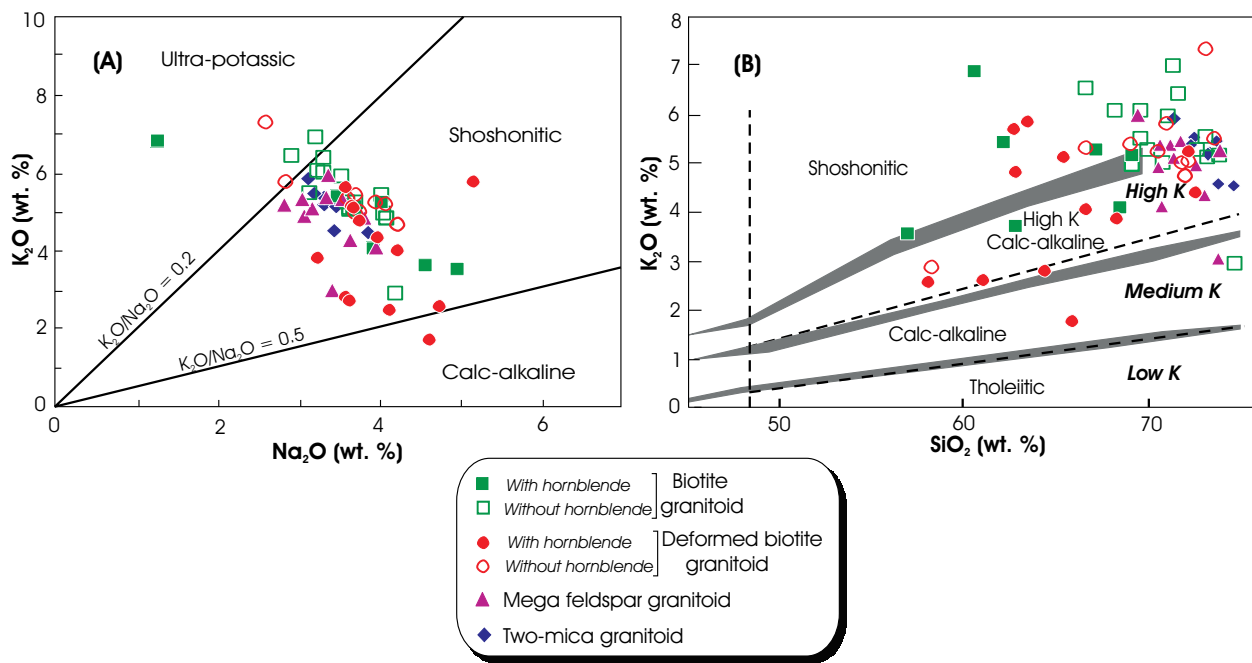


Figure 7.7: Potassic character of the Bafoussam granitoids. **(A)** K_2O versus Na_2O (wt. %) after Turner et al. (1996). **(B)** K_2O versus SiO_2 (wt. %), illustrating the high-K calc-alkaline to shoshonitic affinities of the Bafoussam granitoids. Subdivision boundaries into low-, medium- and high-K domains (broken lines) are after Le Maitre et al. (1989) and into shoshonitic, high K calc-alkaline, calc-alkaline and tholeiitic magmatic series (shadowed boundary fields) as summarized by Rickwood (1989).

The mg-number ($Mg/Mg + Fe$) versus $B = Fe + Mg + Ti$ diagram of Dedon and Le Fort (1988) modified by Debon and Lemmet (1999) allows to distinguish a magnesian magmatic igneous domain from a ferriferous magmatic igneous domain (Fig. 7.8). In contrast to shoshonitic suites (Morrison, 1980; Jiang et al., 2002), the studied granitoids exclusively display a ferriferous character which is consistent with the Fe enrichment of some of their minerals such as biotite and garnet.

The molar ratio $Al_2O_3/(CaO + Na_2O + K_2O)$ is widely used for discriminating granitoids into peraluminous, metaluminous and peralkaline characters. This ratio refers to as A/CNK by Clarke (1981) or as the aluminum saturation index (ASI) by Zen (1986). More recently, Frost et al. (2001) defined ASI as the molecular ratio $Al/(Ca - 1.67P + Na + K)$. The aluminum saturation index is believed to be the reflection of the micas and accessory minerals in the rocks, and is related to the magma sources and conditions of melting. The metaluminous granitoids and the peralkaline granitoids possess $ASI < 1.0$, but with molecular $Na + K <$ molecular Al and molecular $Na + K >$ molecular Al, respectively, following Frost et al. (2001). The peraluminous

group is subdivided into mildly or moderate peraluminous (ASI ratio 1.0–1.1) and strongly peraluminous (ASI ratio ≥ 1.1) by Zen (1986) and Sylvester (1998).

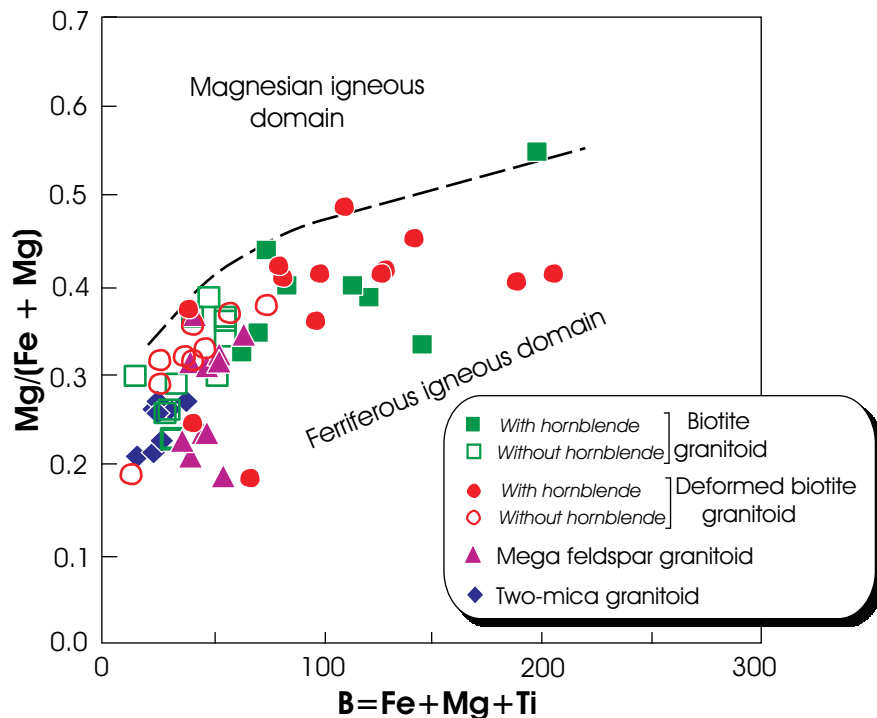


Figure 7.8: The mg-number = $Mg / (Fe + Mg)$ against $B = Fe + Mg + Ti$ (moles) diagram of Debon and Le Fort (1988), where Fe = total iron cations. The broken line separating the magnesian and ferriferous igneous domains is of Debon and Lemmet (1999).

The aluminium saturation index (ASI) versus SiO_2 plot (Fig. 7.9A: Chappell and White, 1974; Frost et al., 2001) shows that for the investigated granitoids, the ASI ratio systematically increases with SiO_2 . Furthermore, the biotite granitoid (ASI ratio 0.70–1.08) and the deformed biotite granitoid (ASI ratio 0.82–1.06) reflect a change from metaluminous to weakly peraluminous compositions, the mega feldspar granitoid (ASI ratio 1.02–1.06) is exclusively weakly peraluminous and the two mica granitoid (ASI ratio 1.07–1.25) is mainly strongly peraluminous (Fig. 7.9A). Similarly, the intermediate nature between metaluminous and peraluminous of the Bafoussam granitoids is documented in the diagram of Maniar and Piccoli (1989), which employs the shand's molar parameter, A/NK versus A/CNK (Fig. 7.9B). This diagram also clearly separates the metaluminous granitoids, which have A/NK ratios defined as molar $Al_2O_3/(NaO + K_2O)$ greater than 1, and the peralkaline granitoids ($A/NK < 1$).

The metaluminous and peraluminous character of the studied granitoids is reflected in the mineralogy of the peraluminous samples, which includes a highly-aluminous primary phase such as aluminous biotite for weakly peraluminous granitoids, and second additional aluminous phases, i.e. muscovite and garnet for stronger peraluminous granitoids, in agreement with Miller (1985). The bearing of the aluminous phases in the peraluminous rocks is marked in their CIPW normative compositions by the permanent presence of corundum (Zen, 1986; 1988). The normative corundum (Table A.3.1, Appendix A.3), which ranges between 0.12 and 3.03 in peraluminous samples, is absent in metaluminous samples. The metaluminous samples contain hornblende, and some of them can contain normative wollastonite, as assumed by Zen (1986) for metaluminous rocks.

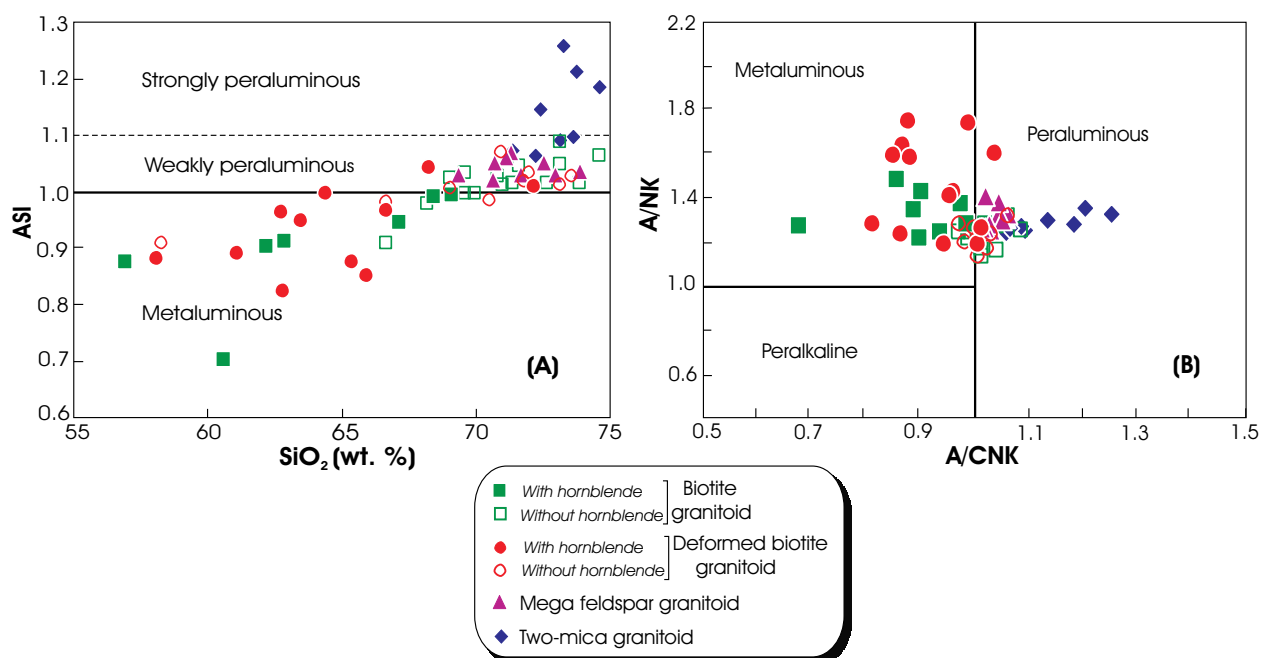


Figure 7.9: Metaluminous to peraluminous characters of the Bafoussam granitoid. (A) Aluminium Saturation Index, ASI = molar $\text{Al}/\text{Ca} + \text{K} + \text{Na} - 1.67\text{P}$) versus SiO_2 (wt. %). The boundary separating the metaluminous and peraluminous domain (continued line) is of Chappell and White (1974), while the dashed line dividing the peraluminous domain in weakly and strongly is as summarized by Zen (1986). (B) Shand's molar parameters, $A/\text{NK} = \text{Al}_2\text{O}_3/(\text{Na}_2\text{O} + \text{K}_2\text{O})$ versus $A/\text{CNK} = \text{Al}_2\text{O}_3 / (\text{CaO} + \text{Na}_2\text{O} + \text{K}_2\text{O})$ in the diagram after Maniar and Piccoli (1989).

To conclude, major element data indicate the intermediate to felsic compositions of the granitoids. The highest values of TiO_2 are displayed by the biotite granitoid and the deformed biotite granitoid samples that contain significant amounts of titanite (up to 5 vol. %) coexisting with hornblende. The Bafoussam granitoids roughly have constant geochemical characteristics,

however with some particularities which separate the biotite granitoid, the deformed biotite granitoid and the mega feldspar granitoid from the two-mica granitoid. The biotite granitoid, deformed biotite granitoid and mega feldspar granitoid are non-alkaline to mid-alkaline, alkali calcic in general, high-K to shoshonitic, ferriferous and metaluminous or moderately peraluminous. The two-mica granitoid is non-alkaline to mid-alkaline, exclusively alkali-calcic, high-K, ferriferous and peraluminous. The shoshonitic affinity mentioned is precluded by the ferriferous character of these granitoids.

7.1.2 Trace elements

The studied granitoids show a wide range of large ion lithophile element (LILE) abundances which are higher in low-silica samples. Among the LILE, Ba appears especially abundant (142–3441 ppm), and Sr and Rb also display quite high contents, respectively 46–1525 and 65–470 ppm. The high-field-strength elements (HFSE) also vary considerably within the analysed granitoids. In contrast to the LILE, silica-rich samples are relatively enriched in HFSE such as Nb (5–40 ppm), Y (8–70 ppm), Ga (14–35 ppm) and Zr which exhibits higher values (43–524 ppm).

Selected Harker variation diagrams for trace elements (Sr, Ba, Zr, Y, Pb, Th, Rb and Nb), as shown in Figure 7.10, lack continuous trends. Nevertheless, observation of poor-defined trends with increase of SiO₂ could be made, according to the geochemical behaviour of the elements and/or the fractionating mineral phases (Fig. 7.10): (1) a gentle decrease for Sr, Ba, and Zr, and clear one for V, may be related to fractionation of plagioclase, biotite, potassium feldspar, zircon, hornblende and iron oxide minerals, respectively; (2) slightly increase in abundance for Th; (3) two-step evolution for Rb and Nb indicated by the switch from compatible to incompatible behaviour for both elements; and (4) decreasing Sr/Ba ratio, while the Rb/Sr ratio remains constant for the low-silica samples and sharply increases for the high-silica samples which probably also reflects the significant effect of mineral fractionation in the genesis of the studied granitoids. Y has more or less constant concentrations with increase of SiO₂. Additionally, a significant feature of these granitoids is their scarcity of incompatible elements.

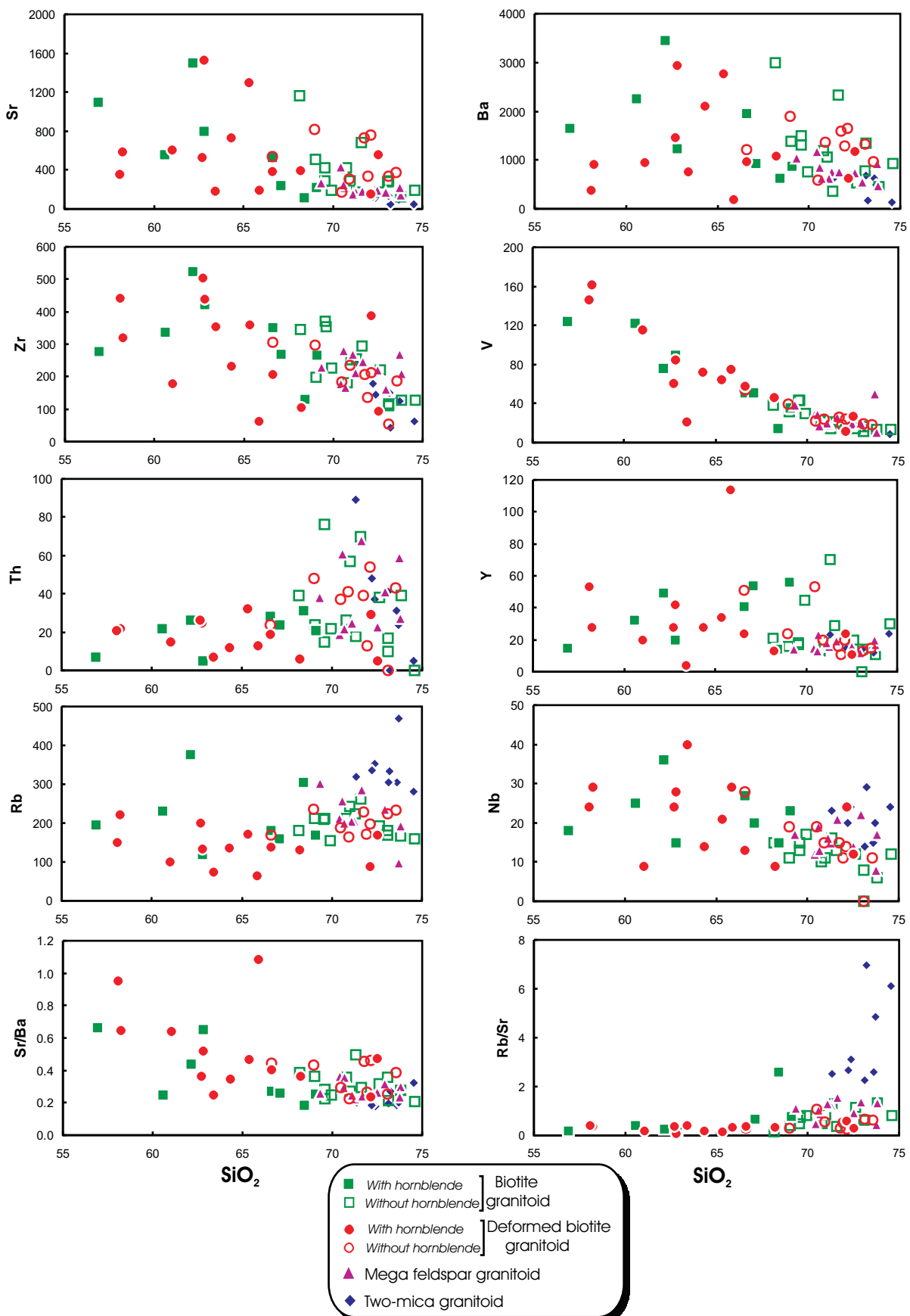


Figure 7.10: Harker variation diagrams of selected trace elements (ppm) and Sr/Ba and Rb/Sr ratios versus SiO_2 content (wt. %) of the Bafoussam granitoids.

7.2 Rare earth element patterns

Rare earth element (REE) geochemical data were obtained for five rock samples of each of the four Bafoussam granitoid types. Results are given in Table A.3.2, Appendix A.3 and the analytical conditions in the Appendix A.1.3. The study of rare earth elements can help for a further geochemical characterization of the investigated granitoids and the magmatic processes involved during their evolution. The obtained rare earth element data have been normalized relative to chondrite abundances, according to the values of McDonough and Sun (1995). The REE fractionation in the studied granitoids is summarized in Table 7.1.

- **The biotite granitoid** contains generally high abundances of REE ($\Sigma\text{REE} = 130\text{--}443 \text{ ppm}$) and exhibits moderate fractionated patterns [$(\text{La/Lu})_{\text{N}} = 22.66\text{--}37.81$] (Fig. 7.11A). The rare earth element fractionation is greater for light rare earth elements [LREE: $(\text{La/Sm})_{\text{N}} = 3.23\text{--}9.65$] than for heavy rare earth elements [HREE: $(\text{Gd/Lu})_{\text{N}} = 1.81\text{--}3.75$] (Fig. 7.11A); the HREE are relatively flat or are slightly concave upward. The europium anomalies are small to negligible ($\text{Eu/Eu}^* = 0.72\text{--}1.08$), because of the low abundance or lack of plagioclase in the residue. Exceptionally, one biotite granitoid sample exhibits a significant europium anomaly ($\text{Eu/Eu}^* = 0.35$) and moderate LREE fractionation compared to the others.

- **The deformed biotite granitoid** rare earth element patterns are quite similar to those of the biotite granitoid (Fig. 7.11B). The deformed biotite granitoid samples are characterized by high total REE ($\Sigma\text{REE} = 151\text{--}433 \text{ ppm}$) and highly fractionated patterns [$(\text{La/Lu})_{\text{N}} = 14.57\text{--}52.13$]. They show slightly varied sloping of the LREE-enriched patterns [$(\text{La/Sm})_{\text{N}} = 4.77\text{--}7.03$] and near-flat to fractionated HREE patterns [$(\text{Gd/Lu})_{\text{N}} = 1.45\text{--}3.62$] with small negative europium anomalies ($\text{Eu/Eu}^* = 0.63\text{--}0.83$) which are consistent with the low abundance of plagioclase in the restite.

- **The mega feldspar granitoid** has high REE abundances ($\Sigma\text{REE} = 251\text{--}415 \text{ ppm}$) and shows homogeneous and strongly fractionated patterns [$(\text{La/Lu})_{\text{N}} = 26.63\text{--}42.21$] (Fig. 7.11C). The LREE fractionation is important [$(\text{La/Sm})_{\text{N}} = 4.41\text{--}6.52$] whereas the HREE display sub-flat profiles with $(\text{Gd/Lu})_{\text{N}}$ ranging between 2.88 and 4.47. Like for the two-mica granitoid, the negative europium anomaly occurs in all the mega feldspar granitoid samples, but in smaller degree ($\text{Eu/Eu}^* = 0.44\text{--}0.77$), which is attributed to the minor retention of Eu^{2+} by residual plagioclase.

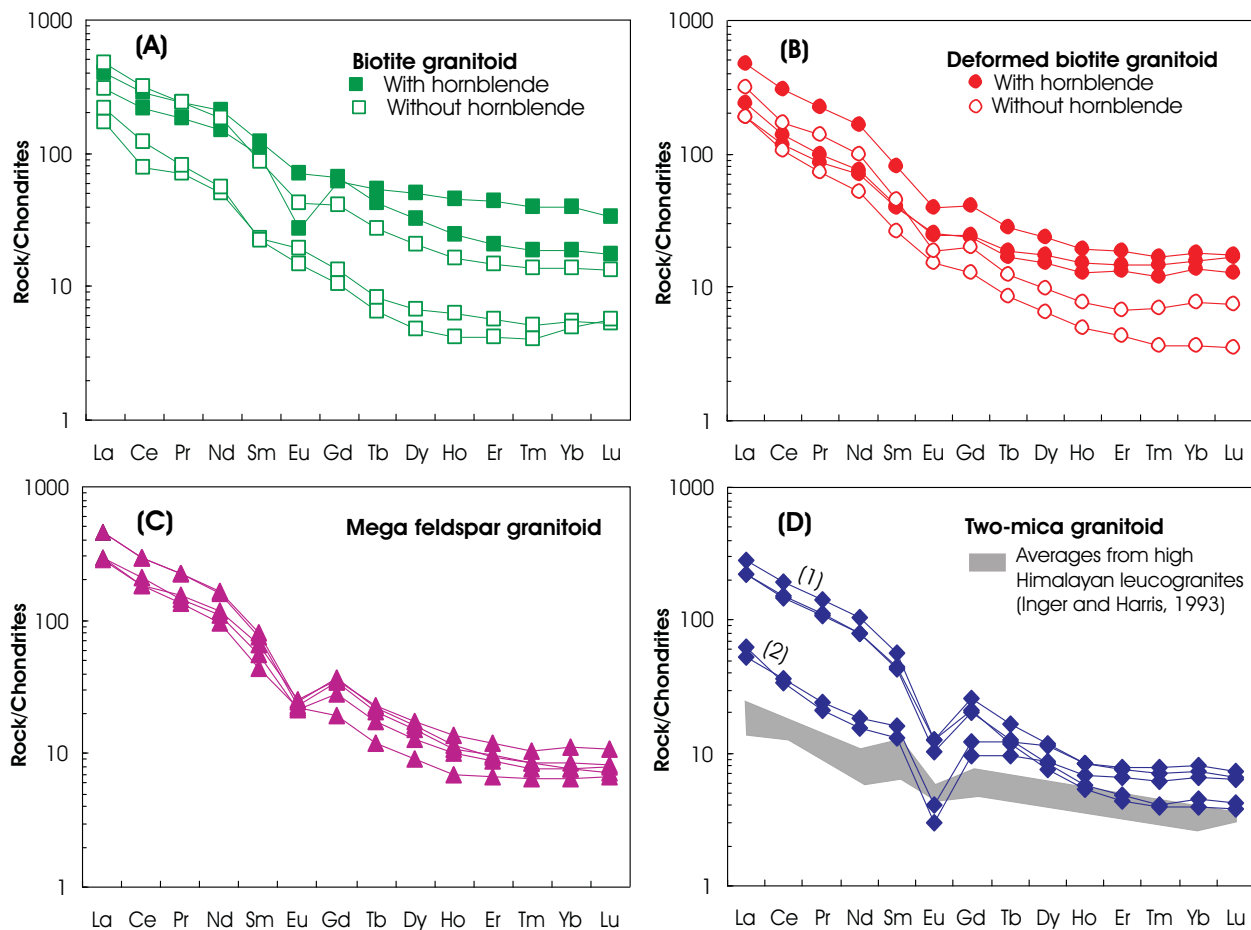


Figure 7.11: Chondrite-normalized REE plots for selected whole rock granitoid samples from the Bafoussam area. Also shown in (D) are averages of the high Himalayan leucogranites (from Inger and Harris, 1993). Normalization coefficients are after McDonough and Sun (1995).

- **The two-mica granitoid** samples display two distinct REE behaviours (Fig. 7.11D): the REE pattern (1) is characterized by high total rare REE contents ($\Sigma\text{REE} = 206\text{--}269 \text{ ppm}$), strongly fractionated REE patterns with an important enrichment in LREE compared to HREE as expressed by the $(\text{La/Lu})_N$ ratio ranging from 43.93 to 58.82, steep LREE pattern [$(\text{La/Sm})_N = 5.00\text{--}5.22$] and fairly curve HREE pattern [$(\text{Gd/Lu})_N = 4.04\text{--}5.54$]. This is probably due to the present of monazite which is also responsible to the important Th concentration ($\text{Th} = 24\text{--}37 \text{ ppm}$) in these samples and the presence of garnet and ilmenite in the residual phase. The REE pattern (2) shows low abundances of rare earth elements ($\Sigma\text{REE} = 54\text{--}57 \text{ ppm}$), moderate REE fractionation, less fractionated LREE-enriched pattern [$(\text{La/Lu})_N = 7.32\text{--}9.59$ and $(\text{La/Sm})_N = 3.33\text{--}4.77$] and relatively flat REE patterns with, however, slight fractionation evidence [$(\text{Gd/Lu})_N = 1.50\text{--}1.68$]. Both REE patterns exhibit substantial negative europium anomalies ($\text{Eu/Eu}^* = 0.28\text{--}0.41$) which are more prominent in REE pattern (2). The negative europium

anomaly is indicative of plagioclase fractionation. The overall REE abundances of the two-mica granitoid more or less coincide with the typical crustal derived granitoids (i.e. La = 20–100 x chondrite, Yb = 0.5–8 x chondrite, Holtz, 1989; Williamson et al., 1996). The Bafoussam two-mica granitoid REE pattern is more fractionated than that of the average REE pattern of high Himalayan leucogranites (Inger and Harris, 1993) shown for comparison (Fig. 7.11D).

In summary, the total REE abundances of each granitoid type vary independently with the SiO₂ content. Generally, the granitoids exhibit significant enrichment in light rare earth elements (LREE) compared to heavy rare earth elements (HREE). The REE patterns are roughly distinct, but some similarities are noticed between the biotite granitoid and the deformed biotite granitoid on the one hand and between the mega feldspar granitoid and the two-mica granitoid on the other hand. The biotite granitoid and the deformed granitoid samples containing hornblende display high HREE fractionation. The REE patterns of the granitoids with general high (La/Lu)_N ratios reflect fractionation mainly of plagioclase and REE-rich accessory phases, i.e. monazite, allanite.

Table 7.1: Summary of the rare earth element fractionation in the Bafoussam granitoids.

Granitoid type	ΣREE	(La/Lu) _N	(La/Sm) _N	(Ga/Lu) _N	(Eu/Eu*) _N
Biotite granitoid	130 – 443	22.66 – 37.81	3.23 – 9.65	1.81 – 3.75	0.72 – 1.08
Deformed biotite granitoid	151 – 433	14.57 – 52.13	4.77 – 7.03	1.45 – 3.62	0.63 – 0.83
Mega feldspar granitoid	251 – 415	26.63 – 42.21	4.41 – 6.52	2.88 – 4.47	0.44 – 0.77
Two-mica granitoid	54 – 269	7.32 – 58.82	3.33 – 5.22	1.50 – 5.54	0.27 – 0.41

7.3 Tectonic setting

The use of the geochemistry of granitoids as indicator for the tectonic setting or environment has been extensively suggested in the literature (e.g., Pitcher, 1987; Pearce et al., 1984; Bachelor and Bowden, 1985; Maniar and Piccoli, 1989; Barbarin, 1990, 1999; Pearce, 1996; Foerster et al., 1997). Following this approach, discrimination diagrams based mainly on trace elements often in combination with major and rare earth elements have been proposed; they

can help in the identification of the original tectonic settings of granitoids. However, the geochemical distinction of tectonic settings for granite generation is often ambiguous; some granitoids are not consistent with the specified classification, exhibiting geochemical compositions that do not conform to the tectonic setting in which they are thought to have formed.

Four groups of granites are distinguished: the ocean ridge granites (ORG), the within plate granites (WPG), the volcanic arc granites (VAG), the collisional granites (COLG). These four groups belong to two major tectonic settings that are (1) divergence plate boundaries, oceanic (oceanic ridge granites) and continental (within plate granites); and (2) convergence plate boundaries, oceanic or continental, subduction-related (volcanic arc granites) and collision-related (collisional granites).

The most widely used tectonic discrimination diagrams for granitoids, classifying them into within plate, volcanic arc, ocean ridge and collisional types, were first proposed by Pearce et al. (1984). In their plot of Nb (ppm) against Y (ppm), the biotite granitoid and deformed biotite granitoid fall in the fields volcanic arc granites (VAG) + syn-collisional granites (syn-COLG) and within plate granites (WPG), whereas the two-mica granitoid and mega feldspar granitoid completely share the common field of volcanic arc granites and syn-collisional granite (Fig. 7.12A). Applying similar plot for Ta (ppm) versus Yb (ppm) that separates the syn-collisional and the volcanic arc granites, the biotite granitoid and the deformed biotite granitoid plot into the volcanic arc granites and within plate granites domains, the mega feldspar granitoid exclusively plots into the volcanic arc granites field and finally the two-mica granitoid mostly falls into the within plate granites field (Fig. 7.12B).

Moreover, in the Pearce et al. (1984) plot of Rb (ppm) versus Y + Nb (ppm), the analysed granitoids straddle the boundary between the fields of syn-collisional granites (syn-COLG), within plate granites (WPG) and volcanic arc granites (VAG) (Fig. 7.12C). Pearce (1996) recognized that such ambiguities are in general distinctive for post-collisional granites (post-COLG) (Fig. 7.12C). In a similar plot using Rb (ppm) and Yb + Ta (ppm), the majority of analysed granitoids fall within the syn-collisional granites field (Fig. 12D).

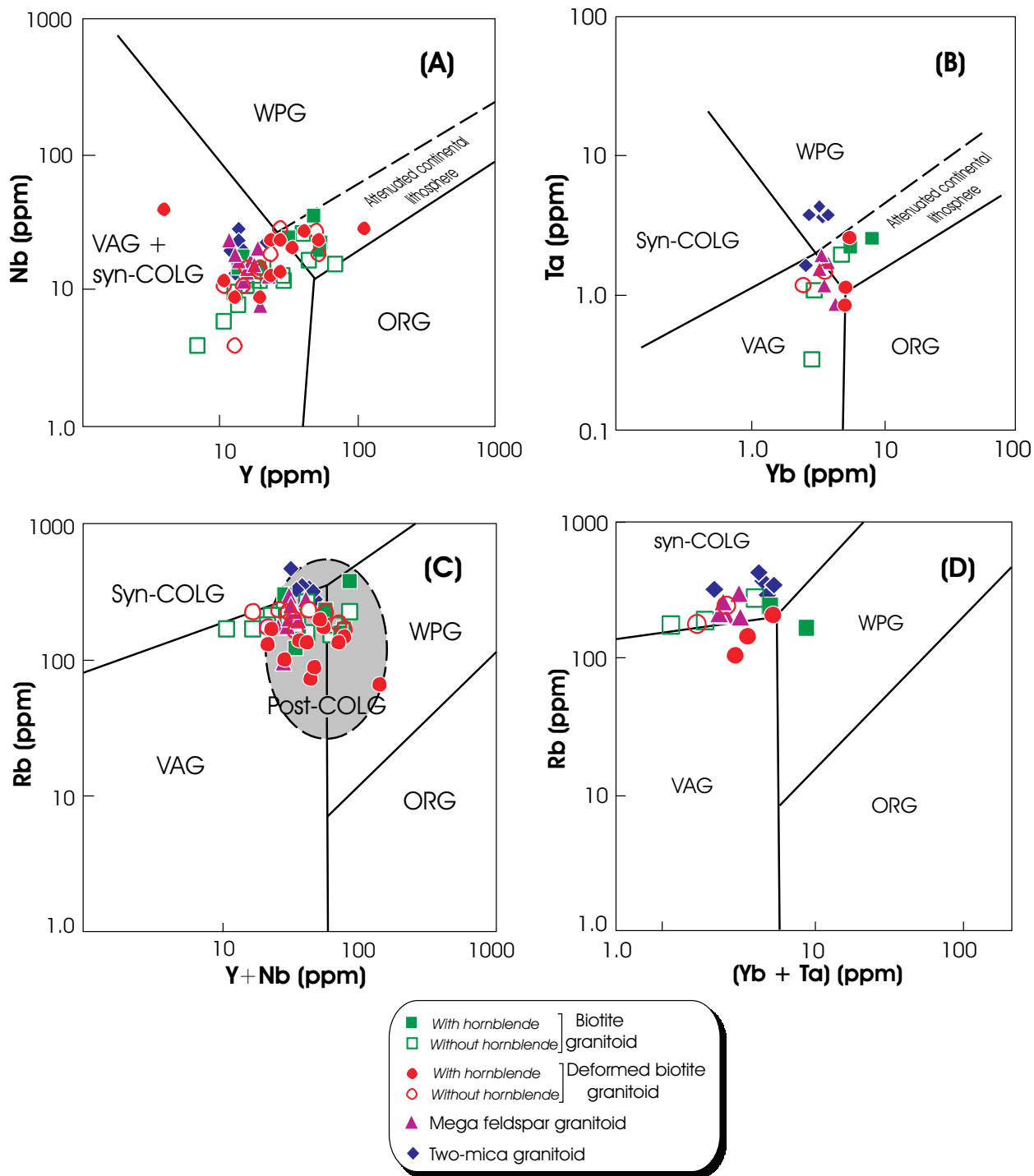


Figure 7.12: (A) Nb versus Y (ppm), (B) Ta versus Yb (ppm), (C) Rb versus Y + Nb (ppm) and (D) Rb (ppm) versus Yb + Ta (ppm) tectonic classification diagrams for the Bafoussam granitoids. Fields after Pearce et al. (1984) and Pearce (1996): WPG = within plate granites, VAG = volcanic arc granites, syn-COLG = syn-collisional granites, ORG = ocean ridge granites and post-COLG = post-collisional granites. The dashed line in (A) and (B) represents the upper compositional boundary for ORG from attenuated continental lithosphere segments.

Following Pearce et al. (1984), several others geotectonic classification diagrams have been introduced such as the Rb/100–Tb–Ta (ppm) and Hf–Rb/30–Ta x 30 (ppm) triangular diagrams after Thiéblemont and Cabanis (1990) and Harris et al. (1986), respectively. In the Rb/100–Tb–Ta diagram (Fig. 7.13A), the biotite granitoid, the deformed biotite granitoid and the mega feldspar granitoid share the common field of post-collisional and syn-subductional granites, whereas the two-mica granitoid occupies the field of syn-collisional granites as in Figure 7.13B in which the other granitoid groups plot rather into the volcanic arc granites domain.

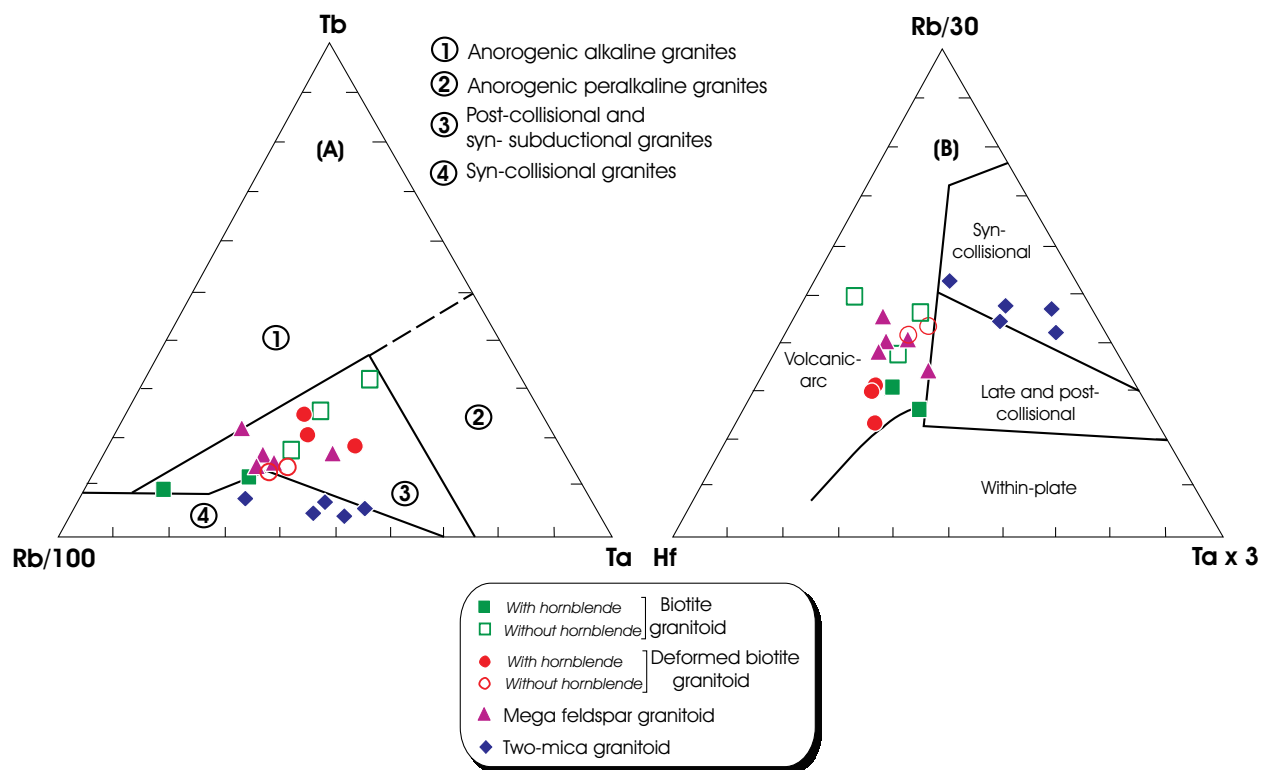


Figure 7.13: (A) Rb/100–Tb–Ta (Thiéblemont and Cabanis, 1990) and (B) Hf–Rb/30–Ta x 30 (Harris et al., 1986) tectonic discrimination diagrams for the Bafoussam granitoids, both indicating that the two-mica granitoid is syn-collision related.

Furthermore, in the multicationic parameters R_1 – R_2 diagram after de la Roche et al. (1980) with the geotectonic discrimination of Bachelor and Bowden (1985) (Fig. 7.14), the biotite granitoid and deformed biotite granitoid are categorized mostly as syn-collision and late-orogenic granites, and as related to post-collision uplift. In the same diagram, the mega feldspar granitoid and the two-mica granitoid are exclusively classified as syn-collision granite. The sub-alkaline trend of the investigated granitoids is portrayed in this diagram where the biotite

granitoid, the mega feldspar granitoid and the two-mica granitoids plot into the field of the monzonitic sub-alkaline magmatism, whereas the deformed biotite granitoid occupies part of the sub-alkaline monzonitic field, part of the field of high-potassic calc-alkaline, and part of the calc-alkaline and trondhjemetic domain as proposed by Lameyre and Bowen (1982).

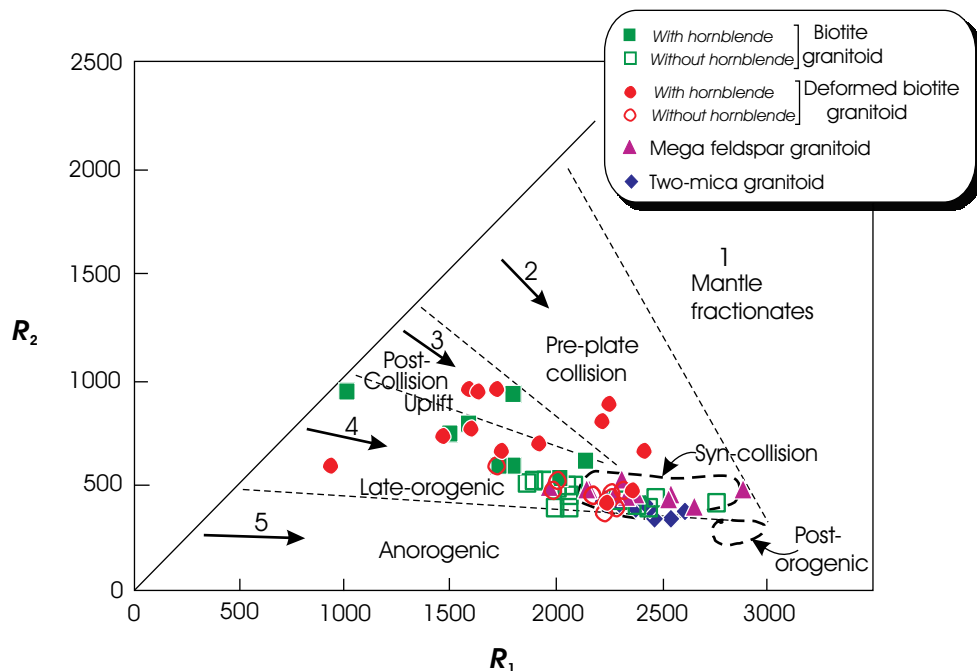


Figure 7.14: $R_1 = 4\text{Si} - 11(\text{Na} + \text{K}) - 2(\text{Fe} + \text{Ti})$ versus $R_2 = 6\text{Ca} + 2\text{Mg} + \text{Al}$ diagram after de la Roche et al. (1980) displaying the geotectonic fields (Bachelor and Bowden, 1995) as well as their petrological equivalents (Lameyre and Bowden, 1982): group 1, tholeiitic; group 2, calc-alkaline and trondhjemetic; group 3, high-potassic calc-alkaline; group 4, sub-alkaline monzonitic; group 5, alkaline and peralkaline.

The tectonic setting of the Bafoussam granitoids can also be inferred by the multi-element spidergrams (Fig 7.15) which show the concentrations of K_2O , Rb , Ba , Th , Ta , Nb , Ce , Hf , Zr , Sm , Y and Yb normalized against those of the ocean ridge granites (ORG: Pearce et al., 1984). The investigated granitoids generally display almost comparable multi-element patterns in the spidergrams, with enrichment in K_2O , Rb , Ba , Th , Ta , Nb and Ce and depletion in Hf , Zr , Sm , Y and Yb with respect to the ORG. They demonstrate positive anomalies in Rb , Th , Ce and Sm , and negative Ba anomalies. The negative Ba anomalies most pronounced in the mega feldspar granitoid and in the two-mica granitoid are largely attributed to fractional crystallization of K-feldspar and biotite. The granitoids are also characterized by pronounced negative anomalies of $\text{Nb}-\text{Ta}$ and $\text{Zr}-\text{Hf}$ relative to neighbouring elements. These elements patterns generally resemble those of "collision granites", including syn- and post-collision granites

(Pearce et al., 1984). For comparison, typical syn- and post-collisional granite patterns after Pearce et al. (1984) are also illustrated in Figure 7.15.

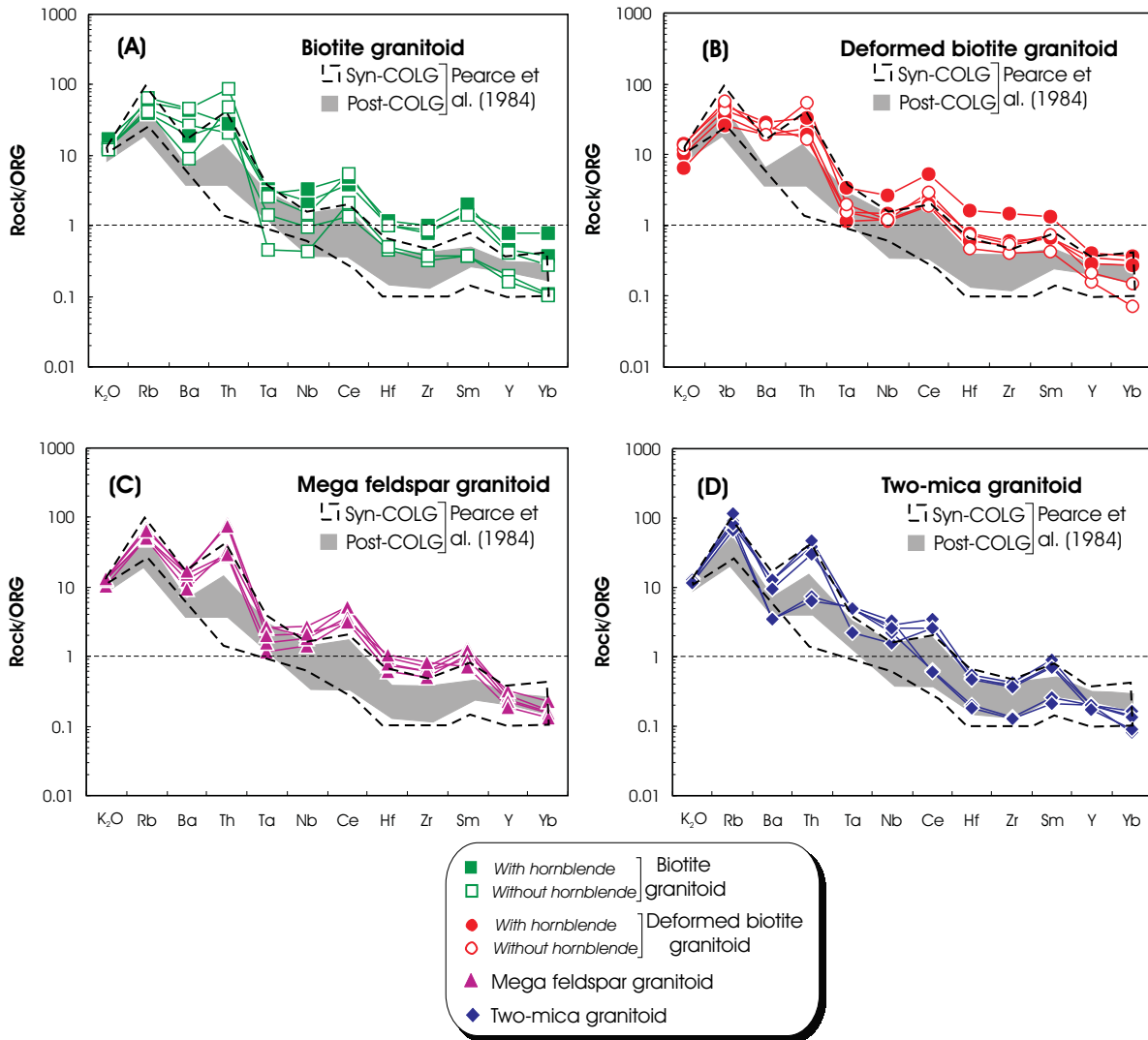


Figure 7.15: Ocean Ridge Granites (ORG) normalized multi-element spidergrams of the Bafoussam granitoids. For comparison, the compositions of typical syn-collision granites (syn-COLG, dashed areas) and post-collision granites (post-COLG, shadowed areas) after Pearce et al. (1984) are shown. The Ocean Ridge Granites normalizing values are from Pearce et al. (1984).

Although the granitoids described in this study formed in a continental collision-related orogenic belt, the data generally occupy simultaneously different tectonic fields in the discrimination diagrams (Figs. 7.12–14). The volcanic arc- and within plate-like geochemical signatures, in addition to the syn- and post-collisional ones are considered to be more likely a function of the source rocks that were melted than the specific tectonic setting in which the

granitoids were generated. Nevertheless, Harris et al. (1986) argued that trace elements can be considered as plausible discriminator of a tectonic setting in convergent continental zones with collision, when lacking detailed structural study.

7.4 Genetic type: I-type and/or S-type?

Since Chappell and White (1974) introduced the concept of I- and S-type granites, genetic links between granitoid types and the geodynamic environments in which they formed have been the focus of many studies. They have demonstrated that the granite composition is basically controlled by source rock compositions. The granitic rocks have then been divided chiefly into I-, S-, M- and A-types, denoting their igneous or infracrustal, sedimentary or supracrustal, mantle or mantle wedge and anorogenic or anhydrous sources, respectively (Chappell and White, 1974: 1984; White, 1979; Loiselle and Wones, 1979). Later contributions furnished further details and listed their major chemical and mineralogical characteristics and field occurrences.

In the P_2O_5 versus SiO_2 and Pb versus SiO_2 diagrams (Fig. 7.16A and B), P_2O_5 decreases with increasing SiO_2 , while Pb scatter but roughly increases with SiO_2 , both following the I-type granite trend proposed by Chappell and White (1992) and Chappell (1999).

Using the NaO_2 versus K_2O discriminate diagram (Fig. 7.16C) after Chappell and White (1984: 2001), the majority of biotite granitoid and deformed biotite granitoid is of I-type, with few of their samples which completely fall out of this field. In contrast, the mega feldspar granitoid and two-mica granitoid tend to have more S-type characteristic. In general, the compositions of more potassic samples overlap the boundary between I-type and S-type granites, with the less-fractionated samples exhibiting I-type affinities. The term *fractionated* is generally used for rock samples having higher Si, and lower Fe and Ca compared to those referred to as unfractionated (Chappell, 1999; Norman et al., 1992).

The Aluminium Saturation Index was also employed by Chappell and White (1974) as a special reference to deduce igneous ($A/CNK \leq 1.1$) or sedimentary origins ($A/CNK > 1.1$). Applying this classification, the studied granitoids mainly constitute an I-type granitoid suite, with however the majority of the two-mica granitoid samples seeming to have a sedimentary

source as it is demonstrated in the A/CNK (molar $\text{Al}_2\text{O}_3 / \text{CaO} + \text{Na}_2\text{O} + \text{K}_2\text{O}$) versus Fe_2O_3^* (total Fe) diagram of Norman et al. (1992) (Fig. 7.16D).

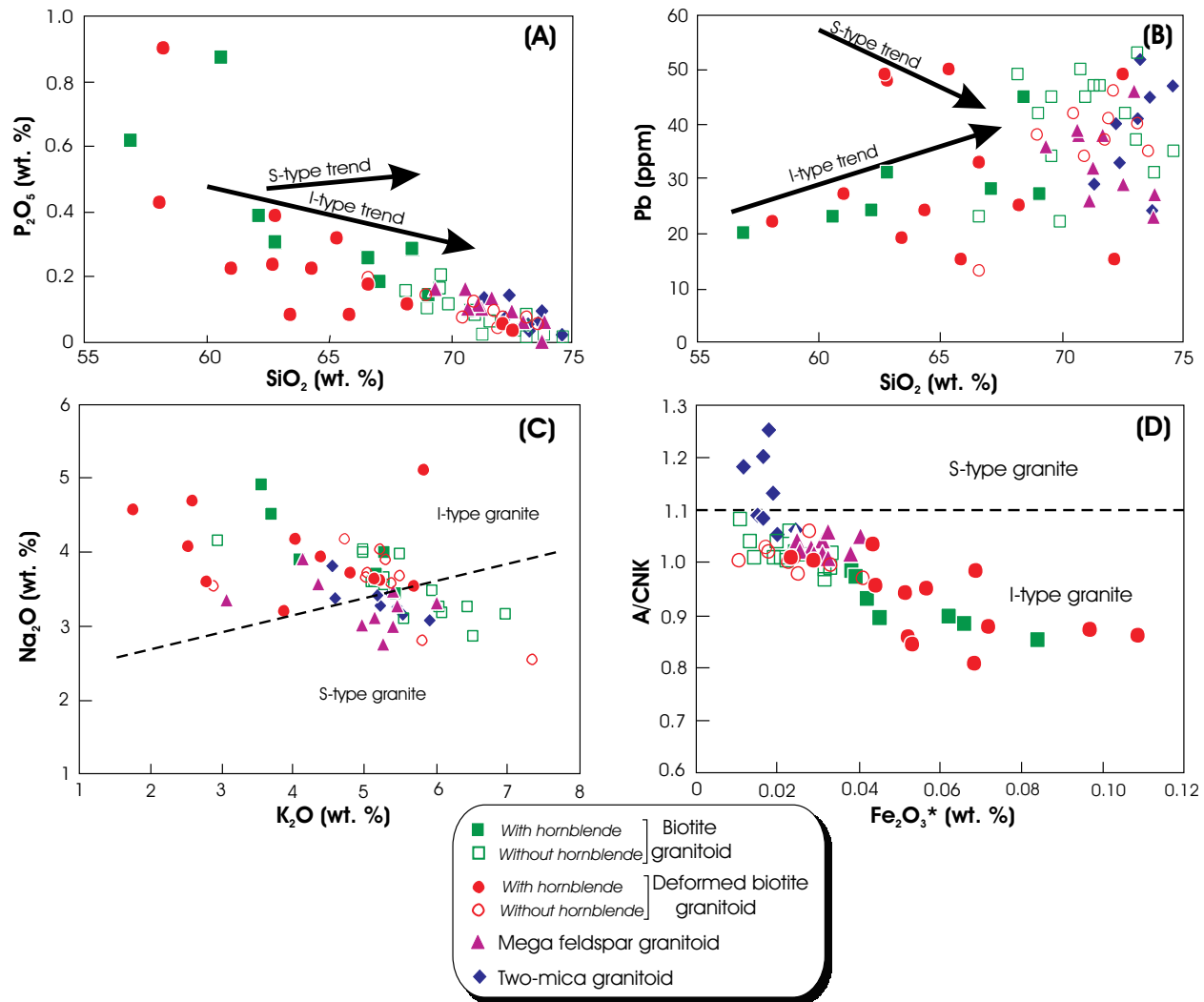


Figure 7.16: Genetic classification of the Bafoussam granitoids, showing their dominating igneous source (I-type) associated with S-type. (A) P_2O_5 versus SiO_2 and (B) Pb versus SiO_2 variation diagrams with the evolution vectors of I- and S-type granites (Chappell and White, 1992; Chappell, 1999). (C) Variation of Na_2O versus K_2O (Chappell and White, 1984: 2001). (D) Aluminum Saturation Index ($\text{A/CNK} = \text{molar } \text{Al}_2\text{O}_3/\text{CaO} + \text{Na}_2\text{O} + \text{K}_2\text{O}$) versus Fe_2O_3^* (total Fe content) diagram, after Norman et al. (1992).

As proposed by Whalen et al. (1987) in some discrimination diagrams with $\text{K}_2\text{O} + \text{Na}_2\text{O}$, FeO^*/MgO , Zr or Nb versus $10000\text{Ga}/\text{Al}$ (Fig. 7.17A, B, C and D), the investigated granitoids straddle the fields of A- and I-, S-, M-types, except in FeO^*/MgO diagram where they occupy only the field of I-, S- and M-types granites.

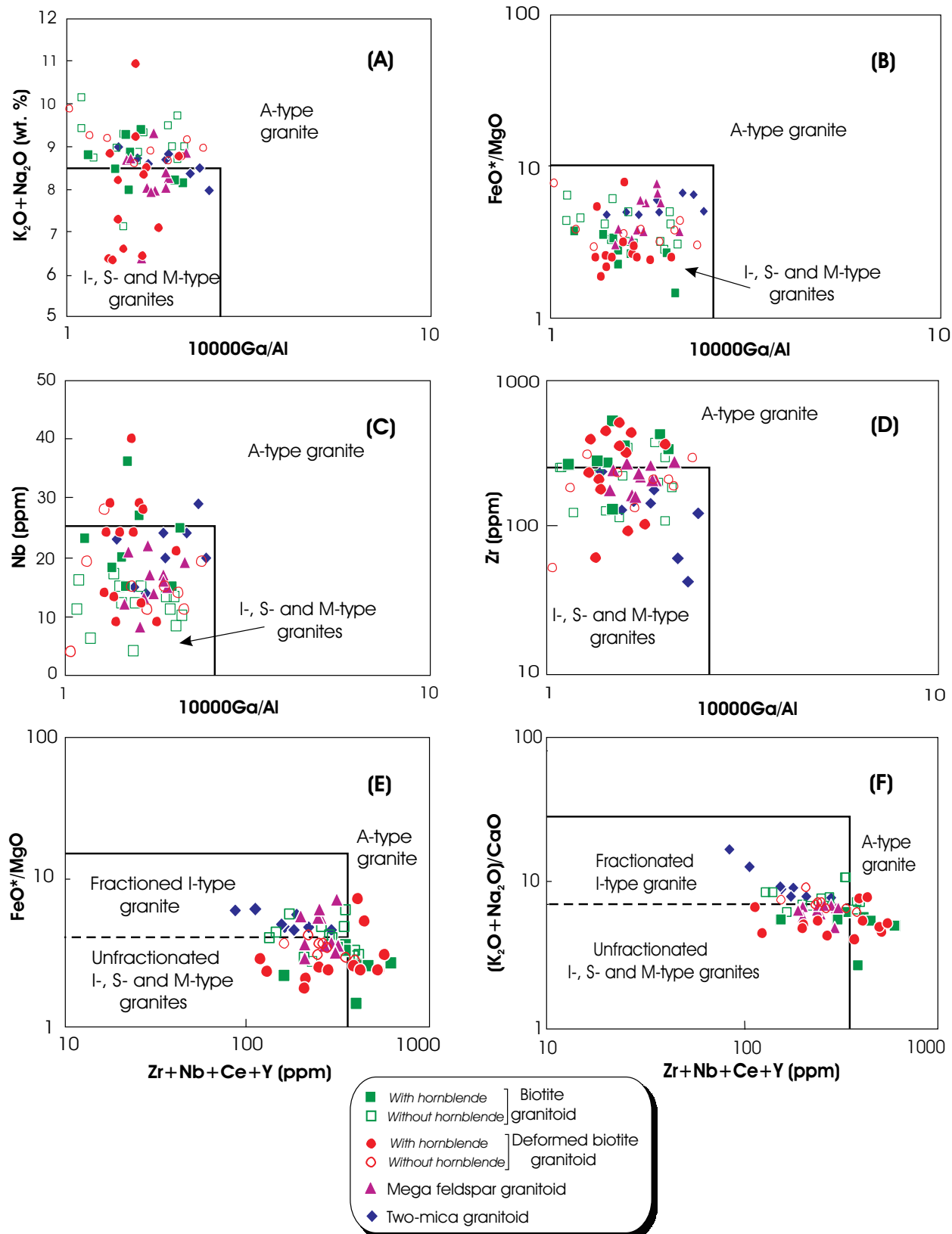


Figure 7.17: (A) $K_2O + Na_2O$, (B) FeO^*/MgO , (C) Nb , (D) Zr versus 10000 Ga/Al and FeO^*/MgO , (E) FeO^*/MgO , (F) $(K_2O + Na_2O)/CaO$ versus $(Zr + Nb + Ca + Y)$ genetic classification diagrams for A-type granitoids (Whalen et al., 1987; Eby et al., 1990), showing the intermediate position between I-, S-, M- and A-types of the Bafoussam granitoids.

Furthermore, in the FeO^*/MgO and $(\text{K}_2\text{O} + \text{Na}_2\text{O})/\text{CaO}$ versus $\text{Zr} + \text{Nb} + \text{Ce} + \text{Y}$ diagrams (Fig. 7.17E, F: Wahlen et al., 1987; Eby, 1990), the studied granitoids variably overlap simultaneously the fields for fractionated I-type granites, unfractionated I-, S- and M-type granites and A-type granites.

The discrimination diagrams used show significant compositional overlaps of the investigated granitoids in the different genetic-type fields and reflect the difficulty of definitive recognition of the different genetic types. However, their genesis in a continental collision-related orogenic belt enables a first constraint to I- and/or S-type (White and Chappell, 1983; Barbarin, 1999). Furthermore, the major mineralogical and geochemical features for the granitoids under study as summarized in Table 7.1, combined with the field relationships clearly suggest that they belong to I-type, except the two-mica granitoid which is most likely to be S-type. The similarities of the Bafoussam I-type granitoids with the A-type in term of high $(\text{K}_2\text{O} + \text{Na}_2\text{O})$, Ga/Al and ZNCY ($\text{Zr} + \text{Nb} + \text{Ce} + \text{Y}$) as illustrated in Figure 7.17 indicate that they belong to the fractionated felsic I-type (King et al., 1997; Chappell, 1999). This is supported by: (1) some transitional compositions noticed between the I-type granitoids and the two-mica S-type granitoid, caused by the more felsic, potassic and slightly peraluminous character of the I-type granitoids; (2) the absence of hornblende and the negative correlation between P_2O_5 and SiO_2 (Fig. 7.16A) due to the fractionation of apatite in the absence of Y-bearing accessory minerals in the studied I-type granitoids (Chappell and White, 1992: 2001); and (3) their mid-alkaline nature portrayed in Figure 7.4 (Sylvester, 1989).

7.5 Fractional crystallization processes

Even though mineral fractionation is shown above by the major and trace elements linear variation (Fig. 7.3; Fig. 7.10; Fig. 7.15) and the REE patterns (Fig. 7.11) as a magmatic process in the evolution of the Bafoussam granitoids, its extent and the influence of the most abundant minerals such as plagioclase, potassium feldspar, biotite and amphibole and accessory minerals need to be evaluated. The behaviour of Rb, Sr and Ba (Fig. 7.18) is then useful and could help to distinguish fractional crystallization from partial melting or more complex processes (e.g., assimilation, magma mixing, restite unmixing) that are mostly controlled the magmatic evolution (Hanson, 1978: 1989).

Table 7.2: Comparison of the geochemical and the mineralogical characteristics of S-type and I-type granites (Chappell and White, 1974; 1992; 2001; White and Chappell, 1983) with the Bafoussam granitoid rocks.

Notes: -: absent; n.d: not determined

* Molar $\text{Al}_2\text{O}_3/(\text{CaO} + \text{Na}_2\text{O} + \text{K}_2\text{O})$

	Bafoussam granitoids				I-type granites	S-type granites
	Biotite granitoid	Deformed biotite granitoid	Mega feldspar granitoid	Two-mica granitoid		
SiO_2 (wt. %)	56.91 – 74.60	58.24 – 73.55	70.42 – 73.74	71.33 – 74.55	wide variation range, 53 – 76	restricted, relatively high (> 65)
$\text{K}_2\text{O}/\text{Na}_2\text{O}$	0.70 – 2.25	0.37 – 2.86	0.89 – 1.88	1.18 – 1.90	low, < 1	high, > 1
CaO (wt. %)	0.82 – 4.59	0.84 – 4.60	1.21 – 1.86	0.37 – 1.17	high	low
$\text{A}/(\text{CNK})^*$	0.67 – 1.06	0.80 – 1.06	1.01 – 1.05	1.05 – 1.25	low, < 1.1 metaluminous (peraluminous for only fractionated I-type)	high, > 1.1 peraluminous
Initial ${}^{87}\text{Sr}/{}^{86}\text{Sr}$	0.706 – 0.708	n.d	0.705 – 0.709	0.708 – 0.720	low, 0.704 – 0.706	high, > 0.708
ϵ_{Nd}	0.2 to –6.3	n.d	–5.6 to –12.1	–9.9 to –14.0	high, + 3.5 to – 8.9	low, < – 5.8
Minerals	± hornblende magnetite titanite	± hornblende magmetite titanite	no hornblende magnetite titanite	garnet ilmenite muscovite	hornblende, clinopyroxene magnetite titanite	Cordierite garnet ilmenite
CIPW norm						
Corundum	0.12 – 1.14	0.22 – 1.10	0.22 – 1.06	1.18 – 3.02	$\text{c} < 1\%$ or di	$\text{c} > 1\%$
Diopside	0.01 – 0.74	0.02 – 4.74	–	–		

In a logarithmic diagram of Rb versus Sr (Fig. 7.18A), it appears that the behaviour of Rb changes during magmatic differentiation and is reflected by a slight decrease of Rb concentration in the least evolved samples, whereas Rb increases in the silica-rich samples with a continuous decrease of Sr concentration from about 1050 to 30 ppm. Sr and Ba are roughly compatible, and their concentrations decrease sharply during the evolution of magma, describing a linear array (Fig. 7.18B).

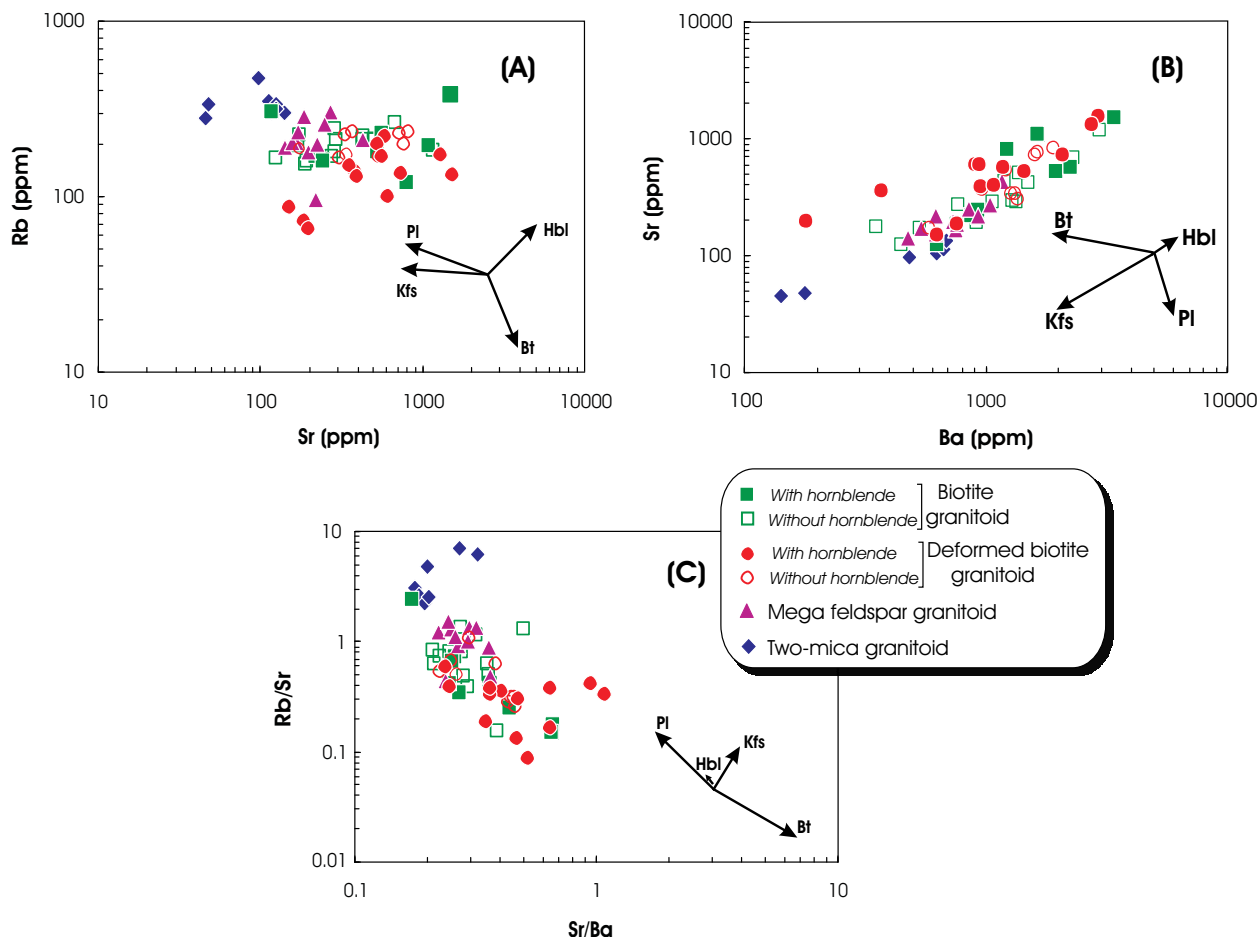


Figure 7.18: Logarithmic plots of (A) Rb versus Sr, (B) Sr versus Ba and (C) Rb/Sr versus Sr/Ba variation diagrams for the Bafoussam granitoids, showing that the plagioclase was the main fractionating phase in the course of differentiation. The vectors denote the influence of fractionation of plagioclase (Pl), potassium feldspar (Kfs), hornblende (Hbl) and biotite (Bt) on the evolution of the studied granitoids; melts governed by fractionation of a specific mineral will evolve in the direction of the arrowhead.

The Rb/Sr versus Sr/Ba plot (Fig. 7.18C) shows a slight decrease of Sr/Ba ratio and a rapid increase of the Rb/Sr ratio from the low- to the high-silica members. According to the summary of Hanson (1978), these observations express the fractionation of plagioclase and potassium feldspar as the important phases in the course the magmatic evolution of the I-type granitoids,

whereas the separation of biotite was less pronounced in the early and later stages, respectively. As for hornblende, it surely played a significant role, at least during the first magmatic stage (decreasing CaO and MgO with increasing SiO₂). Moreover, the decrease of V, Ti, Zr and P₂O₅ respectively reveals that the separation of iron oxide minerals, titanite, zircon and apatite appears to have controlled the variation of these elements. The two-mica granitoid displays internal feldspars fractionation.

A fractionation process including REE-rich accessory phases such as apatite, titanite, zircon, allanite and monazite is less expressed in the REE patterns, although these accessory minerals are largely present in the granitoids described in this study. However, in (La/Lu)_N versus (Eu/Eu*)_N and (La/Lu)_N versus La_N (Fig. 7.19A and B) diagrams, the variation of REE contents seems to be consistent with the fractionation of zircon and to lesser extent, apatite and titanite and allanite during the evolution of I-type granitoids. The separation of monazite and zircon was significant in the two-mica granitoid (Fig. 7.19 B).

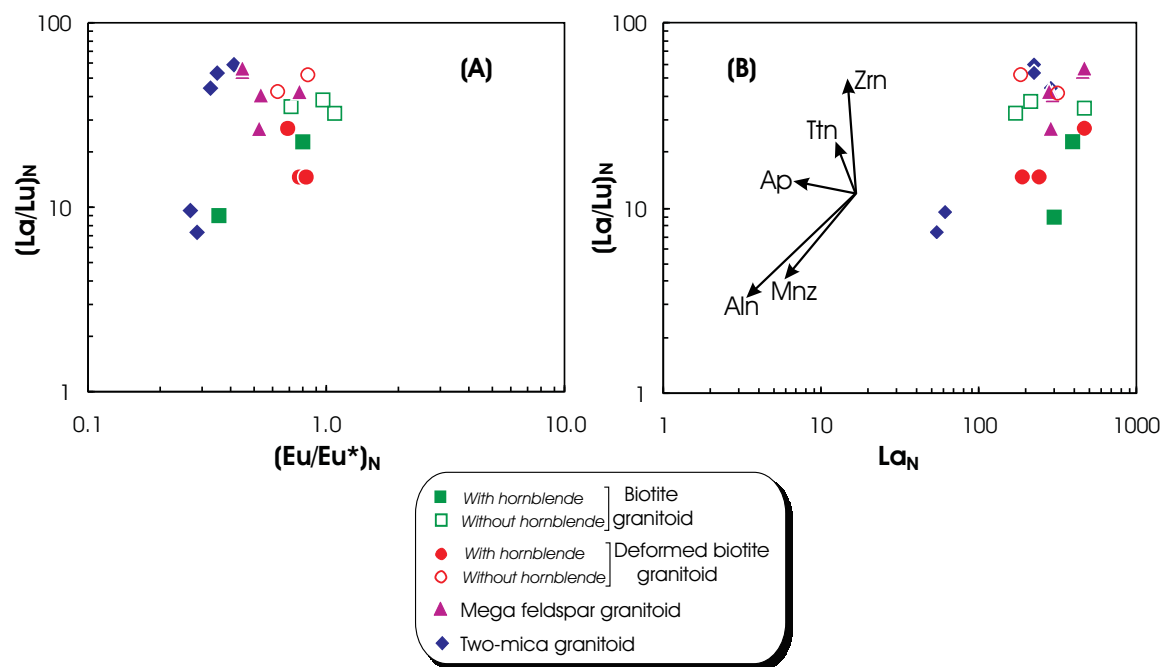


Figure 7.19: (A) (La/Lu)_N versus (Eu/Eu*)_N and (B) (La/Lu)_N versus La_N diagrams showing the variation of REE contents by the fractionation of accessory minerals, particularly zircon. The arrows indicate the effect of fractional crystallization of allanite (Aln), apatite (Ap), monazite (Mnz), titanite (Ttn) and zircon (Zrn) on the composition of residual liquids and point towards the melt direction governed by each of these minerals.

To summarise, fractional crystallization of feldspars, biotite, zircon, titanite, apatite and iron oxides minerals has played considerable role during the formation of the diverse I-type Bafoussam granitoids. The variation of major elements was primarily controlled by the fractionation of biotite and feldspars. The latter also influenced the Rb, Sr, and Ba abundances. The REE variation was performed by the fractionation of zircon, apatite, titanite, allanite and monazite. The general mineralogical and geochemical evolution in these granitoids is consistent with fractional crystallization from quartz-monzdiorite, granodiorite, quartz monzonite, monzogranite, quartz-syenite, syenogranite to alkali-feldspar granite (Fig. 7.11D; Fig. 7.15D; Fig. 7.18; Fig. 7.19). On the other hand, the two-mica granitoid which result from a distinct parental magma has also experienced internal fractionation of feldspar, monazite and zircon. Partial melting of heterogeneous sources or more complex processes (e.g., assimilation, magma mixing, restite unmixing) in the magmatic evolution of these granitoids are not demonstrated.

Considering the major, trace and REE element data, the following preliminary conclusion emerge:

(1) The granitoids under study display a wide range of SiO_2 (56.9–74.6 wt. %) and have high values of alkalis ($\text{K}_2\text{O} + \text{Na}_2\text{O} = 6\text{--}11$ wt. %), total Fe, Fe_2O_3 (0.96–7.8 wt. %) and Al_2O_3 (12.0–17.6 wt. %), but low MnO , MgO , CaO and TiO_2 contents. Trace element chemistry shows variable abundances in large ion lithophile elements (LILE) and high-field-strength elements (HFSE), with the LILE being higher in intermediate granitoids and the HFSE in contrast higher in silica-rich granitoids. The granitoids are enriched in light- relative compared to heavy-REEs, with small to significant negative Eu anomalies. Ocean ridge granites (ORG) normalized multi-elements spidergrams display typical collision-related granites pattern, with characteristic negative anomalies of Ba, Nb and Y, and positive anomaly in Rb, Th and Sm.

(2) The granitoids exhibit chemical characteristics of non-alkaline to mid-alkaline, calc-alkaline, mostly alkali-calcic, high-K, ferriferous affinities and are of two different genetic types: I-type, including the biotite granitoid, the deformed biotite granitoid and the mega feldspar granitoid, and S-type represented exclusively by the two-mica granitoid. I-type granitoids show a wide compositional range, comprising syenogranite (major), alkali-feldspar granite, granodiorite, monzogranite, quartz-syenite, quartz-monzonite to quartz-monzdiorite. They are metaluminous ($\text{ASI} = 0.70\text{--}1.0$) or moderately peraluminous ($\text{ASI} = 1.01\text{--}1.06$) for highly fractionated samples. The variation in composition within the I-type granitoids is probably related to the fractional

crystallization of feldspar, biotite, zircon, titanite, apatite and iron oxides minerals. The two-mica S-type granitoid is peraluminous. It shows permanent presence of corundum (0.12–3.03) in its CIPW normative composition. The fractionation of feldspars, monazite and zircon was considerable in the two-mica granitoid.

(3) The calc-alkaline and the peraluminous nature of the Bafoussam granitoids are in good accordance with the chemical composition of the biotite (Fig. 4.2A and B).

(4) The investigated granitoids have chemical features of syn- and post-collisional, within plate and volcanic arc tectonic environments. Since they emplaced in an orogenic belt, the volcanic arc and within plate signature are then believed to have been inherited from their source rocks.

8 ISOTOPE CHARACTERISTICS

The concentrations and the variations in whole-rock isotopes allow a further discrimination of the Bafoussam granitoid groups. Therefore, twenty-four samples have been analysed for their Sr and Nd whole-rock isotope compositions, including eight samples of the biotite granitoid, eleven samples of the mega feldspar granitoid and five samples of the two-mica granitoid. The data of Rb–Sr and Sm–Nd isotope analyses of the granitoids are listed in Tables A.4.1 and A.4.2 in the Appendix A.4. The analytical techniques are summarized in the Appendix A.1.4. Samples of the deformed biotite granitoid have been excluded from the radiogenic isotope analyses, as the deformation could have potentially induced considerable changes in minerals and in isotopic abundances.

In the approach here adopted, the whole-rock isotope data from the investigated granitoids can be used as tools to: (1) determine ages of magmatic crystallization; and (2) to complete the petrogenetic model developed on the basis of major and trace element data by the important information concerning the magmatic sources.

8.1 Rubidium–Strontium dating method

Rubidium (Rb) is member of the alkali metal group which occurs in nature with two isotopes: radioactive ^{85}Rb and stable ^{87}Rb . ^{87}Rb decays with a half-life of 4.8×10^{10} years to ^{87}Sr by negative beta particle emission. Strontium (Sr) is an alkaline element and has four naturally occurring isotopes (^{88}Sr , ^{87}Sr , ^{86}Sr and ^{84}Sr), all being exclusively stable. The precise isotopic composition of Sr in a rock which contains Rb depends on its age and Rb/Sr ratio. This is the basis for the Rb–Sr dating method, using the following expression:

$$(^{87}\text{Sr}/^{86}\text{Sr})_m = (^{87}\text{Sr}/^{86}\text{Sr})_{\text{initial}} + (^{87}\text{Rb}/^{86}\text{Sr})_m (e^{\lambda t} - 1) \quad (8.1)$$

where:

$(^{87}\text{Sr}/^{86}\text{Sr})_m$ =	measured present-day isotopic ratios of the rock
$(^{87}\text{Sr}/^{86}\text{Sr})_{\text{initial}}$ =	ratio of the rock at the time of its formation
$(^{87}\text{Rb}/^{86}\text{Sr})_m$ =	measured present-day isotopic ratios of the rock
λ =	decay constant of ^{87}Rb , having a conventional value of $1.42 \times 10^{-11} \text{ y}^{-1}$ (Steiger and Jäger, 1977)
t =	age of the rock in years

The Rb–Sr dating method is applicable only for a suite of cogenetic samples, i.e.: samples resulting from the same parental magma, assuming that they have the same initial $^{87}\text{Sr}/^{86}\text{Sr}$ ratio. The age (t) of the cogenetic samples is calculated from a plot of measured $(^{87}\text{Sr}/^{86}\text{Sr})_m$ versus $(^{87}\text{Rb}/^{86}\text{Sr})_m$ ratios in which the sample points fit to a straight line called *isochron*. All the sample points on the isochron represent systems having the same age and the same initial $^{87}\text{Sr}/^{86}\text{Sr}$ ratio. The slope of the isochron is related to the age of the cogenetic samples, whereas the value of the initial $^{87}\text{Sr}/^{86}\text{Sr}$ ratio is given by the intercept of the isochron with the $(^{87}\text{Sr}/^{86}\text{Sr})_m$ axis on the $(^{87}\text{Sr}/^{86}\text{Sr})_m$ versus $(^{87}\text{Rb}/^{86}\text{Sr})_m$ diagram. The age calculations and statistical assessment of the data have been done here utilizing the geochronological statistical software package Isoplot/Ex (version 2.45) of Ludwig (2000).

The biotite granitoid samples give an age of 540 ± 27 Ma with $^{87}\text{Sr}/^{86}\text{Sr}$ initial ratio of 0.7075 ± 0.00022 and a MSWD (Mean Squares of Weighted Deviates) value of 0.39 (Fig. 8.1A). The mega feldspar granitoid samples define an isochron at 587 ± 41 Ma, an initial $^{87}\text{Sr}/^{86}\text{Sr}$ ratio of 0.7077 ± 0.0016 and a MSWD value of 1.5 (Fig. 8.1B). For the two-mica granitoid, an isochron age of 663 ± 62 Ma with an $^{87}\text{Sr}/^{86}\text{Sr}$ initial ratio of 0.7012 ± 0.0091 and a MSWD value of 0.2 is obtained (Fig. 8.1C).

Based on the MSWD values, the ages obtained for biotite granitoid (540 ± 27 Ma), mega feldspar granitoid (587 ± 41 Ma) and two-mica granitoid (663 ± 62 Ma) are considered as real isochrons (Brook et al., 1972; Wendt, 1993), although the two-mica granitoid age calculation exhibits a large uncertainty. Similar Pan-African Rb–Sr whole-rock isochron ages have been recorded from the neighboured granitic plutons (e.g., 603–606: Tchouankoué, 1992; 575 ± 17 Ma: Kwekam, 1993; 657 ± 08 Ma: Tagne-Kamga, 1994; 576 ± 24 Ma: Talla, 1995) and from the other granitoids within the Neoproterozoic belt of Cameroon (e.g., Lasserre et al., 1981a: b; Toteu et al., 1987), as shown by the available geochronological data for the Pan-African granitoids within the Neoproterozoic belt of Cameroon (Table 1.1 and 1.2). The ages obtained from the other plutonic complexes in West Cameroon have been considered as intrusion or crystallization ages. If all three groups of investigated granitoids are considered together, the isochron including all samples yields a model age of 613 ± 18 Ma, an initial $^{87}\text{Sr}/^{86}\text{Sr}$ ratio of 0.7066 ± 0.00054 and a MSWD value of 1.8 (Fig. 8.1D).

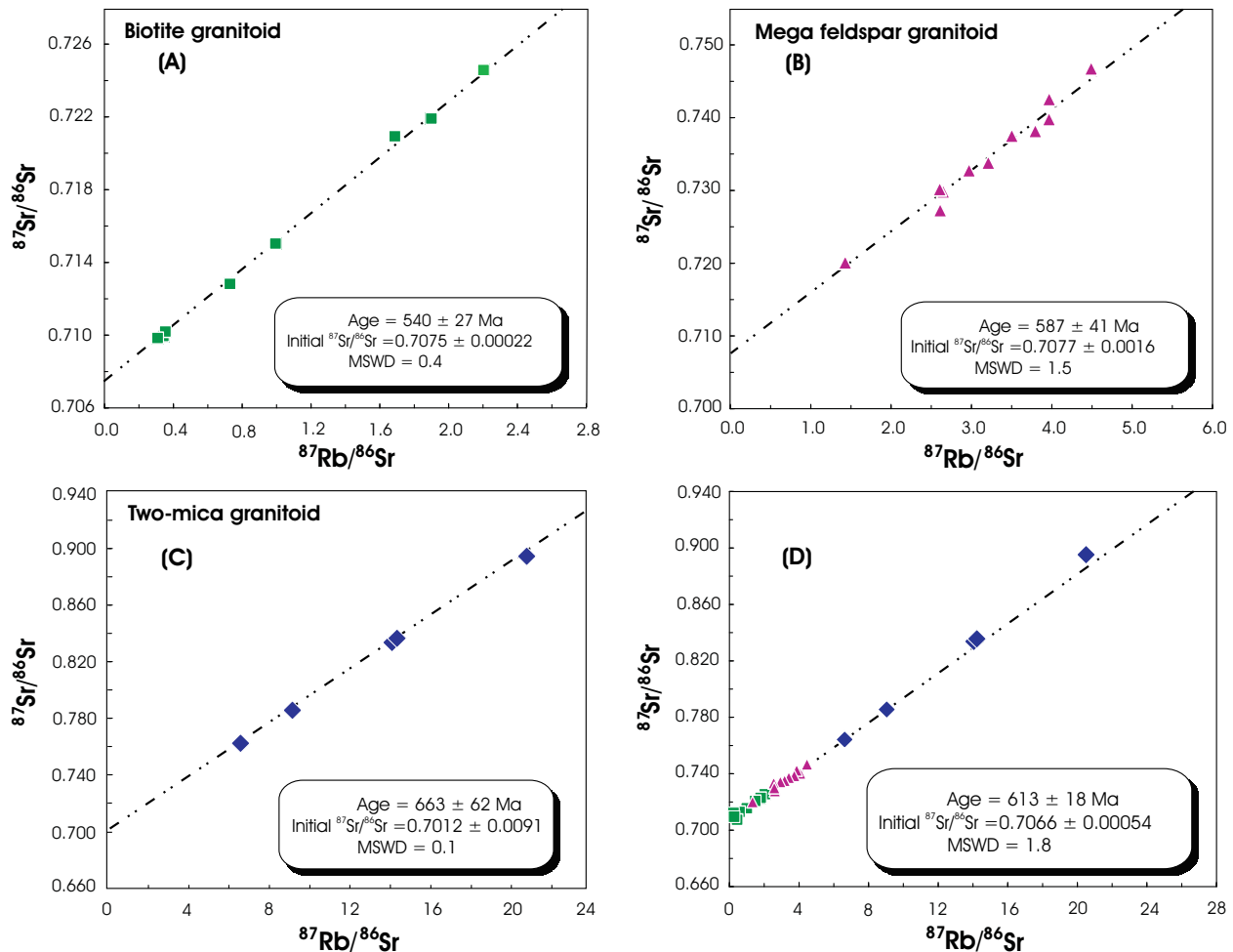


Figure 8.1: Rb–Sr whole-rock isochron diagrams for the Bafoussam granitoids. **(A)** Biotite granitoid, **(B)** Mega feldspar granitoid, **(C)** Two-mica granitoid; **(D)** All three granitoid groups together.

8.2 Samarium–Neodymium dating method

Samarium (Sm) and neodymium (Nd) belong to the light rare earth elements. Sm occurs in the nature with five isotopes, of which ^{147}Sm is radioactive. The neodymium has seven stable isotopes with ^{144}Nd being more abundant. As long as the system containing the neodymium remains closed, the amount of ^{144}Nd remains unchanged and is therefore used as stable reference isotope. The two elements are linked in a parent–daughter relationship by the alpha decay of ^{147}Sm to the stable ^{143}Nd with a half-life of 1.06×10^{11} years (Lugmair and Marti, 1978). The decay of ^{147}Sm and the production of ^{143}Nd are quantified by the equation:

$$(^{143}\text{Nd}/^{144}\text{Nd})_m = (^{143}\text{Nd}/^{144}\text{Nd})_{\text{initial}} + (^{147}\text{Sm}/^{144}\text{Nd})_m(e^{\lambda t} - 1) \quad (8.2)$$

where:

$(^{143}\text{Nd}/^{144}\text{Nd})_m =$	measured present-day isotopic ratio of the rock
$(^{143}\text{Nd}/^{144}\text{Nd})_{\text{initial}} =$	ratio of the rock at the time of its formation
$(^{147}\text{Sm}/^{144}\text{Nd})_m =$	measured present-day isotopic ratio of the rock
$\lambda =$	decay constant of ^{147}Sm having a conventional value of $6.54 \times 10^{-12} \text{ y}^{-1}$ (Lugmair and Marti, 1978).
$t =$	age of the rock in years

The age determination using the Sm–Nd method is commonly done by analyzing separated minerals or cogenetic suites of rocks whose Sm/Nd ratios vary sufficiently to define a slope of an isochron in coordinates of $^{143}\text{Nd}/^{144}\text{Nd}$ and $^{147}\text{Sm}/^{144}\text{Nd}$. The Sm–Nd isochrons are based on the same reasoning as the above Rb–Sr isochron and the geochronological statistical software package Isoplot/Ex (version 2.45) of Ludwig (2000) has been also used for the Sm–Nd age calculations of the granitoids.

The abundance of radiogenic ^{143}Nd , and hence the $^{143}\text{Nd}/^{144}\text{Nd}$ ratio of the Earth, has increased with time due to the decay of ^{147}Sm to ^{143}Nd . The evolution of the $^{143}\text{Nd}/^{144}\text{Nd}$ ratio of the Earth is referred to a model termed *Chondritic Uniform Reservoir* (CHUR; DePaolo and Wasserburg, 1976). This model assumes that total terrestrial Nd has evolved in a uniform reservoir whose Sm/Nd ratio is equal to that of the chondritic meteorites. The CHUR has a present $^{143}\text{Nd}/^{144}\text{Nd}$ ratio of 0.512638 when corrected to $^{146}\text{Nd}/^{144}\text{Nd}$ ratio of 0.7219 (^{146}Nd is one of the seven neodymium stable isotopes), and the present $^{147}\text{Sm}/^{144}\text{Nd}$ ratio of CHUR is 0.1967 (Jacobsen and Wasserburg, 1980; Faure, 1986). The $^{143}\text{Nd}/^{144}\text{Nd}$ ratio of the CHUR at any other time t in the past can be then calculated and the linear evolution of neodymium in CHUR is expressed by the equation:

$$(^{143}\text{Nd}/^{144}\text{Nd})_{\text{CHUR}}^t = (^{143}\text{Nb}/^{144}\text{Nd})_{\text{CHUR}}^0 - (^{147}\text{Sm}/^{144}\text{Nd})_{\text{CHUR}}^0 \times (e^{\lambda t} - 1) \quad (8.3)$$

where:

$(^{143}\text{Nd}/^{144}\text{Nd})_{\text{CHUR}}^t =$	isotopic ratio at any time in the past
$(^{143}\text{Nb}/^{144}\text{Nd})_{\text{CHUR}}^0 =$	isotopic ratio at present time, equal to 0.512638 (Jacobsen and Wasserburg, 1980)
$(^{147}\text{Sm}/^{144}\text{Nd})_{\text{CHUR}}^0 =$	isotopic ratio of CHUR at present time, equal to 0.1967 (Jacobsen and Wasserburg, 1980)
$\lambda =$	decay constant of ^{147}Sm equal to $6.54 \times 10^{-12} \text{ y}^{-1}$ (Lugmair and Marti, 1978)
$t =$	the age of the rock

The $^{147}\text{Sm}/^{144}\text{Nd}$ ratios of the analysed samples broadly fit into the typical range for the crust (Taylor and McLennan, 1985; Samson et al., 1990), with values of 0.088–0.126. However, two samples of the two-mica granitoid have unrealistic high $^{147}\text{Sm}/^{144}\text{Nd}$ ratios (0.162 and 0.180) possibly due to the fractional crystallization of accessory minerals such as garnet or monazite which are present in the Bafoussam two-mica granitoid. These samples having anomalously high Sm–Nd ratios ($^{147}\text{Sm}/^{144}\text{Nd} > 0.160$) have not been further considered.

As is demonstrated in the $^{143}\text{Nd}/^{144}\text{Nd}$ versus $^{147}\text{Sm}/^{144}\text{Nd}$ diagram (Fig. 7.2), the studied granitoid data do not define a straight line. The scatter of the data points and the small range in their $^{147}\text{Sm}/^{144}\text{Nd}$ ratios (Faure, 1986; DePaolo, 1988) exclude a calculation of an isochron through regression. This salient feature has already been noticed in Pan-African granitoids in the Cameroon Neoproterozoic belt (e.g., Toteu et al., 2001; Tagne-Kamga, 2003; Nzolang, 2005).

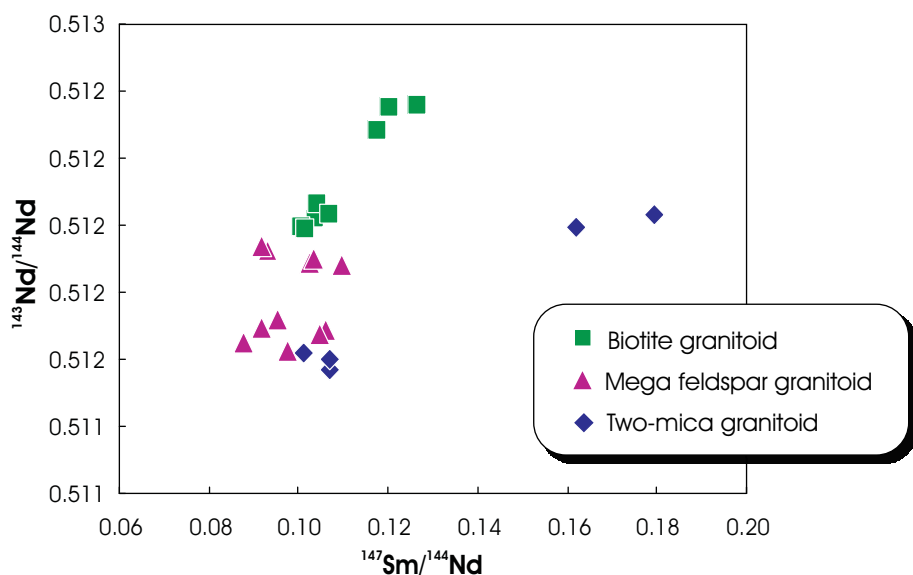


Figure 8.2: $^{143}\text{Nd}/^{144}\text{Nd}$ versus $^{147}\text{Sm}/^{144}\text{Nd}$ variation. The scatter of data points displayed does not allow for any reasonable isochron age.

8.2.1 Epsilon Nd parameter and depleted mantle model ages

DePaolo and Wasserburg (1976) introduced the *epsilon Nd parameter* (ε_{Nd}) to compare the differences between the $^{143}\text{Nd}/^{144}\text{Nd}$ ratios of rocks and the *Chondritic Uniform Reservoir* (CHUR), and to provide information about the rock genesis. The ε_{Nd} values are defined as follows:

$$\varepsilon_{\text{Nd}}^t = [(\text{Nd}^{143}/\text{Nd}^{144})_{\text{rock}}^i / (\text{Nd}^{143}/\text{Nd}^{144})_{\text{CHUR}}^t - 1] \times 10^4 \quad (8.4)$$

$$\varepsilon_{\text{Nd}}^0 = [(\text{Nd}^{143}/\text{Nd}^{144})_{\text{rock}}^m / (\text{Nd}^{143}/\text{Nd}^{144})_{\text{CHUR}}^0 - 1] \times 10^4 \quad (8.5)$$

where:

$\varepsilon_{\text{Nd}}^t$ = initial epsilon value at time t (commonly, t is the crystallization age of a rock derived from the U–Pb isotopic analysis)

$(\text{Nd}^{143}/\text{Nd}^{144})_{\text{rock}}^i$ = initial isotopic ratio of the rock at time t

$(\text{Nd}^{143}/\text{Nd}^{144})_{\text{CHUR}}^t$ = isotopic ratio of CHUR calculated for time t

$\varepsilon_{\text{Nd}}^0$ = present time epsilon value

$(\text{Nd}^{143}/\text{Nd}^{144})_{\text{rock}}^m$ = measured isotopic ratio of the rock

$(\text{Nd}^{143}/\text{Nd}^{144})_{\text{CHUR}}^0$ = isotopic ratio of the CHUR at present time, equal to 0.512638 (Jacobsen and Wasserburg, 1980)

For the Bafoussam granitoids, $\varepsilon_{\text{Nd}}^t$ was calculated at time t equal to 600 Ma [$\varepsilon_{\text{Nd}}(600)$], as this age roughly represented the time of the Pan-African metamorphism and the contemporaneous magmatism within the Cameroon Neoproterozoic belt (Toteu et al., 1994; 2001). The biotite granitoid has the highest $\varepsilon_{\text{Nd}}(600 \text{ Ma})$ values (0.2 to –6.3), followed by the mega feldspar granitoid (–5.6 to –12.1) and the two-mica granitoid (–9.9 to –14.0). Such a large negative range of $\varepsilon_{\text{Nd}}(600 \text{ Ma})$ is in good agreement with a magma derived from enriched mantle or a crustal source, which has a lower Sm/Nd ratio compared to that of CHUR (Clarke et al., 1988; Rollinson, 1993). Two samples of the biotite granitoid show near-chondritic $\varepsilon_{\text{Nd}}(600 \text{ Ma})$ values of 0.2 and –0.1, indicating their relative juvenile rather than recycled character. The generally negative and broad range of initial $\varepsilon_{\text{Nd}}(600 \text{ Ma})$ values of the Bafoussam granitoids point to their long crustal evolution. The $\varepsilon_{\text{Nd}}(600 \text{ Ma})$ and the $\varepsilon_{\text{Nd}}(0)$ values for individual samples are given in Table A.4.2 in the appendix A.4.

The depleted mantle Nd model age (T_{DM}) was introduced by DePaolo (1981) and is taken to reflect the time elapsed since a rock sample or more precisely its Nd, was extracted from the depleted mantle reservoir, assuming that the Sm/Nd ratio of the sample has not been modified by fractionation after its separation from the mantle source. The depleted mantle is attributed to the paucity of Nd, hence to an elevated Sm/Nd ratio in the mantle over time since it is continuously sampled by the crust. The T_{DM} is a powerful method for estimation of the crust formation age for igneous rocks (Rollinson, 1993) and it is obtained by the follows expression:

$$T_{\text{DM}} = 1/\lambda \times \ln \{ [(\text{Nd}^{143}/\text{Nd}^{144})_{\text{rock}}^m - (\text{Nd}^{143}/\text{Nd}^{144})_{\text{DM}}^0] / [(\text{Sm}^{147}/\text{Nd}^{144})_{\text{rock}}^m - (\text{Sm}^{147}/\text{Nd}^{144})_{\text{DM}}^0] + 1 \} \quad (8.6)$$

where:

$$\begin{aligned}\lambda &= \text{decay constant for } {}^{147}\text{Sm to } {}^{143}\text{Nd, equal to } 6.54 \times 10^{-12} \text{ yr}^{-1} \\ (\frac{{}^{143}\text{Nd}}{{}^{144}\text{Nd}})^m_{\text{rock}} &= \text{measured isotopic ratio of the rock} \\ (\frac{{}^{143}\text{Nd}}{{}^{144}\text{Nd}})^0_{\text{DM}} &= \text{isotopic ratio of depleted mantle (DM) at present time equal to } 0.513114 \text{ (Michard et al., 1985)} \\ (\frac{{}^{147}\text{Sm}}{{}^{144}\text{Nd}})^m_{\text{rock}} &= \text{measured isotopic ratio of the rock} \\ (\frac{{}^{147}\text{Sm}}{{}^{144}\text{Nd}})^0_{\text{DM}} &= \text{isotopic ratio of depleted mantle at present time equal to } 0.222 \text{ (Michard et al., 1985)}\end{aligned}$$

The calculated T_{DM} ages of the Bafoussam granitoids are presented in Table A.4.2 in the Appendix A.4. The biotite granitoid yields the younger T_{DM} ages ranging from 1.3 to 1.6 Ga than the mega feldspar granitoid and two-mica granitoid with T_{DM} ages of 1.5–2.1 Ga and 2.1–2.3 Ga, respectively. As expected, the two samples of two-mica granitoid with anomalous high ${}^{147}\text{Sm}-{}^{144}\text{Nd}$ ratios give erroneous T_{DM} ages (3.4 and 4.9 Ga). These samples could be explained by "two-stage" evolution model. The $\varepsilon_{\text{Nd}}(600 \text{ Ma})$ versus age (Ga) diagram (Fig. 8.3) portrays the evolution lines of the Bafoussam granitoids and the corresponding model ages. None of the analyzed granitoids exhibits mean crustal residence (T_{DM}) ages close to their obtained emplacement ages through Rb–Sr dating method, suggesting that they are predominately crustal melts derived from anatexis of Meso- to Paleoproterozoic crust. The degree of reworked Proterozoic and possibly a juvenile mantle-derived component may vary considerably.

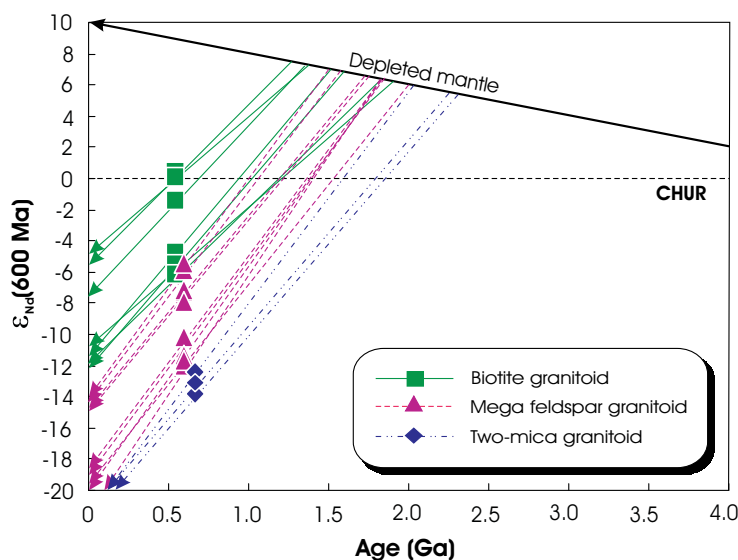


Figure 8.3: Initial $\varepsilon_{\text{Nd}}(600 \text{ Ma})$ as a function of age diagram showing the evolution of the Bafoussam granitoids and their probable sources, the evolution of the undifferentiated Earth (CHUR: DePaolo and Wasserburg, 1976) and depleted mantle (DM: Goldstein et al., 1984). The diagram also shows the evolution trends of the individual samples.

8.3 Combined Nd - and Sr -isotopes and geodynamic implications

DePaolo and Wasserburg (1976) have demonstrated that the $^{143}\text{Nd}/^{144}\text{Nd}$ and $^{87}\text{Sr}/^{86}\text{Sr}$ of young oceanic basalts (e.g., along mid-ocean ridges, on oceanic islands) form a strong correlation array, the "Mantle array". This was the basis for the introduction of an $^{87}\text{Sr}/^{86}\text{Sr}$ ratio for the bulk earth complementary to the Nd data. The evolution of the $^{87}\text{Sr}/^{86}\text{Sr}$ ratios of the earth is named *Uniform Reservoir* (UR: DePaolo and Wasserburg, 1976), the present value of which is 0.7045 (Faure, 1986). The Sr epsilon parameter (ϵ_{Sr}) similar to that defined for Nd is expressed as follows:

$$\epsilon^t_{\text{Sr}} = [({}^{87}\text{Sr}/{}^{86}\text{Sr})_{\text{rock}}^i / ({}^{87}\text{Sr}/{}^{86}\text{Sr})_{\text{UR}}^t - 1] \times 10^4 \quad (8.7)$$

$$\epsilon^0_{\text{Sr}} = [({}^{87}\text{Sr}/{}^{86}\text{Sr})_{\text{rock}}^m / ({}^{87}\text{Sr}/{}^{86}\text{Sr})_{\text{UR}}^0 - 1] \times 10^4 \quad (8.8)$$

where:

$\epsilon^t_{\text{Sr}} =$ initial epsilon value at time t (commonly, t is the crystallization age of a rock derived from the U–Pb isotopic analysis)

$({}^{87}\text{Sr}/{}^{86}\text{Sr})_{\text{rock}}^i =$ initial isotopic ratio of the rock at time t

$({}^{87}\text{Sr}/{}^{86}\text{Sr})_{\text{UR}}^t =$ isotopic ratio of the *Uniform Reservoir* (UR) calculated for time t

$\epsilon^0_{\text{Sr}} =$ present time epsilon value

$({}^{87}\text{Sr}/{}^{86}\text{Sr})_{\text{rock}}^m =$ measured isotopic ratio of the rock

$({}^{87}\text{Sr}/{}^{86}\text{Sr})_{\text{UR}}^0 =$ isotopic ratio of UR at present time taken equal to 0.7045 (Faure, 1986)

Like the Nd epsilon parameter, the ϵ^t_{Sr} of the Bafoussam granitoid was calculated for a time t equal to 600 Ma [$\epsilon_{\text{Sr}}(600)$]. The Bafoussam granitoids display positive $\epsilon_{\text{Sr}}(600 \text{ Ma})$ values, ranging between 26–52 in the biotite granitoid, 16–68 in the mega feldspar granitoid and 55–229 in the two-mica granitoid. The $\epsilon_{\text{Sr}}(600 \text{ Ma})$ and the calculated $\epsilon_{\text{Sr}}(0)$ values for each analysed sample are reported in Table A.4.1 in the Appendix A.4. In igneous rocks, a moderate to high positive value of $\epsilon_{\text{Sr}}(600 \text{ Ma})$ argues for a magma source with a higher Rb–Sr than UR, an enriched mantle or a crustal source (Rollinson, 1993). Typical continental crustal rocks have lower Sm/Nd ratio and hence the $^{143}\text{Nd}/^{144}\text{Nd}$ ratios (negative ϵ_{Nd} values) than those derived from the upper mantle. As a consequence, combined Nd–Sr isotopic studies possibly provide a powerful tracer for contamination of parent magmas by continental crust rocks.

8.3.1 Two components mixing and assimilation – AFC process

Geological activity that involves two component mixtures having different isotopic and element compositions gives a hyperbolic curve in a diagram of initial isotopic ratios against the element concentration of the same element, or a straight line when the element concentration is substituted by 1/element concentration (e.g., $1/\text{Sr}$, $1/\text{Nd}$; Faure, 1986: 1998). Therefore, the compositional variation of the Bafoussam I-type granitoids through a possibly contamination of their parent magma by crustal component can be evaluated. In $^{87}\text{Sr}/^{86}\text{Sr}_{(600 \text{ Ma})}$ versus Sr (ppm) plot (Fig. 8.4A), the data points of the biotite granitoid and mega feldspar granitoid does not show any hyperbolic curvilinear trend. The lack of a distinct curve suggests that the mixing process has no or little influence during the genesis and evolution of the I-type granitoids.

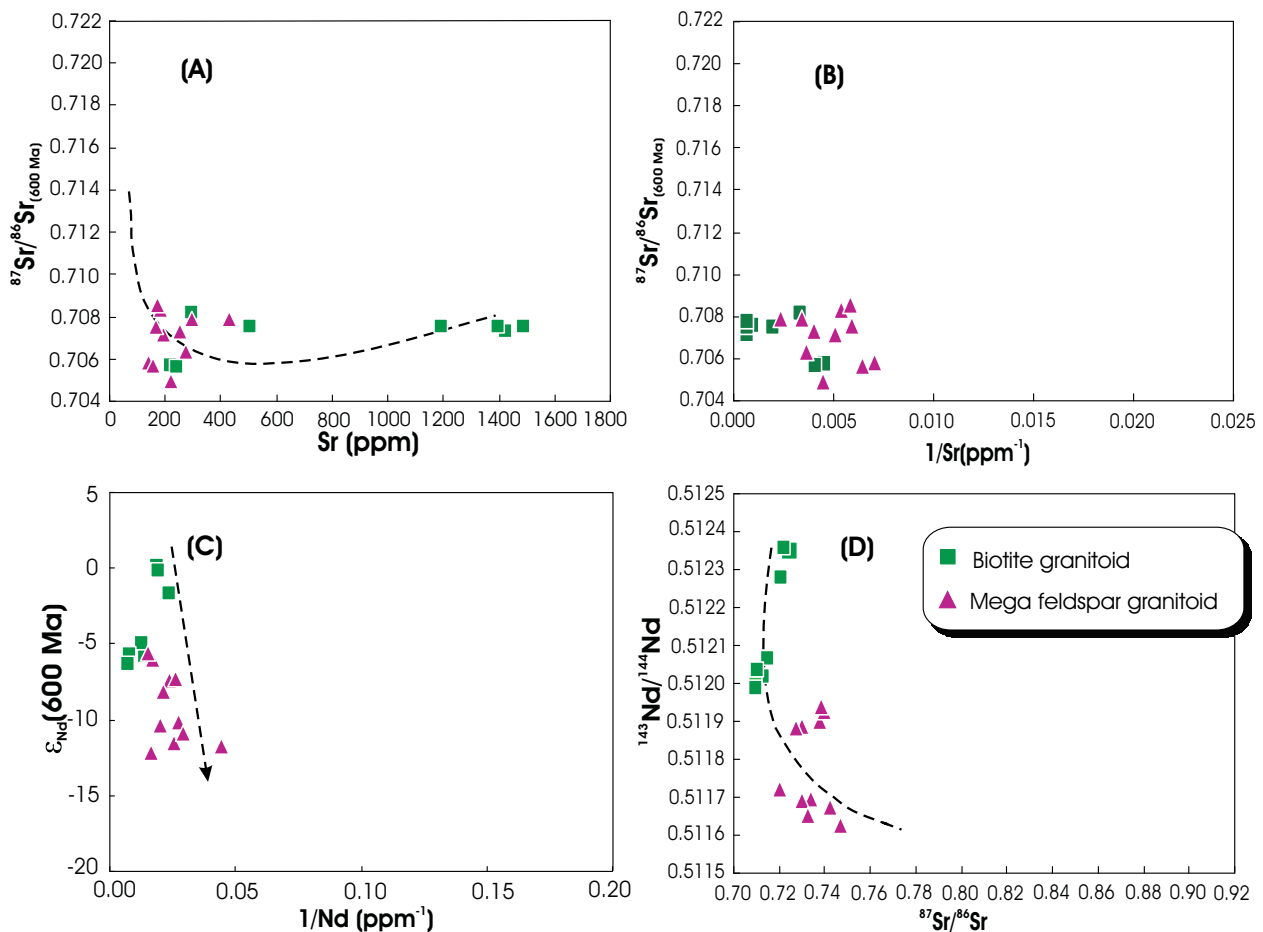


Figure 8.4: Check of a possible binary mixing process involving the Bafoussam granitoids: (A) Plot of $^{87}\text{Sr}/^{86}\text{Sr}_{(600 \text{ Ma})}$ versus Sr abundances (ppm) lacking a clear mixing hyperbolic pattern. (B) Initial $^{87}\text{Sr}/^{86}\text{Sr}_{(600 \text{ Ma})}$ versus $1/\text{Sr}(\text{ppm}^{-1})$ and (C) $\varepsilon_{\text{Nd}}(600 \text{ Ma})$ versus $1/\text{Nd}(\text{ppm}^{-1})$ displaying an approximately rectilinear mixing trend. (D) $^{143}\text{Nd}/^{144}\text{Nd}$ versus $^{87}\text{Sr}/^{86}\text{Sr}$ present day values.

This is supported by the absence of well-developed mixing rectilinear trend in the $^{87}\text{Sr}/^{86}\text{Sr}_{(600 \text{ Ma})}$ versus $1/\text{Sr} (\text{ppm}^{-1})$ and $\epsilon_{\text{Nd}}(600 \text{ Ma})$ versus $1/\text{Nd} (\text{ppm}^{-1})$ plots (Fig. 8.4B, C). Moreover, Sr–Nd isotopic mixture is not displayed by the $^{143}\text{Nd}/^{144}\text{Nd}$ versus $^{87}\text{Sr}/^{86}\text{Sr}$ diagram where the data points do not also manifestly define the standard hyperbolic curve trend (Fig. 8.4D).

Assimilation and combined fractional crystallization (AFC–process) of magma has been recognized as being a common petrogenesis process of calc-alkaline magma series (DePaolo, 1981; Roberts and Clemens, 1995). Plots of $^{87}\text{Sr}/^{86}\text{Sr}_{(600 \text{ Ma})}$ ratios and $\epsilon_{\text{Nd}}(600 \text{ Ma})$ against SiO_2 abundances have been emphasized for identification of an assimilation–AFC character (Stosch, 2001). Generally, assimilation–AFC process involving a parent magma and crustal contaminant of different isotopic compositions is reflected in a positive correlation trend between initial $^{87}\text{Sr}/^{86}\text{Sr}_{(600 \text{ Ma})}$ and SiO_2 and in contrast, negative correlation between $\epsilon_{\text{Nd}}(600 \text{ Ma})$ and SiO_2 .

In the plot of $^{87}\text{Sr}/^{86}\text{Sr}_{(600 \text{ Ma})}$ versus SiO_2 (wt. %), the I-type granitoids exhibit no considerable change in initial $^{87}\text{Sr}/^{86}\text{Sr}_{(600 \text{ Ma})}$ with increasing SiO_2 (Fig. 8.5A). In the $\epsilon_{\text{Nd}}(600 \text{ Ma})$ versus SiO_2 diagram on the other hand, the granitoid samples do not defined a continuous negative trend. The data points form two distinct groups: (1) high $\epsilon_{\text{Nd}}(600 \text{ Ma})$ which increase with increasing SiO_2 for the biotite granitoid; and (2) low initial $\epsilon_{\text{Nd}}(600 \text{ Ma})$ for the mega feldspar granitoid which exhibits almost constant SiO_2 concentrations (Fig. 8.5B).

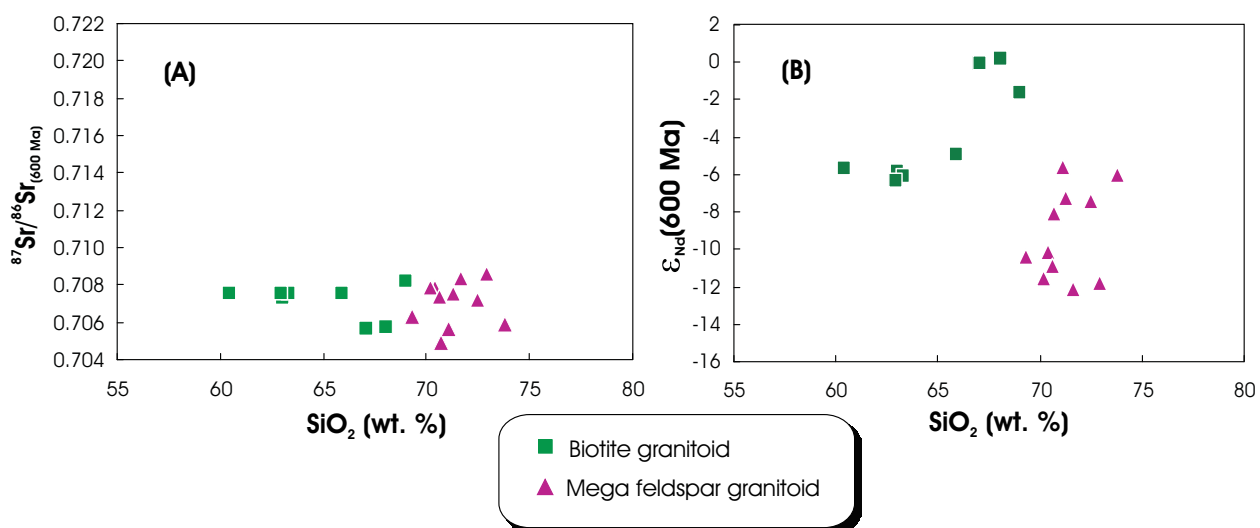


Figure 8.5: Check of a possible assimilation–AFC process involving the Bafoussam granitoids. **(A)** $^{87}\text{Sr}/^{86}\text{Sr}_{(600 \text{ Ma})}$ versus SiO_2 (wt. %) and **(B)** $\epsilon_{\text{Nd}}(600 \text{ Ma})$ versus SiO_2 (wt. %), in both diagrams no assimilation trend is defined.

This indicates that the genesis of the I-type granitoids seem to have not been governed by the assimilation–AFC process.

The plot of $\varepsilon_{\text{Nd}}(600 \text{ Ma})$ versus $\varepsilon_{\text{Sr}}(600 \text{ Ma})$ can also be used for I- and S- type granites classification, and further for identification of petrogenetic processes involving both crustal and mantle contribution as suggested by McCulloch and Chappell (1982). In this isotope correlation diagram (Fig. 8.6), the data of the Bafoussam granitoids are grouped in two separated fields in the lower right quadrant of the diagram. The two fields represent the I-type granitoids field, including the biotite granitoid and the mega feldspar granitoid, while the two-mica granitoid refers to the field of S-type granitoid. This separation is consistent with that mentioned from their mineralogical and chemical characteristics. The studied granitoid fields are distinct from the fields of I- and S- type granites from the Lachan Fold Belt, SE Australia (McCulloch and Chappell, 1982).

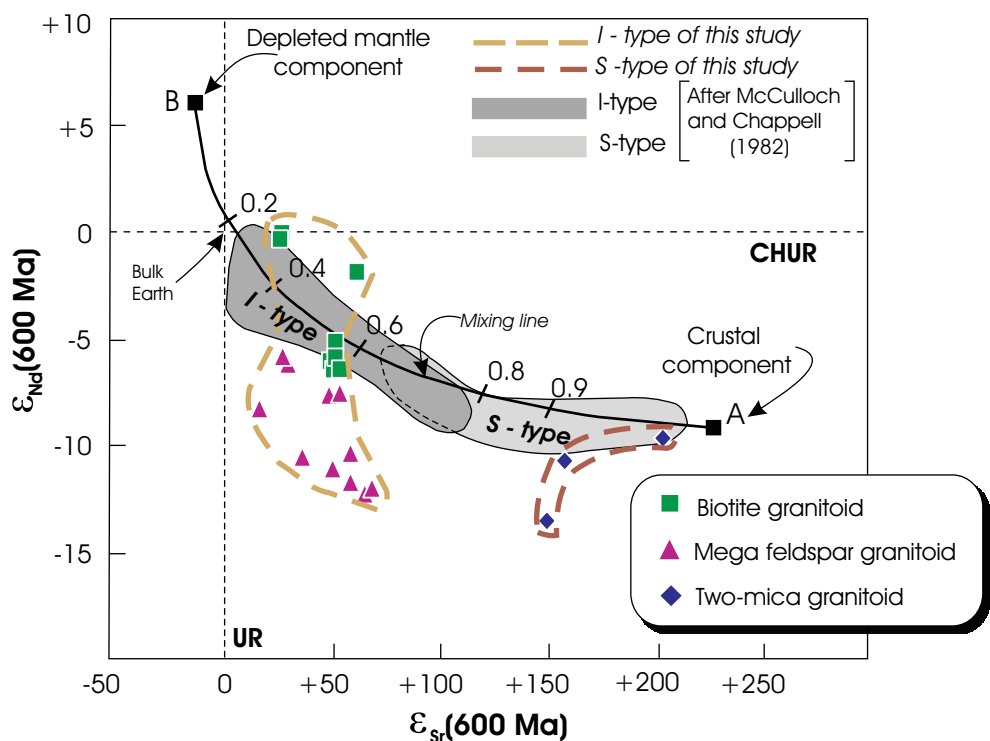


Figure 8.6: $\varepsilon_{\text{Nd}}(600 \text{ Ma})$ versus $\varepsilon_{\text{Sr}}(600 \text{ Ma})$ diagram showing the distribution of the Bafoussam granitoids relative to I- and S- type granites from Australia (McCulloch and Chappell, 1982). A mixing line between depleted mantle component and crustal component does really fit the Bafoussam granitoids array. CHUR: Chondritic Uniform Reservoir, UR: Uniform Reservoir.

The granitoids have in part lower $\epsilon_{\text{Nd}}(600 \text{ Ma})$ values. Consequently, they do not fit the mixing curve trend from crustal values toward positive $\epsilon_{\text{Nd}}(600 \text{ Ma})$ and low initial $^{87}\text{Sr}/^{86}\text{Sr}$ (600 Ma) pointing to the involvement of a depleted mantle component as documented by the I- and S-type granites of the Lachlan Fold Belt.

In the $\epsilon_{\text{Nd}}(600 \text{ Ma})$ versus $^{87}\text{Sr}/^{86}\text{Sr}_{(600 \text{ Ma})}$ diagram (Fig. 8.7), the biotite granitoid and the mega feldspar granitoid plot on the continuation of the mantle array with slightly shift to the right side of the mantle array, far away from the fields for the lower continental crust (LCC) and the upper continental crust (UCC). The shift of some data points from the mantle array suggests a slight contamination by UCC during the magma ascent. For the two-mica granitoid, the data points plot near and on the UCC field, pointing to their crustal genesis.

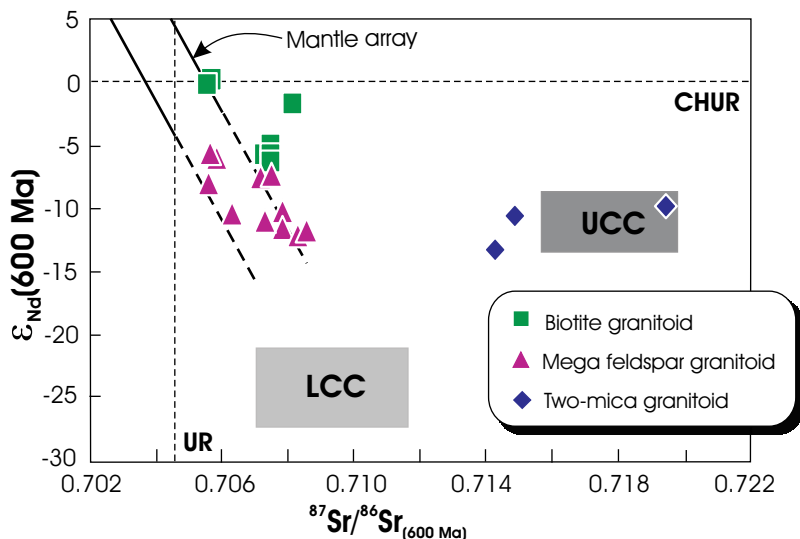


Figure 8.7: $\epsilon_{\text{Nd}}(600 \text{ Ma})$ versus $^{87}\text{Sr}/^{86}\text{Sr}_{(600 \text{ Ma})}$ variation for the Bafoussam granitoids. Isotopic composition fields of the lower continental crust (LCC) and upper continental crust (UCC) are from DePaolo and Wasserburg (1979), Rollinson (1993). CHUR: Chondritic Uniform Reservoir, UR: Uniform Reservoir

The initial $^{87}\text{Sr}/^{86}\text{Sr}$ versus age (Ma) evolution lines in the frame of depleted mantle, enriched mantle and continental crust are illustrated in Figure 8.8. The entire investigated granitoids plot between the enriched mantle and the continental crust, except one sample of two-mica granitoid which falls above the continental crust evolution line. The strontium evolution lines are not parallel to the enriched mantle and increase steeply from biotite granitoid, mega feldspar granitoid to two-mica granitoid. This reflects an enriched mantle source for the parent magmas of the Bafoussam granitoids that has been variably influenced by continental crust of

different initial $^{87}\text{Sr}/^{86}\text{Sr}$ with the crustal material being more pronounced in two-mica granitoid (Rollinson, 1993; Schulz et al., 2004).

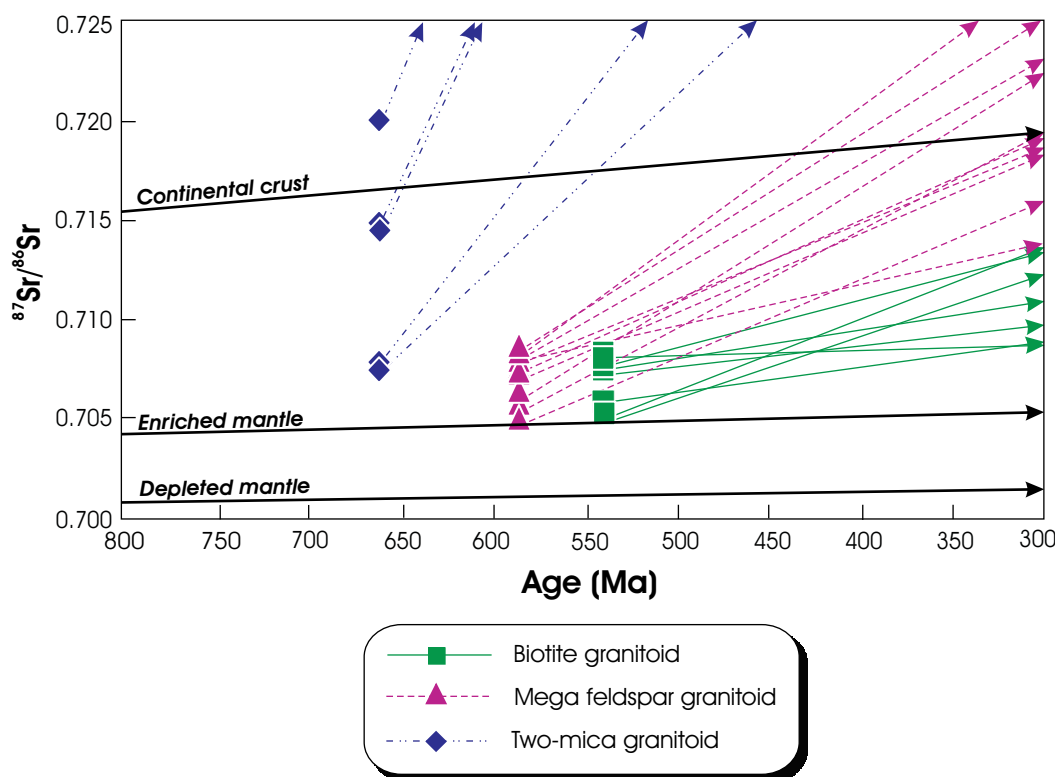


Figure 8.8: Initial $^{87}\text{Sr}/^{86}\text{Sr}$ versus age diagram showing the evolution of the Bafoussam granitoids. Depleted mantle, enriched mantle and continental crust growth curve are after Rollinson (1993). Evolution trends of individual samples are also shown. The arrows point to the measured present day $^{87}\text{Sr}/^{86}\text{Sr}$ values.

In summary, the biotite granitoid and the mega feldspar granitoid yield whole rock Rb–Sr isochron ages of 540 ± 27 Ma and 587 ± 41 Ma, respectively. These ages fit with range of the emplacement age of the Pan-African plutonic rocks in West Cameroon (650–530 Ma: see Table 9.1) and are considered as representing emplacement ages of the granitoids. The Rb–Sr whole-rock isochron age of 663 ± 62 Ma is reported for the two-mica granitoid. This age is older than the emplacement ages obtained for other peraluminous granitoids documented in the Cameroon Neoproterozoic belt. In East Cameroon, the leucogranites yielded Rb–Sr whole-rock isochron emplacement ages of 614 ± 41 Ma and 621 ± 15 M (Soba et al., 1991). Emplacement CHIME ages of 530 ± 9 Ma and 510 ± 25 Ma have been reported for the two-mica granitoid and magnetite-bearing two-mica granitoid from the Nkambe area (West Cameroon: Tetsopgang, 2003). The older age of the studied two-mica granitoid could be explained by the presence of inherited Rb/Sr isotopic ratio. This is also suggested by the very steep evolution lines of some

two-mica granitoid samples in the Figure 8.8. The 663 ± 62 Ma isochron age reported for the two-mica granitoid is thus regarded as a mixing age and is hence meaningless. Nzolang (2005) obtained a cooling Rb–Sr biotite whole-rock isochron age of 536 ± 2 Ma for the Bantoum leucogranite, neighbouring of the Bafoussam area. The contamination process expressed by magma mixing or assimilation–AFC seems to have not affected the parent magma of the I-type granitoids. The Nd–Sr isotopic data of the investigated granitoids are suggestive of their heterogeneous sources as highlighted by the general data point dispersion. The depleted mantle Nd model age (T_{DM}) ranging between 1.5 and 2.3 Ga indicate that older, pre-Pan-African (Eburnian) crustal material played an important role in the generation and evolution of the granitoid melts. The T_{DM} range for the Bafoussam granitoids well matches the presence of remnants of Paleoproterozoic rocks within the Neoproterozoic belt of Cameroon (Penaye et al., 1993; 2004; Toteu et al., 2001).

9 DISCUSSION AND CONCLUSIONS

9.1 Granitoids origin and petrogenesis

The mineralogical and geochemical features summarized in Table 7.1 indicate that the biotite granitoid, deformed biotite granitoid and mega feldspar granitoid are essentially of I-type, whereas the two-mica granitoid displays characteristics of S-type granites. In the absence of direct source rock indicators (e.g., xenoliths), the determination of magma source or protolith composition has to be largely based on indirect geochemical and isotopic constraints.

9.1.1 I-type granitoids

The close similarity of the different I-type granitoids (biotite granitoid, deformed biotite granitoid and mega feldspar granitoid) including their alkali-calcic, high-K calc-alkaline, ferriferous and metaluminous to peraluminous affinities (Figs. 7.6–7.9) suggest that these granitoids were generated by similar processes from a common source. Moreover, the curvilinear trend displayed by the studied I-type granitoids on the $\text{Al}_2\text{O}_3/\text{TiO}_2$ versus TiO_2 diagram (Fig. 9.1A), is consistent with a cogenetic relationship between the granitoids (Garcia et al. 1994).

Partial melting of pre-existing igneous or meta-igneous rocks in the crust is generally assumed for the genesis of the I-type granitoids (Chappell and White, 1974: 1992: 2001; Chappell and Stephens, 1988). Since the studied I-type granitoids have high-K and calc-alkaline nature, the most suitable protoliths could be ancient volcanic rocks that consist of amphibolitized calc-alkaline to high-K calc-alkaline basaltic andesites and andesitic metagreywackes, according to Robert and Clemens (1993). On the other hand, the geochemistry and the mineralogy of the resulting granitic rocks reflect not only the nature of the protoliths from which they were derived, but also the dynamic conditions under which magmas were formed, evolved and eventually solidified (Roberts et al., 2000; Altherr et al., 2000).

With regard to the source rocks, the plot of molar $\text{CaO}/(\text{MgO} + \text{FeO}_t)$ versus molar $\text{Al}_2\text{O}_3/(\text{MgO} + \text{FeO}_t)$ after Altherr et al. (2000) (Fig. 9.1) illustrates the fields of different compositional melts obtained by experimental partial melting of different sources rocks, such as

amphibolites, tonalitic gneisses, metagreywackes and metapelites, under variable melting conditions. For comparison, the average I-type granite compositions from the Lachan Fold Belt, SE Australia (Chappell and White, 1992), European Variscides (Altherr et al. 2000), and the neighboured complexes Ngondo, Batié and Fomopéa (Tagne-Kamga, 1994; 2003; Talla, 1995; Kwékam, 1993) are also plotted.

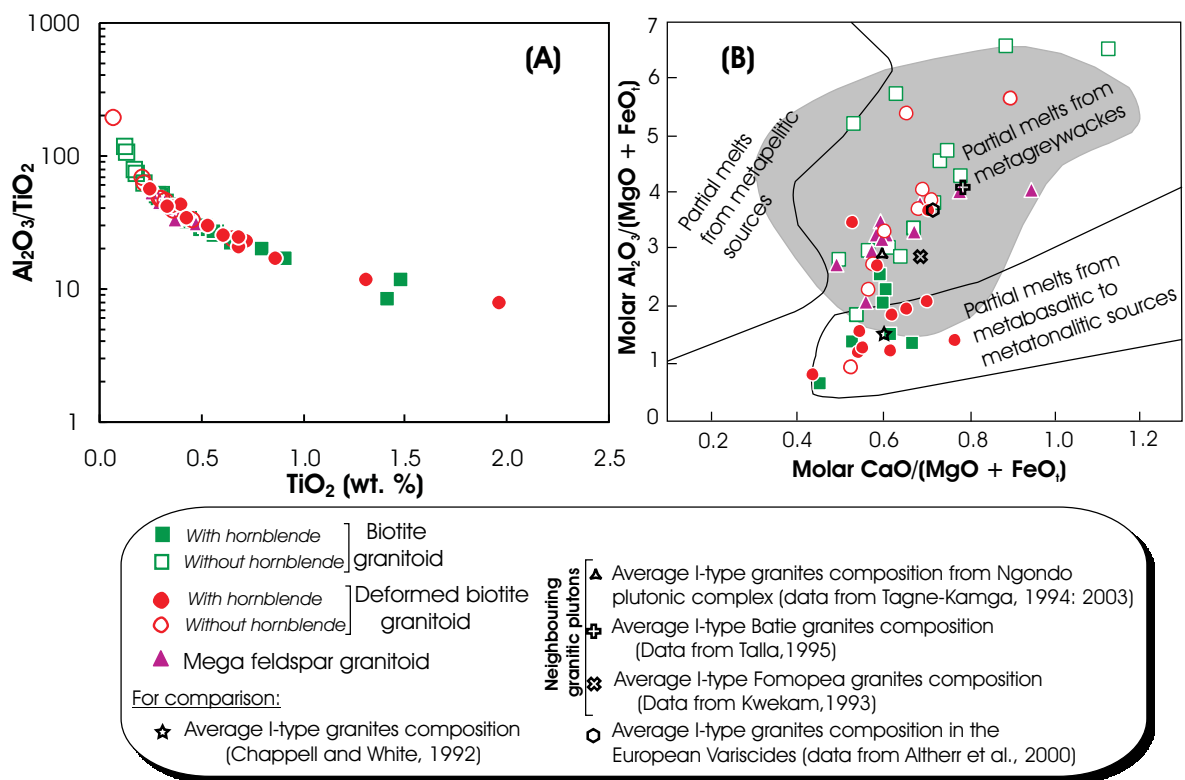


Figure 9.1: (A) $\text{Al}_2\text{O}_3/\text{TiO}_2$ versus TiO_2 diagram (after Garcia et al., 1994) for the investigated I-type granitoids showing one curvilinear trend for all types typical of magmatic differentiation. (B) Molar $\text{CaO}/(\text{MgO} + \text{FeO}_t)$ versus molar $\text{Al}_2\text{O}_3/(\text{MgO} + \text{FeO}_t)$ plot showing the compositions of the Bafoussam I-type granitoids compared to partial melts produced by experimental dehydration melting of various rock compositions (fields of melt compositions compiled by Altherr et al., 2000).

As shown in Figure 9.1B, the geochemical characteristics of the majority of the studied I-type granitoids are more compatible with an origin from metasedimentary rocks (metagreywackes), with, however, a few samples being most likely derived from melting of metabasaltic to metatonalitic (i.e. metaigneous) source rocks like the average for I-type granites from the Lachan Fold Belt (LFB: Chappell and White, 1992). This suggests the presence of a sedimentary component either in their source, or incorporated at later stage by the granitoid magma. On the basis of their geochemical compositions, the studied I-type granitoids could have been generated

by mixing of mantle-derived material with varying amounts of the melted crustal components (metasediments) through assimilation and combined fractional crystallization (AFC–De Paolo, 1981).

It is commonly accepted that the most important evidence for the granitic magma sources is given by the radiogenic isotopes (Rb–Sr and Sm–Nd). The initial $^{87}\text{Sr}/^{86}\text{Sr}_{(600\text{ Ma})}$ ratios range between 0.706–0.708 for the biotite granitoid and 0.705–0.709 for the mega feldspar granitoid (Table A.4.1, Appendix A.4). They are significantly higher than the mantle value (0.704 ± 0.002 ; Goldstein, 1988) and the initial $^{87}\text{Sr}/^{86}\text{Sr}$ range of 0.704–0.706, assumed for typical I-type granites (Table 7.1; Chappell and White, 2001). The high initial $^{87}\text{Sr}/^{86}\text{Sr}_{(600\text{ Ma})}$ ratios suggest incorporation of material derived from an older crustal source. The $\epsilon_{\text{Nd}}(600\text{ Ma})$ values (0.2 to –12.1, mainly < 0) and the T_{DM} model ages (1.3–2.1 Ga) of the I-type granitoids are compatible with the melting of ancient crust having higher Rb/Sr. Like the geochemical signatures, the Nd–Sr isotope data suggest a mixture of the mantle-component with significant crust input from melted metasediments during the genesis of the I-type granitoids.

The metaluminous nature of the studied I-type granitoids suggests a metaluminous protolith such as the mantle or other sources (volcanic or plutonic). The protolith would not have undergone alteration, because hydrothermal or meteoric alteration would increase the aluminum saturation index, ASI ratio [$\text{ASI} = \text{molar Al}_2\text{O}_3/(\text{CaO} + \text{Na}_2\text{O} + \text{K}_2\text{O})$]. The high potassic concentrations of the granitoids could result from accumulation of K-bearing silicates such as biotite and K-feldspar. According to Singh and Johannes (1996), the intermediate to felsic composition of the granitoids is consistent with a derivation from the ancient source of tonalitic to granodioritic composition. The studied I-type granitoids exhibit a transitional character between metaluminous and moderately peraluminous (Fig. 7.9 A and B). The samples with rather peraluminous composition are qualified to be more fractionated than the other of metaluminous nature. They are believed to result largely from the fractional crystallization of originally metaluminous melt (Zen, 1986; Chappell and Stephens, 1988; Chappell, 1999). Direct evidence for this includes: (1) the wide range of composition (56.9–73.8 wt. % SiO_2); (2) the curved trend, typical of magmatic differentiation (Fig. 9.1A); and (3) the compositional variations of the I-type granitoids on Harker diagrams (Figs. 7.1 and 7.10). The field characteristics of these granitoids, including the rare occurrence of mafic and intermediate

enclaves, the absence of evidence for significant interaction with the migmatitic gneiss country rock, the similarities in the petrographic and geochemical nature of each type and the gradational transition between the different varieties of the I-type granitoids, do not privilege the hypothesis that magma mixing or wall-rock assimilation was dominant process in their magmatic evolution (Figs. 8.4 and 8.5). Furthermore, it appears unlikely that restite-melt unmixing as suggested by Chappell et al. (1987) has controlled the chemical variation of these granitoids. Except for a few mafic enclaves (amphibole-bearing and metagabbro) encountered within the biotite granitoid and the deformed biotite granitoid, other evidences that characterized the restite model of Chappell et al. (1987) such as calcic cores of plagioclase, pyroxene inclusion in plagioclase crystals and pyroxene cores in hornblende crystals are not observed in the studied I-type granitoids. Also, the curved trend portrayed by the Figure 9.1 cannot be produced by restite separation (Garcia et al., 1994). Hence, fractional crystallization (Figs. 7.20 and 7.21) was the dominant processes that governed the composition of these granitoids.

To summarize, the Bafoussam I-type granitoids were generated by the same magma-parent that likely derived from the partial melting of a tonalite–granodiorite source. The compositional variation of these granitoids is dominantly caused by fractional crystallization processes.

9.1.2 Two-mica granitoid

9.1.2.1 The peraluminous composition of the two-mica granitoid

Patiño Douce (1999) distinguished three main groups of peraluminous granites: (1) peraluminous leucocratic granites, (2) strongly peraluminous S-type, and (3) Cordilleran peraluminous two-mica granites. The compositional fields of these groups are shown in Figure 9.2A. In this Figure, the average compositions of S-type granites from LFB (Chappell and White, 1992), the two-mica leucogranites from French Massif Central (Williamson et al. 1996), the Himalayan leucogranites (Langtang Valley, Nepal: Inger and Harris, 1993), the garnet-bearing S-type granites from the Damara orogen (Namibia: Jung et al., 2001), and the Bantoum leucogranites and Nkambé two-mica granitoids from Cameroon Neoproterozoic orogenic belt (Nzolang et al., 2003: 2005; Tetsopgang, 2003) are also indicated for comparison. The studied

two-mica granitoid occupies the field of peraluminous leucocratic granites (Fig. 9.2A) and compares to the average compositions of the Bantoum leucogranites and the two-mica leucogranites from French Massif Central. Peraluminous leucocratic granites include two-mica and muscovite-garnet granites and do not contain low-pressure, high-temperature mafic aluminous minerals (e.g., cordierite, sillimanite) and other low-temperature aluminosilicates (e.g., tourmaline, andalousite), which are characteristic of strongly peraluminous S-type granites (Miller et al., 1985; Villaseca et al., 1998). The two-mica granitoid under study is high-K and calc-alkaline (Fig. 7.7B), like the peraluminous leucogranites from typical plutons (e.g., Vidal et al., 1984; Chappell and White, 1992; Nabelek et al., 1992; Inger and Harris, 1993; Williamson et al., 1996).

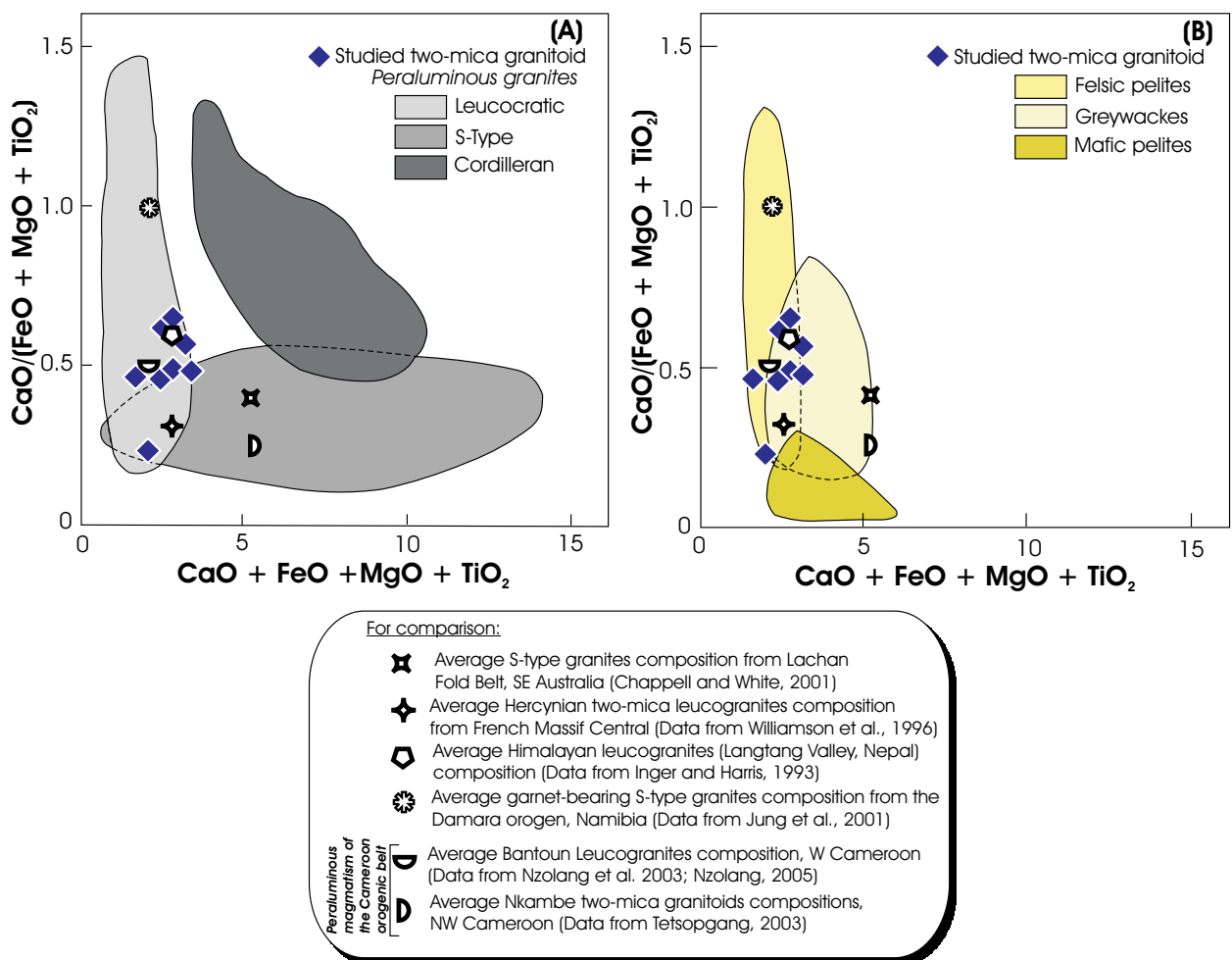


Figure 9.2: $\text{CaO}/(\text{FeO} + \text{MgO} + \text{TiO}_2)$ versus $\text{CaO} + \text{FeO} + \text{MgO} + \text{TiO}_2$ plots showing the composition of the Bafoussam two-mica granitoid compared to (A) the fields of the three peraluminous granites types (fields contours are drawn according to the data of Patiño Douce, 1999); and to (B) the composition of melts obtained in experimental dehydration melting of metasedimentary rocks (fields of melt compositions after Patiño Douce, 1999).

Based on these significant similarities in geological, mineralogical and geochemical signatures, the Bafoussam two-mica granitoid is considered to be a peraluminous leucocratic granitoid or leucogranite.

9.1.2.2 Possible source of the two-mica granitoid magma

Peraluminous leucogranites or "S-type granites" are considered to have originated from supracrustal melting of purely or predominantly upper crustal components (metasedimentary protoliths), according to Chappell and White (1974: 1992: 2001) and White and Chappell (1988). Several models of formation have been proposed for the peraluminous leucogranites. The three most important are: (1) melting of metapelites and metagreywackes, including cases of basalt magma admixture (White and Chappell, 1988; Sylvester, 1998; Patiño Douce, 1999); (2) partial melting of tonalite and granodiorite at pressures ≥ 8 kbar with clinopyroxene in the restite (Miller, 1985; Patiño Douce, 1997: 1999); and (3) evolution of relatively primitive low-Ca metaluminous granites by fractionation of amphibole (Bonin et al., 1998).

Some petrogenetic information can be obtained using the diagram $\text{CaO}/(\text{FeO} + \text{MgO} + \text{TiO}_2)$ versus $\text{CaO} + \text{FeO} + \text{MgO} + \text{TiO}_2$ of Patiño Douce (1999) which illustrated the correlation of the granite compositions with composition of melts produced by experimental dehydration melting of various types of crustal rocks. In that diagram (Fig. 9.2B), the composition of the two-mica granitoid mostly plots within the overlap field of melts originating from dehydration melting of felsic pelite/greywacke rocks, with few samples in the field of felsic pelites alone. Furthermore, the relatively low $\text{CaO}/\text{Na}_2\text{O}$ ratios (0.11–0.38), and the moderate Rb/Sr (2.26–7.00) and Rb/Ba (0.44–2.00) ratios suggest a mixture of "mature" clay-rich, plagioclase-poor pelitic and "immature" clay-poor, plagioclase-rich psammitic (greywackes) sources for this granitoid (Sylvester, 1998).

Furthermore, the initial $^{87}\text{Sr}/^{86}\text{Sr}_{(600 \text{ Ma})}$ ratios range from 0.708–0.720 and are within that of the typical S-type granites, following Chappell and White (2001) (> 0.708 : see Table 7.1). The Sr isotopic signature coupled to the negative $\epsilon_{\text{Nd}}(600 \text{ Ma})$ values (−9.9 to −14.0) and the T_{DM} model ages (2.07–2.25 Ga) is hence in concordance with the genesis from melting of ancient continental crust material. For S-type granitoids it has been suggested that low CaO and

Na_2O ratios along with the high K_2O contents give evidence of the low versus high concentrations of these elements in the source, most likely weathered metasedimentary rocks (e.g., Miller, 1985; Chappell and White, 1992). Detailed studies of typical leucogranite plutons or S-type granites worldwide are in general agreement with their origin from partial melting of a metasedimentary source, with or without mixing with mantle-derived magmas (e.g., Chappell and White, 1992; Nabelek et al., 1992; Inger and Harris, 1993; Williamson et al., 1996).

Recent investigations (Harris and Inger, 1992; McDermott et al., 1996) have demonstrated that the concentration of Rb, Sr and Ba, and their corresponding Rb/Sr and Sr/Ba ratios can be used as discriminator of vapour-present versus vapour-absent (i.e. dehydration) partial melting conditions for a given source rock. Vapour-present melting is identified by low Rb/Sr (0.7–1.6) versus high Sr/Ba (0.5–1.6) ratios of granite and additionally positive Eu anomalies. In contrast, vapour-absent melts have high Rb/Sr (3–6) versus low Sr/Ba (0.2–0.7) ratios and negative Eu anomalies resulting from the residual plagioclase. The two-mica granitoid under study has high Rb/Sr ratios (2.3–7.0), low Sr/Ba ratios (0.2–0.3) and exhibits small to significant negative Eu anomalies ($\text{Eu}/\text{Eu}^* = 0.28\text{--}1.08$). This therefore indicates vapour-absent partial melting of the metasedimentary protolith during the formation of the two-mica granitoid. Moreover, the low $\text{CaO}/\text{Na}_2\text{O}$ (0.11–0.38) and the large range in $\text{Al}_2\text{O}_3/\text{TiO}_2$ (47–204) in this granitoid point to the genesis of the two-mica granitoid by dehydration partial melting, following the melting experiments of Holtz and Johannes (1991). Also, the presence of euhedral magmatic garnet implies that the magma was relatively hot and water-undersaturated (Clemens and Wall, 1981).

Following Harris and Inger (1992), the high Rb/Sr ratios (> 5.0) in leucogranite further indicate a derivation from muscovite dehydration melting, whereas low (< 5.0) values are typical for melting of biotite. The studied two-mica granitoid has Rb/Sr ratios ranging from 2.3 to 7.0 (mainly < 5.0). Hence, the generation of the two-mica granitoid likely involved a biotite dehydration-melting reaction.

McDermott et al. (1996) modelled the vapour-absent biotite dehydration melting reaction by using the large ion lithophile elements (LILE: Rb, Sr and Ba) for a source with variable amount of plagioclase. According to their model, biotite dehydration melting is mainly governed

by the presence of plagioclase or biotite minerals in the source. The low abundance of plagioclase in pelite-dominated sources limits the maximum degree of partial melting (referred to as plagioclase-limited melting), and so the residual material is plagioclase poor but relatively rich in biotite. Thus, the melt is enriched in Sr relative to both Rb and Ba. An increase of the proportion of the greywacke end-member implies an increase of the plagioclase mineral in the residue which is limited by the availability biotite (referred to as biotite-limited melting). The melt then becomes enriched in Rb and Ba relative to Sr resulting high Rb/Sr and Ba/Sr. The two-mica granitoid under study has high values of $Rb/Sr > 1.0$ and $Ba/Sr > 5.0$. This infers that the biotite-limited biotite dehydration melting was the probable mechanism in the generation of the two mica granitoid. This mechanism reflects a greywacke-dominated source (McDermott et al., 1996). Abundance of Eburnian (~ 2.1 Ga) metasedimentary rocks (greywacke-type) associated with volcano-sedimentary rocks throughout the Cameroon orogenic belt (Penaye et al., 1989: 1993; Ganwa, 1998) supports this hypothesis, although they are not yet described in West Cameroon.

In conclusion, the two-mica granitoid under study is a peraluminous leucocratic granitoid or leucogranite. It was produced by partial melting of Eburnean metagreywacke source involving biotite-limited biotite dehydration melting. This generation process fits well into the model of formation (1): "melting of metapelites and metagreywackes, including cases of basalt magma admixture". The biotite-rich surmicaceous enclaves encountered within the two-mica granitoid are interpreted as a biotite concentration rather than representing its protolith xenolith. Peraluminous granitoids are not widespread documented in the Cameroon Neoproterozoic belt. In East Cameroon, the leucogranites have been interpreted as originating from partial melting of immature sediments (Soba, 1989; Soba et al., 1991).

The negative $\varepsilon_{Nd}(600 \text{ Ma})$ values along with the high $^{87}\text{Sr}/^{86}\text{Sr}_{(600 \text{ Ma})}$ ratios of almost all the Bafoussam granitoids reflect the very long crustal residence time of their protoliths before the melting event. The Pan-African granitoids from the Northwest of the Tcholliré-Banyo fault (TBF: considered as major crustal boundary see Fig. 1.5) are generated mainly from juvenile crust or crust with small contamination of older crust, however, local substantial proportion of older crust like for the Bafoussam granitoids has been noticed (Toteu et al., 2001). The initial $^{87}\text{Sr}/^{86}\text{Sr}$ ratios (0.705–0.709) and the $\varepsilon_{Nd}(600 \text{ Ma})$ values (0.2 to –6.3) for I-type granitoids

(Biotite granitoids, deformed biotite granitoid and mega feldspar granitoid) support their generation in the lower crust, whereas the two-mica leucogranite with higher initial $^{87}\text{Sr}/^{86}\text{Sr}$ ratios (0.708–0.720) and lower $\epsilon_{\text{Nd}}(600 \text{ Ma})$ values (−9.9 to −14.0) was produced in the upper crust (DePaolo and Wasserburg, 1979). The involvement of an older continental crust (Archean or Paleo- to Mesoproterozoic) during the genesis of the Pan-African granitoids is also noticed in other segments of the Neoproterozoic belt of Cameroon, particularly southeast of the Tcholliré-Banyo fault (Toteu et al., 2001; Tagne-Kamga et al., 1994: 2003; Nzolang et al., 2003; Nzolang, 2005).

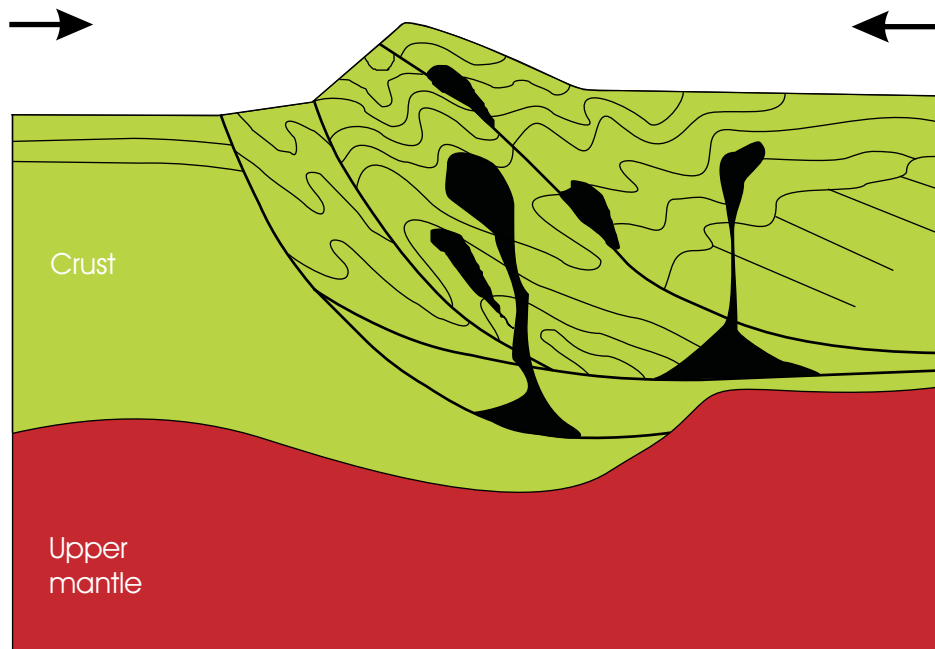
The mineralogical, geochemical and isotopic signatures of the studied granitoids are similar to those described in the adjacent provinces of the Central African Fold Belt (CAFB) such as Nigeria (Ekwueme and Kröner, 1998) and the Central African Republic (Pin and Poidevin, 1987), as well as in the Borborema Province in northeastern Brazil (Sial et al., 1999; Neves et al., 2004 and references therein), suggesting the continuation of the CAFB in the South American continent.

9.2 Geodynamic implications

Many studies have been focused on the genetic links between granitoid types and geodynamic environments. The most detailed and recent classification scheme has been proposed by Barbarin (1996: 1999) and divides granitoids into six types: two types of peraluminous granitoids (MPG and CPG) of purely or essentially crustal origin, two types of calc-alkaline granitoids (KCG and ACG) of mixed origin, and two types of "tholeiitic" or alkaline granitoids (ATG or RTG, and PAG) of mainly mantle-derived origin. Based on mineralogical and geochemical features, the Bafoussam granitoids are compared to two granitoid types in Barbarin's classification: (1) KCG (K-rich calc-alkaline granitoids), represented by the biotite granitoid, the deformed biotite granitoid and the mega feldspar granitoid; and (2) MPG (muscovite-bearing peraluminous granitoids), represented by the two-mica granitoid.

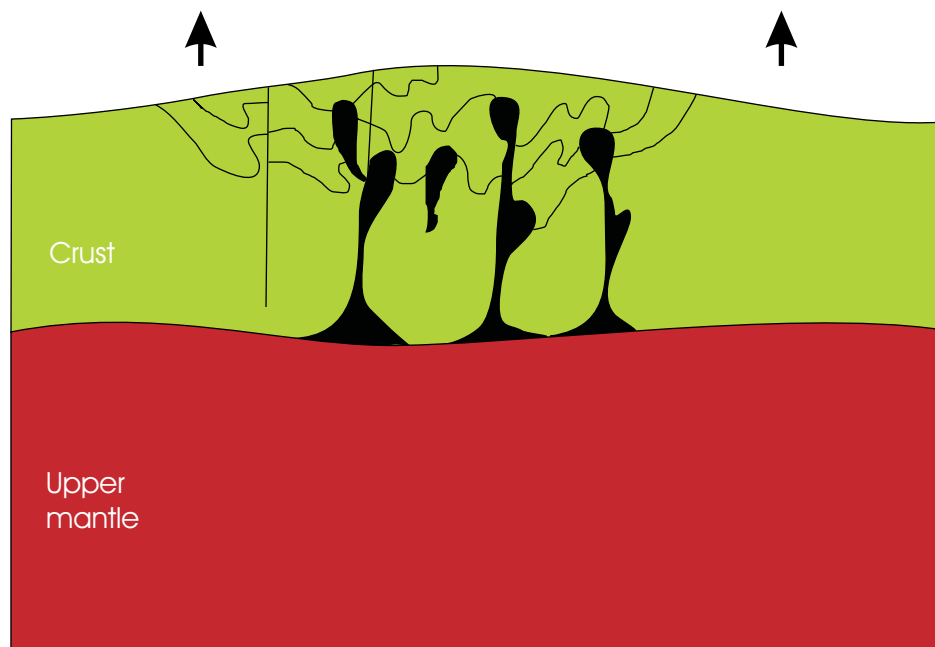
According to Barbarin (1999), peraluminous MPG and CPG are generally formed in collisional belts and are associated with the climax of orogenesis (e.g., Brittany and the French Massif Central, the Lachan Fold Belt, SE Australia and the Higher Himalaya). KCG also form in

collisional belts and are associated with the MPG and CPG, but they typically occur during the post-collisional uplift and orogenic relaxation (e.g., Celadonian plutons of the northern British Isles, Ploumanac'h intrusive complex, Brittany, France). The granitoids under study could have been formed in collisional (two-mica granitoid) and in post-collisional (biotite granitoid, deformed biotite granitoid and mega feldspar granitoid) environments. However, their geochemical features suggest diverse tectonic environments, syn-collision, volcanic arc, within-plate and post-collision (Figs. 7.12–15). The studied granitoids emplaced in an orogenic belt. They do not favour the idea of their formation in volcanic arc and within-plate environments which are considered to be "inappropriate" and instead might be diagnostic for the tectonic settings in which the protoliths were formed. The Y contents of the granitoids generally less than 40 ppm (Fig. 7.10: Y versus SiO₂) suggest that they are related to an orogenesis (Rogers and Greenberg, 1990). The granitoids display deformational features, supporting this hypothesis. Following the Barbarin's classification scheme, it can be therefore inferred that the granitoids under study are syn- to post collision with the two-mica granitoid emplaced during a regional compressional tectonic regime and the biotite granitoid and the mega feldspar granitoid during the post collisional uplift (Fig. 9.3). Since the geological, mineralogical and chemical characteristics of the deformed biotite granitoid are almost the same as those of the biotite granitoid and mega feldspar granitoid, it also should be considered as emplaced during the post collisional uplift. The investigated granitoids display many similarities with neighbouring plutonic complexes (e.g., Bandja, Nguessi-Tchankam, 1994; Nguessi-Tchankam et al., 1997 and Ngondo, Tagne-Kamga, 1994 Tagne-Kamga et al, 1999), which are believed to be syn- to post-collisional and emplaced during the Pan-African D_2 deformation event in Cameroon Neoproterozoic orogenic belt. Table 9.1 shows the Bafoussam granitoids and other dated granitoid plutons northwest to the Tcholliré-Banyo fault, subdivided according to the three classical Pan-African granitoid generations (Pre- to Syn- D_1 , Syn- to post- D_2 and late orogenic) within the Cameroon Neoproterozoic orogenic belt.



(1) Convergence of two continental lithospheres

Emplacement of the two-mica peraluminous granitoid (black spots) during the compressional regime



(2) Relaxation of a continental lithosphere

After the collision, emplacement of the I-type granitoids (black spots: biotite granitoid, deformed biotite granitoid and mega feldspar granitoid) during the continental uplift

Figure 9.3: Schematic tectonic model for the genesis and emplacement of the Bafoussam granitoids.

Table 9.1: Available geochronological data for the Pan-African granitoids situated northwest to the Tcholliré-Banyo fault (TBF) within the Neoproterozoic belt of Cameroon. Locations with asterisk (*) are in the vicinity of the studied area, Bafoussam.

Age scale	Location	Alkalinity	$^{87}\text{Sr}/^{86}\text{Sr}$ (initial)	Material	Age (Ma) with method			Authors
					Rb – Sr	U – Pb	CHIME	
<i>Late tectonic</i>	Papata	alkaline	0.7061 ± 0.0008	WR	505 ± 11 Ma			Lasserre et al. (1981a)
	Godé	alkaline	0.7089 ± 0.0009	WR	516 ± 06 Ma			Lasserre et al. (1981a)
	Dogba	alkaline	0.7077 ± 0.0017	WR	519 ± 07 Ma			Lasserre et al. (1981a)
	Goutchoumi	alkaline	0.7110 ± 0.0142	WR	526 ± 10 Ma			Lasserre et al. (1981b)
	Anloa	alkaline	0.7107 ± 0.0026	WR	531 ± 19 Ma			Lasserre et al. (1981b)
	Makassa	alkaline	0.7096 ± 0.0220	WR	534 ± 15 Ma			Lasserre et al. (1981a)
<i>Syn- to Post-D₂</i>	Nkambé *	calco-alkaline	–	monazite			$510\text{--}552$ Ma	Tetsopgang (2003)
	Bafoussam	calco-alkaline	0.7075 ± 0.0002	WR	540 ± 27 Ma			This study
	Bandja *	calco-alkaline	0.7089 ± 0.0003	WR	557 ± 08 Ma			Nguiessi-Tchankam et al. (1994)
	Fomopéa *	calco-alkaline	0.7090 ± 0.0003	WR	575 ± 17 Ma			Kwékam (1993)
	Batié *	calco-alkaline	0.7077 ± 0.0006	WR	576 ± 24 Ma			Talla (1995)
	Bafoussam	calco-alkaline	0.7077 ± 0.0016	WR	587 ± 27 Ma			This study
	Poli	calco-alkaline	–	zircon		$600\text{--}580$ Ma		Toteu et al. (1990)
	Ngondo *	calco-alkaline	0.7056 ± 0.0018	WR	609 ± 30 Ma			Tagne-Kamga (1994)
<i>Pre- to Syn-D₁</i>	Bangangté *	calco-alkaline	0.7080 ± 0.0006	WR	$606\text{--}630$ Ma			Tchouankoué (1992)
	Bangoua *	calco-alkaline	–	zircon		628 Ma		Toteu et al. (2001)
	Poli	calco-alkaline	–	zircon		$630\text{--}620$ Ma		Toteu et al. (1990b)
	Bakonwa	calco-alkaline	–	zircon		633 ± 03 and 665 ± 10 Ma		Toteu et al. (2001)
	Bandja *	calco-alkaline	–	zircon		640 ± 12 Ma		Nguiessi-Tchakam et al. (1994)
	Kumba-Manfé	calco-alkaline	0.7080 ± 0.0005	WR	655 ± 30 Ma			Lasserre et Soba (1979)
	Ngondo *	calco-alkaline	0.7055 ± 0.0001	WR	657 ± 08 Ma			Tagne-Kamga (1994)
	Manengouba	calco-alkaline	0.7044 ± 0.0002	WR	686 ± 17 Ma			Lamien (1989)

9.3 Salient results

The present study elucidates the tectonic environment and associated geological processes responsible for the origin and evolution of the Bafoussam granitoids for the better understanding of the Pan-African magmatism within the Cameroon Neoproterozoic orogenic belt. The mode of occurrence, magmatic association, mineral chemistry, crystallization conditions (P , T , X , fluids), whole-rock geochemistry and whole-rock isotope (Rb–Sr and Sm–Nd) geochemistry of these granitoids have been documented. Fluid inclusions in quartz from hydrothermal veins have been also examined to characterize fluid evolution (fluid types, fluid composition, temperature and pressure) within the granitoids. The main conclusions drawn from this study are:

- (1) Four groups of granitoids have been recognized in the Bafoussam area: the biotite granitoid, the deformed biotite granitoid, the mega feldspar granitoid and the two-mica granitoid. They are syn- to post-collisional, emplaced into migmatic-gneiss wall-rock of amphibolite facies at 540 ± 27 Ma for the biotite granitoid, 587 ± 41 Ma for the mega feldspar granitoid (whole-rock Rb–Sr isochrons). A probably mixing age of 663 ± 62 Ma is yielded by the Rb–Sr whole-rock isochron for the two-mica granitoid.
- (2) The granitoids under study have a wide range of lithology compositions including syenogranite (major), alkali-feldspar granite, granodiorite, monzogranite, quartz-syenite, quartz-monzonite and quartz-monzdiorite. The petrography is characterized by variable proportion of potassium feldspar ($\text{Or}_{81-97}\text{Ab}_{19-3}$), quartz, plagioclase (mainly oligoclase: $\text{An}_{3-35}\text{Ab}_{96-64}$) and Fe-rich biotite (X_{Fe} : 0.40–0.80) as major phases, with amphibole (edenite and magnesio-hastingsite: X_{Mg} : 0.50–0.62) and accessory minerals. Additionally, the two-mica granitoid contains primary muscovite (X_{Fe} : 0.52–0.82) and igneous garnet (almandine–spessartine).
- (3) The Bafoussam granitoids crystallized under varying pressures (4.2 ± 1.1 to 6.6 ± 1.0 kbar) and a narrow range of temperatures (772 ± 41 to 808 ± 34 °C) from oxidized magma ($\log f\text{O}_2 -17$ to -13), except the two-mica granitoid which was generated by a

moderately reduced parent magma, below the quartz–fayalite–magnetite buffer. The granitoids were emplaced at different depths ranging from 15 to 24 km.

- (4) Fluid inclusions found in hydrothermal quartz veins are secondary in nature and are of two types, mixed aqueous–non-aqueous volatiles fluid inclusions subdivided into non-aqueous volatiles-rich mixed fluid inclusions and aqueous-rich mixed fluid inclusions, and pure aqueous fluid inclusions. The mixed aqueous–non-aqueous volatiles fluid inclusions contain pure CO₂, or dominantly CO₂ and CH₄ as volatiles. The pure aqueous fluid inclusions display a mixing salt system with dominantly NaCl and other divalent cations.
- (5) The investigated granitoids are intermediate to felsic in compositions and have high contents of alkalis with variable range in Fe₂O₃* and alumina contents. The abundances of large ion lithophile elements (LILE) and high-field-strength elements (HFSE) are variable, with the LILE being higher in intermediate granitoids and the HFSE in contrast higher in felsic or silica-rich granitoids. The granitoids exhibit evident enrichment of light relative compared to heavy REEs, with small to significant negative Eu anomalies. They display almost similar magmatic affinities, non-alkaline to mid-alkaline, alkali-calcic, calc-alkaline, K-rich to shoshonitic and ferriferous. Ocean ridge granites (ORG) normalized multi-elements spidergrams are similar to typical collision-related granites pattern.
- (6) Genetically, the studied granitoids are I-type granitoids (biotite granitoid, deformed biotite granitoid and mega feldspar granitoid) and S-type granitoid (two-mica granitoid). I-type granitoids are metaluminous (ASI = 0.70–1.0) or moderately peraluminous (ASI = 1.01–1.06) for the highly fractionated ones. These granitoids are cogenetic and the observed compositional variations result mainly from the fractionation of plagioclase, biotite, K-feldspar and accessory minerals at the level of emplacement. The two-mica, S-type granitoid is exclusively peraluminous (ASI = 1.07–1.25) and has peraluminous leucogranite composition.

(7) The granitoids under study were produced by partial melting of Paleoproterozoic and Mesoproterozoic crustal sources of tonalite–granodiorite composition in the lower crust for the I-type granitoids and greywacke-dominated in the upper crust for the two-mica granitoid. The protoliths of these granitoids have a very long residence time in the crust before the melting event (T_{DM} : 1.5–2.3 Ga)

10 REFERENCES

- ABDEL-RAHMAN, A.M. (1994): Nature of biotites from alkaline, calc-alkaline, and peraluminous magmas. *Journal of Petrology* **35**, 525–541.
- ABDELSALAM, M.G., LIÉGEOIS, J.-P. AND STERN R.J. (2002): The Saharan Metacraton. *Journal of African Earth Sciences* **34**, 119–136.
- AGUE, J.J. (1997): Thermodynamic calculation of the emplacement pressures for batholithic rocks, California: implications for the aluminum-in-hornblende barometer. *Geology* **25**, 563–566.
- AGUE, J.J. AND BRANDON, M.T. (1996): Regional tilt of the Mount Stuart batholith, Washington, determined using aluminum-in-hornblende barometry: implications for northward translation of Baja British Columbia. *Geological Society of American Bulletin* **108**, 471–488.
- AGUE, J.J. AND BRIMHALL, G.H. (1988): Regional variations in Bulk chemistry, mineralogy and the compositions of mafic and accessory minerals in the batholiths of California. *Geological Society of American Bulletin* **100**, 891–911.
- ALKMIN, F.F., MARSHAK, S. AND FONSECA, M.A. (2001): Assembling West Gondwana in the Neoproterozoic: Clues from the São Francisco craton region, Brazil. *Geology* **29**, 319–322.
- ALTHERR, R., HOLL, A., HEGNER, E., LANGER, C. AND KREUZER, H. (2000): High-potassium, calc-alkaline I-type plutonism in the European Variscides: northern Vosges (france and northern Schwarzwald (Germany). *Lithos* **50**, 51–73.
- ALVEREZ, P. (1995): Les facteurs de contrôle de la sédimentation du supergroupe ouest-congolien (Sud-Congo). Rampe carbonatée et activité biologique au Protérozoïque supérieur. *Mémoire du Bureau de Recherche Géologiques et Minières* **239**, 396 p.
- ANDERSON, J.L. (1996): Status of thermobarometry in granitic batholiths. *Transactions of the Royal Society of Edinburgh Earth Sciences* **87**, 125–138.
- ANDERSON, J.L. AND ROWLEY, M.C. (1981): synkinematic intrusion of peraluminous and associated metaluminous granitic magmas, Whipple Mountains, California. *Canadian Mineralogist* **19**, 83–101.
- ANDERSON, J.L. AND SMITH, D.R. (1995): The effects of the temperature and f_{O_2} on the Al-in-hornblende barometer. *American Mineralogist* **80**, 549–559.
- ANGOUA-BIOUELE, S.E. (1988): *Étude structurale et pétrologique de la région de Gamba, bordure est de Poli (Nord Cameroun)*. Thèse de Doctorat, Université de Nancy I, France, 253 pp.
- ARCHANJO, C.J. AND BOUCHEZ, J.L. (1991): Le sérido, une chaîne transpressive dextre au protérozoïque supérieur de Nord-Est du Brésil. *Bulletin de la Société Géologique de France* **162**, 637–647.

- ARCULUS, R.J. (2003): Use and abuse of the terms calc-alkaline and calc-alkalic. *Journal of Petrology* **44**, 929–935.
- ATEBA, B., NTEPE, N., EKODECK, G.E., SOBA, D. AND FAIRHEAD, J.D. (1992): The recent earthquakes of South Cameroon and their possible relationship with main geological features of Central Africa. *Journal of African Earth Sciences* **14**, 365–369.
- ATHERTON, M.P. (1993): Granite magmatism. *Journal of Geological Society, London* **150**, 1009–1023.
- AVILA-SALINAS, W.A. (1990): Tin-bearing granites from the Cordillera, Real, Bolivia: a petrological and geochemical review. *Geological Society of America Special Paper* **241**, 145–159.
- BACHELOR, R.A. AND BOWDEN, P. (1985): Petrographic interpretation of granitoid rocks using multicationic parameters. *Chemical Geology* **48**, 43–55.
- BAKKER, R.J. (1997): Clathrates: computer programs to calculate fluid inclusion V - X properties using clathrate melting temperatures. *Computers & Geosciences* **23**, 1–18.
- BALL, E., BARD, J.P. AND SOBA, D. (1984): Tectonique tangentielle dans la catazone panafricaine du Cameroun: les gneiss de Yaoundé. *Journal of African Earth Sciences* **2**, 91–95.
- BARBARIN, B. (1990): Granitoids: main petrogenetic classification in relation to origin and tectonic setting. *Geological Journal* **25**, 227–238.
- BARBARIN, B. (1996): Genesis of the two main types of peraluminous granitoids. *Geology* **24**, 295–298.
- BARBARIN, B. (1999): A review of the relationships between granitoid types, their origins and their geodynamic environments. *Lithos* **46**, 605–626.
- BARD, J.-P. (1986): *Microtextures of igneous and metamorphic rocks: Petrology and Structural Geology*. Reidel, D. Publishing Company, Dordrechet, 264 p.
- BASSAHAK, J. (1988): *Le complexe plutonique du massif de Kogué (Poli-Nord Cameroun): Pétrologie–Géochimie–Pétrologie structurale. Sa place dans le plutonisme de la chaîne panafricaine au Nord Cameroun*. Thèse de Doctorat, Université de Nancy I, France, 287 pp.
- BASSAHAK, J. AND NJEL, O.U. (2004): Petrogenesis of a Neoproterozoic late collisional I-type plutonism in the Central African fold belt of Cameroon: the Kogué Complex (Poli Nord Cameroon). *20th colloquium of African Geology, B.G.R.M Orleans, France, Abstracts Volume*, p 65.
- BATES, R.L. AND JACKSON, J.A. (eds.) (1980): *Dictionary of geological terms* (third edition). American Geological Institute, Falls Church, Virginia, 571 pp.
- BERTHÉ, D., CHOUKROUNE, P. AND JEGOUZO, P. (1979): Orthogneiss, mylonite and non coaxial deformation of granite: the exemple of the South Armorican Shear Zone. *Journal of Structural Geology* **1**, 31–42.

- BERTRAND, J.M.L. AND JARDIM DE SÁ, E.F. (1990): Where are the Eburnian-Transamazonian collisional belts? *Canadian Journal of Earth Sciences* **27**, 1388–1393.
- BESSOLES, B. AND LASSERRE, M. (1977): Le complexe de base du Cameroun. *Bulletin de la Société Géologique de France* **19**, 1085–1092.
- BESSOLES, B. AND TROMPETTE, M. (1980): Géologie de l'Afrique: La chaîne panafricaine, "zone mobile d'Afrique Central (partie sud) et zone mobile soudanaise". *Mémoire du Bureau de Recherche Géologiques et Minières* **92**, 396 pp.
- BLACK, R. (1978): Propos sur le Pan-Africain. *Bulletin de la Société Géologique de France* **20**, 843–850.
- BLACK, R. (1984): The Pan-African event in the geological framework of Africa. *Pangea* **2**, 6–16.
- BLACK, R. AND LIÉGEOIS, J.-P. (1993): Cratons, mobile belts, alkaline rocks and continental lithospheric mantle: The Pan-African testimony. *Journal of the Geological Society, London* **150**, 89–98.
- BODNAR, R.J. (1993): Revised equation and the table for freezing point depressions of H₂O-NaCl solutions. *Geochimica et Cosmochimica Acta* **57**, 683 – 684.
- BODNAR, R.J. (2003): Introduction to fluid inclusions. In: SAMSON, I., ANDERSON, A. AND MARSHALL, D. (eds.), *Fluid Inclusions: Analysis and Interpretation*. Mineralogical Association of Canada, Short Course **32**, 1–8.
- BONIN, B., AZZOUNI-SEKKAL, A., BUSSY, F. NAD FERRAG, S. (1998): Alkali-calcic and alkaline post-orogenic (PO) granite magmatism: petrologic constraints and geodynamic settings. *Lithos* **45**, 45–70.
- BOULLIER, A.-M. (1999): Fluid inclusions: tectonic indicators. *Journal of Structural Geology* **21**, 1229–1235.
- BOWDEN, P., BATCHELOR, R.A., CHAPPELL, B.W., DIDIER, J. AND LAMEYRE, J. (1984): Petrological, geochemical and source criteria for the classification of granitic rocks: a discussion. *Physics of the Earth and Planetary Interiors* **35**, 1–11.
- BOWDEN, P., BLACK, R., MARTIN, R.F., IKE, E.C., KINNAIRD, J.A. AND BATCHELOR, R.A. (1987): Niger-Nigeria alkaline ring complexes: a classic example of African Phanerozoic anorogenic mid-plate magmatism. In: FITTON, J.G. AND UPTON, B.G.J. (eds.), *alkaline igneous rocks*. Geological Society Special Publication **30**, 357–379.
- BROOKS, C., HART, S.R. AND WENDT, T. (1972): Realistic use of two-error regression treatments as applied to rubidium-strontium data. *Reviews of Geophysical Space Physics* **10**, 551–577.
- BROWNE, S.E. AND FAIRHEAD, J.D. (1983): Gravity study of the Central African Rift system: a model of continental disruption: The Ngaoundéré and Abu Gabra rifts. *Tectonophysics* **94**, 187–203.

- BROWN, P.E. (1989): FLINCOR; a microcomputer program for the reduction and investigation of the fluid-inclusion data. *American Mineralogist* **74**, 1390–1393.
- BROWN, P.E. (1998): Fluid inclusion modelling for hydrothermal systems. In: MCKIBBEN, M.A. AND SHANKS, W.C. (eds), *Applications of microanalytical techniques to understanding mineralizing processes. Review of Economic Geology* **7**, 151–171.
- BROWN, P.E AND LAMB, W.M. (1989): *P–V–T* properties of fluids in the system H₂O ± CO₂ ± NaCl: New graphical presentations and applications for fluids inclusions studies. *Geochimica et Cosmochimica Acta* **53**, 1209–1221.
- BURKE, K. (2001): Origin of the Cameroon Line of volcano-capped swells. *Journal of Geology* **109**, 349–362.
- BURKHARD, D.J.M. (1991): Temperature and redox trend of biotite-bearing rocks: a method of estimation applied to S- and I-type granites from Australia. *Earth and Planetary Sciences Letters* **104**, 89–98.
- BURKHARD, D.J.M. (1993): Biotite crystallization temperatures and redox states in granitic rocks as indicator for tectonic setting. *Geologie en Mijnbouw* **71**, 337–349.
- BURRUSS, R.C. (2003): Petroleum fluid inclusion, an introduction. In: SAMSON, I., ANDERSON, A. AND MARSHALL, D. (eds.), *Fluid Inclusions: Analysis and Interpretation. Mineralogical Association of Canada, Short Course* **32**, 159–174.
- CABY, R. AND BOESSÉ, J.M. (2001): Pan-African nappe system in southwest Nigeria: the Ife-Ilesha belt. *Journal of African Earth Sciences* **33**, 211–225.
- CAEN-VACHETTE, M., TEMPPIER, P. AND NANA, J.M. (1991): Le granite de Lembo (Partie du Complexe volcano-plutonique de Bana), témoins d'un magmatisme tertiaire de Cameroun: Géochronologie. *Bulletin de la Société Géologique de France* **162**, 491–501.
- CAHEN, L. AND SNELLING, N.J. (1966): *The geochronology of Equatorial Africa*. North-Holland Publishing Company, Amsterdam, 195 pp.
- CAHEN, L., SNELLING, N.J., DELHAL, J., VAIL, J.R. AND BONHOMME, M. (1984): *The geochronology and evolution of Africa*. Clarendon, Oxford, 512 pp.
- CAMACHO, A., HENSEN, B.J. AND ARMSTRONG, R.A. (2002): Isotopic test of the thermally driven intraplate orogenic model, Australia. *Geology* **30**, 887–890.
- CANTAGREL, J.-M., JAMOND, C. AND LASSEUR, M. (1978): Le magmatisme de la ligne du Cameroun au tertiaire inférieur: données géochronologiques K–Ar. *Comptes Rendus sommaires de la Société Géologique de France* **6**, 300–303.
- CASTAING, C., FEYBESSE, J.L., THIEBLEMONT, D., TRIBOULET, C. AND CHEVREMONT, P. (1994): Palaeogeographical reconstructions of the Pan-African/Brasiliano Orogen; closure of an oceanic domain or intracontinental convergence between major blocks? *Precambrian Research* **69**, 327–344.

- CARMICHAEL, I.S.E (1991): The redox states of basic and silicic magmas: a reflection of their source regions? *Contributions to Mineralogical and Petrology* **106**, 129–141.
- CASTAING, C., TRIBOULET, C., FEYBESSE, J.L. AND CHÈVREMONT, P. (1993): Tectometamorphic evolution of Ghana, Togo and Benin in the light of the Pan-African/Brasiliano orogeny. *Tectonophysics* **218**, 323–342.
- CHAPPELL, B.W. (1999): Aluminium saturation in I- and S-type granites and the characterization of fractionated haplogranites. *Lithos* **46**, 535–551.
- CHAPPELL, B.W. AND STEPHENS, W.E. (1988): Origin of infracrustal (I-type) granite magmas. *Transactions of the Royal Society of Edinburgh: Earth Sciences* **79**, 71–86.
- CHAPPELL, B.W. AND WHITE, A.J.R. (1974): Two contrasting granite types. *Pacific Geology* **8**, 173–174.
- CHAPPELL, B.W. AND WHITE, A.J.R. (1984): I- and S-type granites in the Lachlan Fold Belt, southeastern Australia. In: XU KEQIN AND TU GUANGCHI (eds), *Geology of granites and their metallogenetic relations*. Beijing: Science Press, 87–101.
- CHAPPELL, B.W. AND WHITE, A.J.R. (1992): I- and S-type granites in the Lachlan Fold Belt. *Transactions of the Royal Society of Edinburgh: Earth Sciences* **83**, 1–26.
- CHAPPELL, B.W. AND WHITE, A.J.R. (2001): Two contrasting granite types: 25 years later. *Australian Journal of Earth Sciences* **48**, 489–499.
- CHAPPELL, B.W., WHITE, A.J.R., WILLIAMS, I.S., WYBORN, D. AND WYBORN, L.A.I. (2000): Lachlan Fold Belt granites revised: high- and low-temperature granites and their implications. *Australian Journal of Earth Sciences* **47**, 123–138.
- CLARKE, D.B. (1981): The mineralogy of peraluminous granites: a review. *Canadian Mineralogist* **19**, 3–17.
- CLARKE, D.B. (1992): *Granitoids rocks*. Chapman & Hall, London, 283 pp.
- CLARKE, D.B., HALLIDAY, A.N. AND HAMILTON, P.J. (1988): Neodymium and strontium isotopic constraints on the origin of the peraluminous granitoids of the South Mountain batholith, Nova Scotia, Canada. *Chemical Geology (Isotope Geoscience Section)* **73**, 15–24.
- CLEMENS, J.D. (1984): Water contents of silicic to intermediate magmas. *Lithos* **17**, 273–287.
- CLEMENS, J.D. AND WALL, V.J. (1981): Origin and crystallization of some peraluminous (S-type) granitic magmas. *Canadian Mineralogist* **19**, 111–131.
- CLIFFORD, T.N. (1970): The structural framework of Africa. In: CLIFFORD, T.N. AND GASS, I.G. (eds.), *African magmatism and tectonics*. Oliver and Boyd, Edinburgh, 1–26.
- COBBING, J. (1996): Granites – an overview. *Episodes* **19**, 103–106.

- CORNACCHIA, M. AND DARS, R. (1983): Un trait structural majeur du continent Africain: les linéaments centrafricains du Cameroun au golfe d'Aden. *Bulletin de la Société Géologique de France* **25**, 101–109.
- CZAMANSKE, G.K., ISHIHARA, S. AND ATKIN, S.A. (1981): Chemistry of rock-forming minerals of the Cretaceous-Paleocene batholith in south western Japan and implications for magma genesis. *Journal of Geophysical Research* **86**, 10431–10469.
- CZAMANSKE, G.K. AND WONES, D.R. (1973): Oxidation during magmatic differentiation, Finnmarka complex, Oslo area, Norway: Part 2, the mafic silicates. *Journal of Petrology* **14**, 349–380.
- DAVIDSON, I., McCARTHY, M., POWELL, D., TORRES, H.H.F. AND SANTOS, C.A. (1995): Laminar flow in shear zones: the Pernambuco shear zone, NE-Brazil. *Journal of Structural Geology* **17**, 149–161.
- DAVIDSON, I., AND SANTOS, R. (1989): Tectonic evolution of the Sergipano Fold Belt, NE Brazil, during the Brasiliano Orogeny. *Precambrian Research* **45**, 319–342.
- DE ALMEIDA, F.F.M., HASUI, H., DE BRITO NEVERS, B.B. AND FUCK, A.R. (1981): Brazilian structural provinces: An introduction. *Earth-Sciences Reviews* **17**, 1–29.
- DEBON, F. AND LE FORT, P. (1988): A cationic classification of common plutonic rocks and their magmatic associations: principles, method, applications. *Bulletin de Minéralogie* **111**, 493–510.
- DEBON, F. AND LEMMET, M. (1999): Evolution of the Mg/Fe ratios in the late Variscan plutonic rocks from external crystalline massifs of the Alps (France, Italy, and Switzerland). *Journal of Petrology* **40**, 431–462.
- DEER, W.A., HOWIE, R.A. AND ZUSSMAN, J. (1962): *An introduction to the rock-forming minerals* (second edition). Longmans, London, 696 pp.
- DE LA ROCHE, H., LETERRIER, J., GRANDCLAUDE, P. AND MARCHAL, M. (1980): A classification of volcanic and plutonic rocks using R_1R_2 -diagram and major-element analyses—its relationships with current nomenclature. *Chemical Geology* **29**, 183–210.
- DELHAL, J. AND LEDENT, L. (1975): Données géochronologiques sur le complexe calco-magnésien du Sud-Cameroun. *Musée Royal d'Afrique Central, Tervuren. Rapports annuels* 1974, 71–75.
- DEPAOLO, G.J. (1981): Trace element and isotopic effects of combined wall-rock assimilation and fractional crystallisation. *Earth and Planetary Sciences Letters* **53**, 189–202.
- DEPAOLO, G.J. (1988): *Neodymium isotope geochemistry: An introduction*. Springer-Verlag, Berlin, Heidelberg, 187 pp.
- DEPAOLO, G.J. AND WASSERBURG, G.J. (1976): Nd isotopic variations and petrogenetic models. *Geophysics Research Letters* **3**, 249–252.

- DEPAOLO, G.J. AND WASSERBURG, G.J. (1979): Petrogenetic mixing models and Nd–Sr isotopic patterns. *Geochemica et Cosmochimica Acta* **43**, 615–627.
- DÉRUELLE, B., MOREAU, C., NKOUUMBOU, C., KAMBOU, R., LISSOM, J., NJONFANG, E., GHOGOMO, R.T. AND NONO, A. (1991): The Cameroon Line: a review. In: KAMPUNZU, A.B. AND LUBALA, R.T. (eds.), *Magmatism in extensional structural settings: the Phanerozoic African Plate*. Springer-Verlag, Berlin, 275–327.
- DÉRUELLE, B., N’NI, J. AND KAMBOU, R. (1987): Mount Cameroon: an active volcano of the Cameroon Line. *Journal of African Earth Sciences* **6**, 197–214.
- DIAMOND, L.W. (1992): Stability of CO₂ clathrate hydrate + CO₂ liquid + CO₂ vapour + aqueous KCl–NaCl solutions: Experimental determination and application to salinity estimates of the fluid inclusions. *Geochemica et Cosmochimica Acta* **56**, 273–280.
- DICKIN, A.P. (2004): *Radiogenic isotope geology* (second edition). Cambridge University Press, United Kingdom, 512 pp.
- DORBATH, C., DORBATH, L., GAULON, R. AND HATZFELD, D. (1985): Seismological investigation of the Bangui magnetic anomaly region and its relation to the margin of the Congo craton. *Earth and Planetary Sciences Letters* **75**, 231–244.
- DU BRAY, E.A. (1988): Garnet compositions and their use as indicators of peraluminous granitoid petrogenesis–Southeastern Arabian Shield. *Contribution to Mineralogy and Petrology* **100**, 205–212.
- DUMONT, J.F.V. (1986): Identification par télédétection de l'accident de la Sanaga (Cameroun): Sa position dans le contexte des grands accidents de l'Afrique Central et de la limite Nord du craton congolais. *Géodynamique* **1**, 13–19.
- DUMORT, J.C. (1968): *Carte géologique de reconnaissance du Cameroun à l'échelle du 1/500000, coupure Douala-Ouest avec notice explicative*. Bulletin de la direction de géologie et des mines, Cameroun, 69 p.
- EBADI, A. AND JOHANNES, W. (1991): Beginning of melting and composition of first melts in the system Qz–Ab–Or–H₂O–CO₂. *Contributions to Mineralogy and Petrology* **106**, 286–295.
- EBY, G.N. (1990): The A-type granitoids: a review of their occurrence and chemical characteristics and speculation on their petrogenesis. *Lithos* **26**, 115–134.
- EKWUEME, B.N. AND KRÖNER, A. (1998): Single zircon evaporation ages from the Oban Massif, southeastern Nigeria. *Journal of African Earth Sciences* **26**, 195–205.
- EL BAGHDADI, M., EL BOUKHARI, A., JOUIDER, A., BENYOUCEF, A. AND NADEM, S. (2003): Calc-alkaline arc I-type granitoid associated with S-type granite in the Pan-African belt of Eastern Anti-atlas (Soghra and Ougnat, South Morocco). *Gondwana Research* **6**, 557–572.
- ENGLER, A., KOLLER, F., MEISEL, T. AND QUEMENEUR, J. (2002): Evolution of the Archean/Proterozoic crust in the southern São Francisco Craton near Perdoes, Minas Gerais, Brazil; petrological and geochemical constraints. *Journal of South American Earth Sciences* **15**, 709–723.

- EVANS, O.C. AND HANSON, G.N. (1993): Accessory-mineral fractionation of the rare-earth element (REE) abundances in granitoid rocks. *Chemical Geology* **110**, 69–93.
- FABRIÈS, J., CONQUÉRÉ, F. AND ARNAUD, G. (1984): The mafic silicates in the Saint quay-Portrieux gabbro-diorite intrusion: crystallization conditions of a calc-alkaline pluton. *Bulletin de Mineralogie* **107**, 715–736.
- FAURE, G. (1986): *Principles of isotopes geology* (second edition). John Wiley & Sons, New York, 589 pp.
- FAURE, G. (1998): *Principles and applications of geochemistry*. Prentice-Hall, New Jersey, 600 pp.
- FERRÉ, E.C., CABY, R., PEUCAT, J.J., CAPDEVILLA, R. AND MONIÉ, P. (1998): Pan-African, post-collisional, ferro-potassic granite and quartz - monzonite plutons of Eastern Nigeria. *Lithos* **45**, 255–279.
- FERRÉ, E.C., GLEIZES, G. AND CABY, R. (2002): Obliquely convergent tectonics and granite emplacement in the Trans-Saharan belt of Eastern Nigeria: a synthesis. *Precambrian Research* **114**, 199–219.
- FERRÉ, E.C. AND LEAKE, B.E. (2001): Geodynamic significance of the early orogenic high-K crustal and mantle melts: example of the Corsica Batholith. *Lithos* **59**, 47–67.
- FEYBESSE, J.L., JOHAN, V., TRIBOULET, C., GUERROT, C., MAYAGA-MIKOLO, F., BOUCHOT, V. AND EKO N'DONG, J. (1998): The West Central African Belt: a model of 2.5–2.0 Ga accretion and two-phase orogenic evolution. *Precambrian Research* **87**, 161–216.
- FITCHES, W.R., AJIBADE, A.C., EGBUNIWE, I.G., HOLT, R.W. AND WRIGHT, J.B. (1985): Late Proterozoic schist belts and plutonism in NW Nigeria. *Journal Geological Society London* **142**, 319–337.
- FITTON, F.G. (1987): The Cameroon Line, West Africa: a comparison between oceanic and continental volcanism. In: FITTON, J.G. AND UPTON, B.G.J. (eds.), *Alkaline Igneous Rocks. Geological Society Special Publication* **30**, 273–291.
- FITTON, J.G. AND DUNLOP, H.M. (1985): The Cameroon Line, West Africa, and its bearing on the origin of the oceanic and continental alkali basalt. *Earth and Planetary Science Letters* **72**, 23–38.
- FLEET, M.E. AND BARNETT, R.L. (1978): $\text{Al}^{\text{IV}}/\text{Al}^{\text{VI}}$ partitioning in calciferous amphiboles from the Frood Mine, Sudbury, Ontario. *Canadian Mineralogist* **16**, 527–532.
- FÖRSTER, H.-J., TISCHENDORF, G. AND TRUMBULL, R.B. (1997): An evaluation of the Rb vs. (Y+Nb) discrimination diagram to infer tectonic setting of silicic igneous rocks. *Lithos* **40**, 261–293.
- FOSTER, M.D. (1960): Interpretation of the composition of trioctahedral mica. *U.S. Geological Survey, professional paper report* **354B**, 11–49.

- FROST, R.B., BARNES, C.G., COLLINS, W.J., ARCUS, R.J., ELLIS, D.J. AND FROST, C.D. (2001): A Geochemical classification for Granitic Rocks. *Journal of Petrology* **42**, 2033–2048.
- GANWA, A.A. (1998): *Contribution à l'étude géologique de la région de Kombé II-Mayabo dans la série panafricaine de Bafia : Géomorphologie structurale, tectonique, pétrologie*. Thèse de Doctorat, Université de Yaoundé I, Cameroun, 173 pp.
- GARCIA, D., FONTEILLES, M. AND MOUTTE, J. (1994): Sedimentary fractionation between Al, Ti, and Zr and the genesis of strongly peraluminous granites. *Journal of geology* **102**, 411–422.
- GHOGOMU, R.T., MOREAU, C., BROWN, W.L. AND ROCCI, G. (1989): The Ntumbaw Complex, NW Cameroon: a typical anorogenic ring complex of intermediate composition. *Journal of African Earth Sciences* **8**, 1–9.
- GILBERT, M.C., HELZ, R.T., POPP, R.K. AND SPEAR, F.S. (1982): Experimental studies of amphibole stability. In: VEBLEN, D.R. AND RIBBE, P.H. (eds.), *Amphiboles: Petrology and experimental phase relations*. Mineralogical Society of America, *Reviews in Mineralogy* **9B**, 229–353.
- GOLDSTEIN, R.H. (2003): Petrographic analysis of fluid inclusions. In: SAMSON, I., ANDERSON, A. AND MARSHALL, D. (eds.), *Fluid Inclusions: Analysis and Interpretation*. Mineralogical Association of Canada, *Short Course* **32**, 9–53.
- GOLDSTEIN, R.H. AND REYNOLDS, T.J. (1994): Systematics of fluid inclusions in diagenetic minerals. *SEPM (Society of Sedimentary Geology) Short Course* **31**, 199 pp.
- GOLDSTEIN, S.L., O' NIONS, R.K. AND HAMILTON, P.J. (1984): A Sm–Nd isotopic study of atmospheric dusts and particulates for major river systems. *Earth and Planetary Science Letters* **70**, 221–236.
- GOODWIN, A.M. (1991): *Precambrian Geology – The dynamic evolution the continental crust*. Academic Press, Harcourt Brace Jovanovich Publishers, 666 pp.
- GREEN, T.H. (1977): Garnet in silicic liquids and its possible use as a $P-T$ indicator. *Contributions to Mineralogy and Petrology* **65**, 59 – 67.
- GREEN, T.H. AND WATSON, E.B. (1982): Crystallization of apatite in natural magmas under high pressure, hydrous conditions, with particular reference to “orogenic” rock series. *Contributions to Mineralogy and Petrology* **79**, 96–105.
- GUIDOTTI, C.V. (1984): Micas in metamorphic rocks. In: BAILEY, S.W. (ed.), *Micas*. Mineralogical Society of America, *Reviews in Mineralogy* **13**, 357–456.
- GUIDOTTI, C.V., CHENEY, J.T. AND GUGGENHEIM, S. (1977): Distribution of titanium between coexisting muscovite and biotite in pelitic schists from northwestern Miane. *American Mineralogist* **62**, 438–448.
- GUIDOTTI, C.V. AND SASSI, F.P. (1976): Muscovite as petrogenetic indicator mineral in politic schists. *Neues Jahrbuch für Mineralogie Abhandlungen* **127**, 94–142.

- GUIRAUD, R. AND MAURIN, J.C. (1991): Le rifting en Afrique au crétacé inférieur: synthèse structurale, mise en évidence de deux étapes dans la genèse des Bassins, relations avec les ouvertures océaniques péri-Africaines. *Bulletin de la Société Géologique de France* **162**, 811–823.
- GUIRAUD, R., BINKS, R.M., FAIRHEAD, J.D. AND WILSON, M. (1992): Chronology and geodynamic setting of Cretaceous–Cenozoic rifting in west and Central Africa. *Tectonophysics* **213**, 227–234.
- HAGGERTY, S.E (1976): Opaque mineral oxides in terrestrial igneous rocks. *Mineralogical Society of America Short Course Notes* **3**, 101–300.
- HALLIDAY, A.N., DICKIN, A.P., FALICK, A.E. AND FITTON, J.G. (1988): Mantle dynamic: an Nd, Sr, Pb and O isotopic study of the Cameroon line volcanic chain. *Journal of Petrology* **29**, 181–211.
- HAMMARSTROM, J.M. AND ZEN, E. (1986): Aluminum-in-hornblende: an empirical igneous geobarometer. *American Mineralogist* **71**, 1297–1313.
- HANCHAR, J.M. AND WATSON, E.B. (2003): Zircon saturation thermometry. In: HANCHAR, J.M AND HOSKIN, P.W.O. (eds.), *Zircon. Reviews in Mineralogy and Geochemistry* **58**, 89–112.
- HANMER, S.K. (1982): Microstructure and geochemistry of plagioclase and microcline in naturally deformed granite. *Journal of Structural Geology* **4**, 197–213.
- HANSON, G.N. (1978): The implication of the trace elements to the petrogenesis of the igneous rocks of granitic composition. *Earth and Planetary Science Letters* **38**, 26–43.
- HANSON, G.N. (1989): An Approach to trace element modelling using a simple igneous system as an example. In: LIPIN, B.R. AND MCKAY, G. (eds.), *Geochemistry and mineralogy of rare earth elements. Mineralogical Society of America, Reviews in Mineralogy* **21**, 79–97.
- HARKER, A. (1909): *The natural history of igneous rocks*. Methuen, London, 384 pp.
- HARRIS, N.B.W., PEARCE, J.A. AND TINDLE, A.G. (1986): Geochemical characteristics of collision-zone magmatism. In: COWARD, M.P. AND RIES, A.C. (eds.), *Collision Tectonics. Geological Society Special Publication* **19**, 67–81.
- HARRISON, T. M. AND WATSON, E.B. (1984): The behaviour of apatite during anatexis: equilibrium and kinetic considerations. *Geochimica et Cosmochimica Acta* **48**, 1467–1477.
- HAWTHORNE, F.C. (1983): The crystal chemistry of the amphiboles. *Canadian Mineralogist* **21**, 17–480.
- HEYEN, G., RAMBOZ, C. AND DUBESSY, A. (1982): Simulation des équilibres de phases dans le système CO₂–CH₄ en dessous de 50 °C et de 100 bar. Application aux inclusions fluides. *Comptes Rendus de l'Academie des Sciences* **294**, 203–206.
- HIBBARD, M.J. (1995): *Petrography to petrogenesis*. Prentice-Hall, Englewood Cliffs, New Jersey, 587 pp.

- HOLLAND, J. AND BLUNDY, J. (1994): Non-ideal interactions in calcic amphiboles and their bearing on amphibole–plagioclase thermometry. *Contributions to Mineralogy and Petrology* **116**, 433–447.
- HOLLISTER, L.S., GRISSOM, G.C., PETERS, E.K., STOWELL, H.H. AND SISSOM, V.B. (1987): Confirmation of the empirical correlation of Al in hornblende with pressure of solidification of Calc-alkaline plutons. *American Mineralogist* **72**, 231–239.
- HOLTZ, F. (1989): Importance of melt fraction and source rock composition in crustal genesis – the example of two granitic suites of northern Portugal. *Lithos* **24**, 21–35.
- HOLTZ, F. AND JOHANNES, W. (1991): Genesis of peraluminous granites. I, Experimental investigation of melt compositions at 3 and 5 kb and various H₂O activities. *Journal of Petrology* **32**, 935–958.
- HOSKIN, P.W.O., KINNY, D.P., WYBORN, D. AND CHAPPELL, B.W. (2000): Identifying accessory mineral saturation during differentiation in granitoids magmas: an integrated approach. *Journal of Petrology* **41**, 1365–1396.
- INGER, S. AND HARRIS, N.B.W. (1993): Geochemical constraints on leucogranite magmatism in the Langtang valley, Nepal Himalaya. *Journal of Petrology* **34**, 345–368.
- ISHIHARA, S. (1977): The magnetite-series and ilmenite-series granitic rocks. *Mining Geology* **27**, 293–305.
- JACKSON, N.J. AND RAMSAY, C.R. (1980): What is the “Pan-African”? A consensus is needed. *Geology* **8**, 210–211.
- JACQUEMIN, H., SHEPPARD, S.M. AND VIDAL, P. (1982): Isotopic geochemistry (O, Sr, Pb) of the Golda Zuelva and Mboutou anorogenic complexes, North Cameroon: mantle origin with evidence for crustal contamination. *Earth and Planetary Science Letters* **61**, 97–111.
- JACOBSEN, S.G. AND WASSERBURG, G.J. (1980): Sm–Nd isotopic evolution of chondrites. *Earth and Planetary Science Letters* **50**, 139–155.
- JIANG, Y.-H., JIANG, A.-Y., LING, H.-L., ZHOU, X.-R., RUI, X.-J. AND YANG, W.-Z. (2002): Petrology and geochemistry of shoshonitic plutons from the western Kunlun orogenic belt, Xinjiang, northwestern China: implication for granitoid geneses. *Lithos* **63**, 165 – 187.
- JOHNSON, M.C. AND RUTHERFORD, M.J. (1989): Experimental calibration of the aluminum-in-hornblende geobarometer with application to long Valley caldera (California) volcanic rocks. *Geology*, 837–841.
- JUNG, S., HOEMES, S. AND MEZGER, K. (2001): Trace element and isotopic (Sr, Nd, Pd, O) arguments for a mid-crustal origin of Pan-African garnet-bearing S-type granites from the Damara orogen (Namibia). *Precambrian Research* **110**, 325–355.
- KAMDEM, J.B., KRAML, M., KELLER, J. AND HENJES-KUNST, F. (2002): Cameroon Line magmatism: conventional K/Ar and single-crystal laser $^{40}\text{Ar}/^{39}\text{Ar}$ age of rocks and minerals from the Hossere Nigo anorogenic complex, Cameroon. *Journal of African Earth Sciences* **35**, 99–105.

- KAMGANG, P. (1986): *Contribution à l'étude géologique et pétrologique de massif de Nkogam (pays Bamoun, Ouest Cameroun)*. Thèse de Doctorat, Université de Yaoundé, Cameroun, 250 pp.
- KELSEY, C.H. (1965): Calculation of the C.I.P.W. norm. *Mineralogical Magazine* **34**, 276–282.
- KENNEDY, W.Q. (1964): The structural differentiation of Africa in the Pan African (\pm 500 million years) tectonic episode. *8th annual Report, Research Institute of African Geology, University of Leeds, England*, 48–49.
- KING, P.L., WHITE, A. J. R., CHAPELLE, B.W. AND ALLEN, C.M. (1997): Characterisation and origin of aluminous A-type granites from the Lachlan Fold Belt, Southeastern Australia. *Journal of Petrology* **38**, 371–391.
- KING, R.J. (1989): Alkali feldspars, Part 1. *Geology Today* **5**, 211–213.
- KONINGS, R.J.M., BOLAND, J.N., VRIEND, S.P. AND JANSEN, J.B.H. (1988): Chemistry of biotites and muscovites in the Abas granite, northern Portugal. *American Mineralogist* **73**, 754–765.
- KORNPROBST, J., CANTAGREL, J.M., FABRIES, M., LASSERRE, M., ROLLET, M. AND SOBA, D. (1976): Existence au Cameroun d'un magmatisme alcalin panafricain ou plus ancien : la syénite néphélinique de Nkonglong. Comparaison avec les roches alcalines connues dans la même région. *Bulletin de la Société Géologique de France* **18**, 1295–1305.
- KRETZ, R. (1983): Symbols for Rock-forming minerals. *American Mineralogist* **68**, 277–279.
- KRÖNER, A. (1980): Pan-African crustal evolution. *Episodes* **2**, 3–8.
- KRUHL, H.J. (1996): Prism- and basal-plane parallel subgrain boundaries in quartz: a microstructural geothermobarometer. *Journal of Metamorphic Geology* **14**, 581–589.
- KÜSTER, D. AND HARMS, U. (1998): Post-collisional potassic granitoids from the southern and northwestern parts of the Late Neoproterozoic East African Orogen: a review. *Lithos* **45**, 177–195.
- KWEKAM, M. (1993): *Le massif plutonique calco-alcalin panafricain de Fomopéa (Ouest Cameroun): cadre structural-pétrochimie-géochimie-interprétations géodynamiques*. Thèse de Doctorat, Université de Yaoundé I, Cameroun, 154 pp.
- LAGARDE, J.-L., CAPDEVILA, R. AND FOURCADE, S. (1992): Granites et collision continentale: L'exemple des granitoïdes carbonifères dans la chaîne hercynienne ouest-européenne. *Bulletin de la Société Géologique de France* **163**, 597–610.
- LALONDE, A.E. AND BERNARD, P. (1993): Composition and colour of biotite from granites: two useful properties in the characterization of plutonic suites from the Hepburn internal zone of the Wopmay orogen, Northwest Territories. *Canadian Mineralogist* **31**, 203–217.
- LAMEYRE, J. AND BONIN, B. (1991): Granites in the main plutonic series. In: DIDIER, J. AND BARBARIN, B. (eds.), *Enclaves and Granites Petrology*, Elsevier, Amsterdam, 3–17.

- LAMEYRE, J. AND BOWDEN, P. (1982): Plutonic rock series: Discrimination of various granitoid series and related rocks. *Journal of Volcanology and Geothermal Research* **14**, 169–186.
- LAMILÉN, B.D. (1989): *Contribution à l'étude du complexe anorogénique du Mont Koupé: un exemple de la série alcaline incomplète*. Thèse de Doctorat, Université de Yaoundé, Cameroun, 183 pp.
- LASSERRE, M. (1978): Mise au point sur les granitoïdes dits "ultimes" du Cameroun: gisement, pétrographie et géochronologie. *Bulletin du Bureau de la Recherche Géologiques et Minières: Géologie Générale* **4**, 143–159.
- LASSERRE, M. AND SOBA, D. (1976a): Âge libérien des granodiorites et des gneiss à pyroxène du Cameroun méridional. *Bulletin du Bureau de la Recherche Géologiques et Minières* **4**, 17–32.
- LASSERRE, M. AND SOBA, D. (1976b): Âges cambriens des granites de Nyibé et de Kongolo (Centre Est Cameroun). *Comptes Rendus de l'Académie des Sciences* **283**, 1695–1698.
- LASSERRE, M. AND SOBA, D. (1979): Migmatisation d'âge Panafricain au sein des formations camerounaises appartenant à la zone mobile de l'Afrique Central. *Compte rendu sommaire de la Société Géologique de France* **2**, 64–68.
- LASSERRE, M., TEMPIER, P. AND SUIRE, J. (1981a): Age (Rb/Sr) cambrien supérieur de quelques granites camerounais situés au sein de la zone mobile de l'Afrique centrale. *Comptes Rendus de l'Académie des Sciences* **292**, 903–907.
- LASSERRE, M., TEMPIER, P. AND SOBA, D. (1981b): Pétrographie et géochronologie Rb/Sr des granites cambriens de Goutchoumi et d'Anloa (Cameroun). *Bulletin de la Société Géologique de France* **23**, 509–512.
- LEAKE, B.E. (1971): On aluminous and edenitic amphiboles. *Mineralogical Magazine* **38**, 389–407.
- LEAKE, B.E. (1990): Granite magmas: their sources, initiation and consequences of emplacement. *Journal of the Geological Society, London* **147**, 579–589.
- LEAKE, B.E., SCHUMACHER, J.C., SMITH, D.C., STEPHENSON, N.C.N., UNGARETTI, L., WHITTAKER, E.J.W. AND YOZHI, G. (1997): Nomenclature of amphiboles. *European Journal of Mineralogy* **9**, 623–642.
- LEAKE, B.E., WOOLLEY, A.L., BIRCH, W.D., BURKE, E.A.J., FERRARIS, G., GRICE, J.D., HAWTHORNE, F.C., KISCH, H.J., KRIVOVICHEV, V.G., SCHUMACHER, J.C., STEPHESON, N.C.N. AND WHITTAKER, E.J.W. (2004): Nomenclature of amphibole: additions and revisions to the International Mineralogical Association's amphibole nomenclature. *European Journal of Mineralogy* **16**, 191–196.
- LE FUR, Y. (1971): Les indices de cuivre du groupe volcano-sédimentaire de Poli (Cameroun). *Bulletin du Bureau de la Recherche Géologique et Minière, section 2: Géologie Appliquée, chronique des mines* **6**, 79 pp.

- LE GUERN, F. AND SIGVALDSSON, G. (eds.) (1989): The Lake Nyos event and Natural CO₂ degassing. *Journal of Volcanology and Geothermal Research Special Issue* **39**, 2–3.
- LE MAITRE, R.W. (ed.), BATEMAN, P., DUBEK, A., KELLER, J., LAMEYRE, J., LE BAS, M.J., SABINE, P.A., SCHMID, R., SØRENSEN, H., STRECKEISEN, A., WOOLLEY, A.R. AND ZANETTIN, B. (1989): *A classification of igneous rocks and glossary of terms. Recommendations of the International Union of Geological Sciences Subcommission on the Systematics of Igneous Rocks*. Blackwell, Oxford, 193 pp.
- LEDRU, P., COCHERIE, A., BARBOSA, J., JOHAN, V. AND ONSTOTT, T. (1994): âges du métamorphisme granulitique dans le craton du São Francisco (Brazil): implication sur la nature de l'orogenèse transamazonien. *Comptes Rendus de l'Académie des Sciences* **318**, 251–257.
- LE FORT, P. (1981): Manaslu leucogranite: a collision signature of the Himalaya, a model for its genesis and emplacement. *Journal of Geophysical Research* **86**, 10545–10568.
- LEE, D.C., HALLIDAY, A.N, FITTON, J.G. AND POLI, G. (1994): Isotopic variations with distance and time in the volcanic islands of the Cameroon Line: evidence for a mantle plume origin. *Earth and Planetary Science Letters* **123**, 119–138.
- LEROUGE, C., COCHERIE, A., TCHAMENI, R., MILESI, J.P., TOTEU, S.F., PENAYE, J., NSIFA, N.E. AND FANNIN C.M. (2004): SHRIMP U-Pb zircon dating for the Nyong Series, South West Cameroon. *20th colloquium of African Geology, B.G.R.M Orleans, France, Abstracts Volume*, p 262.
- LIÉGEOIS, J.-P. AND BLACK, R. (1987): Alkaline magmatism subsequent to collision-related Pan-African belt of the Adrar des Iforas. In: FITTON, J.G., AND UPTON, B.G.J. (eds.), *Alkaline Igneous Rocks*. *Geological Society Special Publication* **30**, 381–401.
- LIÉGEOIS, J.-P., NAVEZ, J., HERTOGEN, J. AND BLACK, R. (1998): Contrasting origin of post-collisional high-K calc-alkaline and shoshonitic versus alkaline and peralkaline granitoids: the use of sliding normalization. *Lithos* **45**, 1–28.
- LOISELLE, M.C. AND WONES, D.R. (1979): Characteristics and origin of anorogenic granites. *Geological Society of America, Abstracts* **11**, pp 468.
- LUGMAIR, G.W. AND MARTI, K. (1978): Lunar initial $^{143}\text{Nd}/^{144}\text{Nd}$: Differential evolution of the lunar crust and mantle. *Earth and Planetary Science Letters* **39**, 3349–3357.
- LUDWIG, K.R. (2000): *Isoplot/Ex (Version 2.45)—A geochronological toolkit for Microsoft Excel*. Berkeley Geochronology Center Special Publication 1b, 54 pp.
- MALLARD, L.D. AND ROGERS, J.J.W. (1997): Relationship of the Avalonian and Cadomian terranes to Grenville and Pan-African events. *Journal of Geodynamics* **23**, 197–222.
- MANIAR, P.D. AND PICCOLI, P.M. (1989): Tectonic discrimination of granitoids. *Geological Society of American Bulletin* **101**, 635–643.
- MARZOLI, A., PICCIRILLO, E.M., RENNE, P.R., BELLINI, G., IACUMIN, M., NYOBE, J.B. AND TONGWA, A.T. (2000): The Cameroon Volcanic Line revised: petrogenesis of continental

- basaltic magmas from lithospheric and asthenospheric mantle sources. *Journal of Petrology* **41**, 87–109.
- MARZOLI, A., RENNE, P.R., PICCIRILLO, E.M., CASTORINA, F., BELLINI, G., MELFI, A.J., NYOBE, J.B. AND N'NI, J. (1999): Silicic magmas from the continental Cameroon Volcanic Line (Oku, Bambouto and Ngaoundéré): 40Ar/39Ar dates, petrology, Sr–Nd–O isotopes and their petrogenetic significance. *Contributions to Mineralogy and Petrology* **135**, 133–150.
- MASSONNE, H.-J. AND SCHREYER, W. (1987): Phengite geobarometry based on the limiting assemblage with K-feldspar, phlogopite and quartz. *Contributions to Mineralogy and Petrology* **96**, 212–224.
- MAURIN, J.C. AND GUIRAUD, R. (1990): Relationships between tectonic and sedimentation in the Barremo - Aptien intracontinental basins of Northern Cameroon. *Journal of African Earth Sciences* **10**, 331–340.
- MAURIZOT, P., ABESSOLO, A., FEYBESSE, J.L., JOHAN, V. AND LECOMTE, P. (1986): Etude de la prospection minière du Sud-Ouest Cameroun. Synthèse des travaux de 1978 à 1985. *Rapport du Bureau de Recherche Géologiques et Minières* **85**, CMR 066, 274 pp.
- MAYER, J.B., ROSENDAL, B.R. AND GROSCHL-BERKER, H. (1996): Deep penetrating MCS imaging of the rift-to-drift transition, offshore Douala and North Gabon basins, West Africa. *Marine Petroleum Geology* **13**, 791–835.
- MCCULLOCH, M.T. AND CHAPPELL, B.W. (1982): Nd isotopic characteristics of S- and I-type granites. *Earth and Planetary Sciences Letters* **58**, 51–64.
- MCDERMOTT, F., HARRIS, N.B.W. AND HAWKESWORTH, C.J. (1996): Geochemical constraints on crustal anatexis: a case study from the Pan-African Damara granitoids of Namibia. *Contributions to Mineralogy and Petrology* **123**, 406–423.
- MCDONOUGH, W.F AND SUN, S.S. (1995): The composition of the Earth. *Chemical Geology* **120**, 223–253.
- MICHARD, A., GURRIET, P., SOUDANT, M. AND ALBAREDE, F. (1985): Nd isotopes in French Phanerozoic shales: external vs. internal aspects of crustal evolution. *Geochimica et Cosmochimica Acta* **49**, 601–610.
- MICHON, G. (1987): Les vauvénrites de l'Est du Massif central français: apport de l'analyse statistique multivariée à l'étude géochimique des éléments majeurs. *Bulletin de la société Géologique de France* **3**, 59–600.
- MIDDLEMOST, E.A.K. (1994): Naming materials in the magma/igneous rock system. *Earth-Science Reviews* **37**, 215–224.
- MIDDLEMOST, E.A.K. (1997): *Magmas, Rocks, and planetary Development*. Longman, Harlow, 299 pp.
- MILLER, C.F., McDOWELL, S.M. AND MAPES, R.W. (2003): Hot and cold granites? Implication of zircon saturation temperatures and preservation of inheritance. *Geology* **31**, 529–532.

- MILLER, C.F. AND STODDARD E.F. (1981): The role of manganese in the paragenesis of magmatic garnet: an example from the old Woman-Piute range California. *Journal of Geology* **89**, 233–246.
- MILLER, C.F., STODDARD, E.F., BRADFISH, L.J. AND DOLLASE, W.A. (1981): Composition of plutonic muscovite: genetic implications. *Canadian Mineralogist* **19**, 25–34.
- MILLER, C.F. (1985): Are strongly peraluminous magmas derived from pelitic sedimentary sources? *Journal of Geology* **93**, 673–643.
- MILLER, C.F., WATSON, E.B. AND HARRISON, T.M. (1988): Perspectives on the source, segregation and transport of granitoid magmas. *Transactions of the Royal Society of Edinburgh: Earth Sciences* **79**, 135–156.
- MIYASHIRO, A. (1978): Nature of alkalic volcanic rock series. *Contributions to Mineralogy and Petrology* **66**, 91–104.
- MONIER, D., MERGOIL-DANIEL, J. AND LABERNARDIERE, H. (1984): Génération successives de muscovites et feldspaths potassiques dans les leucogranites de Massifs de Millevaches (Massif Central français). *Bulletin de Minéralogie* **107**, 55–68.
- MONIER, G AND ROBERT, J.L. (1986): Titanium in muscovites from two mica granites: Substitutional mechanism and partition with coexisting biotites. *Neues Jahrbuch für Mineralogie Abhandlungen* **153**, 147–161.
- MOREAU, C., REGNOULT, J.M., DÉRUELLE, B. AND ROBINEAU, B. (1987): A new tectonic model for the Cameroon Line, Central Africa. *Tectonophysics* **141**, 317–334.
- MORRISON, G.W. (1980): Characteristics and tectonic setting of the shoshonite rock association. *Lithos* **13**, 97–108.
- MÜLLER, D., ROCK, N.M.S. AND GROVES, D.I. (1992): Geochemical discrimination between shoshonitic and potassic volcanic rocks in different tectonic settings: a pilot study. *Mineralogy and Petrology* **46**, 259–289.
- MURPHY, P.J. AND ROBERTS, S. (1995): Laser Raman Spectroscopy of differential partitioning in mixed-gas clathrates in $\text{H}_2\text{O}-\text{CO}_2-\text{N}_2-\text{CH}_4$ fluids inclusions: Implication for microthermometry. *Geochimica et Cosmochimica Acta* **59**, 4809–4824.
- MVONDO, H., DEN BROK, S.W.J. AND MVONDO ONDOA, J. (2003): Evidence for symmetric extension and exhumation of the Yaounde nappe (Pan-African fold belt, Cameroon). *Journal of African Earth Sciences* **36**, 215–231.
- NABELEK, P.I., RUSS-NABELEK, C. AND DENISON, J.R. (1992): The generation and crystallization conditions of the Proterozoic Harney Peak Leucogranite, Black Hills, South Dakota, USA: Petrogenetic and geochemical constraints. *Contributions to Mineralogy and Petrology* **110**, 173–191.
- NACHIT, H. (1986): *Contribution à l'étude analytique et expérimental des biotites des granitoïdes. Applications typologiques.* Thèse de Doctorat, Université de Bretagne Occidentale, Brest, France, 238 pp.

- NACHIT, H., RAZAFIMAHEFA, N., STUSSI, J.-M. AND CARRON, P.J. (1985): Composition chimique des biotites et typologie magmatique des granitoïdes. *Comptes Rendus de l'Académie des Sciences* **301**, 813–818.
- NALINI JR, H.A., BILAL, E. AND CORREIA NEVES, J.M. (2000): Syn-collisional peraluminous magmatism in the Rio Doce region: mineralogy, geochemistry and isotopic data of the Neoproterozoic Urucum suite (Eastern Minas Gerais state, Brazil). *Revista Brasileira de Geociências* **30**, 120–125.
- NANA, J.M. (1988): *Le complexe volcano-plutonique de Bana (Ouest-Cameroun): géologie et pétrologie*. Thèse de Doctorat, Université de Paris XI, France, 131 pp.
- NEDELEC, A., MACAUDIERE, J., NZENTI, J.-P. AND BARBEY, P. (1986): Evolution structurale et métamorphique des schistes de Mbalmayo (Cameroun). Implication sur la structure de la zone mobile panafricaine d'Afrique Centrale au contact du craton du Congo. *Comptes Rendus de l'Académie des Sciences* **303**, 75–80.
- NEDELEC, A., MINYEM, D. AND BARBEY, P. (1993): High-*P*–high-*T* anatexis of Archaean tonalitic grey gneisses; the Eseka migmatites, Cameroon. *Precambrian Research* **62**, 191–205.
- NÉDÉLEC, A., NSIFA, E.N. AND MARTIN, H. (1990): Major and trace element geochemistry of the Archaean Ntem plutonic complex (South Cameroon): Petrogenesis and crustal evolution. *Precambrian Research* **47**, 35–50.
- NEVES, S.P., MELO, S.C., MOURA, C.A.V., MARIANO, G. AND RANGEL DA SILVA, J.M. (2004): Zircon Pb–Pb geochronology of the Garuara, Northeastern Brazil: Temporal constrains on the Proterozoic evolution of Borborema Province. *International Geology Review* **46**, 52–63.
- NGAKO, V., AFFATON, P., NNANGE, J.M. AND NJANKO, T. (2003): Pan-African tectonic evolution in central and southern Cameroon; transpression and transtension during sinistral shear movements. *Journal of African Earth Sciences* **36**, 207–214.
- NGAKO, V., JEGOUZO, P. AND NZENTI, J.-P. (1991): Le cisaillement centre–Camerounais. Rôle structural et géodynamique dans l'orogenèse panafricaine. *Comptes Rendus Académie Sciences, Paris* **313**, 457–463.
- NGAKO, V., JEGOUZO, P. AND SOBA, D. (1989): Déformation et métamorphisme dans la chaîne Panafricaine de Poli (Nord Cameroun): implication géodynamiques et paléogéographiques. *Journal of African Earth Sciences* **9**, 541–555.
- NGNOTUÉ, T., NZENTI, J.P., BARBEY, P. AND TCHOUA, F.M. (2000): The Ntui-Bétamba high-grade gneisses: a northward extension of the Pan-African Yaoundé gneisses in Cameroon. *Journal of African Earth Sciences* **31**, 369–381.
- NGONGÉ, E.G. (1988): *A geological study of the anorogenic complex of the Gwenfalabo (An example of a complete series), in the region west of the Adamawa Highlands, Cameroon*. Doctorate Thesis, University of Yaoundé, Cameroon, 156 pp.

- NGOUNOUNO, I., DÉRUELLE, B., DEMAIFF, D. AND MONTIGNY, R. (2003): Petrology of the Cenozoic volcanism in the upper Benue Valley, northern Cameroon (Central Africa). *Contributions to mineralogy and Petrology* **145**, 88–106.
- NGUÉNÉ, F.R. (1982): *Geology and geochemistry of the Mayo-Darlé tin deposit, West-Central Cameroon, Central Africa*. PhD Thesis, New Mexico Institute of Mining and technology, New Mexico, 188 pp.
- NGUIESSI-TCHANKAM, C. AND VIALETTE, Y. (1994): Données géochronologiques (Rb–Sr, Pb–Pb, U–Pb) sur le complexe plutonique de Bandja (Centre–Ouest Cameroun). *Comptes Rendus de l'Académie Sciences* **319**, 317–324.
- NGUIESSI-TCHANKAM, C. (1994): *Le complexe plutonique calco-alcalin de Bandja lié à la chaîne panafricaine de l'Ouest Cameroun*. Thèse de Doctorat, Université de Nancy I, France, 240 pp.
- NGUIESSI-TCHANKAM, C., NZENTI, J.-P., NSIFA, E.N., TEMPIER, P. AND TCHOUA, F.M. (1997): Les granitoïdes calco-alcalins, syncisaillement de Bandja dans la chaîne panafricaine nord équatoriale au Cameroun. *Comptes Rendus de l'Académie Sciences* **325**, 95–101.
- NJIÉKAK, G., ZULAUF, G. AND TCHOUANKOUÉ, J.-P. (2003): Brittle deformation of the West Cameroon Highlands (Central part of the Cameroon Line). *Zbl. für Geologie und Paläontologie I* **3/4**, 243–265.
- NJEL, U.O. (1988): *Contribution à l'étude de l'orogenèse panafricaine: la ceinture volcanosédimentaire de Poli (Nord Cameroun)*. Thèse Doctorat, Université de Nancy I, France, 220 pp.
- NJOM, B., MOUSSANGO-IBOHN, P., NVONDO-OWONO, F. AND NIYONKURU, J. (2004): Les Pseudotachylites, révélateurs du système néotectonique de la Sanaga. *20th colloquium of African Geology, B.G.R.M Orleans, France, Abstracts Volume*, p 313.
- NJONFANG, E. (1998): *Contribution à l'étude de la relation entre la "Ligne du Cameroun" et la direction de l'Adamaoua: 1. Pétrologie, Géochimie et Structure des Granitoïdes Panafricains de la zone de cisaillement Foumban–Bankim (Ouest–Cameroun et Adamaoua). 2. pétrologie et géochimie des formations magmatiques tertiaires associées*. Thèse de Doctorat d'État, Université de Yaoundé I, Cameroun, 392 pp.
- NJONFANG, E., KANGANG, P., GHOGOMU, R.T. AND TCHOUA, F.M. (1992): The geochemical characteristics of some plutonic-volcanic complexes along the southern part of the Cameroon line. *Journal of African Earth Sciences* **14**, 255–266.
- NJONFANG, E., MOREAU, C. AND TCHOUA, F.M. (1998): La Bande mylonitique Foumban–Bankim, Ouest Cameroun: une zone de cisaillement de haute température. *Comptes Rendus de l'Académie des Sciences* **327**, 735–741.
- NORMAN, M.D., LEEMAN, W.P. AND MERTZMAN, S.A. (1992): Granites and rhyolites from the northwestern U.S.A.: temporal variation in magmatic processes and relations to tectonic setting. *Transactions of the Royal Society of Edinburgh: Earth Sciences* **83**, 71–81.

- NSIFA, E.N. AND RIOU, R. (1990): Post-Archaean migmatization in the charnockitic series of the Ntem complex, Congo craton, southern Cameroon. In: ROCCI, G AND DESCHAMPS, M. (eds.), *Etudes récente sur la géologie de l'Afrique. 15th colloquium of African Geology, Abstract Volume, Occasional Publication* **22**, 33–36.
- NZENTI, J.-P., BARBEY, P., MACAUDIÈRE, J. AND SOBA, D. (1988): Origin and the evolution of the late Precambrian high-grade Yaoundé gneisses (Cameroon). *Precambrian Research* **38**, 91–109.
- NZENTI, J.-P., NGAKO, V., KAMBOU, R., PENAYE, J., BASSAHAK, J. AND NJEL, O.L. (1992): Structures régionales de la chaîne panafricaine du Nord-Cameroun. *Comptes Rendus de l'Académie Sciences* **315**, 209–215.
- NZOLANG, C. (2005): *Crustal evolution of the Precambrian Basement in west Cameroon: inference from geochemistry, Sr–Nd isotopic and experimental investigation of some granitoids and metamorphic rocks*. PhD Thesis, Graduate School of Science and Education, Niigata University, Japan, 207 pp.
- NZOLANG, C., KAGANI, H., NZENTI, J.-P. AND HOLTZ, F. (2003): Geochemistry and preliminary Sr–Nd isotopic data on the Neoproterozoic granitoids from Bantoum area, West, Cameroon: evidence for a derivation from Paleoproterozoic to Archean crust. *Polar Geoscience, Tokyo* **16**, 196–226.
- O'BRIEN, S.J., WARDLE, R.J. AND KING, A.F. (1983): The Avalon Zone: a Pan-African terrane in the Appalachian Orogen of Canada. *Eos, Transactions, American Geophysical Union* **64**, 750 p.
- PARSONS, I. AND BOYED, R. (1971): Distribution of potassium feldspar polymorphs in intrusive sequences. *Mineralogical Magazine* **38**, 295–311.
- PARSONS, I., BROWN, W.L. AND JACQUEMIN, H. (1986): Mineral chemistry and crystallization condition of the Mboutou layered gabbro-syenite-granite complex, North Cameroon. *Journal of Petrology* **27**, 1305–1329.
- PASSCHIER, C.W. AND TROUW, R. A. J. (1998): *Microtectonics* (second edition). Springer-Verlag Berlin Heidelberg, 289 pp.
- PATERSON, S.R., VERNON, R.H. AND TOBISH, O.T. (1989): A review of criteria for the identification of magmatic and tectonic foliations in Granitoids. *Journal of Structural Geology* **11**, 349–363.
- PATIÑO-DOUCE, A.E. (1993): Titanium substitution in biotite: an empirical model with application to thermometry, O₂ and H₂O barometries, and consequences for biotite stability. *Chemical Geology* **108**, 133–162.
- PATIÑO-DOUCE, A.E. (1999): What do experiments tell us about the relative contributions of crust and mantle to the origin of granitic magmas? In: CASTRO, A., FERNANDEZ, C. AND VIGNERESSE, J.L. (eds.), *Understanding Granites: Integrating New and Classical Techniques. Geological Society Special Publication* **168**, 55–75.
- PEARCE, J.A. (1996): Sources and settings of granitic rocks. *Episodes* **19**, 120–125.

- PEARCE, J.A., HARRIS, N.B.W. AND TINDLE, A.G. (1984): Trace element discrimination diagrams for the tectonic interpretation of granitic rocks. *Journal of Petrology* **25**, 956–983.
- PEARCE N.J.G., PERKINS W.T., WESTGATE J.A., GORTON M.P., JACKSON S.E, NEAL C.R, CHENERY S.P. (1997): A compilation of new and published major and trace element data for NIST SRM 610 and NIST SRM 612 glass reference materials. *Geostandards Newsletter* **21**, 115–144.
- PENAYE, J. (1988): *Pétrologie et structure des ensembles métamorphiques au sud-est de Poli (Nord Cameroun): Rôles respectifs du socle protérozoïque inférieur et de l'accrétion crustale panafricaine*. Thèse de Doctorat, Université de Nancy I, France, 196 pp.
- PENAYE, M.P., TOTEU, S.F., MICHAUD, A., BERTRAND, J.M. AND DAUTEL, D. (1989): Reliques granulitiques d'âge Protérozoïque inférieur dans la zone mobile panafricaine d'Afrique Centrale au Cameroun; géochronologie U/Pb sur Zircons. *Comptes Rendus de l'Académie Sciences* **309**, 315–318.
- PENAYE, J., TOTEU, S.F., TCHAMENI, R., VAN SCHMUS, W.R., TCHAKOUNTÉ, J., GANWA, A.A., MINYEM, D. AND NSIFA, E.N. (2004): The 2.1 Ga West Central African Belt in Cameroon: extension and evolution. *Journal of African Earth Sciences* **39**, 159–164.
- PENAYE, J., TOTEU, S.F., VAN SCHMUS, W.R. AND NZENTI, J.-P. (1993): U-Pb and Sm-Nd preliminary geochronologic data on the Yaoundé series, Cameroon: signification of the granulitic rocks in the "centrafrican" belt. *Comptes Rendus de l'Académie des Sciences* **317**, 789–794.
- PE-PIPER, G., PIPER, D.J.W. AND MATARANGAS, D. (2002): Regional implication of the geochemistry and style of emplacement of the Miocene I-type diorite and granite, Delos, Cyclades, Greece. *Lithos* **60**, 47–66.
- PICHAVANT, M., MONTEL, J.-M. AND RICHARD, L.R. (1992): Apatite solubility in peraluminous liquids; experimental data and extension of the Harrison-Watson model. *Geochimica et Cosmochimica Acta* **56**, 3588–3861.
- PICHAVANT, M., HAMMOUDA, T. AND SCAILLET, B. (1996): Control of redox state and Sr isotopic composition of granitic magmas: a critical evaluation of the role of source rocks. *Transactions of the Royal Society of Edinburgh: Earth Sciences* **88**, 321–329.
- PIMENTEL, M.M., FUCK, A.R. AND SOUZA DE ALVARENGA, C.J. (1996): Post-Brasiliano (Pan-African) high-K granitic magmatism in Central Brazil: the role of the Late Precambrian-early Paleozoic extension. *Precambrian Research* **80**, 217–238.
- PIN, C. AND POIDEVIN, J.L. (1987): U-Pb zircon for a Pan-African granulite facies metamorphism in the Central African Republic: a new Interpretation of the high-grade series of the northern border of the Congo Craton. *Precambrian Research* **36**, 303–312.
- PINNA, P., CALVEZ, J.Y., ABESSOLO, A., ANGEL, J.M., MEKOULOU-MEKOULOU, T., MANANGA, G. AND VERNHET, Y. (1994): Neoproterozoic events in the Tcholliré area: Pan-African crustal growth and geodynamics in central-northern Cameroon (Adamawa and North Provinces). *Journal of African Earth Sciences* **18**, 347–353.

- PINNA, P., EDIMO, A., SALPETEUR, I., JÉZÉQUEL, P., EBOYATUK EBOP, S. AND TCHOUNTCHOUI, D. (1989): Inventaire minier du Centre Nord Cameroun, 3ème phase. *Rapport B.R.G.M* **88**, CMR 168, 173 p.
- PITCHER, W.S. (1987): Granite and yet more granites forty years on. *Geologische Rundschau* **76**, 51–79.
- PITCHER, W.S. (1997): *The Nature and Origin of Granite* (second edition). Chapman & Hall, London, 387 pp.
- POIDEVIN, J.L. (1985): *Le protérozoïque supérieure de la république Centrafricaine*. Annales Musée Royal de l'Afrique Centrale, Tervuren, Belgium, Sciences Géologiques **91**, 75 pp.
- PORADA, H. (1989): Pan-African rifting and orogenesis in southern to equatorial Africa and eastern Brazil. *Precambrian Research* **44**, 103–136.
- POTTS, P.J., BOWLES, J.F.W., REED, S.J.B. AND CAVE, M.R. (1995): *Microprobe techniques in the Earth Sciences. Mineralogical Society* **6**, Chapman & Hall, London, 419 pp.
- PRESSLEY, R.A. AND BROWN, M. (1999): The Phillips pluton, Maine, USA: evidence of heterogeneous crustal sources and implications for granite ascent and emplacement mechanisms in convergent orogens. *Lithos* **46**, 335–366.
- PRYER, L.L. AND ROBIN, P.-Y.F. (1995): Retrograde metamorphic reactions in deforming granites and the origin of the flame perthite. *Journal of Metamorphic Geology* **13**, 645–658.
- PUZIEWICZ, J. AND KOEPKE, J. (1991): Controls on the TiO₂ content in the muscovite and biotite from a two-mica granite, the Strzegom–Sobotka Massif, Sudetes, SW Poland. *Neues Jahrbuch für Mineralogie, Monatshefte*, 243–261.
- RAHAMAN, M.A., VAN BREEMEN, O., BOWDEN, P. AND BENNET, J.N. (1984): Age migration of anorogenic ring complexes in Northern Nigeria. *Journal of Geology* **92**, 173–184.
- RIBBE, P.H. (1975): Chemistry, structure and nomenclature of feldspars. In: RIBBE, P.H. (ed.), *Feldspar Mineralogy. Mineralogical Society of America Short Course Note* **2**, 1–52.
- RICE, A. (2000): Rollover in volcanic crater lakes: a possible cause for the lake Nyos type disasters. *Journal of Volcanology and Geothermal Research* **97**, 233–239.
- RICKWOOD, P.C. (1989): Boundary lines within petrologic diagrams which use oxides of major and minor elements. *Lithos* **22**, 247–264.
- RIEDER, M. (2001): Mineral nomenclature in the mica group: the promise and the reality. *European Journal of Mineralogy* **13**, 1009–1012.
- RIEDER, M., CAVAZZINI, G., D'YAKONOV, Y.S., FRANKKAMENETSKII, V.A., GOTTARDI, G., GUGGENHEIM, S., KOVAL, P.V., MÜLLER, G., NEIVA, A.M.R., RADOSLOVICH, E.W., ROBERT, J.-L., SASSI, F.P., TAKEDA, H., WEISS, Z. AND WONES, D.R. (1998): Nomenclature of the mica. *Canadian Mineralogist* **36**, 905–912.

- ROBERT, J.L. (1981): *Études cristallochimiques sur les micas et les amphiboles: applications à la pétrographie et à la géochimie*. Thèse de Doctorat, Université de Paris Sud, Orsay, France, 206 pp.
- ROBERTS, M.P. AND CLEMENS, J.D. (1993): Origin of high-potassium calc-alkaline, I-type granitoids. *Geology* **21**, 825–828.
- ROBERTS, M.P. AND CLEMENS, J.D. (1995): Feasibility of AFC models for the petrogenesis of calc-alkaline magmas series. *Contributions to Mineralogy and Petrology* **121**, 139–147.
- ROBERTS, M.P., PIN, C., CLEMENS, J.D. AND PAQUETTE, J.L. (2000): Petrogenesis of mafic to felsic plutonic rock associations: the Calc-alkaline Quérigut Complex, French Pyrénées. *Journal of Petrology* **41**, 809–844.
- ROBINSON, P., ROSS, M. AND JAFFE, M.W. (1971): Composition of the anthophyllite-gedrite series, comparisons of the gedrite and hornblende, and the anthophyllite-gedrite solvus. *American Mineralogist* **56**, 1005–1041.
- ROEDDER, E. (1984): *Fluid inclusions*. Mineralogical Society of America, Reviews in Mineralogy **12**, 646 pp.
- ROGERS, J.J.W. AND GRENBERG, J.K. (1990): Late-orogenic, Post-orogenic, and anorogenic granites: Distinction by major-element and trace-element chemistry and possible origins. *Journal of Geology* **98**, 291–309.
- ROGERS, J.J.W., UNRUG, R. AND SULTAN, M. (1995): Tectonic assembly of Gondwana. *Journal of Geodynamics* **19**, 1–34.
- ROLLINSON, H.R. (1993): *Using Geochemical Data: evaluation, presentation, interpretation*. Longman Scientific and Technical, Essex, 352 pp.
- ROTTURA, A., BARGOSSI, G.M., CAGIANELLI, A., DEL MORO, A., VISONÀ, D. AND TRANNE, C.A. (1998): Origin and significance of the Permian high-K calc-alkaline magmatism in the central-eastern Southern Alps, Italy. *Lithos* **45**, 329–348.
- RUDNICK, R.L. (1990): Nd and Sr isotopic compositions of lower-crustal xenoliths from north Queensland, Australia: Implication for the Nd model ages and crustal growth processes. *Chemical Geology* **83**, 195–208.
- SAMSON, S.C., PATCHETT, P.J., MCCLELLAND, W.C. AND GEHRELS, G.E. (1990): Nd isotopic characterisation of metamorphic rocks in the Coast Mountains, Alaskan and Canadian Cordillera: ancient crust bounded by juvenile terranes. *Tectonics* **10**, 770–780.
- SCAILLET, B., FRANCE-LANNORD, C. AND LE FORT, P. (1990): Badrinath-Gangotri plutons (Garhwal, India): petrological and geochemical evidence for the fractionation processes in a high Himalayan leucogranite. *Journal of Volcanology and Geothermal research* **44**, 163–188.
- SCHMIDT, M.W. (1992): Amphibole composition in tonalite as a function of pressure: an experimental calibration of the Al-in-hornblende barometer. *Contributions to Mineralogy and Petrology* **110**, 304–310.

- SCHULZ, B., BOMBACH, K., PAWLIG, S. AND BRÄTZ, H. (2004): Neoproterozoic to early-Palaeozoic magmatic evolution in the Gondwana-derived Austroalpine basement to the south of the Tauern Window (Eastern Alps). *International Journal of Earth Sciences (Geologische Rundschau)* **93**, 824–843.
- SHABANI, A.A.T., LALONDE, A.E. AND WHALEN, J.B. (2003): Composition of Biotite from granitic rocks of the Canadian Appalachian orogen: a potential tectonomagmatic indicator? *Canadian Mineralogist* **41**, 1381–1396.
- SHAND, S.J. (1947): *The eruptive rocks: their genesis, composition, classification, and their relation to ore-deposits* (third edition). John Wiley, New York, 444 pp.
- SHANG, C.K. (2001): *Geology, Geochemistry and Geochronology of Archaean rocks from Sangmelima Region, Ntem Complex, NW Congo Craton, South Cameroon*. PhD Thesis, University of Tübingen, Germany, 300 pp.
- SHANG, C.K., SATIR, M., SIEBEL, W., NSIFA, E.N., TAUBALD, H., LIÉGEOIS, J.P. AND TCHOUA, F.M. (2004a): TTG magmatism in the Congo craton; a view from major and trace element geochemistry, Rb–Sr and Sm–Nd systematics: Case of the Sangmelima region, Ntem complex, southern Cameroon. *Journal of African Earth Sciences* **40**, 61–79.
- SHANG, C.K., SIEBEL, W., SATIR, M., CHEN, F. AND MVONDO, J.O. (2004b): Zircon Pb–Pb and U–Pb systematics of TTG rocks in the Congo Craton: Constrains on crust formation, magmatism, and Pan-African lead loss. *Bulletin of Geosciences* **79**, 205 – 219.
- SHELLEY, D. (1993): *Igneous and metamorphic rocks under the microscope: Classification, texture, microstructures and mineral preferred orientations*. Chapman & Hall, London, 445 pp.
- SHEPHERD, B.J., RANKIN, A.H. AND ALDERTON, D.H.M. (1985): A practical guide of Fluid Inclusion Studies. Blackie and Son, Glasgow, 239 pp.
- SIAL, A.N., DALL'AGNOL, R., FERREIRA, V.P., NARDI, L.V.S., PIMENTEL, M.M. AND WIEDEMANN, C.M. (1999): Precambrian granitic magmatism in Brazil. *Episode* **22**, 191–198.
- SIGURDSSON, H., DEVINE, J.D., TCHOUA, F.M., PRESSER, T.S., PRINGLE, M.K.W. AND EVANS, W.C. (1987): Origin of the lethal gas burst from Lake Monoun, Cameroon. *Journal of Volcanology and Geothermal Research* **31**, 1–16.
- SIMPSON, C. AND WINTSCH, R.P. (1989): Evidence for deformation-induced K-feldspar replacement by myrmekite. *Journal of Metamorphic Geology* **7**, 261–275.
- SINGH, J. AND JOHANNES, W. (1996): Dehydration melting of tonalites. Part I. Beginning of melting. *Contributions to Mineralogy and Petrology* **125**, 16–25.
- SOBA, D. (1989): *La série de Lom: Étude géologique et géochronologique d'un bassin volcanosédimentaire de la chaîne panafricaine de l'Est du Cameroun*. Thèse de Doctorat d'État, Université de Paris VI, France, 198 pp.

- SOBA, D., MICHARD, A., TOTEU, S.F., NORMAN, D.I., PENAYE, J., NGAKO, V., NZENTI, J.-P. AND DAUTEL, D. (1991): Données géochronologiques nouvelles (Rb–Sr, U–Pb, Sm–Nd) sur la zone mobile panafricaine de l'Est Cameroun: âge Protérozoïque supérieur de la série de Lom. *Comptes rendus de l' Académie des Sciences* **315**, 1453–1458.
- SPEER, J.A. (1984): Micas in igneous rocks. In: BAILEY, S.W. (ed.), *Micas. Mineralogical Society of America, Reviews in Mineralogy* **13**, 299–356.
- STEIGER, R.H. AND JÄGER, E. (1977): Subcommission on geochronology: Convention on the use of decay constants in geo- and cosmo-chronology. *Earth and Planetary Science Letters* **36**, 359–362.
- STENDAL, H., TOTEU, S.F., FREI, R., NJEL, U.O., KONNERUP-MADSEN, J. BASSAHAK, J., PENAYE, J. AND NNI, J. (2004): Pan-African (?) rutile in the Yaoundé region, Cameroon. *20th colloquium of African Geology, B.G.R.M Orleans, France, Abstracts Volume*, p 385.
- STOSCH, H.G. (2001): Einführung in die isotopen geochemie. Version 2.2.10 (6. Dezember 2001). Source: <http://www.GeologieInfo.de/mineralogie/minskrip5.php>.
- STRECKEISEN, A.L. (1976): To each plutonic rock its proper name. *Earth-Sciences Reviews* **12**, 1–33.
- STRECKEISEN, A.L. AND LE MAITRE, R.W. (1979): A chemical approximation to the modal QAPF classification of igneous rocks. *Neues Jahrbuch für Mineralogie* **136**, 169–206.
- STUSSI, J.M. AND CUNY, M. (1996): Nature of biotite from alkaline, calc-alkaline and peraluminous magmas by Abdel-Fattah M. Abdel-Rahman: A comment. *Journal of Petrology* **37**, 1025–1029.
- SYLVESTER, P.J. (1989): Post-collisional alkaline granites. *Journal of Geology* **97**, 261–280.
- SYLVESTER, P.J. (1998): Post-collisional strongly peraluminous granites. *Lithos* **45**, 29–44.
- TAGNE-KAMGA, G. (1994): *Le complexe plutonique Panafricain de Ngondo (Ouest Cameroun): structure et pétrogenèse*. Thèse de Doctorat, Université de Franche-Comté, France, 224 pp.
- TAGNE-KAMGA, G. (2003): Petrogenesis of the Neoproterozoic Ngondo Plutonic complex (Cameroon, west central Africa): a case of late-collisional ferro-potassic magmatism. *Journal of African Earth Sciences* **36**, 149–171.
- TAGNE-KAMGA, G., MERCIER, E., ROSSY, M. AND NSIFA, N.E. (1999): Synkinematic emplacement of the Pan-African Ngondo igneous complex (west Cameroon, central Africa). *Journal of African Earth Sciences* **28**, 675–691.
- TALLA, V. (1995): *Le Massif granitic panafricain de Batié (Ouest - Cameroun): Pétrologie - Pétrostructurelle - Géochimie*. Thèse de Doctorat, Université de Yaoundé I, Cameroun, 144 pp.
- TAYLOR, R.S. AND McLENNAN, S.M. (1985): *The Continental crust: its composition and evolution*. Blackwell, Oxford, 312 pp.

- TCHAMENI, R. (1997): *Géochimie et géochronologie des formations de l'Archéen et de Paléoprotérozoïque du Sud Cameroun (Groupe de Ntem, Craton du Congo)*. Thèse de Doctorat, Université de Orléans, France, 395 pp.
- TCHAMENI, R., MEZGER, K., NSIFA, E.N. AND POUCLET, A. (2000): Late Archean crustal evolution in the Congo Craton: evidence from the K-rich granitoids of the Ntem Complex, Southern Cameroon. *Journal of African Earth Sciences* **30**, 133–147.
- TCHAMENI, R., MEZGER, K., NSIFA, E.N. AND POUCLET, A. (2001): Crustal origin of the early Proterozoic syenites in the Congo Craton (Ntem Complex, South Cameroon). *Lithos* **57**, 23–42.
- TCHOUA, F.M. (1974): *Contribution à l'étude géologique et pétrographique de quelques volcans de la Ligne du Cameroun (Monts Manengouba et Bambotho)*. Thèse de Doctorat d'État, Université de Clermont-Ferrand, France, 337 pp. et annexes.
- TCHOUANKOUE, J.-P. (1992): *La syénite de Bangangté: Un complexe panafricain à caractères intermédiaires. Pétrologie–Géochimie*. Thèse de Doctorat, Université de Yaoundé I, Cameroun, 130 pp.
- TEMPIER, P. AND LASSERRE, M. (1980): Géochimie des massifs "ultimes" du Cameroun: rapports entre l'évolution magmatique, l'âge et la position géographique. Comparaison avec "les Younger Granites" du Nigeria. *Bulletin de la société géologique de France* **22**, 203–211.
- TEMPIER, P., LASSERRE, M. AND SABOURDY, G. (1981): Les granitoids du Nord Cameroun: Pétrographie et géochimies. *Bulletin de la Société Géologique de France* **23**, 679–688.
- TETSOPGANG, S. (2003): *Petrology, geochemistry and geochronology of Pan-African granitoids in the Nkambé area, Northwestern Cameroon, Africa*. PhD Thesis, Nagoya University, Japan.
- TETSOPGANG, S., KOYANAGI, J., ENAMI, M. AND KIHARA, K. (2003): Hydroxylian pseudorutile in an adamellite from Nkambé area, Cameroon. *Mineralogical Magazine* **67**, 509–516.
- THIEBLEMONT, D. AND CABANIS, B. (1990): Utilisation d'un diagramme (Rb/100)–Tb–Ta pour la discrimination géochimique et l'étude pétrogénétique des roches magmatiques acides. *Bulletin de la Société Géologique de France* **6**, 23 – 25.
- TOTEU, S.F., MACAUDIERE, J., BERTRAND, J.M. AND DAUTEL, D. (1990): Metamorphic zircons from North Cameroon; implication for the Pan-African evolution of Central Africa. *Geologische Rundschau* **79**, 777–778.
- TOTEU, S.F., PENAYE, J. AND POUDJOM DJOMANI, Y. (2004): Geodynamic evolution of the Pan-African belt in central Africa with special reference to Cameroon. *Canadian Journal of Earth Sciences* **41**, 73–85.
- TOTEU, S.F., VAN SCHMUS, W.R., PENAYE, J. AND MICHARD, A. (2001): New U–Pb and Sm–Nd data from north-central Cameroon and the pre-Pan African history of central Africa. *Precambrian Research* **108**, 45–73.

- TOTEU, S.F., VAN SCHUMUS, W.R., PENAYE, J. AND NYOBE, J.B. (1994): U–Pb and Sm–Nd evidence for Eburnian and Pan-African high-grade metamorphism in cratonic rocks of southern Cameroon. *Precambrian Research* **67**, 321–347.
- TRÖGER, W.E. (1982): *Optische Bestimmung der gesteinsbildenden Minerale*, Teil 2. Schweizerbartsche Verlagsbuchhandlung, Stuttgart, 822 pp.
- TROMPETTE, R. (1994): *Geology of Western Gondwana (2000–500 Ma): Pan-African-Bresiliano aggregation of South America and Africa*. Z. Balkema, A. A. Brookfield, Rotterdam, 341 pp.
- TROMPETTE, R. (1997): Neoproterozoic (~ 600 Ma) aggregation of the Western Gondwana: a tentative scenario. *Precambrian Research* **82**, 101–112.
- TROMPETTE, R. (2000): Gondwana evolution; its assembly at around 600 Ma. *Comptes Rendus de l'Académie des Sciences, Paris* **330**, 305–315.
- TULLIS, J. (1990): Experimental studies of deformation mechanisms and microstructure in quartz-feldspathic rocks. In: BARBER, D.J. AND MEREDITH, P.G. (eds.), *Deformation Processes in Minerals, Ceramics and Rocks*. Unwin Hyman, London, 190–227.
- TURNER, S., ARNAUD, N., LIU, J., ROGERS, N., HAWKESWORTH, C., HARRIS, N., KELLEY, S., VAN CALSTEREN, P. AND DENG, W. (1996): Post-collision, shoshonitic volcanism on the Tibetan plateau: implication for convective thinning of the lithosphere and the source of ocean island basalts. *Journal of Petrology* **37**, 45–71.
- VAIL, J.R. (1989): Ring complexes and related rocks in Africa. *Journal of African Earth Sciences* **8**, 19–40.
- VAN DEN KERKHOF, A. (1990): Isochoric phase diagrams in the systems CO₂–CH₄ and CO₂–N₂: Application to fluid inclusions. *Geochimica et Cosmochimica Acta* **54**, 621–629.
- VAN DEN KERKHOF, A. AND HEIN, U.F. (2001): Fluid inclusion petrography. *Lithos* **55**, 27–47.
- VAUCHEZ, A., NEVES, S., CABY, R., CORSINI, M., EGYDIO-SILVA, M., ARTHAUD, M. AND AMARO, V. (1995): The Borborema shear zone system, NE Brazil. *Journal of South America Earth Sciences* **8**, 247–266.
- VEEVERS, J.J. (2003): Pan-African is Pan-Gondwanaland: Oblique convergence drives rotation during 650–500 Ma assembly. *Geology* **31**, 501–504.
- VEEVERS, J.J. (2004): Gondwanaland from 650–500 Ma assembly through 320 Ma mergers in Pangea to 185–100 Ma breakup: supercontinental tectonics via stratigraphy and radiometric dating. *Earth Science Reviews* **68**, 1–132.
- VELDE, B. (1967): Si⁺⁴ content of natural phengites. *Contributions to Mineralogy and Petrology* **14**, 250–258.
- VELDE, B. (1972): Celadonite mica: solid solution and stability. *Contributions to Mineralogy and Petrology* **37**, 235–247.

- VERNON, R.H. (1991): Questions about myrmekite in deformed rocks. *Journal of Structural Geology* **13**, 979–985.
- VICAT, J.-P., LEGER, J.M., NSIFA, E.N., PIGUET, P., NZENTI, P.-J., TCHAMENI, R. AND POUCLÉT, A. (1996): Distinction au sein du craton congolais du Sut-Ouest du Cameroun, de deux épisodes doléritiques initiant les cycles orogéniques éburnéens (Paléoprotérozoïque) et Panafricain (Néoprotérozoïque). *Comptes Rendus de l' Académie Sciences* **333**, 575–582.
- VIDAL, P., BERNARD-GRIFFITHS., J., PEUCAT, J.J., COCHERIE, A., LE FORT, P. AND SHEPPARD, S.M.F. (1984): Geochemical comparison between Himalayan and Hercynian leucogranites. *Physics of the Earth and Planetary Interiors* **35**, 179–190.
- VILLASECA, C., BARBERO, L. AND HERREROS, V. (1998): A re-examination of the typology of peraluminous granite type in intracontinental orogenic belts. *Transactions of the Royal Society: Earth Sciences* **89**, 113–119.
- VINCENT, P.M. (1970): The evolution of the Tibesti volcanic province, eastern Sahara. In: CLIFFORD, T. B. & GASS, I. G. (eds.), *African magmatism and tectonic*. Oliver and Boyd, Edinburgh, 301–309.
- VYHNAL, C.R., MCSWEEN, H.Y. AND SPEER, J.A. (1991): Hornblende chemistry in Southern Appalachian granitoids: Implications for aluminum hornblende thermobarometry and magmatic epidote stability. *American Mineralogist* **76**, 176–188.
- WALL, V.J., CLEMENS, J.D. AND CLARKE, D.B. (1987): Models for the granitoids evolution and source compositions. *Journal of Geology* **95**, 731–749.
- WATSON, E.B. (1979): Zircon saturation in felsic liquids: experimental data and applications to trace element geochemistry. *Contributions to Mineralogy and Petrology* **70**, 407–419.
- WATSON, E.B. AND CAPOBIANO, C.J. (1984): Phosphorus and the rare earth elements in felsic magmas: an assessment of the role of apatite. *Geochimica et Cosmochimica Acta* **45**, 2349–2358.
- WATSON, E.B. AND HARRISON, T.M. (1983): Zircon saturation revised: temperature and composition effects in a variety of crustal magma types. *Earth and Planetary Science Letters* **64**, 295–304.
- WATSON, E.B. AND HARRISON, T.M. (1984): Accessory minerals and the geochemical evolution of crustal magmatic systems: a summary and prospectus of the experimental approaches. *Physics of the Earth and Planetary Interiors* **35**, 19–30.
- WENDT, I. (1993): Isochron or mixing line. *Chemical Geology (Isotope Geoscience section)* **104**, 301–305.
- WHALEN, J.B., CURRIE, K.L. AND CHAPPELL, B.W., (1987): A-type granites: geochemical characteristics, discrimination and petrogenesis. *Contributions to Mineralogy and Petrology* **95**, 407–419.
- WHITE, A.J.R. (1979): Sources of granites magmas. *Geological Society of America, Abstract Programs* **11**, p 539.

- WHITE, A.J.R. AND CHAPPELL, B.W. (1983): Granitoids types and their distribution in the Lachlan Fold Belt, Southeastern Australia. *Memoir–Geological Society of America* **159**, 21–34.
- WHITNEY, J.A. (1988): The origin of granite: the role and source of water in the evolution of granitic magmas. *Geological Society of America Bulletin* **100**, 1886–1897.
- WILKINSON, J.J. (2001): Fluid inclusions in hydrothermal ore deposits. *Lithos* **55**, 229–272.
- WILLIAMSON, B.J., SHAW, A., DOWNES, H. AND THIRLWALL, M.F. (1996): Geochemical constraints on the genesis of Hercynian two-mica leucogranites from the Massif Central, France. *Chemical Geology* **127**, 25–42.
- WILSON, M. (1989): *Igneous petrogenesis*. Unwin Hyman, London, 466 pp.
- WILSON, M. AND GUIRAUD, R. (1992): Magmatism and rifting in Western and Central Africa, from Late Jurassic to Recent times. *Tectonophysics* **213**, 203–225.
- WONES, D.R. (1989): Significance of the assemblage titanite + magnetite + quartz in granitic rocks. *American Mineralogist* **74**, 744–749.
- WONES, D.R. AND EUGSTER, H.R. (1965): Stability of biotite: experiment, theory and application. *American Mineralogist* **50**, 1228–1272.
- WONES, D.R. AND GILBERT, M.C. (1982): Amphiboles in the igneous environment. In: VEBLEN, D.R. (ed.), *Amphiboles: Petrology and Experimental Phase Relations*. *Mineralogical Society of America, Reviews in Mineralogy* **9B**, 355–390.
- YOSHIDA, M. AND SANTOSH, M. (eds.) (1995): *India and Antarctica during the Precambrian*, 412 pp.
- ZEN, E. (1986): Aluminum enrichment in silicate melts by fractional crystallization: some mineralogic and petrographic constraints. *Journal of Petrology* **27**, 1095–1117.
- ZEN, E. (1988): Phase relations of peraluminous granitic rocks and their petrogenetic implication. *Annual Review of Earth and Planetary Sciences* **16**, 21–52.

APPENDIX

A.1 Analytical procedures

A.1.1 Petrography

Petrographical analyses have been made on standard petrological thin sections of about 0.03 mm thickness. The investigation of the thin sections has been done with the helps of a LEITZ polarisation microscope.

A.1.2 Electron microprobe (EMP)

A detailed electron microprobe analysis was made on major and accessory rock-forming minerals of the studied granitoids (biotite, muscovite, garnet, amphibole, K-feldspar, plagioclase, magnetite and ilmenite), using a CAMECA SX-50 electron microprobe instrument with three wavelength-dispersive spectrometers at the Mineralogical Institute, University Würzburg (Germany). Synthetic silicates and oxides were used as reference standards, and matrix correction was carried out by the PAP program supplied by CAMECA. Mineral element concentrations were determined on polished and carbon coated thin sections.

Instrument conditions were 15 kV accelerating voltage and 15 nA beam current on the Faraday cage. The element peaks and backgrounds were measured over 20 sec integration time for all the elements except for Fe and Mn (30 sec). Point analyses were performed with a 1–2 µm beam diameter for garnet, amphibole and oxide minerals, and 4 µm for mica and feldspars. The analytical error is less than 1 % relative for major elements, but higher for low element concentrations. The detection limit for the operating condition is between 0.05 and 0.1 wt. %.

A.1.3 Whole- rock geochemistry

For the chemical analysis, the sample size used depends on the grain size of the rock. The largest sample weighted ~ 10 kg. Much care was taken to remove the altered parts, the state of decomposition of the feldspar being an important indicator. The rocks were crushed with a

steel jawbreaker (Siebtechnik GmbH) into chips of about 1 cm and then were powdered in a wolfram carbide disk mill (Siebtechnik GmbH) for about 120 sec.

- X-ray fluorescence (XRF) spectrometry: Major and trace elements

For the x-ray fluorescence (XRF) analyses, the preparation of the samples was made by mixing 600 mg sample powder with 3.6 g SPECTROMELT A 12 and 500–1000 mg NH₄NO₃ (depending on the Fe-content). The mixture was melted at different temperatures (up to 1000 °C) at five NUTECH burner stations, using platinum crucibles. The obtained fused glass discs after cooling were used to determine the major and trace elements on the Philips PW 1480 XRF spectrometer at the Mineralogical Institute, University Würzburg (Germany). All the analyses were calibrated against international standards. Matrix effects were automatically corrected by the Philips X40 software. The analytical error for major elements is 1 % relative, whereas that of trace elements ranges between 1 and 8 % relative.

- Loss of ignition (LOI)

The loss of ignition (total amount of volatile component such as H₂O, CO₂, SO₂) was determined by heating about 1 g of dried sample powder at 1000 °C during 4 hours. After cooling, the sample was reweighed. The LOI represents the difference between the weights of the sample before and after heating.

- Laser Ablation Inductively Coupled Plasma Mass Spectrometry (LA-ICPMS): Rare earth elements and some trace elements

Whole rock rare earth elements (REE) and some trace elements (Sc, Cr, Ni, Nb, Mo and Sn) were determined using the same fused glass discs prepared for the x-ray fluorescence spectrometry analysis. The analyses were carried out with a 266 nm Nd:YAG New Wave Research (former Merchantek) laser connected to a quadrupole ICPMS [Agilent 7500i; Plasma power: 1290 W; Carrier gas (Ar): 1.17 L/min; Plasma gas (Ar): 14.9L/min; auxiliary gas (Ar): 0.9 L/min] at the Mineralogical Institute, University Würzburg (Germany). Laser parameters used were ablation patterns of 1250 µm long lines, ablated with a scan speed of 40 µm/sec. The diameter of the sample pit created by laser is 50 µm. The frequency was 20 Hz and an energy setting of 0.99–1.12 mJ. Data acquisition was done in Time Resolved Analysis mode with measurements of the instrument background (25 sec) and of granitoids (35 sec). The certified

reference material NIST 612 with the values of Pearce et al. (1997) was used as an external standard. Raw counts for each element were solely corrected subtracting the background counts and processed using the software GLITTER (version 3.0, On-line Interactive Data Reduction for the LA-ICPMS, Macquarie Research Ltd., 2000). The analytical error was < 10 % (1σ) relative for each analysis and the minimum detection limit is 0.5 ppm for Cr, 0.1 ppm for Ni, and 0.05 ppm for Sc and REE. For the spidergram representation, the obtained REE were normalized relative to chondrite abundances, according to the values of McDonough and Sun (1995).

A.1.4 Whole-rock Rb–Sr and Sm–Nd isotope geochemistry

This analysis was carried out by Dr. C. Nzolang at the Graduate School of Science and Education, Niigata University (Japan). Rb, Sr, Sm and Nd concentration were determined using the same sample powders prepared for the x-ray fluorescence spectrometry analysis. The extraction of Rb, Sr, Sm and Nd from sample powders and mass spectrometric analyses were performed following the procedures described by Kagami et al. (1987). Sr and Nd isotope ratios were performed with a Finnigan MAT-262 multi-collector thermal ionization mass spectrometer. Measured $^{87}\text{Sr}/^{86}\text{Sr}$ and $^{143}\text{Nd}/^{144}\text{Nd}$ ratios were normalized to $^{87}\text{Sr}/^{86}\text{Sr} = 0.1194$ and $^{143}\text{Nd}/^{144}\text{Nd} = 0.7219$, respectively. During the running period of the analyses, the NBS987 standard yielded a $^{87}\text{Sr}/^{86}\text{Sr}$ ratio of 0.710225 ± 0.000013 (2σ) on 23 runs. The JNd-1 standard gave a $^{143}\text{Nd}/^{144}\text{Nd}$ mean value of 0.512066 ± 0.000011 (2σ) on 25 runs.

Rb and Sr contents were determined by x-ray fluorescence spectrometry analysis. The $^{143}\text{Nd}/^{144}\text{Nd}$ ratios in this study are reported relative to GSJ standard JNd-1 = 0.512116 that is consistent with 0.511856 ± 6 of La Jolla standard (Tanaka et al., 2000). Measuring errors range between 0.000012 and 0.000024 % (2σ) for $^{87}\text{Sr}/^{86}\text{Sr}$ ratios, and 0.000009 and 0.000024 % (2σ) for the $^{143}\text{Nd}/^{144}\text{Nd}$ ratios. The relative analytical errors were 4 % (1σ) for $^{87}\text{Rb}/^{86}\text{Sr}$, 0.01 % (1σ) for $^{87}\text{Sr}/^{86}\text{Sr}$, 0.1 % (1σ) for $^{147}\text{Sm}/^{144}\text{Nd}$ and 0.01 % (1σ) for $^{143}\text{Nd}/^{144}\text{Nd}$ ratios. The following CHUR parameters were employed for the calculation of initial ϵ_{Sr} and initial ϵ_{Nd} values: $^{87}\text{Sr}/^{86}\text{Sr}$ (present) = 0.7045, $^{87}\text{Sr}/^{86}\text{Sr}$ (present) = 0.0827, $^{143}\text{Nd}/^{144}\text{Nd}$ (present) = 0.512638 and $^{147}\text{Sm}/^{144}\text{Nd}$ (present) = 0.1966. Nd model ages (T_{DM}) were calculated using values of the present-day depleted mantle of Goldstein et al. (1984): $^{143}\text{Nd}/^{144}\text{Nd} = 0.513150$ and $^{147}\text{Sm}/^{144}\text{Nd} = 0.2136$. Decay constants are: $\lambda(^{87}\text{Rb}) = 1.42 \times 10^{-11}\text{y}^{-1}$ and $\lambda(^{147}\text{Sm}) = 6.54 \times 10^{-12}\text{y}^{-1}$.

A.1.5 Microthermometric fluid inclusion studies

The microthermometric study was carried out at the Mineralogical Institute, University Würzburg (Germany) fluid inclusion laboratory. Microthermometric determinations were made on double polished thin sections (about 100 µm thick) using a Fluid INC. equipment (U.S. Geological Survey gas-flow heating/freezing system). The equipment was previously calibrated with synthetic standards of Syn Flinc (critical point of H₂O, critical point of CO₂). The data are reproducible to ± 0.2 °C for the freezing runs and ± 0.4 °C for the heating runs. A total of 50 fluid inclusions was examined by cycles of freezing down to –150 °C and heating up to the appropriate temperature of the total homogenization to control the stability of the inclusions and the representativity of the determinations. These cycles were generally repeated several times in order to exactly detect the phase changes.

A.2 Mineral chemistry

Table A.2.1: Representative analyses of biotite (continued).

Rock type	Biotite granitoid																	
Sample	LE-2 1-Bt1	LE-2 1-Bt1	LE-2 1-Bt1	LE-2 1-Bt2	LE-1 1-Bt2	LE-2 1-Bt4	LE-2 2-Bt1	LE-2 2-Bt2	LE-2 4-Bt1	BL-8 1-Bt1	BL-8 1-Bt2	BL-8 1-Bt3	BL-8 2-Bt1	BL-8 2-Bt2	SE-4 1-Bt1	SE-4 1-Bt2		
<i>Component oxides (wt.%)</i>																		
SiO ₂	36.54	36.85	36.54	36.85	36.66	36.70	36.48	36.98	36.89	36.55	36.66	37.32	37.60	37.48	37.71	37.55	37.94	36.61
TiO ₂	1.97	2.91	1.97	2.91	2.57	1.92	2.09	1.86	1.85	2.38	1.99	1.77	1.66	1.54	1.62	1.71	2.52	2.56
Al ₂ O ₃	14.75	14.94	14.75	14.94	14.90	15.45	15.38	15.15	14.83	14.93	15.05	15.21	15.27	15.53	15.23	15.40	15.30	14.96
Cr ₂ O ₃	0.00	0.02	0.00	0.02	0.00	0.00	0.00	0.05	0.03	0.00	0.08	0.05	0.05	0.00	0.00	0.00	0.03	0.00
MgO	11.99	10.94	11.99	10.94	11.11	11.65	11.42	11.36	11.79	11.24	11.20	11.69	12.04	11.66	12.53	12.70	11.23	11.40
CaO	0.02	0.00	0.02	0.00	0.02	0.00	0.01	0.03	0.01	0.01	0.00	0.02	0.00	0.02	0.00	0.00	0.00	0.00
MnO	0.36	0.38	0.36	0.38	0.31	0.33	0.38	0.31	0.41	0.37	0.39	0.68	0.64	0.67	0.75	0.77	0.81	0.74
FeO	19.84	20.30	19.84	20.30	20.12	19.92	19.32	19.49	19.83	20.16	20.74	19.18	19.11	19.35	18.23	17.50	18.49	18.29
BaO	0.00	0.01	0.00	0.01	0.00	0.00	0.00	0.00	0.06	0.00	0.00	0.09	0.00	0.00	0.00	0.00	0.00	0.00
Na ₂ O	0.13	0.09	0.13	0.09	0.11	0.13	0.06	0.10	0.06	0.05	0.07	0.15	0.05	0.04	0.10	0.09	0.10	0.06
K ₂ O	9.24	9.63	9.24	9.63	9.36	9.58	9.71	9.99	9.74	9.73	9.71	9.28	9.69	9.69	9.57	9.70	9.61	9.36
Total	94.83	96.07	94.88	96.03	95.18	95.65	94.86	95.31	95.48	95.43	95.86	95.39	96.24	95.98	95.85	95.42	96.02	94.06
<i>Mineral structural formulas (a.p.f.u) based on 22 Oxygens</i>																		
Si	5.625	5.616	5.625	5.616	5.629	5.601	5.610	5.665	5.651	5.612	5.615	5.685	5.687	5.683	5.701	5.682	5.722	5.654
Al ^{IV}	2.375	2.384	2.375	2.384	2.371	2.399	2.390	2.335	2.349	2.388	2.385	2.315	2.313	2.317	2.299	2.318	2.278	2.346
Sum T	8.000	8.000	8.000	8.000	8.000	8.000	8.000	8.000	8.000	8.000	8.000	8.000	8.000	8.000	8.000	8.000	8.000	8.000
Al ^{VI}	0.300	0.299	0.300	0.299	0.325	0.380	0.398	0.401	0.329	0.314	0.332	0.416	0.409	0.458	0.414	0.429	0.442	0.377
Cr	0.000	0.003	0.000	0.003	0.000	0.000	0.000	0.006	0.003	0.000	0.010	0.006	0.006	0.000	0.000	0.004	0.000	0.000
Ti	0.228	0.334	0.228	0.334	0.297	0.221	0.241	0.214	0.213	0.274	0.229	0.202	0.188	0.176	0.184	0.195	0.286	0.297
Fe ²⁺	2.554	2.588	2.554	2.588	2.584	2.543	2.485	2.497	2.540	2.589	2.657	2.444	2.417	2.453	2.304	2.214	2.332	2.362
Mn	0.047	0.048	0.047	0.048	0.040	0.043	0.050	0.040	0.053	0.048	0.051	0.088	0.082	0.086	0.096	0.098	0.104	0.096
Mg	2.750	2.486	2.750	2.486	2.543	2.651	2.618	2.595	2.693	2.574	2.556	2.655	2.715	2.635	2.823	2.865	2.524	2.624
Sum VI	5.879	5.757	5.879	5.757	5.789	5.837	5.792	5.753	5.831	5.799	5.835	5.811	5.818	5.808	5.822	5.801	5.692	5.756
Ba	0.000	0.001	0.000	0.001	0.000	0.000	0.000	0.000	0.003	0.000	0.000	0.005	0.000	0.000	0.000	0.000	0.000	0.000
Ca	0.004	0.000	0.004	0.000	0.003	0.000	0.001	0.005	0.001	0.002	0.000	0.004	0.000	0.003	0.000	0.000	0.000	0.000
Na	0.038	0.026	0.038	0.026	0.033	0.037	0.018	0.030	0.017	0.016	0.019	0.044	0.014	0.011	0.028	0.026	0.029	0.016
K	1.815	1.872	1.815	1.872	1.834	1.865	1.905	1.953	1.904	1.906	1.897	1.804	1.870	1.874	1.845	1.873	1.849	1.845
Sum XII	1.856	1.899	1.856	1.899	1.870	1.902	1.924	1.988	1.926	1.924	1.916	1.857	1.885	1.888	1.873	1.899	1.877	1.862
Total	15.736	15.656	15.736	15.656	15.660	15.739	15.716	15.741	15.756	15.724	15.751	15.668	15.703	15.696	15.700	15.569	15.618	
Fe/(Fe+Mg)	0.481	0.510	0.481	0.510	0.504	0.490	0.487	0.490	0.485	0.502	0.510	0.479	0.471	0.482	0.449	0.436	0.480	0.474
ΣAl	2.676	2.683	2.676	2.683	2.697	2.779	2.788	2.736	2.678	2.702	2.716	2.731	2.722	2.775	2.713	2.747	2.720	2.724
ASI	1.440	1.410	1.440	1.410	1.440	1.460	1.450	1.380	1.390	1.400	1.420	1.470	1.440	1.470	1.450	1.450	1.460	

Table A.2.1: Representative analyses of biotite (continued).

Rock type Sample	Biotite granitoid					Deformed biotite granitoid											
	SE-4 1-Bt2	SE-4 1-Bt3	SE-4 1-Bt5	SE-4 2-Bt1	SE-4 2-Bt2	NG-3 1-Bt1	NG-3 1-Bt1	NG-3 1-Bt1	NG-3 1-Bt2	NG-3 1-Bt2	NG-3 1-Bt3	NG-3 1-Bt3	NG-3 1-Bt3	NG-3 1-Bt3	NG-3 1-Bt4	NG-3 1-Bt4	NG-3 1-Bt4
<i>Component oxides (wt.%)</i>																	
SiO ₂	35.50	37.24	37.04	37.24	37.33	36.89	37.21	37.49	36.35	36.99	37.58	37.12	37.03	36.54	36.85	36.66	36.70
TiO ₂	1.64	2.21	3.37	2.48	2.60	2.19	2.18	2.45	2.55	2.78	1.63	2.03	1.89	1.97	2.91	2.57	1.92
Al ₂ O ₃	14.84	14.72	13.71	15.14	14.75	15.42	15.60	15.28	15.41	15.53	15.92	15.68	14.60	14.75	14.94	14.90	15.45
Cr ₂ O ₃	0.01	0.00	0.00	0.01	0.00	0.03	0.00	0.00	0.06	0.00	0.00	0.04	0.02	0.00	0.02	0.00	0.00
MgO	10.52	12.11	11.72	11.23	11.89	11.57	11.65	11.82	10.82	10.99	12.15	12.18	12.91	11.99	10.94	11.11	11.65
CaO	0.02	0.00	0.00	0.00	0.00	0.00	0.00	0.00	0.02	0.00	0.00	0.01	0.02	0.02	0.00	0.02	0.00
MnO	0.70	1.11	0.72	0.69	0.70	0.67	0.81	0.78	0.78	0.79	0.32	0.38	0.49	0.36	0.38	0.31	0.33
FeO	18.09	17.96	19.01	18.53	18.74	19.23	18.57	18.89	20.22	18.82	17.72	18.52	16.04	19.84	20.30	20.12	19.92
BaO	0.03	0.09	0.00	0.00	0.00	0.04	0.00	0.00	0.00	0.00	0.03	0.00	0.00	0.00	0.01	0.00	0.00
Na ₂ O	0.08	0.10	0.05	0.06	0.09	0.11	0.13	0.10	0.09	0.12	0.04	0.13	0.01	0.13	0.09	0.11	0.13
K ₂ O	8.87	9.66	9.74	9.56	9.54	9.64	9.49	9.43	9.69	9.50	9.79	9.68	9.84	9.24	9.63	9.36	9.58
Total	90.45	95.01	95.37	94.93	95.61	95.78	95.63	92.26	95.99	95.48	95.15	95.78	92.93	94.81	96.03	95.18	95.65
<i>Mineral structural formulas (a.p.f.u) based on 22 Oxygens</i>																	
Si	5.705	5.684	5.673	5.691	5.672	5.616	5.644	5.654	5.559	5.629	5.692	5.619	5.733	5.625	5.616	5.629	5.601
Al ^{IV}	2.295	2.316	2.327	2.309	2.328	2.384	2.356	2.346	2.441	2.371	2.308	2.381	2.267	2.375	2.384	2.371	2.399
Sum T	8.000	8.000	8.000	8.000	8.000	8.000	8.000	8.000	8.000	8.000	8.000	8.000	8.000	8.000	8.000	8.000	8.000
Al ^{VI}	0.515	0.332	0.149	0.418	0.312	0.382	0.432	0.371	0.337	0.413	0.534	0.415	0.396	0.300	0.299	0.325	0.380
Cr	0.001	0.000	0.000	0.001	0.000	0.004	0.000	0.000	0.007	0.000	0.000	0.005	0.002	0.000	0.003	0.000	0.000
Ti	0.199	0.254	0.388	0.285	0.297	0.250	0.249	0.278	0.293	0.319	0.186	0.231	0.219	0.228	0.334	0.297	0.221
Fe ²⁺	2.432	2.292	2.436	2.369	2.380	2.448	2.355	2.383	2.587	2.394	2.244	2.345	2.076	2.554	2.588	2.584	2.543
Mn	0.096	0.143	0.094	0.090	0.090	0.086	0.104	0.099	0.102	0.102	0.041	0.049	0.065	0.047	0.048	0.040	0.043
Mg	2.521	2.756	2.675	2.559	2.692	2.625	2.634	2.657	2.467	2.493	2.743	2.748	2.980	2.750	2.486	2.543	2.651
Sum VI	5.764	5.777	5.742	5.720	5.772	5.795	5.775	5.788	5.793	5.722	5.748	5.793	5.738	5.879	5.757	5.789	5.837
Ba	0.002	0.005	0.000	0.000	0.000	0.002	0.000	0.000	0.000	0.000	0.002	0.000	0.000	0.000	0.001	0.000	0.000
Ca	0.004	0.000	0.000	0.000	0.000	0.000	0.000	0.000	0.003	0.000	0.000	0.002	0.004	0.004	0.000	0.003	0.000
Na	0.023	0.029	0.016	0.017	0.028	0.032	0.039	0.028	0.027	0.034	0.012	0.038	0.004	0.038	0.026	0.033	0.037
K	1.819	1.881	1.902	1.864	1.849	1.871	1.836	1.815	1.892	1.844	1.892	1.870	1.943	1.815	1.872	1.834	1.865
Sum XII	1.848	1.916	1.918	1.881	1.876	1.906	1.875	1.844	1.921	1.878	1.906	1.911	1.950	1.856	1.899	1.870	1.902
Total	15.612	15.693	15.660	15.601	15.649	15.701	15.650	15.631	15.714	15.599	15.654	15.704	15.689	15.736	15.656	15.660	15.739
Fe/(Fe+Mg)	0.491	0.454	0.477	0.481	0.469	0.480	0.470	0.470	0.510	0.490	0.450	0.460	0.410	0.480	0.510	0.500	0.490
ΣAl	2.810	2.648	2.476	2.727	2.641	2.766	2.788	2.717	2.778	2.785	2.842	2.797	2.664	2.676	2.683	2.697	2.779
ASI	1.520	1.390	1.290	1.450	1.410	1.450	1.490	1.470	1.450	1.480	1.490	1.460	1.370	1.440	1.410	1.440	1.460

Table A.2.1: Representative analyses of biotite (continued).

Rock type	Deformed biotite granitoid																	
Sample	NG-3 2-Bt1	NG-3 2-Bt1	NG-3 2-Bt1	NG-3 2-Bt1	NG-3 2-Bt2	NG-3 2-Bt2	NG-3 2-Bt2	NG-3 2-Bt3	NG-3 2-Bt3	NG-3 2-Bt4	NG-3 2-Bt4	NG-3 2-Bt5	NG-3 2-Bt5	NG-3 2-Bt5	NG-3 3-Bt1	NG-3 3-Bt1		
<i>Component oxides (wt.%)</i>																		
SiO ₂	36.48	36.98	36.89	36.55	36.66	35.46	35.36	35.58	35.36	36.20	36.38	36.10	36.00	35.56	36.03	37.32	37.60	37.48
TiO ₂	2.09	1.86	1.85	2.38	1.99	2.74	2.71	2.41	2.93	3.41	3.38	3.31	3.10	2.94	2.97	1.77	1.66	1.54
Al ₂ O ₃	15.38	15.15	14.83	14.93	15.05	16.07	16.09	16.06	16.22	15.77	15.01	15.12	15.31	15.03	15.30	15.21	15.27	15.53
Cr ₂ O ₃	0.00	0.05	0.03	0.00	0.08	0.02	0.00	0.00	0.00	0.02	0.07	0.09	0.05	0.05	0.01	0.05	0.05	0.00
MgO	11.42	11.36	11.79	11.24	11.20	6.81	6.91	7.33	7.09	10.18	10.14	10.33	10.45	9.48	9.76	11.69	12.04	11.66
CaO	0.01	0.03	0.01	0.01	0.00	0.00	0.00	0.00	0.00	0.00	0.00	0.00	0.00	0.02	0.00	0.02	0.00	0.02
MnO	0.38	0.31	0.41	0.37	0.39	0.30	0.37	0.31	0.31	0.37	0.45	0.43	0.40	0.41	0.35	0.68	0.64	0.67
FeO	19.32	19.49	19.83	20.16	20.74	24.22	24.43	24.02	23.94	20.86	21.31	20.82	20.72	22.71	21.23	19.18	19.11	19.35
BaO	0.00	0.00	0.06	0.00	0.00	0.18	0.00	0.00	0.00	0.00	0.00	0.01	0.00	0.08	0.09	0.00	0.00	0.00
Na ₂ O	0.06	0.10	0.06	0.05	0.07	0.04	0.06	0.09	0.04	0.11	0.08	0.11	0.06	0.05	0.01	0.15	0.05	0.04
K ₂ O	9.71	9.99	9.74	9.73	9.71	9.45	9.62	9.51	9.60	9.62	9.57	9.50	9.62	9.64	9.48	9.28	9.69	9.69
Total	94.86	95.31	95.48	95.43	95.86	95.19	95.71	95.30	95.50	96.42	96.38	95.83	95.73	95.93	95.22	95.39	96.24	95.98
<i>Mineral structural formulas (a.p.f.u) based on 22 Oxygens</i>																		
Si	5.610	5.665	5.651	5.612	5.615	5.564	5.536	5.568	5.524	5.507	5.560	5.540	5.530	5.515	5.571	5.685	5.687	5.683
Al ^{IV}	2.390	2.335	2.349	2.388	2.385	2.436	2.464	2.432	2.476	2.493	2.440	2.460	2.470	2.485	2.429	2.315	2.313	2.317
Sum T	8.000	8.000	8.000	8.000	8.000	8.000	8.000	8.000	8.000	8.000	8.000	8.000	8.000	8.000	8.000	8.000	8.000	8.000
Al ^{VI}	0.398	0.401	0.329	0.314	0.332	0.536	0.504	0.530	0.511	0.336	0.264	0.275	0.301	0.261	0.358	0.416	0.409	0.458
Cr	0.000	0.006	0.003	0.000	0.010	0.002	0.000	0.000	0.000	0.002	0.008	0.011	0.006	0.006	0.002	0.006	0.006	0.000
Ti	0.241	0.214	0.213	0.274	0.229	0.324	0.319	0.283	0.344	0.390	0.388	0.382	0.358	0.343	0.346	0.202	0.188	0.176
Fe ²⁺	2.485	2.497	2.540	2.589	2.657	3.179	3.198	3.143	3.128	2.655	2.724	2.671	2.661	2.945	2.745	2.444	2.417	2.453
Mn	0.050	0.040	0.053	0.048	0.051	0.040	0.049	0.041	0.041	0.048	0.058	0.055	0.052	0.053	0.046	0.088	0.082	0.086
Mg	2.618	2.595	2.693	2.574	2.556	1.594	1.612	1.709	1.651	2.308	2.310	2.364	2.393	2.192	2.250	2.655	2.715	2.635
Sum VI	5.792	5.753	5.831	5.799	5.835	5.674	5.682	5.706	5.675	5.738	5.751	5.759	5.771	5.801	5.748	5.811	5.818	5.808
Ba	0.000	0.000	0.003	0.000	0.000	0.011	0.000	0.000	0.000	0.000	0.000	0.001	0.000	0.005	0.005	0.000	0.000	0.000
Ca	0.001	0.005	0.001	0.002	0.000	0.000	0.000	0.000	0.000	0.000	0.000	0.000	0.000	0.004	0.000	0.004	0.000	0.003
Na	0.018	0.030	0.017	0.016	0.019	0.011	0.017	0.028	0.013	0.032	0.023	0.032	0.019	0.016	0.003	0.044	0.014	0.011
K	1.905	1.953	1.904	1.906	1.897	1.891	1.920	1.898	1.914	1.867	1.866	1.860	1.885	1.907	1.870	1.804	1.874	
Sum XII	1.924	1.988	1.926	1.924	1.916	1.902	1.948	1.925	1.927	1.899	1.889	1.892	1.904	1.927	1.878	1.857	1.885	1.888
Total	15.716	15.741	15.756	15.724	15.751	15.576	15.629	15.631	15.602	15.637	15.641	15.651	15.676	15.727	15.626	15.668	15.703	15.696
Fe/(Fe+Mg)	0.490	0.490	0.490	0.500	0.510	0.670	0.660	0.650	0.650	0.530	0.540	0.530	0.530	0.570	0.550	0.480	0.470	0.480
ΣAl	2.788	2.736	2.678	2.702	2.716	2.971	2.968	2.962	2.987	2.829	2.704	2.735	2.771	2.747	2.788	2.731	2.722	2.775
ASI	1.450	1.380	1.390	1.400	1.420	1.560	1.530	1.540	1.550	1.490	1.430	1.450	1.460	1.430	1.490	1.470	1.440	1.470

Table A.2.1: Representative analyses of biotite (continued).

Rock type	Deformed biotite granitoid																	
	Sample		NG-3															
	3-Bt1	3-Bt2	3-Bt1	3-Bt2	3-Bt1	3-Bt2	3-Bt3	3-Bt4	3-Bt3	3-Bt4	3-Bt1	3-Bt2	3-Bt3	3-Bt4	3-Bt1	3-Bt2	3-Bt3	3-Bt4
<i>Component oxides (wt.%)</i>																		
SiO ₂	37.71	37.55	37.94	36.61	35.50	37.24	37.04	37.24	37.33	37.67	37.18	37.73	37.58	36.73	36.00	36.30	36.73	36.61
TiO ₂	1.62	1.71	2.52	2.56	1.64	2.21	3.37	2.48	2.60	1.85	1.76	1.40	2.03	1.87	2.69	1.70	1.84	1.86
Al ₂ O ₃	15.23	15.40	15.30	14.96	14.84	14.72	13.71	15.14	14.75	15.45	15.60	16.19	15.48	15.60	15.10	16.29	15.50	15.56
Cr ₂ O ₃	0.00	0.00	0.03	0.00	0.01	0.00	0.00	0.01	0.00	0.02	0.05	0.08	0.00	0.00	0.01	0.01	0.01	0.00
MgO	12.53	12.70	11.23	11.40	10.52	12.11	11.72	11.23	11.89	13.11	13.15	13.41	13.43	11.61	10.96	10.65	11.23	10.93
CaO	0.00	0.00	0.00	0.00	0.02	0.00	0.00	0.00	0.00	0.01	0.05	0.01	0.03	0.03	0.00	0.02	0.06	0.01
MnO	0.75	0.77	0.81	0.74	0.70	1.11	0.72	0.69	0.70	0.59	0.71	0.69	0.71	0.49	0.50	0.44	0.49	0.43
FeO	18.23	17.50	18.49	18.29	18.09	17.96	19.01	18.53	18.74	16.57	17.19	16.71	17.07	20.15	20.71	21.36	20.79	20.89
BaO	0.00	0.00	0.00	0.00	0.03	0.09	0.00	0.00	0.00	0.00	0.00	0.00	0.00	0.00	0.00	0.01	0.01	0.01
Na ₂ O	0.10	0.09	0.10	0.06	0.08	0.10	0.05	0.06	0.09	0.09	0.05	0.07	0.10	0.09	0.08	0.03	0.16	0.16
K ₂ O	9.57	9.70	9.61	9.36	8.87	9.66	9.74	9.56	9.54	9.75	9.57	9.56	9.35	9.61	9.57	9.13	9.43	
Total	95.85	95.42	96.02	94.06	90.45	95.01	95.37	94.93	95.61	94.87	95.49	95.82	95.98	95.98	95.69	96.32	95.94	95.89
<i>Mineral structural formulas (a.p.f.u) based on 22 Oxygens</i>																		
Si	5.701	5.682	5.722	5.654	5.705	5.684	5.673	5.691	5.672	5.694	5.620	5.646	5.636	5.592	5.537	5.538	5.603	5.599
Al ^{IV}	2.299	2.318	2.278	2.346	2.295	2.316	2.327	2.309	2.328	2.306	2.380	2.354	2.364	2.408	2.463	2.462	2.397	2.401
Sum T	8.000	8.000	8.000	8.000	8.000	8.000	8.000	8.000	8.000	8.000	8.000	8.000	8.000	8.000	8.000	8.000	8.000	8.000
Al ^{VI}	0.414	0.429	0.442	0.377	0.515	0.332	0.149	0.418	0.312	0.447	0.400	0.502	0.372	0.391	0.275	0.466	0.390	0.405
Cr	0.000	0.000	0.004	0.000	0.001	0.000	0.000	0.001	0.000	0.003	0.006	0.010	0.000	0.000	0.002	0.001	0.000	
Ti	0.184	0.195	0.286	0.297	0.199	0.254	0.388	0.285	0.297	0.210	0.200	0.157	0.229	0.214	0.312	0.195	0.211	0.214
Fe ²⁺	2.304	2.214	2.332	2.362	2.432	2.292	2.436	2.369	2.380	2.095	2.173	2.092	2.141	2.566	2.664	2.725	2.652	2.672
Mn	0.096	0.098	0.104	0.096	0.096	0.143	0.094	0.090	0.090	0.075	0.090	0.087	0.090	0.063	0.066	0.057	0.064	0.055
Mg	2.823	2.865	2.524	2.624	2.521	2.756	2.675	2.559	2.692	2.953	2.963	2.991	3.001	2.634	2.512	2.421	2.553	2.493
Sum VI	5.822	5.801	5.692	5.756	5.764	5.777	5.742	5.720	5.772	5.783	5.832	5.838	5.834	5.867	5.828	5.865	5.871	5.838
Ba	0.000	0.000	0.000	0.000	0.002	0.005	0.000	0.000	0.000	0.000	0.000	0.000	0.000	0.000	0.000	0.000	0.000	
Ca	0.000	0.000	0.000	0.000	0.004	0.000	0.000	0.000	0.000	0.002	0.008	0.002	0.005	0.005	0.000	0.002	0.009	0.002
Na	0.028	0.026	0.029	0.016	0.023	0.029	0.016	0.017	0.028	0.026	0.014	0.021	0.028	0.028	0.023	0.009	0.047	0.047
K	1.845	1.873	1.849	1.845	1.819	1.881	1.902	1.864	1.849	1.839	1.880	1.826	1.829	1.816	1.886	1.862	1.777	1.840
Sum XII	1.873	1.899	1.877	1.862	1.848	1.916	1.918	1.881	1.876	1.867	1.902	1.850	1.861	1.849	1.909	1.873	1.833	1.890
Total	15.695	15.700	15.569	15.618	15.612	15.693	15.660	15.601	15.649	15.650	15.734	15.688	15.695	15.717	15.737	15.738	15.703	15.728
Fe/(Fe+Mg)	0.450	0.440	0.480	0.470	0.490	0.450	0.480	0.480	0.470	0.410	0.420	0.410	0.420	0.490	0.510	0.530	0.510	0.520
ΣAl	2.713	2.747	2.720	2.724	2.810	2.648	2.476	2.727	2.641	2.753	2.779	2.855	2.736	2.798	2.738	2.928	2.787	2.806
ASI	1.450	1.450	1.450	1.460	1.520	1.390	1.290	1.450	1.410	1.480	1.460	1.540	1.470	1.510	1.430	1.560	1.520	1.480

Table A.2.1: Representative analyses of biotite (continued).

Rock type Sample	Deformed biotite granitoid																		
	NG-3 4-Bt3	NG-3 4-Bt4	NG-3 4-Bt4	NG-3 4-Bt4	NG-3 4-Bt4	NG-3 4-Bt5	NG-3 4-Bt5	NG-3 4-Bt5	NG-3 4-Bt5	NG-3 4-Bt5	TS-2B 1-Bt1	TS-2B 1-Bt1	TK-2B 1-Bt2	TK-2B 1-Bt2	TS-2B 1-Bt3	TK-2B 2-Bt1	TK-2B 2-Bt2		
<i>Component oxides (wt.%)</i>																			
SiO ₂	36.77	36.53	36.07	36.48	36.89	37.21	37.49	36.35	36.99	37.58	37.03	35.46	35.36	37.67	37.18	35.58	37.73	37.58	
TiO ₂	2.70	2.45	2.02	2.17	2.19	2.18	2.45	2.55	2.78	1.63	1.89	2.74	2.71	1.85	1.76	2.41	1.40	2.03	
Al ₂ O ₃	15.27	15.22	15.37	15.46	15.42	15.60	15.28	15.41	15.53	15.92	14.60	16.07	16.09	15.45	15.60	16.06	16.19	15.48	
Cr ₂ O ₃	0.00	0.03	0.01	0.00	0.03	0.00	0.00	0.06	0.00	0.00	0.02	0.02	0.00	0.02	0.05	0.00	0.08	0.00	
MgO	11.16	11.12	11.06	11.58	11.57	11.65	11.82	10.82	10.99	12.15	12.91	6.81	6.91	13.11	13.15	7.33	13.41	13.43	
CaO	0.00	0.00	0.00	0.00	0.00	0.00	0.00	0.02	0.00	0.00	0.02	0.00	0.00	0.01	0.05	0.00	0.01	0.03	
MnO	0.46	0.49	0.51	0.53	0.67	0.81	0.78	0.78	0.79	0.32	0.49	0.30	0.37	0.59	0.71	0.31	0.69	0.71	
FeO	20.42	20.42	19.94	20.10	19.23	18.57	18.89	20.22	18.82	17.72	16.04	24.22	24.43	16.57	17.19	24.02	16.71	17.07	
BaO	0.00	0.00	0.00	0.00	0.04	0.00	0.00	0.00	0.00	0.03	0.00	0.00	0.18	0.00	0.00	0.00	0.00	0.00	
Na ₂ O	0.08	0.09	0.07	0.09	0.11	0.13	0.10	0.09	0.12	0.04	0.01	0.04	0.06	0.09	0.05	0.09	0.07	0.10	
K ₂ O	9.72	9.64	9.75	9.95	9.64	9.49	9.43	9.69	9.50	9.79	9.84	9.45	9.62	9.54	9.75	9.51	9.57	9.56	
Total	97.57	96.02	94.84	96.29	95.78	95.64	96.24	95.99	95.51	95.17	92.84	95.19	95.71	94.87	95.49	95.30	95.82	95.99	
<i>Mineral structural formulas (a.p.f.u) based on 22 Oxygens</i>																			
Si	5.580	5.581	5.579	5.554	5.616	5.644	5.654	5.559	5.629	5.692	5.733	5.564	5.536	5.694	5.620	5.568	5.646	5.636	
Al ^{IV}	2.420	2.419	2.421	2.446	2.384	2.356	2.346	2.441	2.371	2.308	2.267	2.436	2.464	2.306	2.380	2.432	2.354	2.364	
Sum T	8.000	8.000	8.000	8.000	8.000	8.000	8.000	8.000	8.000	8.000	8.000	8.000	8.000	8.000	8.000	8.000	8.000	8.000	
Al ^{VI}	0.310	0.321	0.381	0.327	0.382	0.432	0.371	0.337	0.413	0.534	0.396	0.536	0.504	0.447	0.400	0.530	0.502	0.372	
Cr	0.000	0.004	0.001	0.000	0.004	0.000	0.000	0.007	0.000	0.000	0.002	0.000	0.000	0.003	0.006	0.000	0.010	0.000	
Ti	0.308	0.282	0.235	0.249	0.250	0.249	0.278	0.293	0.319	0.186	0.219	0.324	0.319	0.210	0.200	0.283	0.157	0.229	
Fe ²⁺	2.592	2.609	2.579	2.560	2.448	2.355	2.383	2.587	2.394	2.394	2.244	2.076	3.179	3.198	2.095	2.173	3.143	2.092	2.141
Mn	0.059	0.064	0.067	0.068	0.086	0.104	0.099	0.102	0.102	0.041	0.065	0.040	0.049	0.075	0.090	0.041	0.087	0.090	
Mg	2.525	2.532	2.549	2.629	2.625	2.634	2.657	2.467	2.493	2.743	2.980	1.594	1.612	2.953	2.963	1.709	2.991	3.001	
Sum VI	5.794	5.812	5.812	5.832	5.795	5.775	5.788	5.793	5.722	5.748	5.738	5.674	5.682	5.783	5.832	5.706	5.838	5.834	
Ba	0.000	0.000	0.000	0.000	0.002	0.000	0.000	0.000	0.000	0.002	0.000	0.000	0.011	0.000	0.000	0.000	0.000	0.000	
Ca	0.001	0.000	0.000	0.000	0.000	0.000	0.000	0.003	0.000	0.000	0.004	0.000	0.000	0.002	0.008	0.000	0.002	0.005	
Na	0.022	0.027	0.020	0.027	0.032	0.039	0.028	0.027	0.034	0.012	0.004	0.011	0.017	0.026	0.014	0.028	0.021	0.028	
K	1.882	1.879	1.924	1.932	1.871	1.836	1.815	1.892	1.844	1.892	1.943	1.891	1.891	1.920	1.839	1.880	1.898	1.826	1.829
Sum XII	1.905	1.906	1.945	1.959	1.906	1.875	1.844	1.921	1.878	1.906	1.950	1.902	1.948	1.867	1.902	1.925	1.850	1.861	
Total	15.699	15.718	15.757	15.791	15.701	15.650	15.631	15.714	15.599	15.654	15.689	15.576	15.629	15.650	15.734	15.631	15.688	15.695	
Fe/(Fe+Mg)	0.510	0.510	0.500	0.490	0.480	0.470	0.470	0.510	0.490	0.450	0.410	0.670	0.660	0.410	0.420	0.650	0.410	0.420	
ΣAl	2.730	2.740	2.802	2.773	2.766	2.788	2.717	2.778	2.785	2.842	2.664	2.971	2.968	2.753	2.779	2.962	2.855	2.736	
ASI	1.430	1.440	1.440	1.420	1.450	1.490	1.470	1.450	1.480	1.490	1.370	1.560	1.530	1.480	1.460	1.540	1.540	1.470	

Table A.2.1: Representative analyses of biotite (continued).

Rock type Sample	Deformed biotite granitoid										Mega feldspar granitoid						
	TS-2B 3-Bt1	NN-1A 1-Bt1	NN-1A 1-Bt1	NN-1A 1-Bt3	NN-1A 1-Bt4	NN-1A 1-Bt4	NN-1A 1-Bt5	NN-1A 2-Bt1	NN-1A 2-Bt2	NN-1A 2-Bt3	NN-1A 2-Bt2	BM1 2-Bt1	BM1 2Bt1	BM1 2-Bt2	BM1 2-Bt2	BM1 3-Bt1	BM1 3-Bt2
<i>Component oxides (wt.%)</i>																	
SiO ₂	35.36	36.73	36.00	36.30	36.73	36.61	36.77	36.53	36.07	36.48	37.12	33.56	33.84	33.17	33.93	33.37	33.19
TiO ₂	2.93	1.87	2.69	1.70	1.84	1.86	2.70	2.45	2.02	2.17	2.03	2.35	2.17	2.16	2.46	2.25	2.32
Al ₂ O ₃	16.22	15.60	15.10	16.29	15.50	15.56	15.27	15.22	15.37	15.46	15.68	16.78	16.63	17.09	17.09	17.86	17.52
Cr ₂ O ₃	0.00	0.00	0.00	0.01	0.01	0.00	0.00	0.03	0.01	0.00	0.04	0.00	0.01	0.00	0.00	0.00	0.00
MgO	7.09	11.61	10.96	10.65	11.23	10.93	11.16	11.12	11.06	11.58	12.18	3.90	4.02	3.59	3.83	3.59	3.86
CaO	0.00	0.03	0.00	0.02	0.06	0.01	0.00	0.00	0.00	0.00	0.01	0.00	0.00	0.01	0.00	0.05	0.04
MnO	0.31	0.49	0.50	0.44	0.49	0.43	0.46	0.49	0.51	0.53	0.38	0.69	0.72	0.59	0.74	0.92	0.78
FeO	23.94	20.15	20.71	21.36	20.79	20.89	20.42	20.42	19.94	20.10	18.52	26.73	27.22	26.71	26.93	27.02	27.62
BaO	0.00	0.00	0.00	0.00	0.01	0.01	0.00	0.00	0.00	0.00	0.00	0.00	0.00	0.00	0.00	0.00	0.00
Na ₂ O	0.04	0.09	0.08	0.03	0.16	0.16	0.08	0.09	0.07	0.09	0.13	0.04	0.03	0.03	0.09	0.05	0.06
K ₂ O	9.60	9.35	9.61	9.57	9.13	9.43	9.72	9.64	9.75	9.95	9.68	9.19	9.15	8.80	9.18	8.71	9.09
Total	95.50	95.98	95.69	96.32	95.94	95.89	97.57	96.02	94.84	96.29	95.78	93.22	93.79	92.13	94.25	93.81	94.48
<i>Mineral structural formulas (a.p.f.u) based on 22 Oxygens</i>																	
Si	5.524	5.592	5.537	5.538	5.603	5.599	5.580	5.581	5.579	5.554	5.619	5.471	5.491	5.461	5.466	5.394	5.358
Al ^{IV}	2.476	2.408	2.463	2.462	2.397	2.401	2.420	2.419	2.421	2.446	2.381	2.529	2.509	2.539	2.534	2.606	2.642
Sum T	8.000	8.000	8.000	8.000	8.000	8.000	8.000	8.000	8.000	8.000	8.000	8.000	8.000	8.000	8.000	8.000	8.000
Al ^{VI}	0.511	0.391	0.275	0.466	0.390	0.405	0.310	0.321	0.381	0.327	0.415	0.694	0.671	0.776	0.711	0.798	0.693
Cr	0.000	0.000	0.000	0.002	0.001	0.000	0.000	0.004	0.001	0.000	0.005	0.000	0.001	0.000	0.000	0.000	0.000
Ti	0.344	0.214	0.312	0.195	0.211	0.214	0.308	0.282	0.235	0.249	0.231	0.288	0.264	0.267	0.298	0.273	0.282
Fe ²⁺	3.128	2.566	2.664	2.725	2.652	2.672	2.592	2.609	2.579	2.560	2.345	3.644	3.694	3.678	3.627	3.654	3.729
Mn	0.041	0.063	0.066	0.057	0.064	0.055	0.059	0.064	0.067	0.068	0.049	0.095	0.099	0.082	0.101	0.126	0.107
Mg	1.651	2.634	2.512	2.421	2.553	2.493	2.525	2.532	2.549	2.629	2.748	0.947	0.972	0.882	0.920	0.865	0.929
Sum VI	5.675	5.867	5.828	5.865	5.871	5.838	5.794	5.812	5.812	5.832	5.793	5.668	5.702	5.685	5.657	5.716	5.740
Ba	0.000	0.000	0.000	0.000	0.000	0.000	0.000	0.000	0.000	0.000	0.000	0.000	0.000	0.000	0.000	0.000	0.000
Ca	0.000	0.005	0.000	0.002	0.009	0.002	0.001	0.000	0.000	0.000	0.002	0.000	0.000	0.001	0.000	0.009	0.006
Na	0.013	0.028	0.023	0.009	0.047	0.047	0.022	0.027	0.020	0.027	0.038	0.011	0.010	0.009	0.029	0.014	0.020
K	1.914	1.816	1.886	1.862	1.777	1.840	1.882	1.879	1.924	1.932	1.870	1.912	1.894	1.848	1.887	1.796	1.873
Sum XII	1.927	1.849	1.909	1.873	1.833	1.890	1.905	1.906	1.945	1.959	1.911	1.923	1.904	1.857	1.915	1.819	1.899
Total	15.602	15.717	15.737	15.738	15.703	15.728	15.699	15.718	15.757	15.791	15.704	15.591	15.606	15.543	15.572	15.535	15.639
Fe/(Fe+Mg)	0.650	0.490	0.510	0.530	0.510	0.520	0.510	0.510	0.500	0.490	0.460	0.790	0.790	0.810	0.800	0.810	0.800
ΣAl	2.987	2.798	2.738	2.928	2.787	2.806	2.730	2.740	2.802	2.773	2.797	3.224	3.180	3.315	3.245	3.404	3.334
ASI	1.550	1.510	1.430	1.560	1.520	1.480	1.430	1.440	1.440	1.420	1.460	1.680	1.670	1.790	1.690	1.870	1.760

Table A.2.1: Representative analyses of biotite (continued).

Rock type	Mega feldspar granitoid																	
Sample	BM1 4-Bt1	BM1 4-Bt2	BM1 4-Bt3	DML-1 1-Bt1	DML-1 1-Bt1	DML-1 1-Bt1	DML-1 1-Bt2	DML-1 1-Bt2	DML-1 1-Bt2	DML-1 1-Bt3	DML-1 1-Bt3	DML-1 1-Bt3	DML-1 1-Bt4	DML-1 1-Bt4	DML-1 1-Bt5	DML-1 1-Bt5	KO-12 1-Bt1	KO-12 1-Bt1
<i>Component oxides (wt.%)</i>																		
SiO ₂	33.89	33.92	34.89	34.76	34.70	34.54	34.52	34.21	34.69	33.55	34.43	34.60	34.40	34.60	34.77	34.11	35.00	34.76
TiO ₂	3.21	3.33	2.96	1.77	2.55	1.79	1.87	1.74	1.72	1.74	2.87	2.33	2.44	2.26	3.31	2.31	2.72	2.48
Al ₂ O ₃	16.73	16.60	16.81	16.97	16.31	16.94	16.21	17.02	16.75	16.29	15.96	16.23	16.09	16.40	16.25	16.04	15.62	15.52
Cr ₂ O ₃	0.06	0.00	0.00	0.00	0.02	0.00	0.00	0.00	0.00	0.00	0.02	0.05	0.01	0.00	0.01	0.00	0.01	0.02
MgO	3.40	3.43	3.52	4.21	4.13	4.27	4.22	4.20	4.24	4.10	3.83	4.17	4.14	4.17	3.85	4.11	7.66	7.87
CaO	0.02	0.00	0.03	0.00	0.01	0.02	0.04	0.04	0.02	0.00	0.00	0.00	0.00	0.00	0.00	0.00	0.00	0.01
MnO	0.36	0.50	0.31	0.31	0.38	0.33	0.37	0.30	0.39	0.26	0.31	0.36	0.36	0.31	0.32	0.37	0.41	0.37
FeO	27.54	27.73	26.89	27.60	28.19	27.82	28.34	28.96	28.48	26.13	28.30	28.42	28.35	28.26	28.23	27.72	23.14	23.31
BaO	0.00	0.00	0.00	0.00	0.00	0.00	0.00	0.01	0.00	0.00	0.00	0.00	0.00	0.00	0.00	0.00	0.00	0.00
Na ₂ O	0.15	0.00	0.06	0.04	0.08	0.15	0.02	0.04	0.04	0.07	0.05	0.03	0.04	0.05	0.06	0.05	0.14	0.03
K ₂ O	8.26	9.05	8.36	9.46	9.55	9.11	9.35	8.90	9.29	8.78	9.38	9.40	9.37	9.33	9.39	9.22	9.30	9.40
Total	93.62	94.56	93.83	95.12	95.92	94.97	94.94	95.42	95.60	90.91	95.13	95.59	95.19	95.38	96.18	93.93	93.99	93.77
<i>Mineral structural formulas (a.p.f.u) based on 22 Oxygens</i>																		
Si	5.478	5.458	5.588	5.546	5.519	5.522	5.550	5.469	5.529	5.577	5.526	5.525	5.520	5.527	5.506	5.534	5.544	5.530
Al ^{IV}	2.522	2.542	2.412	2.454	2.481	2.478	2.450	2.531	2.471	2.423	2.474	2.475	2.480	2.473	2.494	2.466	2.456	2.470
Sum T	8.000	8.000	8.000	8.000	8.000	8.000	8.000	8.000	8.000	8.000	8.000	8.000	8.000	8.000	8.000	8.000	8.000	8.000
Al ^{VI}	0.666	0.607	0.760	0.738	0.576	0.714	0.621	0.675	0.676	0.768	0.544	0.580	0.562	0.616	0.539	0.600	0.460	0.439
Cr	0.007	0.000	0.000	0.000	0.003	0.000	0.000	0.000	0.000	0.000	0.002	0.006	0.001	0.000	0.001	0.000	0.001	0.003
Ti	0.391	0.404	0.356	0.213	0.305	0.216	0.226	0.209	0.206	0.217	0.346	0.280	0.294	0.272	0.394	0.282	0.323	0.297
Fe ²⁺ tot	3.723	3.733	3.602	3.683	3.749	3.719	3.810	3.872	3.797	3.632	3.799	3.796	3.805	3.776	3.738	3.761	3.066	3.101
Mn	0.049	0.067	0.042	0.042	0.052	0.044	0.050	0.040	0.052	0.036	0.042	0.048	0.049	0.042	0.043	0.050	0.055	0.049
Mg	0.820	0.823	0.841	1.002	0.979	1.017	1.012	1.001	1.006	1.015	0.917	0.993	0.989	0.992	0.909	0.995	1.808	1.867
Sum VII	5.655	5.634	5.600	5.677	5.663	5.710	5.719	5.797	5.738	5.668	5.650	5.702	5.700	5.698	5.625	5.688	5.713	5.757
Ba	0.000	0.000	0.000	0.000	0.000	0.000	0.000	0.001	0.000	0.000	0.000	0.000	0.000	0.000	0.000	0.000	0.000	0.000
Ca	0.004	0.000	0.006	0.000	0.002	0.003	0.006	0.007	0.003	0.000	0.000	0.000	0.000	0.000	0.000	0.000	0.000	0.002
Na	0.046	0.001	0.019	0.011	0.024	0.048	0.006	0.013	0.013	0.022	0.016	0.010	0.011	0.015	0.019	0.016	0.042	0.008
K	1.704	1.858	1.709	1.926	1.938	1.857	1.918	1.816	1.889	1.862	1.920	1.915	1.919	1.901	1.896	1.909	1.880	1.908
Sum XII	1.754	1.859	1.734	1.937	1.964	1.909	1.931	1.836	1.905	1.884	1.936	1.926	1.930	1.916	1.915	1.925	1.922	1.918
Total	15.409	15.493	15.334	15.614	15.627	15.619	15.650	15.633	15.643	15.553	15.586	15.628	15.629	15.615	15.540	15.613	15.635	15.675
Fe/(Fe+Mg)	0.820	0.820	0.810	0.790	0.790	0.782	0.789	0.790	0.780	0.810	0.790	0.790	0.790	0.800	0.790	0.630	0.621	
ΣAl	3.188	3.149	3.172	3.192	3.056	3.192	3.071	3.206	3.147	3.191	3.018	3.055	3.042	3.089	3.034	3.067	2.916	2.910
ASI	1.820	1.690	1.830	1.650	1.560	1.670	1.599	1.759	1.659	1.690	1.560	1.590	1.580	1.610	1.580	1.590	1.520	1.522

Table A.2.1 Representative analyses of biotite (continued).

Rock type	Mega feldspar granitoid																	
Sample	KO-12 1-Bt1	KO-12 1-Bt2	KO-12 1-Bt2	KO-12 1-Bt2	KO-12 1-Bt3	KO-12 1-Bt3	KO-12 1-Bt3	KO-12 1-Bt4	KO-12 1-Bt4	KO-12 1-Bt4	KO-12 1-Bt5	KO-12 1-Bt5	KO-12 1-Bt5	KO-12 2-Bt1	KO-12 2-Bt1	KO-12 2-Bt2	KO-12 2-Bt2	
<i>Component oxides (wt.%)</i>																		
SiO ₂	35.07	35.41	35.90	35.00	35.60	35.18	35.28	35.50	35.52	35.40	35.38	35.88	36.03	35.44	35.98	35.83	35.83	35.23
TiO ₂	2.60	2.43	0.71	2.14	2.19	2.67	2.54	2.66	2.30	2.66	3.11	2.52	2.92	3.17	3.00	2.46	3.06	2.74
Al ₂ O ₃	15.49	15.26	16.12	15.67	16.27	16.12	15.91	15.43	15.87	15.56	15.64	16.04	16.02	15.59	15.81	16.03	15.44	15.53
Cr ₂ O ₃	0.00	0.00	0.01	0.00	0.02	0.00	0.00	0.01	0.00	0.00	0.00	0.02	0.03	0.00	0.00	0.00	0.01	0.03
MgO	8.03	8.10	9.06	7.77	8.10	7.58	7.64	7.46	7.81	7.71	7.31	7.81	7.46	7.22	7.67	7.91	7.45	7.50
CaO	0.00	0.00	0.01	0.00	0.01	0.02	0.03	0.04	0.05	0.01	0.00	0.00	0.00	0.00	0.04	0.02	0.00	0.00
MnO	0.32	0.37	0.32	0.35	0.31	0.34	0.35	0.35	0.30	0.41	0.40	0.30	0.37	0.42	0.38	0.37	0.31	0.40
FeO	23.46	23.08	22.18	22.57	22.61	22.85	22.93	23.38	22.38	23.25	23.13	22.56	22.90	24.01	22.88	23.24	23.30	23.18
BaO	0.00	0.00	0.00	0.00	0.02	0.00	0.00	0.00	0.00	0.00	0.00	0.00	0.00	0.00	0.00	0.00	0.00	0.00
Na ₂ O	0.08	0.12	0.03	0.07	0.01	0.04	0.05	0.03	0.06	0.00	0.04	0.03	0.03	0.03	0.13	0.05	0.01	0.02
K ₂ O	9.34	9.32	9.34	9.20	9.42	9.49	9.34	9.44	8.99	9.45	9.38	9.43	9.45	9.34	9.22	9.43	9.28	9.28
Total	94.39	94.10	93.67	92.76	94.57	94.30	94.07	94.30	93.28	94.44	94.39	94.58	95.21	95.22	95.11	95.33	94.69	93.90
<i>Mineral structural formulas (a.p.f.u) based on 22 Oxygens</i>																		
Si	5.537	5.595	5.654	5.596	5.572	5.540	5.567	5.604	5.621	5.578	5.572	5.609	5.604	5.553	5.600	5.578	5.616	5.580
Al ^{IV}	2.463	2.405	2.346	2.404	2.428	2.460	2.433	2.396	2.379	2.422	2.428	2.391	2.396	2.447	2.400	2.422	2.384	2.420
Sum T	8.000	8.000	8.000	8.000	8.000	8.000	8.000	8.000	8.000	8.000	8.000	8.000	8.000	8.000	8.000	8.000	8.000	8.000
Al ^{VI}	0.421	0.438	0.645	0.548	0.573	0.532	0.527	0.474	0.581	0.467	0.476	0.564	0.540	0.432	0.500	0.520	0.468	0.478
Cr	0.000	0.000	0.001	0.000	0.002	0.000	0.000	0.001	0.000	0.000	0.000	0.002	0.004	0.000	0.000	0.000	0.001	0.003
Ti	0.308	0.289	0.084	0.257	0.258	0.317	0.302	0.316	0.273	0.316	0.369	0.296	0.341	0.374	0.351	0.288	0.361	0.326
Fe ²⁺ tot	3.098	3.051	2.921	3.017	2.959	3.010	3.027	3.087	2.962	3.064	3.046	2.950	2.978	3.147	2.978	3.025	3.054	3.070
Mn	0.043	0.049	0.042	0.048	0.041	0.046	0.046	0.047	0.041	0.054	0.053	0.040	0.049	0.056	0.051	0.048	0.041	0.054
Mg	1.889	1.909	2.128	1.851	1.889	1.780	1.798	1.756	1.843	1.810	1.716	1.820	1.731	1.687	1.779	1.835	1.741	1.771
Sum VII	5.760	5.736	5.821	5.722	5.723	5.684	5.699	5.682	5.700	5.711	5.660	5.672	5.643	5.695	5.657	5.716	5.667	5.703
Ba	0.000	0.000	0.000	0.000	0.001	0.000	0.000	0.000	0.000	0.000	0.000	0.000	0.000	0.000	0.000	0.000	0.000	0.000
Ca	0.000	0.000	0.002	0.001	0.002	0.004	0.004	0.005	0.007	0.009	0.001	0.000	0.000	0.000	0.007	0.003	0.000	0.000
Na	0.025	0.038	0.010	0.022	0.004	0.013	0.015	0.009	0.020	0.000	0.011	0.008	0.009	0.010	0.040	0.015	0.003	0.005
K	1.881	1.880	1.877	1.876	1.880	1.906	1.881	1.901	1.815	1.900	1.885	1.880	1.875	1.866	1.830	1.873	1.857	1.876
Sum XII	1.906	1.917	1.889	1.898	1.888	1.923	1.901	1.916	1.843	1.901	1.895	1.888	1.884	1.876	1.877	1.891	1.860	1.881
Total	15.666	15.653	15.710	15.620	15.610	15.607	15.600	15.599	15.543	15.612	15.555	15.560	15.527	15.572	15.534	15.607	15.527	15.584
Fe/(Fe+Mg)	0.623	0.624	0.582	0.623	0.610	0.632	0.633	0.640	0.623	0.631	0.640	0.622	0.631	0.65	0.632	0.623	0.643	0.632
ΣAl	2.883	2.843	2.992	2.952	3.001	2.992	2.959	2.870	2.959	2.889	2.904	2.954	2.936	2.879	2.900	2.942	2.852	2.898
ASI	1.511	1.482	1.584	1.561	1.591	1.564	1.560	1.501	1.611	1.523	1.534	1.564	1.563	1.53	1.551	1.561	1.532	1.543

Table A.2.1: Representative analyses of biotite (continued).

Rock type	Mega feldspar granitoid																	
	KO-12 2-Bt3	KO-12 2-Bt3	KO-12 2-Bt3	KO-12 2-Bt4	KO-12 2-Bt4	KO-12 3-Bt1	KO-12 3-Bt1	KO-12 3-Bt2	KO-12 3-Bt2	KO-12 3-Bt3	KO-12 3-Bt3	TE-6 1-Bt1	TE-6 1-Bt2	TE-6 1-Bt3	TE-6 2-Bt1	TE-6 2-Bt2		
<i>Component oxides (wt.%)</i>																		
SiO ₂	35.38	35.64	35.80	35.52	35.52	35.98	35.74	35.59	35.45	35.30	35.38	35.68	35.51	36.20	36.38	36.10	36.00	35.56
TiO ₂	2.58	2.54	2.71	2.58	2.80	2.33	3.05	2.19	2.55	2.60	3.15	2.96	2.99	3.41	3.38	3.31	3.10	2.94
Al ₂ O ₃	15.46	15.74	16.23	15.65	15.85	16.25	15.45	15.67	15.42	15.62	15.46	16.04	16.10	15.77	15.01	15.12	15.31	15.03
Cr ₂ O ₃	0.01	0.04	0.06	0.05	0.02	0.07	0.02	0.00	0.05	0.00	0.00	0.03	0.00	0.02	0.07	0.09	0.05	0.05
MgO	7.81	7.59	7.55	7.71	7.44	7.99	7.34	7.74	7.99	7.76	7.94	7.91	7.58	10.18	10.14	10.33	10.45	9.48
CaO	0.02	0.02	0.00	0.03	0.00	0.00	0.00	0.03	0.01	0.04	0.00	0.00	0.00	0.00	0.00	0.00	0.00	0.02
MnO	0.30	0.34	0.34	0.32	0.36	0.37	0.31	0.31	0.32	0.33	0.32	0.34	0.64	0.37	0.45	0.43	0.40	0.41
FeO	23.70	23.34	22.50	23.18	23.47	22.63	22.66	22.68	22.59	22.72	22.21	22.74	22.39	20.86	21.31	20.82	20.72	22.71
BaO	0.00	0.00	0.04	0.00	0.00	0.00	0.00	0.00	0.04	0.00	0.00	0.00	0.00	0.00	0.00	0.00	0.01	0.00
Na ₂ O	0.10	0.13	0.10	0.07	0.07	0.05	0.07	0.07	0.03	0.11	0.05	0.08	0.03	0.11	0.08	0.11	0.06	0.05
K ₂ O	9.48	9.16	9.31	9.20	9.22	9.36	9.19	8.97	9.21	9.19	9.46	9.33	9.35	9.62	9.57	9.50	9.62	9.64
Total	94.83	94.53	94.63	94.29	94.74	95.02	93.83	93.24	93.66	93.67	93.96	95.10	94.60	96.42	96.38	95.83	95.73	95.93
<i>Mineral structural formulas (a.p.f.u) based on 22 Oxygens</i>																		
Si	5.565	5.597	5.592	5.592	5.571	5.597	5.636	5.643	5.609	5.587	5.577	5.554	5.559	5.507	5.560	5.540	5.530	5.515
Al ^{IV}	2.435	2.403	2.408	2.408	2.429	2.403	2.364	2.357	2.391	2.413	2.423	2.446	2.441	2.493	2.440	2.460	2.470	2.485
Sum T	8.000	8.000	8.000	8.000	8.000	8.000	8.000	8.000	8.000	8.000	8.000	8.000	8.000	8.000	8.000	8.000	8.000	8.000
Al ^{VI}	0.431	0.510	0.580	0.495	0.501	0.575	0.509	0.571	0.484	0.501	0.448	0.497	0.529	0.336	0.264	0.275	0.301	0.261
Cr	0.001	0.005	0.008	0.006	0.002	0.008	0.002	0.000	0.006	0.000	0.000	0.003	0.000	0.002	0.008	0.011	0.006	0.006
Ti	0.305	0.300	0.318	0.306	0.331	0.272	0.362	0.261	0.303	0.310	0.373	0.347	0.352	0.390	0.388	0.382	0.358	0.343
Fe ²⁺ tot	3.118	3.065	2.939	3.051	3.078	2.944	2.989	3.007	2.989	3.007	2.927	2.961	2.931	2.655	2.724	2.671	2.661	2.945
Mn	0.039	0.045	0.044	0.042	0.048	0.049	0.042	0.041	0.043	0.045	0.042	0.044	0.085	0.048	0.058	0.055	0.052	0.053
Mg	1.832	1.778	1.758	1.810	1.739	1.853	1.726	1.828	1.884	1.831	1.865	1.836	1.770	2.308	2.310	2.364	2.393	2.192
Sum VII	5.727	5.703	5.647	5.710	5.699	5.702	5.629	5.709	5.710	5.694	5.656	5.688	5.666	5.738	5.751	5.759	5.771	5.801
Ba	0.000	0.000	0.002	0.000	0.000	0.000	0.000	0.000	0.002	0.000	0.000	0.000	0.000	0.000	0.000	0.000	0.001	0.000
Ca	0.004	0.003	0.000	0.004	0.000	0.000	0.000	0.005	0.002	0.007	0.000	0.000	0.000	0.000	0.000	0.000	0.000	0.004
Na	0.030	0.041	0.030	0.020	0.023	0.015	0.023	0.022	0.008	0.033	0.015	0.024	0.009	0.032	0.023	0.032	0.019	0.016
K	1.902	1.834	1.855	1.847	1.844	1.857	1.849	1.815	1.858	1.856	1.903	1.852	1.868	1.867	1.866	1.860	1.885	1.907
Sum XII	1.936	1.879	1.887	1.872	1.867	1.872	1.872	1.841	1.870	1.896	1.917	1.876	1.877	1.899	1.889	1.892	1.904	1.927
Total	15.662	15.582	15.535	15.581	15.566	15.574	15.501	15.550	15.580	15.590	15.573	15.564	15.637	15.641	15.651	15.676	15.727	
Fe/(Fe+Mg)	0.631	0.632	0.631	0.634	0.642	0.613	0.632	0.620	0.611	0.620	0.612	0.623	0.622	0.531	0.543	0.532	0.533	0.573
ΣAl	2.867	2.914	2.988	2.903	2.930	2.978	2.872	2.929	2.876	2.914	2.871	2.943	2.970	2.829	2.704	2.735	2.771	2.747
ASI	1.482	1.552	1.594	1.551	1.571	1.594	1.531	1.591	1.540	1.540	1.501	1.571	1.582	1.490	1.430	1.451	1.463	1.431

Table A.2.1: Representative analyses of biotite (continued).

Rock type Sample	TE-6 2-Bt3	Two-mica granitoid															
		BM-3 1-Bt1	BM-3 1-Bt2	BM-3 1Bt3	BM-3 1-Bt4	BAN-6 1-Bt1	BAN-6 1-Bt1	BAN-6 1-Bt2	BAN-6 1-Bt2	BAN-6 1-Bt3	BAN-6 1-Bt3	BAN-6 1-Bt4	BAN-6 1-Bt4	BAN-6 1-Bt4	BAN-6 1-Bt5	BAN-6 1-Bt5	BAN-6 2-Bt1
<i>Component oxides (wt.%)</i>																	
SiO ₂	36.03	33.89	34.01	33.98	34.24	34.65	34.54	34.91	34.86	34.62	34.16	34.81	34.30	34.99	35.20	34.84	35.13
TiO ₂	2.97	3.32	3.36	3.60	2.91	1.97	1.78	2.21	2.59	2.56	2.65	2.47	2.74	2.23	2.67	2.56	2.12
Al ₂ O ₃	15.30	16.80	16.89	16.66	17.18	17.73	17.67	17.59	17.73	18.33	17.45	17.63	17.88	17.79	17.97	17.76	17.71
Cr ₂ O ₃	0.01	0.00	0.01	0.03	0.00	0.04	0.00	0.08	0.00	0.00	0.01	0.00	0.00	0.05	0.00	0.02	0.00
MgO	9.76	3.65	3.74	3.69	3.86	4.10	4.37	4.13	3.88	3.75	3.82	3.91	3.78	4.19	3.99	4.08	3.88
CaO	0.00	0.00	0.00	0.01	0.00	0.00	0.02	0.00	0.00	0.00	0.04	0.00	0.00	0.02	0.00	0.02	0.02
MnO	0.35	0.54	0.57	0.58	0.55	0.53	0.37	0.37	0.52	0.49	0.51	0.38	0.38	0.44	0.56	0.50	0.43
FeO	21.23	27.37	27.04	27.56	26.48	25.25	25.34	25.19	25.30	25.14	24.73	24.55	25.18	24.52	23.97	25.29	24.21
BaO	0.08	0.00	0.00	0.00	0.00	0.00	0.00	0.00	0.00	0.00	0.00	0.00	0.00	0.00	0.00	0.00	0.00
Na ₂ O	0.01	0.07	0.05	0.05	0.07	0.08	0.02	0.06	0.03	0.08	0.09	0.06	0.05	0.05	0.07	0.03	0.06
K ₂ O	9.48	9.28	9.12	9.10	9.25	9.00	8.89	9.14	9.10	9.16	9.09	9.03	8.57	9.28	9.44	9.06	8.70
Total	95.22	94.92	94.92	94.92	94.54	93.35	93.00	93.68	94.02	94.12	92.55	92.85	92.89	93.56	93.85	94.16	92.27
<i>Mineral structural formulas (apfu) based on 22 Oxygens</i>																	
Si	5.571	5.432	5.432	5.432	5.476	5.559	5.558	5.575	5.550	5.502	5.529	5.589	5.513	5.580	5.583	5.537	5.651
Al ^{IV}	2.429	2.568	2.568	2.568	2.524	2.441	2.442	2.425	2.450	2.498	2.471	2.411	2.487	2.420	2.417	2.463	2.349
Sum T	8.000	8.000	8.000	8.000	8.000	8.000	8.000	8.000	8.000	8.000	8.000	8.000	8.000	8.000	8.000	8.000	8.000
Al ^{VI}	0.358	0.606	0.606	0.606	0.714	0.910	0.909	0.886	0.877	0.935	0.859	0.925	0.901	0.923	0.941	0.864	1.007
Cr	0.002	0.000	0.000	0.000	0.000	0.005	0.000	0.010	0.000	0.000	0.001	0.000	0.000	0.006	0.000	0.002	0.000
Ti	0.346	0.401	0.401	0.401	0.350	0.238	0.216	0.265	0.311	0.306	0.322	0.298	0.331	0.267	0.318	0.306	0.257
Fe ²⁺ tot	2.745	3.669	3.669	3.669	3.542	3.387	3.410	3.364	3.369	3.341	3.348	3.297	3.385	3.271	3.178	3.362	3.257
Mn	0.046	0.073	0.073	0.073	0.074	0.072	0.050	0.050	0.071	0.066	0.069	0.052	0.051	0.060	0.075	0.067	0.058
Mg	2.250	0.873	0.873	0.873	0.920	0.981	1.047	0.984	0.920	0.888	0.923	0.937	0.905	0.997	0.943	0.967	0.931
Sum VII	5.748	5.621	5.621	5.621	5.599	5.592	5.632	5.558	5.547	5.536	5.522	5.509	5.574	5.524	5.456	5.567	5.509
Ba	0.005	0.000	0.000	0.000	0.000	0.000	0.000	0.000	0.000	0.000	0.000	0.000	0.000	0.000	0.000	0.000	0.000
Ca	0.000	0.000	0.000	0.000	0.000	0.004	0.000	0.000	0.000	0.000	0.007	0.001	0.001	0.004	0.000	0.003	0.003
Na	0.003	0.021	0.021	0.021	0.023	0.024	0.006	0.020	0.009	0.023	0.028	0.020	0.016	0.014	0.020	0.010	0.019
K	1.870	1.898	1.898	1.898	1.888	1.842	1.825	1.862	1.848	1.858	1.878	1.850	1.758	1.887	1.909	1.836	1.785
Sum XII	1.878	1.919	1.919	1.919	1.911	1.866	1.834	1.881	1.857	1.881	1.914	1.871	1.775	1.905	1.929	1.849	1.808
Total	15.626	15.540	15.540	15.540	15.510	15.459	15.466	15.440	15.405	15.416	15.436	15.380	15.349	15.429	15.385	15.416	15.317
Fe/(Fe+Mg)	0.550	0.808	0.808	0.808	0.794	0.775	0.765	0.774	0.785	0.790	0.784	0.779	0.789	0.766	0.771	0.777	0.778
ΣAl	2.788	3.174	3.174	3.174	3.238	3.351	3.351	3.310	3.327	3.433	3.330	3.336	3.388	3.344	3.358	3.326	3.357
ASI	1.490	1.651	1.653	1.654	1.691	1.801	1.833	1.764	1.791	1.831	1.742	1.781	1.911	1.763	1.743	1.803	1.863

Table A.2.1: Representative analyses of biotite (continued).

Rock type	Two-mica granitoid																	
Sample	BAN-6 2-Bt1	BAN-6 3-Bt1	NO30 1-Bt1	NO30 1-Bt1	NO30 1-Bt1	NO-30 1-Bt2	NO-30 1-Bt2	NO-30 1-Bt3	NO-30 1-Bt3	NO-30 1-Bt4	NO-30 1-Bt4	NO-30 1-Bt5	NO-30 1-Bt5	NO-30 2-Bt1	NO-30 2-Bt1	NO-30 2-Bt1	NO-30 2-Bt1	NO-30 2-Bt2
<i>Component oxides (wt.%)</i>																		
SiO ₂	35.01	35.31	34.97	35.26	34.45	34.96	34.34	34.72	35.47	34.19	34.02	33.56	34.68	34.85	35.14	34.99	34.72	35.11
TiO ₂	3.09	2.18	2.76	2.68	2.76	2.88	2.86	2.85	2.53	2.76	2.44	2.65	3.16	3.44	2.79	3.38	3.09	3.07
Al ₂ O ₃	17.79	17.69	15.81	15.85	15.80	15.60	15.85	16.27	15.59	15.67	15.76	15.48	16.05	15.61	15.90	15.69	15.70	15.94
Cr ₂ O ₃	0.00	0.00	0.00	0.00	0.00	0.01	0.02	0.01	0.01	0.00	0.02	0.01	0.00	0.03	0.00	0.00	0.03	0.05
MgO	4.01	4.12	6.49	6.82	6.85	7.02	6.64	6.61	7.69	6.67	6.94	6.69	6.38	6.05	6.15	5.81	6.20	5.97
CaO	0.02	0.00	0.03	0.03	0.03	0.02	0.00	0.01	0.08	0.03	0.07	0.04	0.00	0.01	0.01	0.55	0.04	0.00
MnO	0.59	0.43	0.26	0.26	0.21	0.23	0.27	0.23	0.19	0.27	0.26	0.22	0.19	0.24	0.24	0.11	0.19	0.20
FeO	24.75	24.77	24.84	23.46	24.29	24.70	24.71	24.67	24.01	24.87	24.73	24.88	25.22	24.60	25.25	25.24	25.23	25.15
BaO	0.00	0.00	0.00	0.00	0.00	0.02	0.00	0.00	0.00	0.00	0.01	0.00	0.00	0.00	0.00	0.00	0.00	0.00
Na ₂ O	0.07	0.06	0.05	0.09	0.09	0.08	0.08	0.03	0.14	0.09	0.11	0.06	0.04	0.05	0.03	0.05	0.06	0.00
K ₂ O	9.29	9.04	9.32	8.76	8.79	9.45	9.32	9.42	8.94	9.46	8.98	9.21	9.46	9.49	9.46	9.03	9.30	9.50
Total	94.62	93.61	94.52	93.22	93.22	94.95	94.10	94.81	94.65	93.99	93.32	92.81	95.18	94.37	94.97	94.86	94.55	95.00
<i>Mineral structural formulas (apfu) based on 22 Oxygens</i>																		
Si	5.529	5.620	5.546	5.609	5.522	5.481	5.486	5.577	5.477	5.473	5.452	5.477	5.539	5.556	5.535	5.519	5.547	
Al ^{IV}	2.471	2.380	2.454	2.391	2.391	2.478	2.519	2.514	2.423	2.523	2.527	2.548	2.523	2.461	2.444	2.465	2.481	2.453
Sum T	8.000	8.000	8.000	8.000	8.000	8.000	8.000	8.000	8.000	8.000	8.000	8.000	8.000	8.000	8.000	8.000	8.000	8.000
Al ^{VI}	0.840	0.938	0.501	0.581	0.581	0.425	0.463	0.517	0.465	0.436	0.461	0.415	0.463	0.464	0.519	0.461	0.460	0.515
Cr	0.000	0.000	0.000	0.000	0.000	0.001	0.002	0.002	0.000	0.002	0.001	0.000	0.004	0.000	0.000	0.004	0.006	
Ti	0.367	0.261	0.329	0.321	0.321	0.342	0.343	0.338	0.299	0.333	0.295	0.324	0.375	0.411	0.331	0.403	0.369	0.365
Fe ²⁺ tot	3.268	3.297	3.294	3.121	3.121	3.263	3.299	3.259	3.156	3.331	3.328	3.380	3.331	3.270	3.339	3.339	3.354	3.323
Mn	0.079	0.058	0.035	0.035	0.035	0.030	0.037	0.031	0.025	0.036	0.035	0.030	0.026	0.032	0.032	0.015	0.025	0.027
Mg	0.943	0.978	1.534	1.618	1.618	1.654	1.579	1.556	1.802	1.592	1.665	1.620	1.502	1.433	1.449	1.370	1.469	1.407
Sum VII	5.497	5.532	5.693	5.676	5.676	5.715	5.721	5.704	5.748	5.727	5.786	5.770	5.697	5.614	5.670	5.588	5.681	5.644
Ba	0.000	0.000	0.000	0.000	0.000	0.001	0.000	0.000	0.000	0.000	0.000	0.000	0.000	0.000	0.000	0.000	0.000	
Ca	0.004	0.000	0.004	0.005	0.005	0.004	0.000	0.002	0.014	0.004	0.011	0.007	0.000	0.001	0.002	0.092	0.007	0.000
Na	0.021	0.019	0.016	0.029	0.029	0.026	0.026	0.009	0.042	0.026	0.034	0.020	0.012	0.015	0.010	0.015	0.017	0.000
K	1.872	1.836	1.886	1.779	1.779	1.904	1.897	1.899	1.793	1.932	1.843	1.909	1.905	1.925	1.908	1.821	1.886	1.914
Sum XII	1.898	1.856	1.906	1.812	1.812	1.934	1.924	1.910	1.849	1.963	1.889	1.937	1.917	1.941	1.920	1.929	1.910	1.914
Total	15.395	15.388	15.599	15.488	15.488	15.649	15.646	15.613	15.597	15.690	15.675	15.707	15.614	15.555	15.590	15.518	15.591	15.558
Fe/(Fe+Mg)	0.776	0.771	0.682	0.659	0.659	0.664	0.676	0.677	0.637	0.677	0.667	0.676	0.689	0.695	0.697	0.709	0.695	0.703
ΣAl	3.310	3.319	2.955	2.972	2.904	2.982	3.031	2.888	2.959	2.988	2.963	2.987	2.924	2.963	2.926	2.940	2.968	
ASI	1.741	1.793	1.552	1.641	1.643	1.504	1.554	1.591	1.563	1.513	1.584	1.531	1.562	1.513	1.541	1.524	1.552	

Table A.2.1: Representative analyses of biotite (continued).

Rock type	Two-mica granitoid																	
Sample	NO-30 2-Bt3	NO-30 2-Bt3	NO-30 2-Bt3	NO-30 2-Bt4	NO-30 2-Bt4	NO-30 2-Bt4	NO-30 3-Bt1	NO-30 3-Bt1	NO-30 3-Bt2	NO-30 3-Bt2	NO-30 3-Bt2	NO-30 3-Bt3	NO-30 3-Bt3	NO-30 3-Bt4	NO-30 4-Bt1	NO-30 4-Bt1	NO-30 4-Bt1	
<i>Component oxides (wt.%)</i>																		
SiO ₂	34.18	34.71	35.15	34.03	34.28	33.62	34.78	34.75	34.51	35.07	34.93	35.00	34.21	34.25	34.58	34.57	34.67	34.92
TiO ₂	3.83	2.71	2.61	3.03	3.02	2.90	3.11	3.16	2.71	2.79	2.74	2.80	3.24	3.19	3.26	2.86	2.18	2.81
Al ₂ O ₃	15.84	16.51	16.46	16.32	16.15	16.22	16.35	16.31	16.16	16.66	16.50	16.25	16.35	16.08	16.19	16.08	16.78	15.65
Cr ₂ O ₃	0.01	0.01	0.02	0.00	0.00	0.01	0.00	0.00	0.01	0.00	0.00	0.01	0.05	0.01	0.00	0.02	0.00	0.07
MgO	5.26	6.00	6.22	5.77	5.79	5.60	6.00	5.90	6.05	6.24	6.38	6.35	5.86	5.97	5.83	5.94	5.92	6.40
CaO	0.00	0.00	0.01	0.00	0.01	0.00	0.00	0.00	0.02	0.01	0.00	0.00	0.00	0.00	0.00	0.00	0.00	0.00
MnO	0.27	0.20	0.22	0.24	0.28	0.30	0.22	0.26	0.23	0.21	0.23	0.21	0.23	0.20	0.17	0.23	0.18	0.20
FeO	25.85	25.91	24.70	25.94	26.56	26.45	25.01	25.23	25.56	24.30	24.54	24.28	25.57	25.14	25.21	25.75	24.96	25.58
BaO	0.00	0.00	0.00	0.00	0.00	0.01	0.02	0.00	0.00	0.00	0.00	0.00	0.00	0.00	0.00	0.00	0.00	0.00
Na ₂ O	0.05	0.13	0.09	0.13	0.06	0.04	0.05	0.05	0.05	0.07	0.12	0.08	0.08	0.07	0.03	0.06	0.06	0.08
K ₂ O	9.46	9.30	9.36	9.42	9.44	9.38	9.45	9.51	9.16	9.31	9.48	9.35	9.58	9.35	9.42	9.36	9.33	9.49
Total	94.75	95.47	94.82	94.87	95.59	94.53	94.97	95.16	94.44	94.66	94.92	94.32	95.16	94.26	94.68	94.86	94.08	95.18
<i>Mineral structural formulas (apfu) based on 22 Oxygens</i>																		
Si	5.453	5.472	5.543	5.421	5.433	5.397	5.494	5.488	5.495	5.527	5.507	5.542	5.424	5.465	5.487	5.492	5.522	5.525
Al ^{IV}	2.547	2.528	2.457	2.579	2.567	2.603	2.506	2.512	2.505	2.473	2.493	2.458	2.576	2.535	2.513	2.508	2.478	2.475
Sum T	8.000	8.000	8.000	8.000	8.000	8.000	8.000	8.000	8.000	8.000	8.000	8.000	8.000	8.000	8.000	8.000	8.000	8.000
Al ^{VI}	0.431	0.540	0.601	0.485	0.450	0.467	0.538	0.524	0.528	0.621	0.572	0.574	0.478	0.490	0.516	0.502	0.671	0.444
Cr	0.002	0.001	0.002	0.000	0.000	0.001	0.000	0.000	0.001	0.000	0.000	0.001	0.006	0.002	0.000	0.002	0.000	0.009
Ti	0.459	0.322	0.309	0.363	0.360	0.350	0.369	0.375	0.324	0.331	0.325	0.334	0.386	0.383	0.389	0.342	0.261	0.334
Fe ²⁺ tot	3.449	3.417	3.257	3.457	3.520	3.551	3.304	3.332	3.404	3.202	3.236	3.215	3.391	3.355	3.346	3.420	3.325	3.385
Mn	0.036	0.027	0.030	0.033	0.037	0.041	0.029	0.035	0.031	0.027	0.030	0.028	0.031	0.026	0.023	0.031	0.024	0.026
Mg	1.250	1.411	1.462	1.370	1.368	1.341	1.412	1.388	1.436	1.467	1.500	1.499	1.385	1.420	1.378	1.406	1.405	1.509
Sum VII	5.627	5.717	5.661	5.707	5.734	5.750	5.653	5.653	5.723	5.648	5.663	5.651	5.678	5.676	5.651	5.703	5.686	5.706
Ba	0.000	0.000	0.000	0.000	0.000	0.001	0.001	0.000	0.000	0.000	0.000	0.000	0.000	0.000	0.000	0.000	0.000	0.000
Ca	0.000	0.000	0.001	0.000	0.002	0.000	0.000	0.000	0.003	0.001	0.000	0.000	0.000	0.000	0.000	0.000	0.000	0.000
Na	0.017	0.039	0.028	0.040	0.018	0.013	0.017	0.015	0.015	0.021	0.037	0.024	0.026	0.021	0.009	0.018	0.018	0.025
K	1.925	1.870	1.883	1.914	1.908	1.921	1.904	1.917	1.860	1.872	1.907	1.889	1.937	1.904	1.908	1.897	1.896	1.917
Sum XII	1.941	1.909	1.912	1.954	1.928	1.935	1.922	1.932	1.878	1.894	1.943	1.913	1.963	1.925	1.917	1.914	1.914	1.942
Total	15.569	15.626	15.574	15.661	15.662	15.685	15.575	15.585	15.601	15.542	15.607	15.564	15.641	15.601	15.568	15.618	15.599	15.648
Fe/(Fe+Mg)	0.734	0.708	0.690	0.716	0.720	0.726	0.701	0.706	0.703	0.686	0.683	0.682	0.710	0.703	0.708	0.709	0.703	0.692
ΣAl	2.978	3.068	3.059	3.064	3.017	3.069	3.044	3.036	3.032	3.095	3.066	3.032	3.055	3.025	3.028	3.010	3.149	2.918
ASI	1.531	1.611	1.603	1.571	1.560	1.590	1.591	1.573	1.613	1.634	1.583	1.592	1.561	1.571	1.581	1.574	1.652	1.502

Table A.2.1: Representative analyses of biotite (continued).

Rock type	Two-mica granitoid																	
Sample	NO-30 4-Bt2	NO-30 4-Bt2	NO-30 4-Bt2	NO-30 4-Bt3	NO-30 4-Bt3	NO-30 4-Bt3	NO-30 4-Bt3	NO-30 4-Bt3	NO-30 4-Bt3	NO-30 4-Bt4	NO-30 4-Bt4	NO-30 4-Bt4	NO-30 4-Bt4	NO-30 4-Bt5	NO-30 4-Bt5	NO-30 4-Bt5	NO-30 4-Bt5	
<i>Component oxides (wt.%)</i>																		
SiO ₂	35.15	34.25	34.84	34.05	35.04	34.16	34.41	34.24	34.49	34.41	34.49	34.31	34.26	34.98	34.04	33.64	34.58	
TiO ₂	2.68	2.52	2.75	2.99	2.92	3.19	2.82	2.56	2.78	2.89	3.17	2.95	3.03	2.81	2.82	2.71	2.96	
Al ₂ O ₃	15.88	16.32	16.55	16.00	15.94	16.43	16.40	15.91	15.55	15.89	16.09	16.30	15.86	16.21	15.66	16.50	16.19	
Cr ₂ O ₃	0.00	0.05	0.00	0.02	0.02	0.02	0.04	0.03	0.00	0.00	0.03	0.03	0.05	0.00	0.03	0.00	0.04	
MgO	6.15	6.25	6.26	5.80	6.00	5.81	5.98	6.07	6.21	6.17	6.10	6.02	5.79	6.28	6.05	6.06	6.15	
CaO	0.00	0.00	0.00	0.02	0.00	0.00	0.00	0.00	0.00	0.00	0.00	0.04	0.04	0.03	0.03	0.00	0.00	
MnO	0.16	0.26	0.20	0.17	0.18	0.29	0.19	0.23	0.20	0.23	0.17	0.27	0.27	0.22	0.19	0.26	0.22	
FeO	25.48	25.17	24.86	25.90	25.68	25.83	25.02	25.52	25.73	25.50	25.36	25.31	25.95	25.50	25.99	25.98	26.20	
BaO	0.00	0.00	0.00	0.00	0.00	0.00	0.00	0.00	0.00	0.00	0.00	0.00	0.00	0.00	0.00	0.00	0.00	
Na ₂ O	0.06	0.07	0.07	0.15	0.09	0.06	0.10	0.11	0.08	0.06	0.06	0.13	0.17	0.10	0.17	0.13	0.06	
K ₂ O	9.43	9.41	9.61	9.14	9.39	9.40	9.38	9.31	9.43	9.42	9.36	9.18	9.22	9.30	9.15	9.09	9.30	
Total	94.98	94.29	95.12	94.26	95.26	95.18	94.33	93.98	94.47	94.56	94.83	94.54	94.63	95.43	94.15	94.37	95.69	
<i>Mineral structural formulas (apfu) based on 22 Oxygens</i>																		
Si	5.559	5.466	5.493	5.453	5.533	5.416	5.478	5.493	5.511	5.484	5.471	5.457	5.469	5.506	5.466	5.385	5.452	
Al ^{IV}	2.441	2.534	2.507	2.547	2.467	2.584	2.522	2.507	2.489	2.516	2.529	2.543	2.531	2.494	2.534	2.615	2.548	
Sum T	8.000	8.000	8.000	8.000	8.000	8.000	8.000	8.000	8.000	8.000	8.000	8.000	8.000	8.000	8.000	8.000	8.000	
Al ^{VI}	0.520	0.535	0.568	0.474	0.499	0.487	0.556	0.502	0.439	0.468	0.479	0.514	0.453	0.512	0.430	0.498	0.460	
Cr	0.000	0.006	0.000	0.002	0.002	0.002	0.004	0.004	0.000	0.000	0.004	0.004	0.006	0.000	0.003	0.000	0.005	
Ti	0.319	0.303	0.326	0.360	0.347	0.381	0.338	0.308	0.334	0.347	0.378	0.352	0.364	0.332	0.341	0.326	0.351	
Fe ²⁺ tot	3.371	3.359	3.278	3.469	3.391	3.425	3.331	3.424	3.438	3.398	3.364	3.367	3.464	3.356	3.490	3.478	3.455	
Mn	0.022	0.036	0.026	0.023	0.024	0.039	0.026	0.031	0.027	0.031	0.022	0.037	0.036	0.030	0.026	0.036	0.029	
Mg	1.449	1.486	1.470	1.385	1.412	1.373	1.420	1.452	1.479	1.466	1.443	1.428	1.377	1.474	1.449	1.446	1.446	
Sum VII	5.681	5.725	5.667	5.714	5.676	5.706	5.675	5.722	5.717	5.710	5.690	5.702	5.700	5.705	5.740	5.784	5.746	
Ba	0.000	0.000	0.000	0.000	0.000	0.000	0.000	0.000	0.000	0.000	0.000	0.000	0.000	0.000	0.000	0.000	0.000	
Ca	0.000	0.000	0.000	0.004	0.000	0.000	0.000	0.000	0.000	0.000	0.000	0.006	0.006	0.005	0.006	0.000	0.000	
Na	0.018	0.020	0.021	0.046	0.028	0.018	0.031	0.035	0.024	0.019	0.018	0.041	0.053	0.030	0.053	0.039	0.017	
K	1.902	1.916	1.932	1.868	1.891	1.902	1.905	1.905	1.923	1.916	1.894	1.862	1.877	1.866	1.875	1.857	1.870	
Sum XII	1.921	1.936	1.953	1.918	1.918	1.921	1.936	1.940	1.947	1.935	1.911	1.910	1.936	1.902	1.934	1.896	1.887	
Total	15.601	15.661	15.620	15.632	15.594	15.627	15.611	15.662	15.664	15.645	15.601	15.612	15.637	15.607	15.673	15.680	15.634	
Fe/(Fe+Mg)	0.699	0.693	0.690	0.715	0.706	0.714	0.701	0.702	0.699	0.699	0.700	0.702	0.716	0.695	0.707	0.706	0.705	
ΣAl	2.960	3.069	3.075	3.021	2.966	3.071	3.078	3.009	2.928	2.984	3.008	3.056	2.984	3.006	2.964	3.113	3.008	
ASI	1.541	1.592	1.573	1.584	1.552	1.603	1.592	1.553	1.504	1.541	1.572	1.603	1.540	1.581	1.533	1.642	1.519	

Table A.2.2: Representative analyses of muscovite (continued).

Rock type	Two-mica granitoid																	
Sample	BM-3 1-Ms1	BM-3 1-Ms1	BM-3 1-Ms2	BM-3 1-Ms2	BM-3 2-Ms2	BM-3 2-Ms2	BM-3 3-Ms1	BM-3 3-Ms1	BM-3 3-Ms1	BM-3 4-Ms2	BM-3 4-Ms2	BM-3 4-Ms2	NO-30 1-Ms1	NO-30 1-Ms1	NO-30 1-Ms2	NO-30 1-Ms4		
<i>Component oxides (wt.%)</i>																		
SiO ₂	45.28	45.12	45.33	45.10	44.86	44.95	44.99	44.75	44.60	44.27	44.86	45.49	45.60	45.66	45.92	45.90	45.08	45.40
TiO ₂	0.57	0.71	0.96	0.54	0.42	0.40	0.46	0.30	0.37	0.31	0.37	0.49	0.46	0.69	0.80	1.11	0.90	1.05
Al ₂ O ₃	30.28	30.54	31.14	30.63	32.14	32.46	30.96	32.98	32.90	33.09	32.82	30.75	31.01	30.10	30.76	30.02	31.65	31.01
Cr ₂ O ₃	0.01	0.00	0.00	0.04	0.00	0.00	0.01	0.00	0.01	0.01	0.05	0.00	0.00	0.01	0.00	0.04	0.00	0.00
MgO	0.98	0.95	0.93	0.99	0.78	0.67	0.96	0.63	0.61	0.58	0.58	1.02	0.90	1.08	1.26	1.42	0.95	1.05
CaO	0.00	0.01	0.00	0.02	0.01	0.00	0.00	0.00	0.00	0.00	0.00	0.00	0.00	0.00	0.01	0.00	0.03	0.00
MnO	0.07	0.03	0.05	0.07	0.10	0.06	0.01	0.02	0.00	0.03	0.01	0.05	0.04	0.07	0.03	0.05	0.04	0.05
FeO	5.85	5.33	4.80	5.40	4.82	4.83	5.23	4.52	4.47	4.34	4.66	5.11	5.28	5.41	5.49	5.32	4.83	4.77
BaO	0.00	0.00	0.00	0.00	0.03	0.00	0.00	0.08	0.00	0.00	0.00	0.04	0.02	0.01	0.00	0.07	0.06	
Na ₂ O	0.26	0.23	0.28	0.27	0.42	0.47	0.47	0.37	0.39	0.36	0.39	0.33	0.29	0.25	0.26	0.28	0.39	0.31
K ₂ O	10.65	10.64	10.79	10.71	10.60	10.48	10.52	10.69	10.61	10.58	10.50	10.75	10.61	10.69	10.70	10.63	10.48	10.58
Total	93.94	93.57	94.27	93.78	94.17	94.33	93.60	94.33	93.96	93.58	94.25	93.98	94.23	93.97	95.25	95.27	94.419	94.29
<i>Mineral structural formulas (a.p.f.u) based on 22 Oxygens</i>																		
Si	6.288	6.274	6.243	6.264	6.183	6.175	6.249	6.146	6.143	6.120	6.160	6.291	6.287	6.324	6.274	6.274	6.195	6.247
Al ^{IV}	1.712	1.726	1.757	1.736	1.817	1.825	1.751	1.854	1.857	1.880	1.840	1.709	1.713	1.676	1.726	1.726	1.805	1.753
Sum T	8.000	8.000	8.000	8.000	8.000	8.000	8.000	8.000	8.000	8.000	8.000	8.000	8.000	8.000	8.000	8.000	8.000	8.000
Al ^{VI}	3.823	3.823	3.823	3.823	3.823	3.823	3.823	3.823	3.823	3.823	3.823	3.823	3.823	3.823	3.823	3.823	3.227	3.823
Cr	0.001	0.000	0.000	0.004	0.000	0.000	0.001	0.000	0.001	0.001	0.005	0.000	0.000	0.001	0.000	0.000	0.000	0.000
Ti	0.059	0.074	0.099	0.057	0.044	0.041	0.048	0.031	0.038	0.032	0.038	0.051	0.048	0.072	0.083	0.083	0.093	0.108
Fe ²⁺	0.679	0.620	0.553	0.628	0.555	0.555	0.608	0.519	0.515	0.502	0.535	0.591	0.609	0.627	0.627	0.627	0.555	0.549
Mn	0.008	0.004	0.006	0.008	0.011	0.007	0.001	0.002	0.000	0.004	0.002	0.006	0.004	0.008	0.003	0.003	0.005	0.006
Mg	0.203	0.198	0.191	0.205	0.159	0.138	0.198	0.128	0.126	0.120	0.119	0.209	0.185	0.223	0.257	0.257	0.195	0.216
Sum VI	4.195	4.174	4.146	4.181	4.172	4.174	4.174	4.164	4.163	4.170	4.171	4.160	4.171	4.169	4.198	4.198	4.169	4.156
Ba	0.000	0.000	0.000	0.000	0.002	0.000	0.000	0.004	0.000	0.000	0.000	0.000	0.002	0.001	0.001	0.001	0.004	0.003
Ca	0.000	0.002	0.000	0.002	0.001	0.000	0.000	0.000	0.000	0.000	0.000	0.000	0.000	0.000	0.001	0.001	0.004	0.000
Na	0.071	0.063	0.073	0.074	0.113	0.126	0.125	0.099	0.105	0.096	0.105	0.089	0.077	0.067	0.069	0.069	0.105	0.083
K	1.887	1.886	1.895	1.898	1.863	1.836	1.864	1.873	1.864	1.866	1.839	1.897	1.867	1.889	1.865	1.865	1.837	1.858
Sum XII	1.958	1.951	1.968	1.974	1.979	1.963	1.989	1.976	1.969	1.962	1.944	1.986	1.946	1.956	1.936	1.936	1.949	1.944
Total	14.153	14.125	14.115	14.155	14.151	14.136	14.162	14.140	14.132	14.133	14.115	14.145	14.118	14.125	14.134	14.119	14.100	
Margarite	0.00	0.10	0.00	0.11	0.07	0.00	0.00	0.00	0.00	0.00	0.00	0.00	0.00	0.08	0.08	0.20	0.00	
Paragonite	3.62	3.23	3.73	3.74	5.69	6.43	6.30	5.01	5.34	4.88	5.38	4.47	3.97	3.41	3.59	3.59	5.38	4.26
Celadorite	14.41	13.68	12.14	13.22	9.15	8.77	12.46	7.28	7.16	6.02	8.01	14.53	14.36	16.19	13.70	13.70	9.77	12.37
Muscovite	81.98	82.99	84.13	82.92	85.10	84.79	81.24	87.71	87.49	89.10	86.61	81.00	81.67	80.40	82.64	82.64	84.64	83.37
X _{Fe}	0.77	0.76	0.74	0.75	0.78	0.80	0.75	0.80	0.80	0.81	0.82	0.74	0.77	0.74	0.71	0.71	0.74	0.72

Table A.2.2: Representative analyses of muscovite (continued).

Rock type	Two-mica granitoid																	
Sample	NO-30 1-Ms4	NO-30 1-Ms4	NO-30 2-Ms2	NO-30 2-Ms2	NO-30 3-Ms2	NO-30 3-Ms2	NO-30 4-Ms4	NO-30 4-Ms4	NO-30 4-Ms4	BAN-6 1-Ms1	BAN-6 1-Ms2	BAN-6 1-Ms2	BAN-6 1-Ms2	BAN-6 1-Ms4	BAN-6 1-Ms4	BAN-6 1-Ms4	BAN-6 2-Ms4	
<i>Component oxides (wt.%)</i>																		
SiO ₂	45.05	44.81	45.06	44.75	44.64	44.83	44.96	45.56	45.52	45.50	45.27	44.84	45.09	44.77	45.58	45.63	46.13	46.66
TiO ₂	1.11	1.00	1.01	1.02	1.10	1.11	1.04	1.35	1.09	0.90	1.05	1.08	0.97	1.03	1.01	0.94	0.98	0.21
Al ₂ O ₃	30.00	28.56	31.44	31.36	31.15	31.29	31.01	30.21	31.00	31.51	33.50	34.03	33.04	33.30	31.80	31.67	30.39	32.48
Cr ₂ O ₃	0.07	0.00	0.02	0.07	0.08	0.02	0.00	0.00	0.03	0.01	0.02	0.00	0.00	0.00	0.00	0.04	0.00	0.00
MgO	1.25	1.56	1.00	0.98	1.03	1.06	1.07	1.20	1.06	1.02	0.77	0.81	0.89	0.87	1.19	1.14	1.38	1.12
CaO	0.00	0.00	0.01	0.00	0.00	0.00	0.00	0.00	0.00	0.00	0.00	0.00	0.00	0.00	0.00	0.01	0.00	0.00
MnO	0.00	0.06	0.00	0.04	0.02	0.00	0.01	0.03	0.00	0.00	0.05	0.05	0.06	0.09	0.03	0.00	0.06	0.07
FeO	5.39	5.87	4.83	4.70	4.67	4.51	5.11	4.77	4.74	5.02	2.55	2.23	2.96	2.81	3.17	4.12	3.84	2.94
BaO	0.00	0.07	0.03	0.03	0.00	0.01	0.02	0.00	0.04	0.08	0.00	0.01	0.00	0.01	0.00	0.02	0.00	0.01
Na ₂ O	0.22	0.24	0.37	0.40	0.32	0.32	0.45	0.26	0.36	0.44	0.53	0.60	0.33	0.45	0.35	0.30	0.29	0.26
K ₂ O	10.89	10.87	10.42	10.65	10.44	10.47	10.74	10.36	10.56	10.61	10.29	10.33	10.60	10.52	10.49	9.97	10.33	10.63
Total	93.97	93.05	94.18	93.99	93.45	93.61	94.40	94.481	94.403	95.089	94.022	93.961	93.938	93.86	93.64	93.83	93.40	94.38
<i>Mineral structural formulas (a.p.f.u) based on 22 Oxygens</i>																		
Si	6.257	6.316	6.204	6.186	6.194	6.203	6.203	6.312	6.253	6.217	6.157	6.099	6.162	6.124	6.252	6.254	6.357	6.33
Al ^{IV}	1.743	1.684	1.796	1.814	1.806	1.797	1.797	1.688	1.747	1.783	1.843	1.901	1.838	1.876	1.748	1.746	1.643	1.67
Sum T	8.000	8.000	8.000	8.000	8.000	8.000	8.000	8.000	8.000	8.000	8.000	8.000	8.000	8.000	8.000	8.000	8.000	8.00
Al ^{VI}	3.167	3.060	3.305	3.295	3.289	3.305	3.244	3.181	3.823	3.823	3.823	3.823	3.484	3.823	3.393	3.370	3.292	3.51
Cr	0.007	0.000	0.002	0.007	0.009	0.002	0.000	0.001	0.003	0.001	0.002	0.000	0.000	0.000	0.005	0.000	0.00	0.00
Ti	0.116	0.106	0.105	0.106	0.115	0.115	0.108	0.081	0.113	0.092	0.108	0.110	0.099	0.106	0.104	0.097	0.101	0.02
Fe ²⁺	0.626	0.692	0.556	0.543	0.542	0.522	0.590	0.649	0.545	0.573	0.290	0.253	0.338	0.322	0.363	0.472	0.442	0.33
Mn	0.000	0.007	0.000	0.004	0.003	0.000	0.001	0.005	0.000	0.000	0.005	0.006	0.007	0.011	0.004	0.000	0.007	0.01
Mg	0.258	0.329	0.204	0.201	0.214	0.218	0.220	0.273	0.217	0.208	0.157	0.163	0.181	0.176	0.244	0.232	0.284	0.23
Sum VI	4.175	4.192	4.172	4.156	4.171	4.161	4.163	4.189	4.149	4.166	4.088	4.088	4.109	4.107	4.108	4.176	4.127	4.10
Ba	0.000	0.004	0.002	0.001	0.000	0.000	0.001	0.000	0.002	0.004	0.000	0.000	0.001	0.000	0.001	0.000	0.000	0.00
Ca	0.000	0.000	0.002	0.000	0.000	0.001	0.000	0.000	0.001	0.000	0.000	0.000	0.000	0.000	0.000	0.001	0.00	0.00
Na	0.059	0.067	0.098	0.106	0.086	0.087	0.120	0.057	0.095	0.116	0.138	0.158	0.088	0.119	0.094	0.079	0.077	0.07
K	1.929	1.954	1.830	1.878	1.848	1.849	1.890	1.909	1.851	1.849	1.785	1.792	1.849	1.836	1.836	1.742	1.816	1.84
Sum XII	1.988	2.025	1.932	1.986	1.934	1.937	2.010	1.966	1.949	1.923	1.950	1.936	1.956	1.930	1.823	1.894	1.91	
Total	14.162	14.217	14.104	14.142	14.106	14.098	14.173	14.155	14.097	14.135	14.011	14.037	14.046	14.063	14.038	13.999	14.021	14.01
Margarite	0.00	0.00	0.10	0.00	0.00	0.03	0.00	0.01	0.00	0.00	0.01	0.00	0.00	0.02	0.00	0.05	0.00	
Paragonite	2.95	3.30	5.08	5.34	4.46	4.48	5.95	2.91	4.90	5.90	7.21	8.10	4.50	6.12	4.85	4.36	4.09	3.61
Celadorite	12.86	15.78	10.22	9.28	9.71	10.13	10.13	15.61	12.60	10.90	7.92	5.00	8.10	6.21	12.60	12.71	17.84	16.29
Muscovite	84.19	80.92	84.61	85.38	85.82	85.36	83.92	81.47	82.50	83.20	84.90	86.90	87.40	87.70	82.54	82.93	78.01	80.10
X _{Fe}	0.71	0.68	0.73	0.73	0.72	0.71	0.73	0.70	0.72	0.73	0.65	0.61	0.65	0.60	0.67	0.61	0.59	

Table A.2.2: Representative analyses of muscovite (continued).

Rock type	Two-mica granitoid																	
Sample	BAN-6 2-Ms4	BAN-6 2-Ms4	BAN-6 3-Ms4	BAN-6 3-Ms4	BAN-6 3-Ms4	TA-9 1-Ms1	TA-9 1-Ms1	TA-9 1-Ms1	TA-9 1-Ms4	TA-9 1-Ms4	TA-9 3-Ms1	TA-9 3-Ms2	TA-9 4-Ms1	TA-9 4-Ms1	TA-9 4-Ms3	TA-9 4-Ms3	TA-9 4-Ms3	
<i>Component oxides (wt.%)</i>																		
SiO ₂	45.52	45.52	45.64	45.54	45.43	46.06	45.34	45.52	45.99	45.83	46.20	45.66	45.89	45.45	44.86	45.08	45.03	45.49
TiO ₂	0.97	0.95	0.95	0.99	1.03	0.93	1.04	1.06	1.00	0.72	0.58	0.90	0.83	0.80	0.99	0.58	0.61	0.48
Al ₂ O ₃	33.32	33.79	33.37	32.90	33.27	32.52	32.98	33.27	31.13	30.53	32.52	30.93	30.97	31.02	31.36	31.66	31.01	31.03
Cr ₂ O ₃	0.02	0.00	0.01	0.01	0.00	0.00	0.00	0.05	0.00	0.06	0.00	0.00	0.02	0.02	0.00	0.01	0.01	0.00
MgO	0.86	0.78	0.87	0.95	0.93	0.93	0.85	0.78	1.20	1.30	0.97	0.95	0.97	1.04	1.02	0.86	1.05	1.16
CaO	0.00	0.03	0.00	0.00	0.00	0.00	0.00	0.00	0.00	0.00	0.00	0.00	0.00	0.00	0.00	0.00	0.00	0.00
MnO	0.01	0.09	0.02	0.06	0.00	0.06	0.11	0.05	0.08	0.11	0.12	0.09	0.08	0.06	0.08	0.11	0.11	0.16
FeO	2.68	2.91	2.60	2.84	2.85	3.61	3.26	3.04	4.13	4.30	3.91	4.52	4.30	4.27	4.34	4.44	4.38	4.39
BaO	0.01	0.05	0.00	0.00	0.00	0.01	0.00	0.00	0.04	0.11	0.00	0.02	0.06	0.04	0.13	0.08	0.12	
Na ₂ O	0.42	0.46	0.37	0.35	0.44	0.33	0.38	0.37	0.29	0.29	0.29	0.26	0.29	0.30	0.36	0.37	0.25	0.28
K ₂ O	10.35	10.49	10.53	10.60	10.55	10.57	10.49	10.52	10.34	10.62	10.44	10.53	10.48	10.58	10.34	10.31	10.44	10.62
Total	94.17	95.06	94.81	94.24	94.49	95.01	94.45	94.67	94.16	93.80	95.15	93.85	93.83	93.61	93.39	93.56	92.97	93.71
<i>Mineral structural formulas (apfu) based on 22 Oxygens</i>																		
Si	6.18	6.14	6.178	6.197	6.164	6.235	6.169	6.169	6.296	6.322	6.252	6.294	6.315	6.280	6.214	6.234	6.267	6.287
Al ^{IV}	1.82	1.86	1.822	1.803	1.836	1.765	1.831	1.831	1.704	1.678	1.748	1.706	1.685	1.720	1.786	1.766	1.733	1.713
Sum T	8.00	8.00	8.000	8.000	8.000	8.000	8.000	8.000	8.000	8.000	8.000	8.000	8.000	8.000	8.000	8.000	8.000	8.000
Al ^{VI}	3.52	3.52	3.464	3.472	3.484	3.423	3.458	3.482	3.823	3.823	3.823	3.823	3.823	3.823	3.823	3.823	3.823	3.823
Cr	0.00	0.00	0.000	0.001	0.000	0.000	0.000	0.006	0.000	0.007	0.000	0.000	0.002	0.003	0.000	0.001	0.001	0.000
Ti	0.10	0.10	0.105	0.102	0.105	0.095	0.106	0.108	0.103	0.074	0.059	0.093	0.086	0.083	0.103	0.061	0.064	0.050
Fe ²⁺	0.30	0.33	0.356	0.324	0.323	0.408	0.371	0.344	0.473	0.496	0.442	0.522	0.495	0.493	0.503	0.513	0.509	0.507
Mn	0.00	0.01	0.006	0.007	0.000	0.006	0.013	0.006	0.010	0.013	0.014	0.011	0.010	0.007	0.010	0.013	0.013	0.018
Mg	0.17	0.16	0.182	0.192	0.189	0.188	0.172	0.158	0.244	0.268	0.196	0.194	0.198	0.215	0.210	0.178	0.218	0.239
Sum VI	4.10	4.11	4.114	4.097	4.101	4.120	4.120	4.105	4.149	4.144	4.150	4.139	4.128	4.133	4.159	4.159	4.160	4.157
Ba	0.00	0.00	0.000	0.000	0.000	0.001	0.000	0.000	0.000	0.002	0.006	0.000	0.001	0.003	0.002	0.007	0.004	0.006
Ca	0.00	0.00	0.000	0.000	0.000	0.000	0.000	0.000	0.000	0.000	0.000	0.000	0.000	0.000	0.000	0.000	0.000	0.000
Na	0.11	0.12	0.081	0.092	0.115	0.087	0.099	0.096	0.077	0.077	0.077	0.069	0.077	0.081	0.096	0.099	0.066	0.074
K	1.79	1.81	1.837	1.841	1.826	1.825	1.820	1.819	1.805	1.868	1.803	1.851	1.840	1.866	1.827	1.819	1.853	1.872
Sum XII	1.90	1.93	1.918	1.933	1.941	1.912	1.919	1.916	1.882	1.948	1.886	1.921	1.917	1.950	1.925	1.926	1.924	1.952
Total	14.00	14.04	14.033	14.030	14.041	14.032	14.040	14.021	14.031	14.091	14.035	14.060	14.045	14.083	14.084	14.085	14.084	14.108
Margarite	0.00	0.22	0.00	0.00	0.00	0.00	0.00	0.00	0.00	0.00	0.00	0.00	0.00	0.00	0.00	0.00	0.00	0.00
Paragonite	5.84	6.17	4.23	4.78	5.91	4.54	5.17	5.02	4.10	3.97	4.09	3.62	4.00	4.17	4.97	5.18	3.46	3.79
Celadonite	9.12	7.07	8.90	9.84	8.22	11.76	8.46	8.44	14.81	16.08	12.59	14.72	15.75	14.00	10.71	11.68	13.36	14.34
Muscovite	85.04	86.54	86.87	85.38	85.87	83.69	86.37	86.54	81.09	79.95	83.32	81.66	80.25	81.83	84.31	83.13	83.18	81.87
X _{Fe}	0.64	0.68	0.66	0.63	0.63	0.69	0.68	0.68	0.66	0.65	0.69	0.73	0.71	0.70	0.71	0.74	0.70	0.68

Table A.2.3: Representative analyses of garnet.

Rock type Sample	Two-mica granitoid																	
	TA-9 1-Grt1 rim	TA-9 1-Grt1 rim	TA-9 1-Grt2 core	TA-9 1-Grt3 rim	TA-9 1-Grt3 core	TA-9 2-Grt1 rim	TA-9 2-Grt1 rim	TA-9 2-Grt2 rim	TA-9 2-Grt3 core	TA-9 3-Grt1 rim	TA-9 3-Grt1 core	TA-9 3-Grt2 core	TA-9 4-Grt1 core	TA-9 4-Grt1 rim	TA-9 5-Grt1 rim	TA-9 5-Grt1 core	TA-9 5-Grt2 rim	TA-9 5-Grt2 core
<i>Component oxydes (wt.%)</i>																		
SiO ₂	36.04	35.35	35.76	35.78	35.38	35.84	35.49	35.94	35.72	36.03	36.00	35.82	35.78	35.76	36.59	36.17	35.91	35.19
TiO ₂	0.06	0.00	0.03	0.02	0.06	0.01	0.02	0.06	0.04	0.12	0.03	0.07	0.05	0.00	0.06	0.06	0.06	0.00
Al ₂ O ₃	20.55	20.47	20.53	20.57	20.42	20.45	20.70	20.40	20.55	20.49	20.69	20.59	20.48	20.69	20.95	20.51	20.43	20.20
Cr ₂ O ₃	0.01	0.02	0.04	0.00	0.05	0.01	0.02	0.00	0.03	0.00	0.00	0.02	0.05	0.00	0.00	0.00	0.00	0.02
Fe ₂ O ₃	0.60	0.82	0.65	0.37	0.97	0.19	0.78	0.59	0.13	0.47	0.45	0.31	0.67	0.13	0.13	0.12	0.51	0.76
MgO	0.11	0.09	0.16	0.08	0.12	0.07	0.06	0.09	0.11	0.09	0.05	0.09	0.07	0.05	0.09	0.09	0.13	0.05
CaO	0.46	0.16	0.20	0.20	0.17	0.20	0.22	0.56	0.22	0.62	0.19	0.20	0.25	0.17	0.63	0.19	0.19	0.15
MnO	19.72	21.41	19.58	20.46	21.46	20.84	22.73	19.67	19.36	19.29	23.28	21.63	21.56	19.82	18.92	21.65	19.95	23.27
FeO	22.78	20.95	22.97	22.08	20.96	21.64	19.86	22.51	23.11	23.04	19.67	20.94	21.04	22.92	24.06	21.10	22.69	18.80
Total	100.32	99.26	99.92	99.56	99.58	99.25	99.86	99.82	99.26	100.16	100.36	99.66	99.96	99.55	101.42	99.91	99.87	98.44
<i>Mineral structural formulas (apfu) based on 24 Oxygens</i>																		
Si	5.940	5.901	5.923	5.942	5.890	5.968	5.887	5.951	5.949	5.947	5.935	5.941	5.926	5.941	5.958	5.980	5.949	5.921
Al	0.060	0.099	0.077	0.058	0.110	0.032	0.113	0.049	0.051	0.053	0.065	0.059	0.074	0.059	0.042	0.020	0.051	0.079
Ti	0.007	0.000	0.004	0.003	0.007	0.001	0.003	0.007	0.005	0.015	0.003	0.008	0.006	0.000	0.007	0.007	0.008	0.000
Al	3.934	3.927	3.932	3.969	3.896	3.980	3.933	3.933	3.982	3.933	3.956	3.967	3.924	3.993	3.978	3.977	3.938	3.927
Cr	0.002	0.002	0.005	0.000	0.006	0.001	0.003	0.000	0.004	0.000	0.000	0.002	0.006	0.000	0.000	0.000	0.000	0.003
Fe ³⁺	0.074	0.103	0.082	0.047	0.122	0.024	0.097	0.073	0.016	0.058	0.055	0.038	0.084	0.016	0.016	0.015	0.064	0.096
Mg	0.026	0.022	0.038	0.020	0.029	0.018	0.014	0.023	0.027	0.023	0.013	0.022	0.017	0.012	0.021	0.023	0.031	0.012
Ca	0.081	0.029	0.035	0.035	0.030	0.036	0.038	0.100	0.039	0.110	0.034	0.035	0.045	0.030	0.109	0.034	0.034	0.027
Mn	2.754	3.026	2.747	2.878	3.027	2.939	3.194	2.759	2.731	2.697	3.251	3.039	3.025	2.789	2.609	3.032	2.799	3.317
Fe ²⁺	3.140	2.924	3.182	3.067	2.919	3.013	2.756	3.117	3.218	3.180	2.711	2.905	2.915	3.185	3.277	2.918	3.143	2.646
Total	16.018	16.033	16.025	16.018	16.036	16.013	16.037	16.014	16.020	16.016	16.023	16.017	16.023	16.025	16.017	16.007	16.017	16.027
<i>End-members (Mol.%)</i>																		
Uvarovite	0.04	0.05	0.13	0.00	0.15	0.02	0.07	0.00	0.09	0.00	0.00	0.05	0.15	0.00	0.00	0.00	0.00	0.07
Andradite	1.32	0.42	0.45	0.58	0.34	0.57	0.57	1.66	0.52	1.82	0.56	0.53	0.59	0.40	0.58	0.55	0.58	0.38
Grossular	0.00	0.00	0.00	0.00	0.00	0.00	0.00	0.00	0.04	0.02	0.00	0.00	0.00	0.10	1.23	0.02	0.00	0.00
Almandine	52.32	48.73	53.02	51.12	48.62	50.17	45.92	51.96	53.51	52.91	45.13	48.41	48.57	52.94	54.47	48.57	52.32	44.07
Spessartine	45.88	50.43	45.76	47.97	50.41	48.93	53.22	45.99	45.40	44.87	54.10	50.64	50.40	46.37	43.38	50.47	46.59	55.27
Pyrope	0.44	0.36	0.64	0.33	0.48	0.30	0.23	0.39	0.44	0.38	0.21	0.36	0.29	0.19	0.34	0.38	0.52	0.20
X _{Fe}	0.99	0.99	0.99	0.99	0.99	0.99	1.00	0.99	0.99	0.99	1.00	0.99	1.01	1.00	0.99	0.99	0.99	1.00
X _{Mn}	0.47	0.51	0.46	0.48	0.51	0.49	0.54	0.47	0.46	0.46	0.54	0.51	0.51	0.47	0.44	0.51	0.47	0.56

Table A.2.4: Representative analyses of amphibole (continued).

Rock type	Biotite granitoid																	
	Sample		BL-8	BL-8	BL-8	BL-8	BL-8	LE-2										
	1-am1	1-am2	1-am3	2-am1	2-am2	2-am3	1-am1	1-am1	1-am2	1-am3	1-am3	1-am3	1-am4	1-am4	2-am1	2-am2	2-am3	2-am4
	core	core	core	core	core	core	rim	core										
<i>Compoment oxydes (wt.%)</i>																		
SiO ₂	44.75	43.27	44.34	42.84	43.58	42.82	43.64	42.79	42.62	43.65	42.40	42.44	42.58	42.77	43.78	43.15	42.88	42.40
TiO ₂	0.91	1.07	1.07	0.47	0.69	0.57	0.75	0.72	1.00	0.87	0.71	0.78	1.21	1.44	1.13	1.32	1.19	0.79
Al ₂ O ₃	7.61	8.82	8.46	9.51	8.74	9.66	9.14	9.80	9.72	8.92	9.92	9.84	9.47	9.04	8.52	9.19	9.28	9.51
Fe ₂ O ₃	4.77	5.51	4.84	5.83	5.40	5.54	4.27	5.56	5.50	4.71	5.22	4.45	4.60	4.24	4.11	3.87	4.33	5.20
Cr ₂ O ₃	0.04	0.00	0.01	0.05	0.03	0.00	0.01	0.00	0.00	0.02	0.01	0.00	0.02	0.01	0.02	0.04	0.02	0.00
MgO	10.20	9.45	9.79	8.80	9.15	8.87	9.64	9.42	9.37	9.83	8.97	9.36	9.54	9.64	10.20	9.76	9.84	10.02
CaO	11.56	11.36	11.63	11.57	11.54	11.62	11.81	11.69	11.64	11.72	11.63	11.68	11.67	11.41	11.68	11.54	11.64	11.87
MnO	1.07	1.00	1.02	1.00	1.13	0.98	0.47	0.56	0.55	0.55	0.46	0.56	0.47	0.52	0.50	0.48	0.41	0.43
FeO	14.80	15.70	15.46	15.73	15.83	15.78	15.85	15.42	15.25	15.46	15.73	15.53	15.58	15.75	15.28	15.89	15.59	14.04
Na ₂ O	1.20	1.54	1.26	1.39	1.40	1.41	1.35	1.55	1.31	1.34	1.31	1.46	1.40	1.45	1.32	1.48	1.54	1.26
K ₂ O	0.87	1.17	1.09	1.17	1.12	1.15	1.08	1.11	1.17	1.09	1.16	1.22	1.27	1.18	1.10	1.19	1.16	1.15
FeOT	19.09	20.66	19.82	20.98	20.70	20.76	19.69	20.43	20.19	19.70	20.43	19.54	19.72	19.56	18.98	19.37	19.48	18.72
Total	97.77	98.89	98.98	98.36	98.62	98.38	98.01	98.63	98.11	98.15	97.51	97.33	97.81	97.44	97.63	97.91	97.86	96.68
<i>Mineral structural formulas based (a.p.f.u) on 23 Oxygens</i>																		
Si	6.756	6.529	6.643	6.505	6.592	6.497	6.600	6.457	6.458	6.591	6.471	6.481	6.475	6.521	6.630	6.540	6.505	6.485
Ti	0.103	0.122	0.121	0.054	0.079	0.065	0.086	0.082	0.114	0.099	0.082	0.090	0.138	0.165	0.128	0.150	0.136	0.091
Al ^{IV}	1.244	1.47	1.357	1.495	1.408	1.503	1.400	1.543	1.542	1.409	1.529	1.519	1.524	1.479	1.37	1.46	1.495	1.515
Al ^{VI}	0.110	0.097	0.138	0.208	0.149	0.223	0.230	0.199	0.194	0.179	0.256	0.253	0.172	0.145	0.151	0.181	0.163	0.199
Fe ³⁺	0.542	0.626	0.546	0.666	0.615	0.632	0.485	0.631	0.627	0.535	0.600	0.511	0.527	0.486	0.469	0.442	0.494	0.598
Cr	0.005	0.000	0.001	0.006	0.004	0.000	0.001	0.000	0.000	0.002	0.001	0.000	0.002	0.002	0.002	0.005	0.002	0.000
Mg	2.295	2.124	2.188	1.993	2.063	2.005	2.174	2.120	2.116	2.213	2.040	2.131	2.162	2.191	2.302	2.205	2.224	2.284
Ca	1.870	1.836	1.867	1.882	1.870	1.889	1.914	1.891	1.890	1.895	1.901	1.912	1.901	1.865	1.896	1.873	1.891	1.946
Mn	0.137	0.128	0.130	0.128	0.145	0.126	0.060	0.071	0.070	0.070	0.060	0.073	0.060	0.067	0.063	0.062	0.053	0.056
Fe ²⁺	1.869	1.981	1.937	1.998	2.003	2.001	2.005	1.946	1.932	1.953	2.008	1.984	1.982	2.008	1.935	2.014	1.978	1.795
Na	0.351	0.451	0.365	0.408	0.411	0.414	0.396	0.454	0.384	0.393	0.386	0.431	0.412	0.430	0.386	0.435	0.452	0.374
K	0.168	0.226	0.209	0.227	0.216	0.223	0.208	0.214	0.226	0.209	0.225	0.238	0.247	0.229	0.212	0.230	0.225	0.225
Total	15.450	15.591	15.502	15.571	15.554	15.578	15.558	15.608	15.552	15.549	15.560	15.622	15.603	15.587	15.545	15.598	15.620	15.568
X _{Mg}	0.55	0.52	0.53	0.50	0.51	0.50	0.52	0.52	0.52	0.53	0.50	0.52	0.52	0.54	0.52	0.53	0.56	

Table A.2.4: Representative analyses of amphibole (continued).

Rock type Sample	Deformed biotite granitoid																	
	NG-3 3-am1 rim	NG-3 3-am1 core	NG-3 3-am2 rim	NG-3 3-am2 core	NG-3 4-am4 rim	NG-3 4-am4 core	BFS-7 1-am1 rim	BFS-7 1-am1 rim	BFS-7 1-am1 core	BFS-7 1-am1 rim	ND-2 2-am2 rim	ND-2 2-am2 core	ND-2 2-am3 rim	ND-2 3-am3 rim	ND-2 3-am3 core	ND-2 3-am3 rim	ND-2 4-am4 core	
<i>Component oxydes (wt.%)</i>																		
SiO ₂	43.05	43.10	43.62	44.19	45.69	45.15	45.72	45.08	44.90	45.79	45.45	45.68	45.64	50.59	45.18	44.78	47.00	45.56
TiO ₂	0.64	0.75	0.97	1.28	0.52	0.88	1.25	1.33	1.21	1.23	0.67	0.48	0.62	0.24	0.71	1.07	0.27	0.69
Al ₂ O ₃	10.07	10.01	9.37	8.78	7.15	7.80	7.68	8.29	8.41	7.65	7.35	7.59	7.34	4.09	7.63	7.90	6.66	7.39
Fe ₂ O ₃	4.56	4.48	4.24	4.29	3.55	3.82	3.02	3.44	2.81	3.02	4.59	4.05	4.14	3.57	4.54	2.90	4.08	3.55
Cr ₂ O ₃	0.04	0.04	0.01	0.00	0.00	0.04	0.00	0.01	0.01	0.04	0.01	0.04	0.05	0.00	0.05	0.00	0.04	0.00
MgO	9.38	9.35	10.01	10.50	11.23	11.12	11.12	10.62	11.29	11.91	11.25	11.54	11.46	14.42	11.08	11.19	11.87	11.59
CaO	11.49	11.31	11.42	11.17	11.68	11.52	12.00	11.49	11.60	11.77	11.98	11.88	11.78	12.27	11.64	11.68	11.95	11.73
MnO	1.04	1.01	1.04	1.07	0.68	0.70	0.54	0.62	0.50	0.49	0.66	0.59	0.75	0.62	0.70	0.53	0.66	0.59
FeO	15.43	15.16	14.81	14.52	14.08	14.18	14.83	15.11	14.31	13.75	13.84	13.70	13.60	11.39	13.69	14.77	13.83	14.06
Na ₂ O	1.62	1.42	1.48	1.53	1.19	1.32	1.07	1.26	1.44	1.29	1.14	1.27	1.24	0.66	1.07	1.50	1.25	1.41
K ₂ O	1.16	1.19	1.15	1.12	0.76	0.96	0.89	0.90	0.95	0.86	0.80	0.85	0.82	0.38	0.94	1.08	0.68	0.90
Total	98.47	97.81	98.12	98.45	96.53	97.49	98.11	98.13	97.42	97.81	97.74	97.66	97.43	98.24	97.23	97.39	98.29	97.46
<i>Mineral structural formulas based (a.p.f.u) on 23 Oxygens</i>																		
Si	6.495	6.528	6.572	6.619	6.911	6.786	6.819	6.742	6.736	6.817	6.812	6.833	6.845	7.347	6.802	6.751	6.969	6.838
Ti	0.073	0.086	0.110	0.144	0.060	0.099	0.141	0.149	0.136	0.138	0.075	0.054	0.069	0.026	0.080	0.121	0.030	0.077
Al ^{IV}	1.505	1.472	1.428	1.381	1.089	1.214	1.181	1.258	1.264	1.183	1.188	1.167	1.155	0.653	1.198	1.249	1.031	1.162
Al ^{VI}	0.286	0.316	0.235	0.17	0.185	0.168	0.168	0.203	0.223	0.159	0.111	0.17	0.143	0.046	0.156	0.155	0.133	0.145
Fe ³⁺	0.517	0.510	0.481	0.484	0.404	0.432	0.339	0.387	0.317	0.338	0.518	0.455	0.467	0.390	0.515	0.329	0.456	0.400
Cr	0.004	0.004	0.001	0.000	0.000	0.005	0.000	0.001	0.001	0.005	0.002	0.004	0.006	0.000	0.006	0.000	0.005	0.000
Mg	2.110	2.110	2.248	2.344	2.532	2.491	2.474	2.367	2.524	2.643	2.513	2.573	2.563	3.121	2.488	2.516	2.625	2.592
Ca	1.858	1.836	1.844	1.793	1.893	1.855	1.917	1.841	1.865	1.877	1.923	1.904	1.893	1.910	1.877	1.888	1.898	1.885
Mn	0.133	0.129	0.133	0.136	0.087	0.089	0.068	0.079	0.063	0.062	0.084	0.074	0.095	0.077	0.090	0.068	0.083	0.075
Fe ²⁺	1.946	1.920	1.866	1.819	1.782	1.782	1.850	1.889	1.796	1.712	1.735	1.714	1.706	1.383	1.723	1.863	1.714	1.764
Na	0.473	0.416	0.431	0.443	0.349	0.386	0.309	0.364	0.419	0.373	0.332	0.367	0.361	0.186	0.312	0.438	0.360	0.410
K	0.224	0.230	0.222	0.214	0.147	0.183	0.169	0.172	0.181	0.164	0.152	0.163	0.156	0.071	0.180	0.208	0.129	0.172
Total	15.625	15.558	15.572	15.548	15.438	15.490	15.435	15.453	15.525	15.471	15.445	15.479	15.459	15.210	15.427	15.585	15.433	15.522
X _{Mg}	0.52	0.52	0.55	0.56	0.59	0.58	0.57	0.56	0.58	0.61	0.59	0.60	0.60	0.69	0.59	0.57	0.60	0.60

Table A.2.4: Representative analyses of amphibole (continued).

Rock type Sample	Deformed biotite granitoid										
	ND-2 4-am4 rim	TK-2 1-am1 core	TK-2 1-am2 core	TK-2 1-am3 core	TK-2 2-am3 core	NN-1a 1-am1 rim	NN-1a 1-am1 core	NN-1a 1-am1 rim	NN-1a 1-am2 rim	NN-1a 1-am2 rim	NN-1a 2-am1 core
<i>Component oxydes (wt.%)</i>											
SiO ₂	46.08	44.05	44.22	44.08	44.99	42.63	41.68	42.64	42.89	42.53	42.10
TiO ₂	0.53	1.44	1.62	1.39	1.42	1.23	1.07	1.30	1.10	1.06	0.68
Al ₂ O ₃	7.17	8.19	8.73	8.42	7.86	10.16	9.90	10.24	10.09	10.42	10.66
Fe ₂ O ₃	4.45	4.29	3.52	3.47	3.41	4.92	7.66	4.94	5.01	5.08	5.91
Cr ₂ O ₃	0.00	0.00	0.00	0.01	0.00	0.02	0.07	0.05	0.07	0.04	0.04
MgO	11.96	10.73	11.08	11.01	11.63	9.49	9.97	9.73	9.41	9.18	8.87
CaO	11.86	11.65	11.49	11.37	11.51	11.52	10.75	11.66	11.68	11.66	11.76
MnO	0.64	0.95	0.94	0.91	0.91	0.61	0.74	0.71	0.61	0.72	0.61
FeO	13.03	14.10	13.96	14.24	13.51	15.25	12.52	14.89	15.52	15.29	15.13
Na ₂ O	1.24	1.32	1.46	1.62	1.45	1.38	1.26	1.44	1.29	1.29	1.21
K ₂ O	0.77	1.01	1.15	1.08	0.95	1.30	1.24	1.33	1.33	1.30	1.24
Total	97.73	97.72	98.16	97.61	97.61	98.51	96.85	98.95	99.00	98.56	98.21
<i>Mineral structural formulas based (a.p.f.u) on 23 Oxygens</i>											
Si	6.868	6.640	6.616	6.644	6.738	6.426	6.363	6.398	6.442	6.414	6.381
Ti	0.059	0.164	0.182	0.157	0.159	0.140	0.123	0.147	0.125	0.120	0.077
Al ^{IV}	1.132	1.36	1.384	1.356	1.262	1.574	1.637	1.601	1.558	1.586	1.619
Al ^{VI}	0.128	0.095	0.155	0.14	0.125	0.23	0.143	0.21	0.228	0.266	0.286
Fe ³⁺	0.499	0.487	0.396	0.394	0.384	0.558	0.880	0.558	0.566	0.576	0.674
Cr	0.000	0.000	0.000	0.002	0.000	0.003	0.008	0.006	0.009	0.005	0.005
Mg	2.657	2.411	2.471	2.474	2.595	2.133	2.268	2.177	2.106	2.065	2.005
Ca	1.893	1.881	1.842	1.836	1.847	1.860	1.758	1.875	1.879	1.884	1.909
Mn	0.081	0.122	0.119	0.116	0.115	0.078	0.096	0.091	0.078	0.092	0.079
Fe ²⁺	1.625	1.777	1.747	1.794	1.691	1.923	1.598	1.869	1.949	1.929	1.917
Na	0.357	0.385	0.423	0.474	0.420	0.402	0.372	0.418	0.377	0.377	0.356
K	0.146	0.194	0.219	0.208	0.181	0.251	0.242	0.255	0.256	0.249	0.239
Total	15.446	15.515	15.555	15.594	15.517	15.578	15.488	15.604	15.570	15.563	15.547
X _{Mg}	0.62	0.58	0.59	0.58	0.61	0.53	0.59	0.54	0.52	0.52	0.51

Table A.2.5a: Representative analyses of potassium feldspar (continued).

Rock type Sample	Biotite granitoid							Deformed biotite granitoid									
	LE-2 1-Kfs1 core	LE-2 1-Kfs1 core	SE-4 1-Kfs2 rim	SE-4 1-Kfs2 core	SE-4 2-Kfs1 core	SE-4 2-Kfs2 core	SE-4 2-Kfs3 core	NG-3 4-Kfs1 rim	NG-3 2-Kfs2 rim	NN-1A 1-Kfs1 rim	NN-1A 1-Kfs1 core	NN-1A 1-Kfs1 core	BFS-7 1-Kfs1 rim	BFS-7 1-Kfs1 core	BFS-7 1-Kfs1 rim	ND-2 5-Pl5 rim	
<i>Compoment oxydes (wt.%)</i>																	
SiO ₂	64.13	63.91	64.00	63.33	64.36	63.95	64.03	64.38	64.51	64.85	65.05	65.01	64.33	64.14	63.68	63.56	
Al ₂ O ₃	18.53	18.44	18.34	18.71	18.74	18.75	18.55	18.71	18.42	19.18	19.47	19.02	18.56	18.55	18.67	18.66	
MgO	0.03	0.02	0.00	0.00	0.01	0.01	0.00	0.00	0.00	0.00	0.00	0.00	0.00	0.00	0.00	0.00	
CaO	0.00	0.00	0.01	0.00	0.00	0.00	0.03	0.00	0.00	0.03	0.00	0.00	0.00	0.00	0.00	0.00	
MnO	0.00	0.00	0.00	0.00	0.00	0.00	0.00	0.00	0.00	0.00	0.00	0.00	0.00	0.00	0.00	0.00	
FeO	0.05	0.11	0.03	0.02	0.07	0.06	0.10	0.02	0.03	0.04	0.05	0.03	0.03	0.03	0.00	0.02	
BaO	0.75	0.85	0.47	0.55	0.42	0.46	0.55	0.69	0.53	0.53	0.47	0.47	0.71	1.00	1.00	0.86	
Na ₂ O	0.71	0.55	0.70	0.45	0.81	0.72	0.53	0.52	0.31	0.70	1.06	0.82	0.55	0.65	0.44	0.46	
K ₂ O	15.48	15.46	15.51	15.91	15.02	15.49	15.69	15.59	16.02	15.61	15.08	15.39	15.65	15.27	15.43	15.50	
Total	99.68	99.34	99.06	98.97	99.43	99.43	99.49	99.90	99.82	100.95	101.17	100.73	99.82	99.64	99.21	99.06	
<i>Mineral structural formulas (a.p.f.u) based on 8 Oxygens</i>																	
Si	2.983	2.985	2.990	2.971	2.986	2.977	2.983	2.985	2.994	2.973	2.967	2.981	2.987	2.986	2.979	2.977	
Al	1.016	1.015	1.010	1.034	1.024	1.029	1.019	1.022	1.008	1.036	1.047	1.028	1.016	1.018	1.029	1.030	
Mg	0.002	0.001	0.000	0.000	0.000	0.001	0.000	0.000	0.000	0.000	0.000	0.000	0.000	0.000	0.000	0.000	
Ca	0.000	0.000	0.001	0.000	0.000	0.000	0.001	0.000	0.000	0.002	0.000	0.000	0.000	0.000	0.000	0.000	
Mn	0.000	0.000	0.000	0.000	0.000	0.000	0.000	0.000	0.000	0.000	0.000	0.000	0.000	0.000	0.000	0.000	
Fe	0.002	0.004	0.001	0.001	0.003	0.002	0.004	0.001	0.001	0.002	0.002	0.001	0.001	0.001	0.000	0.001	
Ba	0.014	0.016	0.009	0.010	0.008	0.008	0.010	0.013	0.010	0.009	0.008	0.008	0.013	0.018	0.018	0.016	
Na	0.064	0.050	0.064	0.041	0.073	0.065	0.048	0.046	0.028	0.062	0.094	0.073	0.049	0.059	0.040	0.042	
K	0.918	0.921	0.925	0.952	0.889	0.920	0.933	0.922	0.948	0.913	0.878	0.900	0.927	0.907	0.921	0.926	
Total	5.000	4.993	4.999	5.009	4.983	5.001	4.998	4.988	4.990	4.997	4.995	4.991	4.993	4.988	4.987	4.992	
Si+Al	4.003	4.001	4.001	4.003	4.011	4.010	4.002	4.010	4.002	4.010	4.012	4.010	4.001	4.002	4.010	4.007	
Na+Ca+K	1.002	0.987	1.003	1.002	0.971	0.991	0.992	0.981	0.986	0.990	0.981	0.981	0.993	0.981	0.980	0.984	
An(Na/Ca)	0.002	0.000	0.061	0.000	0.000	0.000	0.130	0.003	0.000	0.150	0.000	0.001	0.002	0.005	0.001	0.003	
Ab(Na/Ca)	6.401	5.084	6.375	4.102	7.541	6.558	4.840	4.737	2.845	6.330	9.565	7.390	4.966	5.990	4.091	4.267	
Or	92.232	93.342	92.711	94.901	91.665	92.610	94.010	93.975	96.175	92.545	89.570	91.750	93.730	92.161	94.052	94.126	
Ce	1.367	1.575	0.855	1.000	0.787	0.840	1.019	1.281	0.985	0.956	0.855	0.862	1.300	1.851	1.861	1.597	

Table A.2.5a: Representative analyses of potassium feldspar (continued).

Rock type Sample	Mega feldspar granitoid																	
	DML-1 1-Kfs1 rim	DML-1 1-Kfs1 core	DML-1 1-Kfs1 core	DML-1 1-Kfs1 rim	DML-1 1-Kfs2 rim	DML-1 1-Kfs2 core	DML-1 1-Kf2 core	DML-1 1-Kfs2 rim	DML-1 2-Kfs2 rim	DML-1 2-Kfs2 core	DML-1 2-Kfs2 rim	DML-1 2-Kfs3 core	DML-1 2-Kfs4 core	KO-12 3-Kfs1 core	KO-12 3-Kfs1 rim	KO-12 3-Kfs2 core	KO-12 3-Kfs2 rim	KO-12 3-Kfs3 core
<i>Compoment oxydes (wt.%)</i>																		
SiO ₂	64.89	63.79	64.88	64.18	64.28	64.76	64.49	64.37	64.19	64.29	64.26	64.62	64.12	64.88	64.18	66.76	64.34	63.20
Al ₂ O ₃	18.39	18.50	18.64	18.44	18.53	18.43	18.48	18.45	18.23	18.43	18.38	18.20	18.46	18.63	18.43	18.91	18.60	18.37
MgO	0.00	0.00	0.03	0.00	0.00	0.00	0.00	0.00	0.01	0.00	0.00	0.03	0.01	0.03	0.00	0.00	0.00	0.01
CaO	0.00	0.00	0.01	0.00	0.00	0.00	0.00	0.00	0.00	0.02	0.00	0.00	0.00	0.01	0.00	0.08	0.00	0.00
MnO	0.00	0.00	0.00	0.00	0.00	0.00	0.00	0.00	0.00	0.00	0.00	0.00	0.00	0.00	0.00	0.00	0.00	0.00
FeO	0.04	0.00	0.02	0.05	0.03	0.00	0.04	0.00	0.02	0.00	0.00	0.01	0.08	0.02	0.05	0.03	0.04	0.00
BaO	0.07	0.21	0.15	0.20	0.27	0.21	0.13	0.13	0.21	0.20	0.27	0.21	0.26	0.15	0.20	0.10	0.39	0.34
Na ₂ O	0.56	0.65	0.93	0.47	0.47	0.55	0.66	0.84	0.56	1.01	0.44	0.50	0.62	0.93	0.47	6.10	0.49	0.37
K ₂ O	15.96	15.70	15.39	15.90	15.71	16.11	15.62	15.50	15.84	15.22	15.71	16.02	15.61	15.39	15.90	7.86	15.52	15.76
Total	99.90	98.86	100.04	99.24	99.28	100.07	99.43	99.28	99.07	99.15	99.07	99.61	99.16	100.04	99.24	99.84	99.38	98.05
<i>Mineral structural formulas (a.p.f.u) based on 8 Oxygens</i>																		
Si	2.999	2.984	2.991	2.991	2.995	2.994	2.992	2.996	2.991	2.996	3.001	2.989	2.991	2.991	3.000	2.990	2.984	
Al	1.002	1.020	1.012	1.012	1.016	1.005	1.011	1.011	1.003	1.010	1.010	0.996	1.014	1.012	1.012	1.001	1.019	1.022
Mg	0.000	0.000	0.002	0.000	0.000	0.000	0.000	0.000	0.000	0.000	0.002	0.001	0.002	0.000	0.000	0.000	0.001	
Ca	0.000	0.000	0.000	0.000	0.000	0.000	0.000	0.000	0.000	0.000	0.000	0.000	0.000	0.000	0.004	0.000	0.000	
Mn	0.000	0.000	0.000	0.000	0.000	0.000	0.000	0.000	0.000	0.000	0.000	0.000	0.000	0.000	0.000	0.000	0.000	
Fe	0.001	0.000	0.001	0.002	0.001	0.000	0.002	0.000	0.000	0.000	0.000	0.001	0.003	0.000	0.002	0.001	0.002	
Ba	0.001	0.004	0.003	0.004	0.005	0.004	0.002	0.002	0.004	0.004	0.005	0.004	0.005	0.003	0.004	0.002	0.007	0.006
Na	0.050	0.059	0.083	0.042	0.042	0.050	0.060	0.075	0.051	0.091	0.040	0.045	0.056	0.083	0.042	0.531	0.044	0.034
K	0.941	0.937	0.905	0.945	0.933	0.951	0.925	0.919	0.943	0.903	0.935	0.949	0.928	0.905	0.945	0.450	0.921	0.949
Total	4.995	5.004	4.997	4.997	4.988	5.003	4.993	5.000	4.999	5.000	4.986	4.998	4.996	4.997	4.997	4.990	4.983	4.997
Si + Al	4.001	4.004	4.003	4.003	4.007	4.002	4.000	4.002	4.001	4.001	4.011	4.001	4.003	4.000	4.002	4.001	4.011	4.006
Na+Ca+K	0.993	1.000	0.991	0.991	0.980	1.001	0.990	1.000	1.001	1.002	0.978	1.002	0.990	0.993	0.990	0.991	0.972	0.990
An(Na/Ca)	0.000	0.003	0.033	0.004	0.001	0.000	0.000	0.003	0.000	0.100	0.001	0.000	0.003	0.021	0.005	0.387	0.002	0.00
Ab(Na/Ca)	5.081	5.933	8.363	4.267	4.343	4.942	6.062	7.565	5.102	9.082	4.100	4.550	5.711	8.355	4.272	53.820	4.565	3.46
Or	94.802	93.691	91.342	95.369	95.170	94.691	93.701	92.201	94.521	90.461	95.389	95.061	93.820	91.337	95.355	45.611	94.701	95.91
Ce	0.122	0.381	0.272	0.365	0.504	0.370	0.241	0.240	0.378	0.355	0.510	0.387	0.465	0.270	0.373	0.191	0.731	0.63

Table A.2.5a: Representative analyses of potassium feldspar (continued).

Rock type Sample	Mega feldspar granitoid												Two-mica granitoid								
	KO-12 3-Kfs3 core	KO-12 3-Kfs3 rim	KO-12 3-Kfs4 rim	KO-12 3-Kfs4 rim	KO-12 3-Kfs4 core	KO-12 3-Kfs4 core	TE-6 3-Kfs1 core	TE-6 3-Kfs2 rim	TE-6 3-Kfs2 core	TE-6 3-Kfs2 core	TE-6 3-Kfs2 rim	BM-3 1-Kfs1 rim	BM-3 1-Kfs1 core	BM-3 2-Kfs3 rim	BM-3 2-Kfs3 core	BM-3 2-Kfs3 rim	BM-3 3-Kfs1 rim				
<i>Component oxydes (wt.%)</i>																					
SiO ₂	63.87	64.50	63.25	63.23	63.61	63.85	63.71	65.28	66.03	63.88	64.09	64.16	64.17	64.32	63.89	63.64	64.22				
Al ₂ O ₃	18.33	18.35	18.54	18.50	18.26	18.56	18.55	19.53	19.14	18.43	18.57	18.47	18.35	18.43	18.38	18.40	18.91				
MgO	0.02	0.01	0.01	0.01	0.01	0.06	0.02	0.00	0.00	0.00	0.00	0.00	0.00	0.00	0.01	0.00	0.00	0.01			
CaO	0.00	0.00	0.05	0.00	0.02	0.03	0.02	0.00	0.01	0.00	0.00	0.03	0.01	0.00	0.06	0.00	0.03				
MnO	0.00	0.00	0.00	0.00	0.00	0.00	0.00	0.00	0.00	0.00	0.00	0.00	0.00	0.00	0.00	0.00	0.00				
FeO	0.05	0.00	0.09	0.01	0.04	0.05	0.10	0.04	0.02	0.08	0.02	0.20	0.05	0.00	0.05	0.00	0.00	0.02			
BaO	0.31	0.05	0.32	0.26	0.25	0.31	0.56	0.58	0.74	0.59	0.76	0.02	0.00	0.10	0.01	0.02	0.01				
Na ₂ O	0.61	0.68	0.73	0.62	0.71	0.59	0.88	0.80	2.51	0.61	0.65	1.60	0.75	0.77	0.85	0.55	0.62				
K ₂ O	15.53	15.57	15.37	15.57	15.39	15.54	15.01	15.05	12.85	15.35	15.45	14.06	15.31	15.36	15.16	15.70	15.55				
Total	98.71	99.17	98.34	98.19	98.29	98.97	98.85	101.28	101.29	98.94	99.55	98.53	98.63	98.99	98.41	98.30	99.37				
<i>Mineral structural formulas (a.p.f.u) based on 8 Oxygens</i>																					
Si	2.991	2.999	2.976	2.979	2.990	2.982	2.981	2.972	2.987	2.988	2.984	2.989	2.996	2.995	2.991	2.989	2.979				
Al	1.012	1.006	1.028	1.027	1.012	1.022	1.023	1.048	1.020	1.016	1.019	1.014	1.010	1.011	1.014	1.018	1.034				
Mg	0.001	0.000	0.001	0.001	0.000	0.004	0.001	0.000	0.000	0.000	0.000	0.000	0.000	0.001	0.000	0.000	0.001				
Ca	0.000	0.000	0.002	0.000	0.001	0.002	0.001	0.000	0.000	0.000	0.000	0.001	0.000	0.000	0.003	0.000	0.001				
Mn	0.000	0.000	0.000	0.000	0.000	0.000	0.000	0.000	0.000	0.000	0.000	0.000	0.000	0.000	0.000	0.000	0.000				
Fe	0.002	0.000	0.003	0.000	0.002	0.002	0.004	0.002	0.001	0.003	0.001	0.008	0.002	0.000	0.002	0.000	0.001				
Ba	0.006	0.001	0.006	0.005	0.005	0.006	0.010	0.010	0.013	0.011	0.014	0.000	0.000	0.002	0.000	0.000	0.000				
Na	0.055	0.062	0.066	0.056	0.065	0.053	0.080	0.070	0.221	0.055	0.059	0.144	0.068	0.069	0.078	0.050	0.055				
K	0.928	0.924	0.922	0.936	0.923	0.926	0.896	0.874	0.742	0.916	0.918	0.835	0.912	0.912	0.905	0.940	0.920				
Total	4.995	4.991	5.005	5.004	4.998	4.996	4.996	4.976	4.984	4.990	4.995	4.993	4.989	4.990	4.993	4.997	4.992				
Si +Al	4.003	4.001	4.004	4.006	4.002	4.004	4.003	4.021	4.01	4.001	4.003	4.004	4.006	4.006	4.005	4.007	4.013				
Na+Ca+K	0.989	0.992	0.997	0.997	0.994	0.986	0.991	0.950	0.98	0.980	0.991	0.981	0.980	0.983	0.986	0.990	0.977				
An(Na/Ca)	0.099	0.003	0.229	0.009	0.100	0.167	0.077	0.004	0.042	0.000	0.002	0.141	0.029	0.003	0.290	0.003	0.151				
Ab(Na/Ca)	5.579	6.242	6.661	5.659	6.517	5.393	8.109	7.371	22.601	5.632	5.959	14.678	6.941	7.052	7.861	5.032	5.660				
Or	93.841	93.671	92.521	93.871	92.913	93.871	90.771	91.543	76.023	93.271	92.651	85.136	93.032	92.768	91.831	94.941	94.184				
Ce	0.582	0.098	0.594	0.493	0.473	0.5670	1.043	1.009	1.338	1.093	1.403	0.036	0.002	0.176	0.020	0.031	0.012				

Table A.2.5a: Representative analyses of potassium feldspar (continued).

Rock type Sample	Two-mica granitoid																	
	BM-3		BM-3		BM-3		BAN-6		NO-30									
	3-Kfs1	3-Kfs1	3-Kfs1	3-Kfs1	1-Kfs1	1-Kfs1	1-Kfs1	1-Kfs1	1-Kfs1	1-Kfs1	1-Kfs2	1-Kfs2	1-Kfs2	1-Kfs2	1-Kfs2	1-Kfs1	1-Kfs1	1-Kfs1
Component oxydes (wt.%)																		
SiO ₂	63.61	63.75	63.91	64.08	64.14	63.68	64.10	63.86	64.25	63.78	63.82	63.78	64.15	63.79	63.92	63.63	63.75	63.31
Al ₂ O ₃	18.52	18.44	18.56	18.71	18.39	18.43	18.31	18.37	18.29	18.39	18.47	18.46	18.60	18.56	18.34	18.45	18.42	18.38
MgO	0.00	0.00	0.02	0.00	0.01	0.00	0.01	0.019	0.00	0.00	0.03	0.00	0.00	0.00	0.02	0.00	0.00	0.00
CaO	0.02	0.00	0.00	0.01	0.00	0.00	0.00	0.014	0.00	0.01	0.00	0.00	0.00	0.03	0.00	0.00	0.00	0.00
MnO	0.00	0.00	0.00	0.00	0.00	0.00	0.00	0.00	0.00	0.00	0.00	0.00	0.00	0.00	0.00	0.00	0.00	0.00
FeO	0.03	0.00	0.02	0.00	0.00	0.00	0.04	0.024	0.01	0.01	0.02	0.00	0.00	0.00	0.01	0.00	0.00	0.00
BaO	0.00	0.04	0.00	0.09	0.13	0.09	0.09	0.128	0.23	0.20	0.12	0.38	0.19	0.22	0.19	0.22	0.17	0.12
Na ₂ O	0.85	0.88	1.06	1.94	1.10	0.87	0.95	0.486	0.43	0.72	0.78	0.75	1.14	1.17	1.07	0.75	0.40	0.81
K ₂ O	15.47	15.41	15.14	13.74	14.91	15.29	15.24	15.759	15.99	15.39	15.11	15.17	14.80	14.97	15.15	15.57	16.00	15.46
Total	98.50	98.51	98.69	98.56	98.68	98.35	98.73	98.66	99.20	98.51	98.36	98.53	98.87	98.74	98.70	98.62	98.74	98.08
Mineral structural formulas (a.p.f.u) based on 8 Oxygens																		
Si	2.981	2.986	2.984	2.982	2.993	2.987	2.994	2.991	2.996	2.989	2.988	2.987	2.981	2.989	2.983	2.987	2.983	
Al	1.023	1.018	1.021	1.026	1.011	1.019	1.008	1.014	1.014	1.016	1.020	1.019	1.021	1.022	1.011	1.020	1.017	1.021
Mg	0.000	0.000	0.001	0.000	0.001	0.000	0.000	0.001	0.000	0.000	0.002	0.000	0.000	0.001	0.000	0.000	0.000	0.000
Ca	0.001	0.000	0.000	0.000	0.000	0.000	0.000	0.001	0.000	0.001	0.000	0.000	0.000	0.002	0.000	0.000	0.000	0.000
Mn	0.000	0.000	0.000	0.000	0.000	0.000	0.000	0.000	0.000	0.000	0.000	0.000	0.000	0.000	0.000	0.000	0.000	0.000
Fe	0.001	0.000	0.001	0.000	0.000	0.000	0.002	0.001	0.000	0.001	0.001	0.000	0.000	0.000	0.000	0.000	0.000	0.000
Ba	0.000	0.001	0.000	0.002	0.002	0.002	0.002	0.002	0.004	0.004	0.002	0.007	0.004	0.004	0.004	0.004	0.003	0.002
Na	0.077	0.080	0.096	0.175	0.100	0.079	0.086	0.044	0.039	0.066	0.071	0.068	0.103	0.106	0.097	0.068	0.036	0.074
K	0.925	0.921	0.902	0.816	0.888	0.915	0.908	0.941	0.951	0.920	0.903	0.907	0.879	0.892	0.904	0.931	0.956	0.929
Total	5.008	5.005	5.004	5.000	4.995	5.001	4.999	4.995	4.996	4.996	4.988	4.989	4.993	5.007	5.006	5.006	5.000	5.009
Si + Al	4.004	4.004	4.005	4.008	4.004	4.005	4.002	4.004	4.006	4.005	4.009	4.008	4.008	4.003	4.000	4.003	4.005	4.003
Na+Ca+K	1.003	1.001	0.997	0.992	0.990	0.995	0.996	0.989	0.997	0.991	0.976	0.982	0.985	1.004	1.004	1.003	0.996	1.006
An(Na/Ca)	0.110	0.000	0.000	0.040	0.000	0.000	0.071	0.000	0.061	0.015	0.020	0.000	0.150	0.000	0.000	0.000	0.000	0.000
Ab(Na/Ca)	7.667	7.949	9.579	17.596	10.081	7.906	8.638	4.463	3.932	6.642	7.248	6.922	10.428	10.535	9.694	6.769	3.632	7.367
Or	92.223	91.976	90.421	82.193	89.681	91.927	91.195	95.228	95.656	92.923	92.513	92.348	89.214	88.907	89.958	92.830	96.060	92.411
Ce	0.000	0.075	0.000	0.171	0.238	0.166	0.167	0.238	0.437	0.375	0.224	0.709	0.357	0.409	0.348	0.401	0.308	0.222

Table A.2.5a: Representative analyses of potassium feldspar (continued).

Rock type Sample	Two-mica granitoid																	
	NO-30 2-Kfs1 rim	NO-30 2-Kfs1 core	NO-30 2-Kfs1 core	NO-30 2-Kfs1 rim	NO-30 4-Kfs1 rim	NO-30 4-Kfs1 core	NO-30 4-Kfs1 rim	NO-30 4-Kfs1 core	NO-30 4-Kfs2 rim	NO-30 4-Kfs2 core	NO-30 4-Kfs3 rim	NO-30 4-Kfs3 core	NO-30 4-Kfs3 rim	NO-30 4-Kfs3 core	TA-9 3-Kfs3 core	TA-9 3-Kfs3 rim	TA-9 4-Kfs1 rim	
<i>Component oxydes (wt.%)</i>																		
SiO ₂	63.53	63.56	64.25	64.28	63.72	63.36	64.05	63.42	63.08	63.26	63.30	62.89	63.51	63.73	63.53	64.26	63.76	63.98
Al ₂ O ₃	18.50	18.39	18.89	18.69	18.52	18.48	18.64	18.54	18.62	18.53	18.71	18.71	18.54	18.56	18.34	18.50	18.55	18.53
MgO	0.00	0.02	0.00	0.01	0.00	0.00	0.01	0.01	0.00	0.00	0.03	0.00	0.00	0.01	0.00	0.00	0.01	0.00
CaO	0.02	0.03	0.00	0.03	0.01	0.00	0.01	0.00	0.00	0.04	0.03	0.02	0.01	0.04	0.02	0.00	0.00	0.00
MnO	0.00	0.00	0.00	0.00	0.00	0.00	0.00	0.00	0.00	0.00	0.00	0.00	0.00	0.00	0.00	0.00	0.00	0.00
FeO	0.06	0.00	0.05	0.05	0.01	0.00	0.00	0.08	0.06	0.00	0.01	0.02	0.08	0.05	0.02	0.03	0.03	0.00
BaO	0.18	0.12	0.14	0.17	0.27	0.12	0.18	0.18	0.31	0.18	0.23	0.15	0.21	0.14	0.10	0.30	0.31	0.09
Na ₂ O	0.99	0.82	2.08	1.31	0.79	0.54	0.56	0.70	0.69	0.68	1.09	0.82	0.79	1.55	0.58	0.52	0.63	0.48
K ₂ O	14.94	15.35	13.73	14.53	15.45	15.75	15.57	15.77	15.45	15.36	14.84	15.40	15.43	14.25	15.66	15.51	15.28	15.58
Total	98.21	98.28	99.14	99.06	98.76	98.26	99.02	98.70	98.21	98.05	98.24	98.01	98.57	98.33	98.25	99.12	98.57	98.66
<i>Mineral structural formulas (a.p.f.u) based on 8 Oxygens</i>																		
Si	2.983	2.985	2.975	2.985	2.982	2.981	2.986	2.975	2.972	2.980	2.972	2.967	2.979	2.981	2.988	2.993	2.986	2.991
Al	1.024	1.018	1.031	1.022	1.022	1.025	1.024	1.025	1.034	1.029	1.035	1.040	1.025	1.023	1.016	1.016	1.024	1.021
Mg	0.000	0.001	0.000	0.001	0.000	0.000	0.000	0.000	0.000	0.000	0.002	0.000	0.000	0.000	0.000	0.000	0.001	0.000
Ca	0.001	0.002	0.000	0.001	0.000	0.000	0.000	0.000	0.000	0.002	0.002	0.001	0.001	0.002	0.001	0.000	0.000	0.000
Mn	0.000	0.000	0.000	0.000	0.000	0.000	0.000	0.000	0.000	0.000	0.000	0.000	0.000	0.000	0.000	0.000	0.000	0.000
Fe	0.002	0.000	0.002	0.002	0.000	0.000	0.000	0.003	0.002	0.000	0.001	0.001	0.003	0.002	0.001	0.001	0.001	0.000
Ba	0.003	0.002	0.003	0.003	0.005	0.002	0.003	0.003	0.006	0.003	0.004	0.003	0.004	0.003	0.002	0.006	0.006	0.002
Na	0.090	0.075	0.187	0.118	0.072	0.049	0.051	0.064	0.063	0.062	0.099	0.075	0.071	0.140	0.053	0.047	0.057	0.044
K	0.895	0.920	0.811	0.861	0.923	0.946	0.926	0.944	0.929	0.923	0.889	0.927	0.923	0.851	0.940	0.922	0.913	0.929
Total	4.998	5.003	5.009	4.993	5.004	5.004	4.991	5.016	5.007	4.998	5.004	5.013	5.006	5.003	5.000	4.983	4.987	4.986
Si + Al	4.006	4.003	4.006	4.007	4.004	4.006	4.011	4.001	4.006	4.008	4.008	4.007	4.004	4.004	4.004	4.017	4.010	4.011
Na+Ca+K	0.989	0.998	1.001	0.983	0.999	0.997	0.987	1.011	0.998	0.990	0.994	1.005	0.999	0.996	0.995	0.971	0.976	0.974
An(Na/Ca)	0.092	0.156	0.000	0.132	0.030	0.000	0.040	0.010	0.000	0.209	0.167	0.101	0.050	0.216	0.091	0.005	0.000	0.000
Ab(Na/Ca)	9.129	7.481	18.706	11.963	7.156	4.941	5.161	6.332	6.355	6.236	9.973	7.415	7.154	14.092	5.296	4.802	5.880	4.493
Or	90.454	92.147	81.034	87.595	92.317	94.837	94.462	93.338	93.072	93.220	89.427	92.201	92.411	85.435	94.435	94.632	93.541	95.342
Ce	0.326	0.216	0.259	0.311	0.497	0.222	0.345	0.320	0.574	0.336	0.433	0.283	0.384	0.256	0.178	0.575	0.579	0.165

Table A.2.5b: Representative analyses of plagioclase (continued).

Rock type Sample	Biotite granitoid																	
	LE-2 1-P11 rim	LE-2 1-P11 core	LE-2 1-P11 rim	LE-2 1-P12 core	LE-2 2-P11 core	Bl-8 1-P11 rim	Bl-8 1-P11 core	Bl-8 1-p11 core	Bl-8 1-P11 core	Bl-8 2-P11 rim	Bl-8 2-p11 core	Bl-8 2-P11 core	Bl-8 2-p11 core	SE-4 1-p11 core	SE-4 1-p11 core	SE-4 1-P11 core		
<i>Component oxydes (wt.%)</i>																		
SiO ₂	61.95	63.00	62.67	62.63	62.76	62.19	62.88	63.40	62.76	62.40	63.03	62.62	59.76	61.76	64.67	63.97	64.08	63.69
Al ₂ O ₃	23.31	23.68	23.49	23.27	23.31	23.30	23.55	23.57	23.50	23.77	23.28	23.48	25.97	24.23	23.13	22.86	23.19	23.06
MgO	0.00	0.01	0.00	0.00	0.00	0.00	0.00	0.00	0.00	0.00	0.00	0.00	0.00	0.00	0.00	0.00	0.00	0.02
CaO	4.63	4.69	4.81	4.50	4.53	4.62	4.76	4.62	4.84	5.07	4.41	4.66	7.46	5.55	3.77	3.71	3.98	4.03
MnO	0.00	0.00	0.00	0.00	0.00	0.00	0.00	0.00	0.00	0.00	0.00	0.00	0.00	0.00	0.00	0.00	0.00	0.00
FeO	0.20	0.05	0.04	0.11	0.10	0.09	0.09	0.06	0.04	0.13	0.21	0.10	0.04	0.10	0.12	0.03	0.07	0.08
BaO	0.00	0.06	0.01	0.01	0.05	0.05	0.05	0.00	0.02	0.00	0.00	0.00	0.03	0.00	0.01	0.00	0.00	0.00
Na ₂ O	8.91	8.77	8.79	8.92	8.82	8.96	8.64	9.04	8.65	8.55	9.24	8.87	7.34	8.67	9.21	9.18	9.19	8.90
K ₂ O	0.16	0.15	0.30	0.20	0.13	0.19	0.17	0.18	0.21	0.14	0.09	0.14	0.10	0.11	0.27	0.28	0.25	0.35
Total	99.15	100.40	100.11	99.64	99.70	99.39	100.14	100.88	100.01	100.05	100.26	99.87	100.71	100.42	101.18	100.02	100.76	100.13
<i>Mineral Structural formulas (a.p.f.u) based on 8 Oxygens</i>																		
Si	2.769	2.776	2.773	2.782	2.785	2.773	2.778	2.781	2.777	2.762	2.784	2.775	2.646	2.732	2.820	2.821	2.808	2.809
Al	1.228	1.230	1.225	1.218	1.219	1.224	1.226	1.219	1.225	1.240	1.212	1.226	1.355	1.263	1.189	1.188	1.198	1.199
Mg	0.000	0.000	0.000	0.000	0.000	0.000	0.000	0.000	0.000	0.000	0.000	0.000	0.000	0.000	0.000	0.000	0.000	0.001
Ca	0.222	0.221	0.228	0.214	0.215	0.221	0.225	0.217	0.230	0.240	0.209	0.221	0.354	0.263	0.176	0.175	0.187	0.191
Mn	0.000	0.000	0.000	0.000	0.000	0.000	0.000	0.000	0.000	0.000	0.000	0.000	0.000	0.000	0.000	0.000	0.000	0.000
Fe	0.008	0.002	0.001	0.004	0.004	0.004	0.003	0.002	0.001	0.005	0.008	0.004	0.001	0.004	0.004	0.001	0.003	0.003
Ba	0.000	0.001	0.000	0.000	0.001	0.001	0.001	0.000	0.000	0.000	0.000	0.000	0.001	0.000	0.000	0.000	0.000	0.000
Na	0.772	0.749	0.754	0.769	0.759	0.775	0.740	0.769	0.742	0.734	0.791	0.762	0.630	0.743	0.779	0.784	0.781	0.761
K	0.009	0.008	0.017	0.011	0.007	0.011	0.010	0.010	0.012	0.008	0.005	0.008	0.006	0.006	0.015	0.016	0.014	0.019
Total	5.007	4.988	5.000	4.999	4.989	5.008	4.984	4.999	4.987	4.989	5.008	4.997	4.994	5.012	4.983	4.985	4.990	4.982
Si+Al	4.003	4.006	3.999	4.000	4.003	3.997	4.004	4.000	4.002	4.002	3.996	4.002	4.002	3.995	4.009	4.009	4.006	4.007
Na+Ca+K	1.007	0.980	0.999	0.994	0.982	1.007	0.976	0.996	0.984	0.982	1.005	0.991	0.991	1.013	0.970	0.975	0.982	0.971
An(Na/Ca)	22.122	22.581	22.799	21.540	21.904	21.912	23.075	21.807	23.345	24.469	20.778	22.320	35.749	25.977	18.137	17.979	19.048	19.622
Ab(Na/Ca)	76.991	76.457	75.471	77.316	77.249	76.940	75.830	77.165	75.416	74.737	78.717	76.876	63.607	73.399	80.278	80.425	79.516	78.374
Or	0.890	0.860	1.712	1.134	0.761	1.068	1.005	1.028	1.205	0.794	0.505	0.804	0.587	0.624	1.560	1.592	1.435	2.004
Ce	0.000	0.102	0.019	0.009	0.087	0.080	0.090	0.000	0.033	0.000	0.000	0.000	0.056	0.000	0.025	0.004	0.000	0.000

Table A.2.5b: Representative analyses of plagioclase (continued).

Rock type Sample	Biotite granitoid				Deformed biotite granitoid												
	SE-4 1-Pl2 core	SE-4 2-Pl1 rim	SE-4 2-Pl1 core	SE-4 2-Pl3 core	NG-3 1-Pl1 rim	NG-3 1-Pl1 core	NG-3 1-Pl1 core	NG-3 1-Pl1 rim	NG-3 1-Pl2 rim	NG-3 1-Pl2 core	NG-3 2-Pl1 core	NG-3 2-Pl1 rim	NG-3 2-Pl2 core	NG-3 2-Pl2 rim	NG-3 1-Pl2 core	NG-3 1-Pl2 rim	NG-3 1-Pl3 core
<i>Component oxydes (wt.%)</i>																	
SiO ₂	64.70	64.02	64.45	64.53	71.33	64.29	66.06	65.59	81.84	65.94	65.28	66.03	63.76	63.54	63.83	62.52	62.88
Al ₂ O ₃	23.01	23.20	23.41	22.90	17.38	22.97	21.09	21.82	12.65	20.82	22.24	21.67	22.78	23.15	23.21	24.02	23.52
MgO	0.00	0.00	0.00	0.00	0.00	0.00	0.00	0.02	0.00	0.00	0.00	0.01	0.00	0.00	0.00	0.00	0.00
CaO	3.53	3.71	3.73	3.58	3.90	4.00	1.92	2.88	2.00	1.87	3.06	2.51	4.17	4.54	4.37	5.06	4.67
MnO	0.00	0.00	0.00	0.00	0.00	0.00	0.00	0.00	0.00	0.00	0.00	0.00	0.00	0.00	0.00	0.00	0.00
FeO	0.09	0.05	0.00	0.06	0.08	0.02	0.03	0.08	0.04	0.02	0.00	0.04	0.07	0.10	0.12	0.01	0.06
BaO	0.01	0.09	0.06	0.03	0.00	0.00	0.00	0.02	0.06	0.04	0.00	0.04	0.00	0.01	0.00	0.00	0.02
Na ₂ O	9.44	9.56	9.27	9.62	7.82	9.19	10.41	9.80	5.14	10.53	9.69	9.82	8.99	8.97	8.90	8.79	8.89
K ₂ O	0.16	0.15	0.27	0.16	0.11	0.16	0.27	0.13	0.13	0.12	0.14	0.16	0.17	0.26	0.23	0.11	0.19
Total	100.93	100.77	101.18	100.88	100.62	100.62	99.78	100.33	101.86	99.34	100.41	100.27	99.94	100.56	100.65	100.51	100.23
<i>Mineral Structural formulas (a.p.f.u) based on 8 Oxygens</i>																	
Si	2.825	2.807	2.811	2.823	3.080	2.818	2.908	2.875	3.387	2.914	2.859	2.891	2.816	2.796	2.802	2.755	2.777
Al	1.184	1.199	1.203	1.181	0.885	1.187	1.094	1.127	0.617	1.084	1.148	1.118	1.186	1.200	1.201	1.248	1.224
Mg	0.000	0.000	0.000	0.000	0.000	0.000	0.000	0.001	0.000	0.000	0.000	0.001	0.000	0.000	0.000	0.000	0.000
Ca	0.165	0.174	0.174	0.168	0.181	0.188	0.091	0.135	0.089	0.089	0.144	0.118	0.197	0.214	0.205	0.239	0.221
Mn	0.000	0.000	0.000	0.000	0.000	0.000	0.000	0.000	0.000	0.000	0.000	0.000	0.000	0.000	0.000	0.000	0.000
Fe	0.003	0.002	0.000	0.002	0.003	0.001	0.001	0.003	0.001	0.001	0.000	0.001	0.003	0.004	0.004	0.000	0.002
Ba	0.000	0.002	0.001	0.001	0.000	0.000	0.000	0.000	0.001	0.001	0.000	0.001	0.000	0.000	0.000	0.000	0.000
Na	0.799	0.813	0.783	0.816	0.655	0.781	0.888	0.833	0.412	0.903	0.823	0.833	0.769	0.765	0.758	0.751	0.761
K	0.009	0.008	0.015	0.009	0.006	0.009	0.015	0.007	0.007	0.007	0.008	0.009	0.010	0.014	0.013	0.006	0.011
Total	4.987	5.004	4.987	4.999	4.808	4.983	4.997	4.981	4.514	4.998	4.982	4.971	4.981	4.994	4.983	4.999	4.997
Si+Al	4.010	4.006	4.014	4.005	3.964	4.005	4.002	4.002	4.004	3.999	4.008	4.009	4.002	3.996	4.003	4.003	4.001
Na+Ca+K	0.974	0.997	0.974	0.991	0.841	0.978	0.994	0.976	0.509	0.999	0.974	0.960	0.976	0.994	0.976	0.996	0.993
An(Na/Ca)	16.983	17.495	17.886	16.901	21.460	19.194	9.114	13.865	17.450	8.870	14.748	12.259	20.203	21.531	21.036	23.990	22.271
Ab(Na/Ca)	82.099	81.525	80.475	82.184	77.826	79.897	89.344	85.366	80.993	90.364	84.438	86.747	78.810	77.004	77.633	75.401	76.624
Or	0.910	0.825	1.537	0.870	0.714	0.910	1.542	0.728	1.360	0.694	0.815	0.919	0.987	1.441	1.331	0.610	1.080
Ce	0.009	0.155	0.102	0.060	0.000	0.000	0.000	0.040	0.198	0.071	0.000	0.075	0.000	0.024	0.000	0.000	0.030

Table A.2.5b: Representative analyses of plagioclase (continued).

Rock type Sample	Deformed biotite granitoid																		
	NG-3 1-Pl4 core	TS-2B 1-Pl1 rim	TS-2B 1-Pl1 core	TS-2B 1-Pl1 core	TS-2B 1-Pl2 core	TK-2 1-Pl2 rim	TK-2 1-Pl3 core	TK-2 2-Pl1 core	TK-2 2-Pl2 core	NN-1A 1-Pl1 rim	NN-1A 1-Pl1 core	NN-1A 2-Pl1 rim	NN-1A 2-Pl1 core	NN-1A 2-Pl2 core	BFS-7 1-Pl1 core	BFS-7 1-Pl1 core			
<i>Component oxydes (wt.%)</i>																			
SiO ₂	64.85	64.07	63.53	63.60	63.40	62.99	61.54	62.21	62.48	64.57	62.18	60.98	61.51	61.73	61.54	61.35	62.90	62.48	
Al ₂ O ₃	22.49	22.38	22.88	23.25	23.00	23.14	23.89	23.80	23.39	24.40	24.07	24.63	24.95	24.79	24.79	24.90	23.71	23.51	
MgO	0.00	0.00	0.00	0.00	0.00	0.00	0.00	0.00	0.00	0.00	0.00	0.00	0.00	0.00	0.00	0.00	0.00	0.00	
CaO	3.22	3.56	4.39	4.01	4.17	4.37	4.97	5.20	4.87	4.68	5.12	6.03	5.98	5.98	5.96	6.05	4.84	4.86	
MnO	0.00	0.00	0.00	0.00	0.00	0.00	0.00	0.00	0.00	0.00	0.00	0.00	0.00	0.00	0.00	0.00	0.00	0.00	
FeO	0.04	0.08	0.04	0.03	0.01	0.03	0.03	0.09	0.08	0.00	0.08	0.09	0.09	0.09	0.07	0.07	0.08	0.10	0.05
BaO	0.01	0.01	0.02	0.00	0.06	0.00	0.00	0.02	0.07	0.00	0.07	0.00	0.01	0.00	0.00	0.00	0.05	0.04	
Na ₂ O	9.58	9.61	9.02	9.18	9.21	9.07	8.56	8.55	8.76	8.77	8.53	8.11	8.19	8.38	8.33	8.28	8.72	8.44	
K ₂ O	0.06	0.08	0.19	0.16	0.13	0.09	0.20	0.18	0.22	0.08	0.20	0.22	0.20	0.14	0.21	0.21	0.14	0.13	
Total	100.25	99.78	100.07	100.21	99.98	99.70	99.19	100.06	99.87	102.50	100.23	100.06	100.93	101.08	100.89	100.86	100.44	99.51	
<i>Mineral Structural formulas (a.p.f.u) based on 8 Oxygens</i>																			
Si	2.846	2.833	2.806	2.802	2.803	2.793	2.749	2.756	2.773	2.780	2.750	2.710	2.709	2.714	2.712	2.705	2.772	2.776	
Al	1.163	1.166	1.191	1.207	1.198	1.209	1.258	1.243	1.223	1.238	1.254	1.290	1.295	1.285	1.287	1.294	1.231	1.231	
Mg	0.000	0.000	0.000	0.000	0.000	0.000	0.000	0.000	0.000	0.000	0.000	0.000	0.000	0.000	0.000	0.000	0.000	0.000	
Ca	0.152	0.169	0.208	0.189	0.198	0.207	0.238	0.247	0.231	0.216	0.243	0.287	0.282	0.282	0.281	0.286	0.228	0.231	
Mn	0.000	0.000	0.000	0.000	0.000	0.000	0.000	0.000	0.000	0.000	0.000	0.000	0.000	0.000	0.000	0.000	0.000	0.000	
Fe	0.001	0.003	0.001	0.001	0.001	0.001	0.001	0.003	0.003	0.000	0.003	0.003	0.003	0.003	0.002	0.003	0.003	0.002	
Ba	0.000	0.000	0.000	0.000	0.001	0.000	0.000	0.000	0.001	0.000	0.001	0.000	0.000	0.000	0.000	0.000	0.001	0.001	
Na	0.815	0.823	0.772	0.784	0.789	0.780	0.741	0.735	0.754	0.732	0.731	0.699	0.699	0.714	0.712	0.708	0.745	0.727	
K	0.003	0.004	0.011	0.009	0.007	0.005	0.011	0.010	0.012	0.005	0.011	0.013	0.011	0.008	0.012	0.012	0.008	0.007	
Total	4.981	4.998	4.990	4.991	4.996	4.995	4.998	4.995	4.999	4.970	4.994	5.001	4.999	5.005	5.006	5.007	4.989	4.975	
Si+Al	4.013	3.999	3.997	4.009	4.001	4.002	4.007	3.999	3.996	4.017	4.005	3.999	4.003	3.999	3.999	3.999	4.003	4.007	
Na+Ca+K	0.975	0.997	0.991	0.982	0.995	0.992	0.991	0.992	0.999	0.953	0.986	0.998	0.993	1.004	1.005	1.005	0.982	0.966	
An(Na/Ca)	15.621	16.918	20.940	19.266	19.864	20.901	24.024	24.892	23.161	22.670	24.606	28.756	28.413	28.085	28.015	28.435	23.261	23.961	
Ab(Na/Ca)	84.002	82.632	77.917	79.846	79.296	78.587	74.837	74.040	75.475	76.858	74.158	69.984	70.454	71.149	70.821	70.379	75.880	75.222	
Or	0.363	0.430	1.103	0.887	0.742	0.513	1.139	1.037	1.235	0.473	1.121	1.260	1.120	0.766	1.164	1.186	0.779	0.751	
Ce	0.021	0.019	0.040	0.000	0.097	0.000	0.000	0.031	0.129	0.000	0.114	0.000	0.012	0.000	0.000	0.081	0.067		

Table A.2.5b: Representative analyses of plagioclase (continued).

Rock type Sample	Deformed biotite granitoid												Mega feldspar granitoid				
	BFS-7 2-Pl2 rim	BFS-7 2-Pl2 core	BFS-7 2-Pl2 core	BFS-7 2-Pl2 core	BFS-7 2-Pl2 rim	ND-2 2-Pl2 rim	ND-2 2-Pl2 core	ND-2 2-Pl2 core	ND-2 2-Pl2 rim	ND-2 2-Pl2 core	ND-2 5-Pl5 core	ND-2 5-Pl5 rim	ND-2 5-Pl5 core	DML-1 2-Pl2 core	DML-1 2-Pl2 rim	DML-1 2-Pl3 core	
<i>Component oxydes (wt.%)</i>																	
SiO ₂	63.27	63.60	62.80	63.08	64.01	67.91	64.29	63.86	63.55	64.18	99.64	66.02	63.66	63.85	64.70	63.86	63.58
Al ₂ O ₃	23.40	23.45	23.65	23.57	23.33	20.25	22.69	22.44	22.90	22.73	0.01	22.56	22.35	22.42	22.07	22.47	22.67
MgO	0.00	0.00	0.00	0.00	0.00	0.00	0.00	0.00	0.00	0.00	0.01	0.01	0.00	0.00	0.00	0.00	0.00
CaO	4.74	5.00	4.67	4.74	4.44	0.79	3.62	3.48	3.77	3.45	0.00	3.17	3.68	3.44	3.33	3.77	3.92
MnO	0.00	0.00	0.00	0.00	0.00	0.00	0.00	0.00	0.00	0.00	0.00	0.00	0.00	0.00	0.00	0.00	0.00
FeO	0.00	0.07	0.07	0.05	0.07	0.05	0.02	0.03	0.06	0.07	0.09	0.06	0.10	0.04	0.09	0.00	0.05
BaO	0.09	0.01	0.00	0.00	0.01	0.00	0.05	0.08	0.00	0.05	0.00	0.05	0.00	0.04	0.04	0.00	0.00
Na ₂ O	8.89	8.83	9.08	9.05	9.17	11.16	9.17	9.38	9.31	9.57	0.00	9.75	9.33	9.59	9.86	9.48	9.36
K ₂ O	0.20	0.18	0.14	0.10	0.10	0.05	0.10	0.08	0.08	0.12	0.00	0.19	0.11	0.10	0.18	0.10	0.12
Total	100.59	101.15	100.40	100.59	101.13	100.22	99.95	99.35	99.66	100.17	99.74	101.80	99.24	99.47	100.27	99.69	99.69
<i>Mineral Structural formulas (a.p.f.u) based on 8 Oxygens</i>																	
Si	2.785	2.784	2.770	2.776	2.798	2.963	2.833	2.833	2.813	2.826	3.998	2.855	2.830	2.831	2.848	2.827	2.816
Al	1.214	1.210	1.229	1.223	1.202	1.041	1.178	1.174	1.194	1.180	0.000	1.150	1.171	1.172	1.145	1.172	1.183
Mg	0.000	0.000	0.000	0.000	0.000	0.000	0.000	0.000	0.000	0.000	0.000	0.001	0.000	0.000	0.000	0.000	0.000
Ca	0.223	0.235	0.221	0.223	0.208	0.037	0.171	0.165	0.179	0.163	0.000	0.147	0.175	0.163	0.157	0.179	0.186
Mn	0.000	0.000	0.000	0.000	0.000	0.000	0.000	0.000	0.000	0.000	0.000	0.000	0.000	0.000	0.000	0.000	0.000
Fe	0.000	0.003	0.003	0.002	0.003	0.002	0.001	0.001	0.002	0.003	0.003	0.002	0.004	0.002	0.003	0.000	0.002
Ba	0.002	0.000	0.000	0.000	0.000	0.000	0.001	0.001	0.000	0.001	0.000	0.001	0.000	0.001	0.000	0.000	0.000
Na	0.759	0.750	0.776	0.772	0.777	0.944	0.783	0.807	0.799	0.817	0.000	0.817	0.804	0.824	0.841	0.814	0.804
K	0.011	0.010	0.008	0.006	0.005	0.003	0.006	0.004	0.004	0.007	0.000	0.010	0.006	0.005	0.010	0.006	0.006
Total	4.993	4.991	5.007	5.002	4.992	4.990	4.973	4.986	4.992	4.996	4.002	4.983	4.990	4.998	5.005	4.997	4.997
Si+Al	3.998	3.994	4.000	3.999	4.000	4.004	4.011	4.007	4.007	4.006	3.998	4.005	4.001	4.003	3.993	3.999	3.999
Na+Ca+K	0.995	0.995	1.004	1.001	0.990	0.984	0.961	0.978	0.982	0.987	0.000	0.975	0.986	0.993	1.009	0.998	0.996
An(Na/Ca)	22.455	23.590	21.962	22.307	20.987	3.739	17.796	16.912	18.200	16.465	15.555	15.039	17.765	16.437	15.559	17.920	18.662
Ab(Na/Ca)	76.260	75.361	77.276	77.144	78.437	95.967	81.517	82.487	81.363	82.751	84.445	83.809	81.579	82.948	83.374	81.498	80.686
Or	1.129	1.033	0.762	0.549	0.552	0.294	0.597	0.457	0.437	0.694	0.000	1.058	0.656	0.547	0.996	0.583	0.652
Ce	0.156	0.016	0.000	0.000	0.024	0.000	0.090	0.144	0.000	0.089	0.000	0.094	0.000	0.068	0.070	0.000	0.000

Table A.2.5b: Representative analyses of plagioclase (continued).

Rock type Sample	Mega feldspar granitoid																	
	DML-1 2-Pl4 core	DML-1 2-Pl5 core	DML-1 2-Pl6 core	DML-1 2-Pl6 rim	KO-12 1-Pl1 core	KO-12 1-Pl1 rim	KO-12 1-Pl2 core	KO-12 1-Pl2 rim	KO-12 1-Pl3 core	KO-12 1-Pl4 core	KO-12 2-Pl1 core	KO-12 2-Pl1 rim	KO-12 2-Pl2 core	KO-12 2-Pl2 rim	KO-12 2-Pl2 core	KO-12 2-Pl2 rim		
<i>Compoment oxydes (wt.%)</i>																		
SiO ₂	63.80	63.89	63.64	67.23	62.96	63.35	62.77	61.76	61.71	62.50	62.13	61.84	61.86	62.96	61.52	61.68	62.53	61.26
Al ₂ O ₃	22.50	22.49	22.60	20.31	23.14	22.81	23.41	23.85	23.60	23.34	23.27	23.78	23.50	22.75	23.69	23.59	23.59	23.74
MgO	0.00	0.00	0.00	0.00	0.00	0.00	0.00	0.00	0.00	0.03	0.00	0.00	0.00	0.00	0.00	0.00	0.00	0.00
CaO	3.63	3.69	3.62	0.97	4.48	4.10	4.92	5.40	5.13	4.73	4.89	5.11	4.88	4.20	5.18	5.08	4.97	5.46
MnO	0.00	0.00	0.00	0.00	0.00	0.00	0.00	0.00	0.00	0.00	0.00	0.00	0.00	0.00	0.00	0.00	0.00	0.00
FeO	0.00	0.03	0.06	0.09	0.01	0.03	0.11	0.03	0.07	0.03	0.03	0.08	0.05	0.04	0.07	0.06	0.03	0.07
BaO	0.01	0.06	0.00	0.08	0.01	0.02	0.10	0.00	0.02	0.00	0.05	0.00	0.02	0.00	0.00	0.00	0.05	0.00
Na ₂ O	9.76	9.72	9.61	11.37	9.11	9.24	8.83	8.41	8.57	8.92	8.47	8.54	8.66	9.23	8.53	8.52	8.94	8.37
K ₂ O	0.10	0.04	0.07	0.06	0.11	0.11	0.21	0.20	0.14	0.19	0.20	0.20	0.17	0.21	0.25	0.22	0.16	0.28
Total	99.80	99.92	99.60	100.10	99.82	99.66	100.35	99.64	99.24	99.71	99.05	99.54	99.13	99.38	99.24	99.14	100.28	99.18
<i>Mineral structural formulas (a.p.f.u) based on 8 Oxygens</i>																		
Si	2.823	2.824	2.820	2.946	2.790	2.808	2.774	2.749	2.756	2.776	2.776	2.753	2.764	2.802	2.750	2.757	2.765	2.742
Al	1.173	1.172	1.180	1.049	1.208	1.192	1.219	1.251	1.242	1.222	1.225	1.248	1.237	1.193	1.248	1.243	1.229	1.253
Mg	0.000	0.000	0.000	0.000	0.000	0.000	0.000	0.000	0.000	0.000	0.002	0.000	0.000	0.000	0.000	0.000	0.000	0.000
Ca	0.172	0.175	0.172	0.046	0.212	0.195	0.233	0.257	0.245	0.225	0.234	0.244	0.234	0.200	0.248	0.243	0.236	0.262
Mn	0.000	0.000	0.000	0.000	0.000	0.000	0.000	0.000	0.000	0.000	0.000	0.000	0.000	0.000	0.000	0.000	0.000	0.000
Fe	0.000	0.001	0.002	0.003	0.000	0.001	0.004	0.001	0.003	0.001	0.001	0.003	0.002	0.001	0.003	0.002	0.001	0.003
Ba	0.000	0.000	0.000	0.001	0.000	0.000	0.002	0.000	0.000	0.000	0.000	0.000	0.000	0.000	0.000	0.000	0.001	0.000
Na	0.837	0.833	0.825	0.966	0.783	0.794	0.756	0.725	0.743	0.768	0.733	0.737	0.750	0.796	0.739	0.739	0.767	0.727
K	0.006	0.002	0.004	0.003	0.006	0.006	0.012	0.011	0.008	0.011	0.011	0.010	0.012	0.014	0.013	0.009	0.016	
Total	5.011	5.008	5.004	5.014	5.000	4.996	5.000	4.994	4.998	5.002	4.984	4.997	4.997	5.005	5.003	4.997	5.008	5.002
Si Al	3.997	3.996	4.001	3.995	3.998	4.000	3.993	3.999	3.999	3.998	4.001	4.002	4.002	3.995	3.998	4.000	3.995	3.995
Na+Ca+K	1.015	1.011	1.001	1.016	1.002	0.995	1.003	0.994	0.996	1.004	0.980	0.992	0.993	1.008	1.002	0.994	1.012	1.004
An(Na/Ca)	16.952	17.264	17.172	4.492	21.209	19.546	23.226	25.891	24.630	22.440	23.898	24.585	23.517	19.883	24.777	24.462	23.274	26.082
Ab(Na/Ca)	82.466	82.394	82.444	95.053	78.129	79.764	75.442	72.990	74.535	76.510	74.853	74.276	75.483	78.951	73.777	74.270	75.735	72.355
Or	0.562	0.245	0.384	0.314	0.638	0.648	1.153	1.120	0.807	1.050	1.169	1.139	0.970	1.166	1.446	1.268	0.914	1.564
Ce	0.021	0.096	0.000	0.142	0.024	0.042	0.180	0.000	0.028	0.000	0.080	0.000	0.030	0.000	0.000	0.077	0.000	

Table A.2.5b: Representative analyses of plagioclase (continued).

Rock type Sample	Mega feldspar granitoid																	
	KO-12 2-Pl3 rim	KO-12 2-Pl3 core	KO-12 2-Pl3 rim	KO-12 3-Pl3 rim	KO-12 3-Pl3 core	KO-12 1-Pl1 rim	KO-12 1-Pl1 core	KO-12 1-Pl1 rim	KO-12 1-Pl1 core	KO-12 1-Pl2 rim	KO-12 1-Pl2 core	KO-12 1-Pl2 rim	TE-6 1-Pl2 core	TE-6 1-Pl2 rim	TE-6 1-Pl2 core	TE-6 1-Pl2 rim	TE-6 1-Pl3 core	
<i>Compoment oxydes (wt.%)</i>																		
SiO ₂	62.42	63.05	62.22	62.73	62.89	62.79	63.68	64.35	64.20	64.57	62.51	63.39	63.15	61.43	61.68	61.65	61.37	62.68
Al ₂ O ₃	22.83	23.02	23.56	23.66	23.38	22.86	22.70	22.42	22.23	22.13	23.31	23.00	23.05	24.05	24.00	23.88	24.11	23.89
MgO	0.00	0.00	0.00	0.01	0.00	0.00	0.00	0.00	0.01	0.00	0.00	0.00	0.00	0.00	0.00	0.00	0.00	0.00
CaO	4.50	4.35	4.86	5.01	4.85	3.95	3.90	3.40	3.52	3.06	4.68	4.37	4.17	5.48	5.33	5.57	5.41	4.96
MnO	0.00	0.00	0.00	0.00	0.00	0.00	0.00	0.00	0.00	0.00	0.00	0.00	0.00	0.00	0.00	0.00	0.00	0.00
FeO	0.00	0.04	0.05	0.07	0.06	0.00	0.00	0.00	0.02	0.03	0.05	0.04	0.00	0.04	0.13	0.04	0.06	0.18
BaO	0.00	0.00	0.01	0.00	0.02	0.09	0.04	0.03	0.00	0.06	0.04	0.00	0.01	0.02	0.00	0.00	0.01	0.00
Na ₂ O	9.24	9.10	8.75	8.86	8.68	9.52	9.30	9.56	9.53	10.00	8.80	9.27	9.14	8.34	8.44	8.46	8.39	8.61
K ₂ O	0.21	0.25	0.29	0.23	0.20	0.13	0.11	0.13	0.16	0.08	0.23	0.32	0.26	0.23	0.21	0.18	0.18	0.26
Total	99.21	99.81	99.73	100.56	100.08	99.34	99.72	99.90	99.66	99.93	99.62	100.40	99.77	99.61	99.78	99.78	99.52	100.59
<i>Mineral structural formulas (a.p.f.u) based on 8 Oxygens</i>																		
Si	2.788	2.795	2.765	2.766	2.781	2.797	2.818	2.839	2.840	2.848	2.779	2.796	2.798	2.737	2.743	2.743	2.736	2.762
Al	1.202	1.203	1.234	1.229	1.218	1.200	1.184	1.166	1.159	1.151	1.221	1.196	1.204	1.263	1.258	1.252	1.267	1.241
Mg	0.000	0.000	0.000	0.001	0.000	0.000	0.000	0.000	0.001	0.000	0.000	0.000	0.000	0.000	0.000	0.000	0.000	0.000
Ca	0.215	0.206	0.232	0.237	0.230	0.188	0.185	0.161	0.167	0.145	0.223	0.207	0.198	0.262	0.254	0.265	0.258	0.234
Mn	0.000	0.000	0.000	0.000	0.000	0.000	0.000	0.000	0.000	0.000	0.000	0.000	0.000	0.000	0.000	0.000	0.000	0.000
Fe	0.000	0.002	0.002	0.002	0.002	0.000	0.000	0.000	0.001	0.001	0.002	0.002	0.000	0.002	0.005	0.001	0.002	0.007
Ba	0.000	0.000	0.000	0.000	0.000	0.002	0.001	0.001	0.000	0.001	0.001	0.000	0.000	0.000	0.000	0.000	0.000	0.000
Na	0.800	0.782	0.754	0.757	0.744	0.822	0.798	0.818	0.817	0.856	0.759	0.793	0.785	0.721	0.728	0.730	0.725	0.735
K	0.012	0.014	0.016	0.013	0.011	0.008	0.006	0.007	0.009	0.005	0.013	0.018	0.014	0.013	0.012	0.010	0.010	0.015
Total	5.017	5.002	5.003	5.005	4.987	5.017	4.992	4.991	4.994	5.006	4.997	5.011	5.000	4.998	4.998	5.001	4.999	4.993
Si Al	3.990	3.998	3.999	3.995	3.999	3.998	4.002	4.005	3.999	3.999	4.000	3.992	4.002	4.001	4.000	3.995	4.003	4.002
Na+Ca+K	1.028	1.003	1.002	1.007	0.985	1.019	0.989	0.986	0.993	1.006	0.995	1.018	0.998	0.996	0.993	1.005	0.994	0.984
An(Na/Ca)	20.956	20.587	23.126	23.526	23.328	18.471	18.682	16.302	16.789	14.395	22.404	20.309	19.831	26.263	25.544	26.400	25.981	23.784
Ab(Na/Ca)	77.863	78.014	75.248	75.217	75.476	80.634	80.632	82.906	82.296	85.061	76.234	77.938	78.694	72.361	73.240	72.589	72.997	74.709
Or	1.181	1.399	1.613	1.257	1.162	0.736	0.622	0.736	0.915	0.448	1.294	1.753	1.451	1.336	1.216	1.011	1.013	1.507
Ce	0.000	0.000	0.012	0.000	0.033	0.159	0.063	0.056	0.000	0.096	0.068	0.000	0.024	0.040	0.000	0.009	0.000	0.000

Table A.2.5b: Representative analyses of plagioclase (continued).

Rock type Sample	Mega feldspar granitoid			Two-mica granitoid													
	TE-6 2-Pl1 core	TE-6 1-Pl1 core	TE-6 1-Pl2 rim	BM-3 1-Pl1 core	BM-3 1-Pl2 rim	BM-3 1-Pl2 core	BM-3 2-Pl3 rim	BM-3 2-Pl3 core	BM-3 2-Pl4 rim	BM-3 2-Pl4 core	BM-3 2-Pl5 core	BM-3 2-Pl5 core	BM-3 2-Pl5 rim	BM-3 3-Pl1 rim			
<i>Compoment oxydes (wt.%)</i>																	
SiO ₂	61.53	61.89	62.01	65.13	67.54	66.96	66.47	65.67	65.75	65.45	65.39	66.61	67.00	65.74	65.88	67.05	67.68
Al ₂ O ₃	24.01	23.79	24.02	21.13	20.26	20.52	20.55	20.93	21.03	21.35	21.46	21.06	20.60	21.18	20.79	21.35	19.99
MgO	0.00	0.00	0.00	0.02	0.02	0.01	0.01	0.00	0.01	0.00	0.03	0.03	0.01	0.00	0.03	0.00	0.00
CaO	5.46	5.24	5.42	1.84	0.83	0.99	1.17	1.72	1.81	2.11	2.22	1.57	1.19	1.51	1.45	1.37	0.50
MnO	0.00	0.00	0.00	0.00	0.00	0.00	0.00	0.00	0.00	0.00	0.00	0.00	0.00	0.00	0.00	0.00	0.00
FeO	0.03	0.11	0.09	0.00	0.03	0.03	0.07	0.02	0.01	0.00	0.04	0.00	0.03	0.13	0.00	0.00	0.00
BaO	0.06	0.00	0.00	0.00	0.00	0.00	0.07	0.01	0.00	0.04	0.00	0.03	0.00	0.00	0.00	0.00	0.04
Na ₂ O	8.51	8.54	8.48	10.91	11.28	10.93	11.02	10.81	10.55	10.43	10.45	10.94	10.97	10.34	10.71	10.60	11.39
K ₂ O	0.23	0.14	0.28	0.06	0.14	0.11	0.12	0.16	0.13	0.11	0.13	0.13	0.10	0.22	0.16	0.17	0.19
Total	99.82	99.71	100.30	99.08	100.10	99.54	99.47	99.33	99.28	99.49	99.71	100.36	99.88	99.11	99.00	100.55	99.80
<i>Mineral structural formulas (a.p.f.u) based on 8 Oxygens</i>																	
Si	2.738	2.752	2.745	2.891	2.955	2.944	2.932	2.906	2.907	2.891	2.884	2.914	2.938	2.909	2.919	2.920	2.968
Al	1.259	1.247	1.253	1.106	1.045	1.063	1.068	1.092	1.096	1.112	1.116	1.086	1.065	1.105	1.086	1.096	1.033
Mg	0.000	0.000	0.000	0.001	0.001	0.001	0.000	0.000	0.001	0.000	0.002	0.002	0.000	0.000	0.002	0.000	0.000
Ca	0.260	0.250	0.257	0.087	0.039	0.046	0.055	0.082	0.086	0.100	0.105	0.074	0.056	0.072	0.069	0.064	0.024
Mn	0.000	0.000	0.000	0.000	0.000	0.000	0.000	0.000	0.000	0.000	0.000	0.000	0.000	0.000	0.000	0.000	0.000
Fe	0.001	0.004	0.003	0.000	0.001	0.001	0.002	0.001	0.000	0.000	0.001	0.000	0.001	0.005	0.000	0.000	0.000
Ba	0.001	0.000	0.000	0.000	0.000	0.000	0.001	0.000	0.000	0.001	0.000	0.001	0.000	0.000	0.000	0.000	0.001
Na	0.734	0.737	0.728	0.939	0.957	0.931	0.942	0.927	0.904	0.893	0.894	0.928	0.933	0.887	0.920	0.895	0.968
K	0.013	0.008	0.016	0.003	0.008	0.006	0.007	0.009	0.007	0.006	0.007	0.007	0.005	0.012	0.009	0.009	0.011
Total	5.006	4.997	5.001	5.027	5.005	4.993	5.009	5.016	5.001	5.003	5.009	5.011	4.998	4.989	5.003	4.984	5.005
Si Al	3.997	3.999	3.997	3.997	3.999	4.007	4.000	3.997	4.003	4.003	4.000	4.000	4.003	4.013	4.004	4.016	4.001
Na+Ca+K	1.009	0.994	1.000	1.030	1.004	0.984	1.006	1.018	0.997	1.000	1.006	1.009	0.994	0.971	0.997	0.969	1.004
An(Na/Ca)	25.786	25.125	25.671	8.491	3.872	4.724	5.504	8.014	8.604	9.983	10.431	7.283	5.626	7.391	6.884	6.600	2.360
Ab(Na/Ca)	72.820	74.076	72.766	91.179	95.374	94.622	93.679	91.064	90.666	89.339	88.853	91.939	93.834	91.353	92.237	92.425	96.494
Or	1.295	0.799	1.563	0.325	0.751	0.650	0.694	0.898	0.730	0.603	0.716	0.725	0.540	1.256	0.879	0.975	1.076
Ce	0.099	0.000	0.000	0.005	0.003	0.005	0.124	0.024	0.000	0.074	0.000	0.053	0.000	0.000	0.000	0.000	0.070

Table A.2.5b: Representative analyses of plagioclase (continued).

Rock type Sample	Two-mica granitoid																	
	BM-3 3-P11 core	BM-3 3-P11 core	BM-3 3-P11 rim	BM-3 3-P12 rim	BM-3 4-P11 rim	BM3 4-P11 core	BM-3 4-P11 rim	BAN-6 1-P11 rim	BAN-6 1-P11 core	BAN-6 1-P11 rim	BAN-6 1-P12 core	BAN-6 1-P12 core	BAN-6 1-P13 rim	BAN-6 1-P13 core	BAN-6 1-P13 rim	BAN-6 2-P11 core	BAN-6 2-P11 rim	BAN-6 2-P11 core
	Component oxydes (wt.%)																	
SiO ₂	67.68	67.45	67.51	67.17	64.97	65.73	65.34	64.94	65.16	65.82	65.90	65.57	64.79	67.15	65.51	67.11	65.01	64.47
Al ₂ O ₃	20.06	20.07	20.46	19.96	21.37	21.42	21.33	21.74	21.46	21.38	21.00	21.31	21.55	20.14	21.39	20.20	21.96	21.85
MgO	0.00	0.00	0.01	0.00	0.00	0.00	0.00	0.00	0.00	0.00	0.00	0.00	0.01	0.00	0.00	0.01	0.00	0.00
CaO	0.55	0.58	0.73	0.63	2.21	1.94	2.10	2.74	2.60	2.23	2.02	1.95	2.55	0.78	2.30	1.04	2.75	2.79
MnO	0.00	0.00	0.00	0.00	0.00	0.00	0.00	0.00	0.00	0.00	0.00	0.00	0.00	0.00	0.00	0.00	0.00	0.00
FeO	0.04	0.02	0.06	0.04	0.05	0.01	0.00	0.02	0.00	0.02	0.06	0.03	0.07	0.00	0.00	0.01	0.00	0.00
BaO	0.00	0.05	0.07	0.03	0.06	0.00	0.00	0.04	0.00	0.02	0.00	0.02	0.00	0.00	0.00	0.00	0.00	0.08
Na ₂ O	11.54	11.39	11.10	11.47	10.54	10.45	10.64	10.00	10.30	10.20	10.54	10.65	10.41	11.16	10.11	11.06	10.01	10.05
K ₂ O	0.17	0.16	0.19	0.07	0.15	0.18	0.15	0.04	0.08	0.11	0.06	0.15	0.21	0.11	0.16	0.08	0.25	0.20
Total	100.04	99.72	100.12	99.38	99.35	99.73	99.55	99.52	99.59	99.78	99.58	99.67	99.58	99.35	99.46	99.50	99.97	99.43
Mineral structural formulas (a.p.f.u.) based on 8 Oxygens																		
Si	2.963	2.962	2.952	2.961	2.880	2.895	2.887	2.870	2.879	2.896	2.906	2.892	2.868	2.958	2.892	2.953	2.863	2.858
Al	1.035	1.039	1.054	1.037	1.116	1.112	1.111	1.133	1.117	1.109	1.091	1.108	1.124	1.046	1.113	1.047	1.140	1.142
Mg	0.000	0.000	0.001	0.000	0.000	0.000	0.000	0.000	0.000	0.000	0.000	0.000	0.000	0.000	0.000	0.000	0.000	0.000
Ca	0.026	0.027	0.034	0.030	0.105	0.092	0.099	0.130	0.123	0.105	0.095	0.092	0.121	0.037	0.109	0.049	0.130	0.133
Mn	0.000	0.000	0.000	0.000	0.000	0.000	0.000	0.000	0.000	0.000	0.000	0.000	0.000	0.000	0.000	0.000	0.000	0.000
Fe	0.002	0.001	0.002	0.001	0.002	0.000	0.000	0.000	0.000	0.000	0.002	0.001	0.002	0.000	0.000	0.000	0.000	0.000
Ba	0.000	0.001	0.001	0.001	0.001	0.000	0.000	0.000	0.000	0.000	0.000	0.000	0.000	0.000	0.000	0.000	0.000	0.001
Na	0.979	0.970	0.941	0.980	0.906	0.892	0.912	0.857	0.882	0.870	0.902	0.911	0.893	0.953	0.865	0.943	0.855	0.864
K	0.009	0.009	0.010	0.004	0.009	0.010	0.009	0.002	0.004	0.006	0.004	0.008	0.012	0.006	0.009	0.005	0.014	0.011
Total	5.014	5.008	4.996	5.013	5.019	5.001	5.017	4.993	5.006	4.987	5.001	5.013	5.022	4.999	4.988	4.998	5.001	5.008
Si Al	3.998	4.001	4.007	3.997	3.997	4.006	3.998	4.003	3.996	4.005	3.998	4.001	3.993	4.003	4.005	4.000	4.003	4.000
Na+Ca+K	1.015	1.007	0.987	1.015	1.021	0.994	1.019	0.990	1.010	0.981	1.001	1.011	1.026	0.996	0.983	0.997	0.998	1.009
An(Na/Ca)	2.556	2.715	3.442	2.927	10.276	9.225	9.735	13.113	12.204	10.696	9.539	9.095	11.774	3.706	11.075	4.908	12.987	13.154
Ab(Na/Ca)	96.530	96.303	95.379	96.625	88.782	89.751	89.425	86.586	87.371	88.655	90.097	90.066	87.054	95.702	88.013	94.619	85.611	85.615
Or	0.914	0.901	1.052	0.393	0.848	1.023	0.841	0.234	0.424	0.606	0.360	0.812	1.172	0.592	0.911	0.473	1.402	1.099
Ce	0.000	0.080	0.127	0.054	0.094	0.000	0.000	0.067	0.000	0.042	0.003	0.027	0.000	0.000	0.000	0.000	0.000	0.133

Table A.2.5b: Representative analyses of plagioclase (continued).

Rock type Sample	Two-mica granitoid																	
	BAN-6	NO-30	NO-30	NO-30	NO-30	NO-30	NO-30	NO-30	NO-30	NO-30	NO-30	NO-30	NO-30	NO-30	NO-30	NO-30	NO-30	NO-30
	2-PI1 rim	2-PI2 rim	2-P2 core	2-PI2 core	2-PI2 rim	2-PI3 rim	2-PI3 core	2-PI3 rim	3-PI1 core	3-PI1 core	3-PI1 rim	3-PI2 core	3-PI2 rim	3-PI2 core	3-PI2 rim	3-PI1 core	3-PI1 rim	4-PI2 core
<i>Component oxydes (wt.%)</i>																		
SiO ₂	64.78	63.45	62.76	62.90	63.01	62.19	63.24	63.02	63.01	63.18	62.85	62.94	64.07	62.81	63.54	63.24	65.02	63.01
Al ₂ O ₃	21.38	22.60	22.97	23.13	22.84	23.45	22.80	22.76	22.69	22.58	22.77	23.12	22.46	23.03	22.40	22.65	21.68	22.73
MgO	0.00	0.00	0.00	0.00	0.00	0.01	0.00	0.01	0.00	0.00	0.00	0.00	0.00	0.00	0.00	0.00	0.00	0.00
CaO	2.52	3.76	4.18	4.25	4.11	4.64	4.00	3.86	4.01	3.80	3.97	4.13	3.65	4.11	3.47	3.71	2.48	3.69
MnO	0.00	0.00	0.00	0.00	0.00	0.00	0.00	0.00	0.00	0.00	0.00	0.00	0.00	0.00	0.00	0.00	0.00	0.00
FeO	0.04	0.05	0.00	0.02	0.05	0.05	0.06	0.02	0.04	0.01	0.04	0.04	0.05	0.08	0.00	0.02	0.05	0.04
BaO	0.00	0.00	0.03	0.00	0.03	0.00	0.00	0.00	0.00	0.10	0.00	0.00	0.11	0.01	0.04	0.00	0.00	0.00
Na ₂ O	10.21	9.28	9.17	9.07	9.24	8.98	9.22	9.34	9.32	9.43	9.32	9.23	9.69	9.56	9.88	9.61	10.46	9.55
K ₂ O	0.15	0.20	0.27	0.23	0.21	0.14	0.14	0.15	0.18	0.15	0.23	0.19	0.21	0.23	0.10	0.13	0.20	0.18
Total	99.08	99.33	99.39	99.60	99.47	99.44	99.46	99.15	99.24	99.24	99.18	99.64	100.22	99.83	99.43	99.37	99.89	99.19
<i>Mineral structural formulas (a.p.f.u.) based on 8 Oxygens</i>																		
Si	2.878	2.819	2.794	2.793	2.801	2.769	2.808	2.807	2.807	2.814	2.802	2.793	2.826	2.788	2.823	2.812	2.868	2.807
Al	1.120	1.184	1.205	1.210	1.197	1.231	1.193	1.195	1.191	1.185	1.197	1.209	1.168	1.205	1.173	1.187	1.127	1.193
Mg	0.000	0.000	0.000	0.000	0.000	0.000	0.000	0.000	0.000	0.000	0.000	0.000	0.000	0.000	0.000	0.000	0.000	0.000
Ca	0.120	0.179	0.200	0.202	0.196	0.221	0.190	0.184	0.191	0.181	0.189	0.196	0.172	0.196	0.165	0.177	0.117	0.176
Mn	0.000	0.000	0.000	0.000	0.000	0.000	0.000	0.000	0.000	0.000	0.000	0.000	0.000	0.000	0.000	0.000	0.000	0.000
Fe	0.002	0.002	0.000	0.001	0.002	0.002	0.002	0.000	0.001	0.000	0.002	0.001	0.002	0.003	0.000	0.001	0.002	0.001
Ba	0.000	0.000	0.001	0.000	0.000	0.000	0.000	0.000	0.000	0.002	0.000	0.000	0.002	0.000	0.001	0.000	0.000	0.000
Na	0.879	0.799	0.792	0.781	0.796	0.775	0.794	0.806	0.805	0.814	0.806	0.794	0.828	0.823	0.851	0.829	0.895	0.825
K	0.008	0.011	0.015	0.013	0.012	0.008	0.008	0.009	0.010	0.009	0.013	0.011	0.012	0.013	0.006	0.007	0.011	0.010
Total	5.006	4.994	5.007	4.999	5.004	5.007	4.996	5.003	5.006	5.005	5.009	5.005	5.010	5.027	5.019	5.013	5.021	5.014
Si Al	3.997	4.003	4.000	4.003	3.998	4.000	4.002	4.002	3.998	3.999	3.999	4.002	3.994	3.993	3.996	3.999	4.001	
Na+Ca+K	1.007	0.990	1.007	0.996	1.004	1.004	0.992	0.999	1.007	1.006	1.008	1.001	1.014	1.032	1.023	1.013	1.023	1.011
An(Na/Ca)	11.892	18.100	19.820	20.312	19.474	22.030	19.178	18.441	19.015	18.037	18.788	19.603	16.990	18.954	16.151	17.446	11.469	17.436
Ab(Na/Ca)	87.275	80.766	78.630	78.369	79.293	77.194	80.028	80.700	79.963	80.940	79.931	79.334	81.691	79.794	83.208	81.821	87.420	81.576
Or	0.833	1.134	1.500	1.313	1.186	0.775	0.794	0.859	1.022	0.853	1.281	1.063	1.138	1.235	0.576	0.734	1.111	0.983
Ce	0.000	0.000	0.050	0.005	0.047	0.000	0.000	0.000	0.000	0.170	0.000	0.000	0.181	0.017	0.065	0.000	0.000	0.005

Table A.2.5b: Representative analyses of plagioclase (continued).

Rock type Sample	Two-mica granitoid																
	NO-30 4-Pl2 rim	NO-30 4-Pl3 rim	NO-30 4-Pl3 core	NO-30 4-Pl3 core	NO-30 4-Pl4 rim	NO-30 4-Pl4 core	NO-30 4-Pl4 rim	NO-30 4-Pl5 core	TA-9 3-Pl2 rim	TA-9 3-Pl2 core	TA-9 3-Pl2 rim	TA-9 3-Pl3 rim	TA-9 3-Pl3 core	TA-9 3-Pl4 rim	TA-9 3-Pl4 core	TA-9 3-Pl4 rim	
<i>Component oxydes (wt.%)</i>																	
SiO ₂	64.65	62.80	63.14	63.14	63.24	63.12	62.62	67.09	64.64	64.70	64.37	65.54	66.10	64.95	65.47	65.62	65.78
Al ₂ O ₃	21.66	22.78	22.63	22.66	22.80	22.52	22.73	20.58	21.92	21.59	21.73	21.30	21.35	21.37	21.40	21.26	21.58
MgO	0.00	0.00	0.00	0.00	0.00	0.00	0.00	0.00	0.00	0.00	0.00	0.00	0.00	0.00	0.00	0.01	0.00
CaO	2.46	3.80	3.94	3.81	3.82	3.86	4.13	2.12	2.79	2.80	2.69	2.06	2.08	2.52	2.11	1.99	2.24
MnO	0.00	0.00	0.00	0.00	0.00	0.00	0.00	0.00	0.00	0.00	0.00	0.00	0.00	0.00	0.00	0.00	0.00
FeO	0.04	0.07	0.01	0.05	0.03	0.07	0.04	0.00	0.00	0.00	0.05	0.04	0.02	0.05	0.02	0.01	0.00
BaO	0.00	0.00	0.00	0.00	0.06	0.00	0.03	0.00	0.03	0.00	0.02	0.01	0.05	0.01	0.00	0.00	0.01
Na ₂ O	10.33	9.66	9.45	9.35	9.37	9.39	9.42	10.26	10.12	9.92	10.07	10.25	10.39	10.23	10.36	10.52	10.36
K ₂ O	0.13	0.12	0.15	0.22	0.18	0.24	0.16	0.10	0.09	0.20	0.20	0.10	0.11	0.13	0.12	0.13	0.18
Total	99.28	99.23	99.32	99.23	99.49	99.20	99.13	100.15	99.59	99.21	99.13	99.29	100.09	99.25	99.47	99.53	100.14
<i>Mineral structural formulas (a.p.f.u.) based on 8 Oxygens</i>																	
Si	2.867	2.800	2.810	2.812	2.809	2.813	2.797	2.935	2.859	2.871	2.861	2.897	2.900	2.880	2.891	2.896	2.887
Al	1.132	1.197	1.187	1.189	1.194	1.183	1.197	1.061	1.142	1.129	1.138	1.110	1.104	1.117	1.114	1.106	1.116
Mg	0.000	0.000	0.000	0.000	0.000	0.000	0.000	0.000	0.000	0.000	0.000	0.000	0.000	0.000	0.000	0.000	0.000
Ca	0.117	0.182	0.188	0.182	0.182	0.184	0.198	0.099	0.132	0.133	0.128	0.098	0.098	0.120	0.100	0.094	0.105
Mn	0.000	0.000	0.000	0.000	0.000	0.000	0.000	0.000	0.000	0.000	0.000	0.000	0.000	0.000	0.000	0.000	0.000
Fe	0.002	0.003	0.000	0.002	0.001	0.003	0.001	0.000	0.000	0.000	0.002	0.001	0.000	0.002	0.001	0.000	0.000
Ba	0.000	0.000	0.000	0.000	0.001	0.000	0.000	0.000	0.000	0.000	0.000	0.000	0.000	0.000	0.000	0.000	0.000
Na	0.888	0.835	0.815	0.808	0.806	0.811	0.815	0.870	0.868	0.854	0.868	0.878	0.883	0.879	0.887	0.900	0.881
K	0.007	0.007	0.009	0.012	0.010	0.014	0.009	0.006	0.005	0.011	0.011	0.006	0.006	0.007	0.007	0.007	0.010
Total	5.014	5.022	5.008	5.004	5.003	5.008	5.018	4.972	5.007	4.998	5.009	4.990	4.993	5.005	4.999	5.004	5.000
Si Al	4.000	3.997	3.997	4.001	4.002	3.996	3.993	3.997	4.001	4.000	4.000	4.007	4.004	3.997	4.005	4.002	4.004
Na+Ca+K	1.013	1.023	1.011	1.002	1.000	1.009	1.023	0.975	1.006	0.998	1.008	0.982	0.988	1.006	0.994	1.001	0.997
An(Na/Ca)	11.563	17.742	18.558	18.139	18.188	18.253	19.335	10.198	13.126	13.323	12.714	9.944	9.884	11.890	10.024	9.383	10.566
Ab(Na/Ca)	87.739	81.591	80.583	80.630	80.687	80.390	79.711	89.224	86.302	85.531	86.119	89.472	89.428	87.387	89.312	89.903	88.431
Or	0.698	0.667	0.859	1.231	1.015	1.358	0.908	0.578	0.527	1.146	1.126	0.569	0.606	0.703	0.663	0.714	0.983
Ce	0.000	0.000	0.000	0.000	0.110	0.000	0.046	0.000	0.045	0.000	0.041	0.016	0.082	0.021	0.000	0.000	0.021

Table A.2.6a: Representative analyses of magnetite (continued).

Rock type Sample	Biotite granitoid															BFS-7
	NG-3	NG-3	NG-3	NG-3	NG-3	LE-2	LE-2	LE-2	BL-8	BL-8	BL-8	2-Mag1 (titanite)	SE-4	SE-4	SE-4	
	1-Mag1	2-Mag1	2-Mag2	2-Mag3	3-Mag1	4-Mag1	4-Mag2	4-Mag3	4-Mag4	2-Mag1	2-Mag2	2-Mag3	1-Mag1	1-Mag2	2-Mag1	2-Mag1
<i>Component oxides (wt.%)</i>																
SiO ₂	0.03	0.06	0.09	0.00	0.03	0.04	0.04	0.00	0.03	0.07	0.06	0.08	0.00	0.03	0.02	0.00
TiO ₂	0.01	0.03	0.02	0.01	0.00	0.02	0.03	0.00	0.00	0.01	0.00	0.00	0.01	0.00	0.00	0.00
Al ₂ O ₃	0.00	0.02	0.00	0.00	0.01	0.04	0.00	0.06	0.02	0.01	0.00	0.00	0.00	0.00	0.00	0.00
Cr ₂ O ₃	0.02	0.00	0.04	0.02	0.02	0.07	0.01	0.00	0.00	0.02	0.01	0.01	0.07	0.02	0.02	0.00
Fe ₂ O ₃	62.89	60.34	62.42	61.94	62.63	62.69	62.55	62.58	62.06	62.29	43.73	63.13	43.75	60.41	62.57	62.50
MgO	0.05	0.04	0.00	0.00	0.00	0.15	0.00	0.07	0.05	0.03	0.00	0.02	0.04	0.10	0.06	0.00
CaO	0.00	0.00	0.00	0.00	0.00	0.00	0.00	0.00	0.00	0.00	0.00	0.00	0.00	0.00	0.00	0.00
MnO	0.07	0.10	0.11	0.06	0.00	0.08	0.06	0.12	0.05	0.10	0.00	0.24	0.00	0.17	0.11	0.23
FeO	28.13	26.99	28.07	27.83	28.20	27.95	28.13	27.93	27.82	27.93	19.72	28.18	19.66	26.84	27.99	27.92
ZnO	0.00	0.00	0.00	0.00	0.00	0.00	0.00	0.00	0.00	0.00	0.00	0.00	0.00	0.00	0.00	0.00
NiO	0.00	0.00	0.00	0.00	0.00	0.00	0.00	0.00	0.00	0.00	0.00	0.00	0.00	0.00	0.00	0.00
Total	91.21	87.59	90.75	89.85	90.89	91.02	90.83	90.76	90.02	90.46	63.53	91.65	63.52	87.59	90.77	90.67
<i>Mineal structural formulas (a.p.f.u) based on 4 Oxygens</i>																
A-position																
Mg	0.003	0.003	0.000	0.000	0.000	0.009	0.000	0.005	0.003	0.002	0.000	0.001	0.003	0.007	0.004	0.000
Ca	0.000	0.000	0.000	0.000	0.000	0.000	0.000	0.000	0.000	0.000	0.000	0.000	0.000	0.000	0.000	0.000
Mn	0.003	0.004	0.004	0.002	0.000	0.003	0.002	0.004	0.002	0.004	0.000	0.008	0.000	0.006	0.004	0.008
Fe ²⁺	0.993	0.992	0.996	0.998	1.000	0.988	0.998	0.991	0.995	0.994	1.000	0.990	0.997	0.986	0.993	0.992
Zn	0.000	0.000	0.000	0.000	0.000	0.000	0.000	0.000	0.000	0.000	0.000	0.000	0.000	0.000	0.000	0.000
Ni	0.000	0.000	0.000	0.000	0.000	0.000	0.000	0.000	0.000	0.000	0.000	0.000	0.000	0.000	0.000	0.000
Sum A	0.999	0.998	1.000	1.000	1.000	1.000	1.000	1.000	1.000	1.000	1.000	0.999	1.000	0.999	1.001	1.000
B-position																
Si	0.001	0.003	0.004	0.000	0.001	0.002	0.002	0.000	0.001	0.003	0.004	0.003	0.000	0.001	0.001	0.000
Ti	0.000	0.001	0.001	0.000	0.000	0.001	0.001	0.000	0.000	0.000	0.000	0.000	0.000	0.000	0.000	0.001
Al	0.000	0.001	0.000	0.000	0.000	0.002	0.000	0.003	0.001	0.001	0.000	0.000	0.000	0.000	0.000	0.000
Cr	0.001	0.000	0.001	0.001	0.001	0.002	0.000	0.000	0.000	0.001	0.000	0.000	0.003	0.001	0.001	0.000
Fe ³⁺	1.998	1.995	1.993	1.999	1.997	1.993	1.996	1.997	1.998	1.995	1.995	1.995	1.996	1.998	1.998	1.999
Sum B	2.000	2.000	1.999	2.000	2.000	2.000	1.999	2.000	2.000	1.999	1.999	1.999	2.000	2.000	1.999	2.000
A+B	2.999	2.998	2.999	3.000	3.000	2.999	2.999	3.000	3.000	2.999	2.999	2.999	3.000	3.000	3.000	3.000

Table A.2.6a: Representative analyses of magnetite (continued).

Rock type Sample	Deformed biotite granitoid						Mega feldspar granitoid				
	BFS-7 2-Mag2	ND-2 2-Mag1	ND-2 2-Mag2	ND-2 4-Mag1	NN-1 1-Mag1	NN-1 1-Mag2	TS-2 2-Mag1	TK-2 1-Mag1	TK-2 1-Mag2	TE-6 3-Mag1	TE-6 3-Mag1
<i>Component oxides (wt.%)</i>											
SiO ₂	0.01	0.04	0.00	0.03	0.02	0.03	0.00	0.02	0.06	0.05	0.03
TiO ₂	0.03	0.03	0.07	0.17	0.04	0.00	0.00	0.04	0.03	0.01	0.01
Al ₂ O ₃	0.03	0.03	0.00	0.00	0.00	0.02	0.00	0.06	0.04	0.00	0.00
Cr ₂ O ₃	0.01	0.00	0.11	0.15	0.07	0.05	0.04	0.02	0.03	0.01	0.00
Fe ₂ O ₃	61.97	62.49	62.71	62.08	63.50	63.78	62.49	62.49	62.34	62.73	62.63
MgO	0.02	0.02	0.06	0.00	0.03	0.01	0.02	0.04	0.00	0.03	0.02
CaO	0.00	0.00	0.00	0.00	0.00	0.00	0.00	0.00	0.00	0.00	0.00
MnO	0.04	0.06	0.04	0.17	0.03	0.02	0.00	0.16	0.07	0.07	0.10
FeO	27.86	28.09	28.18	27.97	28.56	28.72	28.11	27.93	28.09	28.12	28.08
ZnO	0.00	0.00	0.00	0.00	0.00	0.00	0.00	0.00	0.00	0.00	0.00
NiO	0.00	0.00	0.00	0.00	0.00	0.00	0.00	0.00	0.00	0.00	0.00
Total	89.97	90.76	91.16	90.56	92.26	92.64	90.66	90.75	90.64	91.02	90.86
<i>Mineal structural formulas (a.p.f.u) based on 4 Oxygens</i>											
A-position											
Mg	0.001	0.001	0.004	0.000	0.002	0.001	0.001	0.003	0.000	0.002	0.001
Ca	0.000	0.000	0.000	0.000	0.000	0.000	0.000	0.000	0.000	0.000	0.000
Mn	0.002	0.002	0.001	0.006	0.001	0.001	0.000	0.006	0.002	0.003	0.004
Fe ²⁺	0.997	0.997	0.995	0.994	0.997	0.999	0.999	0.991	0.998	0.995	0.995
Zn	0.000	0.000	0.000	0.000	0.000	0.000	0.000	0.000	0.000	0.000	0.000
Ni	0.000	0.000	0.000	0.000	0.000	0.000	0.000	0.000	0.000	0.000	0.000
Sum A	1.000	1.000	1.000	1.000	1.000	1.000	1.000	0.999	1.000	0.999	1.000
B-position											
Si	0.001	0.002	0.000	0.001	0.001	0.001	0.000	0.001	0.003	0.002	0.001
Ti	0.001	0.001	0.002	0.005	0.001	0.000	0.000	0.001	0.001	0.000	0.000
Al	0.001	0.001	0.000	0.000	0.000	0.001	0.000	0.003	0.002	0.000	0.000
Cr	0.000	0.000	0.004	0.005	0.002	0.002	0.001	0.001	0.001	0.000	0.000
Fe ³⁺	1.996	1.995	1.993	1.986	1.995	1.995	1.999	1.994	1.993	1.997	1.998
Suml B	2.000	1.999	1.999	1.997	1.999	2.000	2.000	2.000	1.999	2.000	1.999
A+B	3.000	2.999	2.999	2.998	2.999	3.000	3.000	2.999	2.999	2.999	3.000

Table A.2.6b: Representative analyses of ilmenite.

Rock type Sample	Two-mica granitoid									Mega feldspar granitoid					
	NO-30 1-ilm2	NO-30 1-ilm3	NO-30 1-ilm3	NO-30 4-ilm1	NO-30 4-ilm2	NO-30 4-ilm3	NO-30 4-ilm4	BAN-6 1-ilm4	BAN-6 2-ilm2	KO-12 1-ilm3	KO-12 1-ilm3	KO-12 1-ilm4	KO 12 2-ilm2	KO 12 2-ilm3	KO 12 2-ilm3
<i>Component oxydes (wt %)</i>															
SiO ₂	0.00	0.00	0.02	0.03	0.04	0.04	0.02	0.00	0.05	0.06	0.05	0.03	0.05	0.00	0.00
TiO ₂	45.69	46.20	45.89	46.18	35.19	48.70	48.77	40.39	37.83	44.38	43.00	43.63	43.89	42.97	42.15
Al ₂ O ₃	0.01	0.04	0.02	0.02	0.05	0.00	0.01	0.02	0.07	0.01	0.05	0.00	0.01	0.00	0.05
Cr ₂ O ₃	0.00	0.00	0.00	0.00	0.00	0.00	0.00	0.00	0.00	0.00	0.00	0.00	0.00	0.00	0.00
Fe ₂ O ₃	0.12	0.12	0.12	0.11	0.34	0.08	0.08	0.22	0.30	0.18	0.17	0.19	0.18	0.20	0.21
MgO	0.04	0.02	0.00	0.04	3.46	0.03	0.00	0.00	0.03	0.10	0.17	0.03	0.07	0.03	0.05
MnO	0.00	0.00	0.00	0.00	0.00	0.00	0.00	0.00	0.00	0.01	0.00	0.03	0.00	0.00	0.04
FeO	3.38	3.29	3.36	3.00	9.29	2.17	2.14	5.92	8.08	4.90	4.74	5.18	4.93	5.47	5.69
Total	49.24	49.66	49.43	49.38	48.36	51.03	51.01	46.54	46.36	49.63	48.19	49.08	49.13	48.68	48.18
<i>Mineral structural formulas (a.p.f.u.) based on 6 Oxygens</i>															
A-Position															
Si	0.000	0.000	0.002	0.002	0.004	0.003	0.002	0.000	0.005	0.005	0.005	0.002	0.004	0.000	0.000
Ti	2.873	2.877	2.873	2.884	2.391	2.919	2.923	2.763	2.656	2.807	2.800	2.801	2.807	2.790	2.773
Al	0.001	0.004	0.002	0.002	0.005	0.000	0.000	0.002	0.007	0.001	0.005	0.000	0.001	0.000	0.005
Cr	0.000	0.000	0.000	0.000	0.000	0.000	0.000	0.000	0.000	0.000	0.000	0.000	0.000	0.000	0.000
Fe ³⁺	0.010	0.010	0.010	0.010	0.020	0.000	0.000	0.010	0.020	0.010	0.010	0.010	0.010	0.010	0.010
Sum A	2.882	2.888	2.885	2.896	2.423	2.927	2.930	2.779	2.689	2.824	2.822	2.816	2.824	2.804	2.792
B-Position															
Mg	0.005	0.002	0.000	0.005	0.465	0.003	0.000	0.000	0.005	0.013	0.022	0.003	0.009	0.004	0.006
Mn	0.000	0.000	0.000	0.000	0.000	0.000	0.000	0.000	0.000	0.000	0.000	0.002	0.000	0.000	0.003
Fe ²⁺	0.236	0.228	0.234	0.208	0.702	0.144	0.143	0.450	0.631	0.345	0.343	0.370	0.351	0.395	0.416
Sum B	0.241	0.230	0.235	0.213	1.167	0.148	0.143	0.450	0.636	0.358	0.365	0.375	0.359	0.399	0.426
A + B	3.123	3.118	3.120	3.109	3.591	3.075	3.073	3.229	3.325	3.182	3.187	3.191	3.183	3.203	3.218
Ilmenite	98.03	94.46	99.88	88.72	99.76	98.37	99.24	99.57	980.24	97.20	95.82	98.29	97.40	98.90	98.26
Pyrophanite	0.00	0.00	0.00	0.00	0.00	0.18	0.00	0.00	0.00	0.13	0.08	0.54	0.00	0.07	0.69
Geikielite	1.96	0.86	0.21	2.27	0.86	2.33	0.00	0.00	0.72	3.61	5.97	0.85	2.40	1.06	1.50

A.3 Whole-rock geochemistry

Table A.3.1: Major and trace element data – X-ray fluorescence (XRF) analyses (continued).

Rock type	Biotite granitoid								
Sample	BD-2	BD-1	BAD-13	BAPI-14	NKj-1	BAN-5	TA-7	SAN-1	NG-7
<i>Major elements (wt %)</i>									
SiO ₂	69.03	71.59	70.99	66.25	70.78	69.93	74.6	68.16	73.11
TiO ₂	0.36	0.32	0.28	0.62	0.30	0.44	0.18	0.50	0.12
Al ₂ O ₃	15.34	14.36	14.6	15.95	15.15	14.57	13.21	14.74	14.33
Fe ₂ O ₃	2.21	1.61	1.8	2.5	1.98	2.66	1.88	2.57	0.88
MnO	0.04	0.02	0.04	0.03	0.04	0.06	0.08	0.04	0.02
MgO	0.7	0.29	0.37	0.49	0.58	0.58	0.28	0.75	0.19
CaO	1.7	0.82	1.31	1.47	1.59	1.65	1.34	1.83	0.99
Na ₂ O	4.04	3.28	3.49	3.68	4.01	3.67	4.17	3.27	3.61
K ₂ O	4.95	6.41	5.92	6.7	4.96	5.26	2.92	6.03	5.08
P ₂ O ₅	0.11	0.07	0.09	0.2	0.1	0.12	0.02	0.16	0.02
S	b.d.l.	b.d.l.	b.d.l.	b.d.l.	b.d.l.	b.d.l.	b.d.l.	b.d.l.	b.d.l.
LOI (1000°C)	0.53	0.51	0.44	0.49	0.41	0.34	0.37	0.41	0.5
Total	99.01	99.28	99.33	98.38	99.49	99.28	99.05	98.46	98.85
<i>Trace elements (ppm)</i>									
Sc	b.d.l.	b.d.l.	b.d.l.	b.d.l.	b.d.l.	b.d.l.	b.d.l.	b.d.l.	b.d.l.
V	32	21	21	36	22	30	13	38	12
Cr	21	16	b.d.l.	b.d.l.	19	11	21	17	13
Co	39	38	23	18	30	24	37	44	52
Ni	b.d.l.	b.d.l.	b.d.l.	b.d.l.	b.d.l.	b.d.l.	b.d.l.	b.d.l.	b.d.l.
Zn	57	39	52	78	46	51	68	72	21
Ga	30	29	16	28	32	20	19	24	29
Rb	212	263	242	271	212	154	160	182	180
Sr	506	684	289	1001	427	189	193	1162	287
Y	16	29	18	17	13	45	30	21	14
Zr	197	294	252	487	182	227	127	345	110
Nb	11	13	11	8	10	17	12	15	8
Mo	b.d.l.	b.d.l.	b.d.l.	b.d.l.	b.d.l.	b.d.l.	b.d.l.	b.d.l.	b.d.l.
Sn	b.d.l.	b.d.l.	b.d.l.	b.d.l.	b.d.l.	b.d.l.	b.d.l.	b.d.l.	b.d.l.
Ba	1386	2324	1067	2820	1195	761	920	2993	1349
Pb	42	47	45	40	50	22	35	49	53
Th	24	70	57	41	26	22	b.d.l.	39	17
U	8	10	b.d.l.	b.d.l.	9	b.d.l.	b.d.l.	b.d.l.	b.d.l.
<i>CIPW norm</i>									
Quartz	22.21	25.99	24.93	15.89	24.48	24.39	35.94	21.54	30.32
Corundum	0.51	0.70	0.28	0.45	0.53	0.13	0.80	0.00	1.14
Orthoclase	29.25	37.88	34.98	39.59	29.31	31.08	17.26	35.64	30.02
Albite	34.19	27.75	29.53	31.14	33.93	31.05	35.29	27.67	30.55
Anorthite	7.72	3.61	5.91	5.99	7.24	7.40	6.52	7.73	4.78
Diopside	0.00	0.00	0.00	0.00	0.00	0.00	0.00	0.00	0.00
Hypersthene	1.74	0.72	0.92	1.22	1.44	1.44	0.70	1.87	0.47
Ilmenite	0.09	0.04	0.09	0.06	0.09	0.13	0.17	0.09	0.04
Apatite	0.25	0.16	0.21	0.46	0.23	0.28	0.05	0.37	0.05
Hematite	2.21	1.61	1.80	2.50	1.98	2.66	1.88	2.57	0.88
Titanite	0.00	0.00	0.00	0.00	0.00	0.00	0.00-	0.21	0.00
Rutile	0.31	0.30	0.23	0.59	0.25	0.37	0.09	0.37	0.10
Total	98.48	98.77	98.89	97.89	99.49	98.94	98.68	97.84	98.35
Solidification Index	13.18	6.77	10.46	10.24	12.68	12.46	13.00	13.36	9.38
Differentiation Index	85.65	91.62	89.44	86.62	87.73	86.53	88.48	84.84	90.89
Color Index	4.04	2.38	2.81	3.78	3.51	4.23	2.75	4.52	1.40
Agpaitic Index	0.78	0.86	0.83	0.83	0.79	0.81	0.76	0.81	0.80
Mg#	71.51	58.80	61.96	60.83	69.89	63.34	54.13	69.81	63.11

Table A.3.1: Major and trace element data (continued).

* Sample containing amphibole minerals; Mg# = 100Mg/(Mg + Fe)

Rock type	Biotite granitoid								
Sample	BJD-33	SE-1	SE-2	SE-5	PA-1	PA-2	TEN-31	TJ-2	BL-13*
<i>Major elements (wt %)</i>									
SiO ₂	68.84	73.39	72.62	69.56	69.58	73.82	73.08	71.32	66.6
TiO ₂	0.54	0.19	0.22	0.57	0.51	0.17	0.13	0.29	0.64
Al ₂ O ₃	15.19	13.77	13.95	15.2	14.71	13.44	14.12	14.51	14.34
Fe ₂ O ₃	2.65	1.25	1.71	2.57	2.7	1.16	1.1	1.57	3.66
MnO	0.04	0.03	0.02	0.03	0.03	0.02	0.03	0.02	0.09
MgO	0.74	0.28	0.31	0.73	0.71	0.23	0.31	0.22	1.24
CaO	1.73	0.93	1.23	1.6	1.44	1.01	1.36	0.89	2.33
Na ₂ O	3.91	3.59	3.57	3.99	3.2	3.61	3.12	3.18	2.88
K ₂ O	5.26	5.53	5.26	5.47	6.06	5.12	5.52	6.95	6.49
P ₂ O ₅	0.16	0.04	0.04	0.17	0.21	0.03	0.09	0.03	0.26
S	b.d.l.	b.d.l.	b.d.l.	b.d.l.	b.d.l.	b.d.l.	b.d.l.	b.d.l.	b.d.l.
LOI (1000°C)	0.3	0.32	0.43	0.27	0.57	0.37	0.36	0.24	0.4
Total	99.36	99.32	99.36	100.16	99.72	98.98	99.22	99.22	98.88
<i>Trace elements (ppm)</i>									
Sc	b.d.l.	b.d.l.	b.d.l.	b.d.l.	13	b.d.l.	b.d.l.	b.d.l.	b.d.l.
V	46	23	14	43	43	13	16	14	51
Cr	17	12	b.d.l.	15	15	17	14	b.d.l.	16
Co	19	38	51	34	37	47	34	34	22
Ni	7	b.d.l.	6						
Zn	70	25	37	82	62	21	25	20	71
Ga	20	15	22	29	21	16	22	16	23
Rb	206	219	194	209	212	167	170	225	181
Sr	387	310	171	425	293	124	275	175	527
Y	20	20	20	18	17	11	b.d.l.	70	41
Zr	373	135	221	372	354	126	115	254	351
Nb	14	15	12	13	15	6	b.d.l.	16	27
Mo	b.d.l.	12	b.d.l.						
Sn	b.d.l.	b.d.l.	b.d.l.	b.d.l.	b.d.l.	b.d.l.	b.d.l.	b.d.l.	b.d.l.
Ba	1333	881	537	1501	1302	451	774	351	1953
Pb	36	43	42	45	34	31	37	47	23
Th	21	35	38	15	76	39	10	18	28
U	b.d.l.	7	b.d.l.	b.d.l.	5	11	b.d.l.	b.d.l.	b.d.l.
<i>CIPW norm</i>									
Quartz	21.61	29.05	28.74	21.38	24.22	30.80	30.68	24.07	19.51
Corundum	0.30	0.28	0.24	0.21	0.77	0.19	0.75	0.21	0.00
Orthoclase	31.08	32.68	31.08	32.33	35.81	30.26	32.62	41.07	38.35
Albite	33.09	30.38	30.21	33.76	27.08	30.55	26.40	26.91	24.37
Anorthite	7.54	4.35	5.84	6.83	5.77	4.81	6.16	4.22	7.03
Diopside	0.00	0.00	0.00	0.00	0.00	0.00	0.00	0.00	0.74
Hypersthene	1.84	0.70	0.77	1.82	1.77	0.57	0.77	0.55	2.74
Ilmenite	0.09	0.06	0.04	0.06	0.06	0.04	0.06	0.04	0.19
Apatite	0.37	0.09	0.09	0.39	0.49	0.07	0.21	0.07	0.60
Hematite	2.65	1.25	1.71	2.57	2.70	1.16	1.10	1.57	3.66
Titanite	0.00	0.00	0.00	0.00	0.00	0.00	0.00	0.00	1.32
Rutile	0.49	0.16	0.20	0.54	0.48	0.15	0.10	0.27	0.00
Total	99.06	99.00	98.93	99.89	99.15	98.61	98.86	98.98	98.53
Solidification Index	12.77	8.23	10.45	11.74	10.75	9.27	12.25	7.07	15.17
Differentiation Index	85.78	92.10	90.03	87.47	87.11	91.61	89.71	92.05	82.24
Color Index	4.58	2.01	2.52	4.45	4.53	1.78	1.94	2.16	7.34
Agpaitic Index	0.80	0.86	0.83	0.82	0.80	0.85	0.79	0.88	0.82
Mg#	68.87	63.96	58.96	69.24	67.57	61.11	69.07	52.62	72.86

Table A.3.1: Major and trace element data (continued).

* Sample containing amphibole minerals

Rock type	Biotite granitoid								
Sample	BL-8*	BG-1*	BL-4*	BL-9*	BL-5*	TE-2*	TE-1*	LE-2*	NG-2a*
Major elements (wt %)									
SiO ₂	69.08	67.09	62.15	60.58	56.91	66.6	60.06	62.82	72.52
TiO ₂	0.53	0.56	0.91	1.41	1.48	0.65	1.48	0.8	0.25
Al ₂ O ₃	14.79	15.24	15.44	12.02	17.61	15.53	15.17	16.18	14.11
Fe ₂ O ₃	3.09	3.41	5.33	6.45	6.77	3.32	6.9	5.01	1.9
MnO	0.07	0.06	0.13	0.16	0.08	0.06	0.09	0.07	0.04
MgO	0.75	0.91	1.71	3.97	1.72	1.02	2.27	1.69	0.57
CaO	1.91	2.23	3.25	4.59	4.79	2.13	3.81	3.64	1.51
Na ₂ O	3.65	4.00	3.46	1.25	4.92	3.91	3.43	4.52	3.95
K ₂ O	5.13	5.26	5.4	6.86	3.54	5.28	4.42	3.66	4.36
P ₂ O ₅	0.15	0.19	0.39	0.87	0.62	0.2	0.69	0.31	0.04
S	b.d.l.	b.d.l.	b.d.l.	b.d.l.	b.d.l.	b.d.l.	b.d.l.	b.d.l.	b.d.l.
LOI (1000°C)	0.33	0.37	0.54	0.66	0.48	0.51	0.6	0.47	0.49
Total	99.48	99.32	98.71	98.82	98.92	99.21	98.92	99.18	99.74
Trace elements (ppm)									
Sc	b.d.l.	b.d.l.	15	23	b.d.l.	b.d.l.	22	b.d.l.	11
V	36	51	76	122	124	54	85	89	27
Cr	17	15	21	108	18	22	55	15	19
Co	33	32	25	29	28	19	23	41	55
Ni	b.d.l.	b.d.l.	8	38	8	b.d.l.	22	b.d.l.	b.d.l.
Zn	54	56	120	151	118	66	143	89	47
Ga	17	22	23	25	24	20	23	32	23
Rb	168	160	377	230	195	169	203	120	170
Sr	221	244	1500	559	1097	538	637	798	559
Y	56	54	49	32	15	51	35	20	11
Zr	265	269	524	336	278	307	656	421	94
Nb	23	20	36	25	18	28	41	15	12
Mo	b.d.l.	b.d.l.	b.d.l.	b.d.l.	b.d.l.	b.d.l.	b.d.l.	b.d.l.	b.d.l.
Sn	b.d.l.	b.d.l.	b.d.l.	b.d.l.	b.d.l.	b.d.l.	b.d.l.	b.d.l.	b.d.l.
Ba	872	931	3441	2247	1651	1214	1740	1224	1179
Pb	27	28	24	23	20	35	44	31	49
Th	21	24	26	22	7	24	44	5	5
U	b.d.l.	7	b.d.l.	b.d.l.	b.d.l.	b.d.l.	b.d.l.	6	b.d.l.
CIPW norm									
Quartz	23.43	18.47	13.58	15.95	4.57	18.14	13.90	13.72	28.89
Corundum	0.12	0.00	0.00	0.00	0.00	0.00	0.00	0.00	0.24
Orthoclase	30.32	31.08	31.91	40.54	20.92	31.20	26.12	21.63	25.77
Albite	30.89	33.85	29.28	10.58	41.63	33.09	29.02	38.25	33.42
Anorthite	8.50	8.09	10.65	6.93	15.51	9.23	12.94	13.05	7.23
Diopside	0.00	0.01	0.21	4.59	0.00	0.00	0.00	0.37	0.00
Hypersthene	1.87	2.26	4.16	7.77	4.28	2.54	5.65	4.04	1.42
Ilmenite	0.15	0.13	0.28	0.34	0.17	0.13	0.19	0.15	0.09
Apatite	0.35	0.44	0.90	2.02	1.44	0.46	1.60	0.72	0.09
Hematite	3.09	3.41	5.33	6.45	6.77	3.32	6.90	5.01	1.90
Titanite	0.00	1.21	1.87	3.02	2.96	0.02	1.03	1.77	0.00
Rutile	0.45	0.00	0.00	0.00	0.18	0.57	0.96	0.00	0.20
Total	99.15	98.95	98.17	98.17	98.44	98.70	98.32	98.70	99.25
Solidification Index	13.86	14.97	18.64	23.97	23.93	14.55	20.53	21.63	12.88
Differentiation Index	84.63	83.40	74.77	67.07	67.12	82.42	69.05	73.60	88.07
Color Index	5.11	5.81	9.98	19.15	11.23	5.99	12.75	9.57	3.41
Agpaitic Index	0.78	0.81	0.75	0.79	0.68	0.78	0.69	0.70	0.80
Mg#	65.79	67.89	71.77	82.99	66.81	70.88	72.28	72.77	70.39

Table A.3.1: Major and trace element data (continued).

* Sample containing amphibole minerals

Rock type Sample	Biotite granite		Deformed biotite granite					
	NO-1*	NG-3a*	BFS-1	BNF-14	BNF-7	BAS-25	BAS-26	BAS-27
<i>Major elements (wt %)</i>								
SiO ₂	65.87	68.42	71.94	70.92	73.09	72.12	71.75	68.98
TiO ₂	0.43	0.37	0.21	0.36	0.07	0.29	0.30	0.45
Al ₂ O ₃	14.89	14.78	14.72	14.3	13.72	14.00	14.24	14.74
Fe ₂ O ₃	4.28	3.17	1.40	2.27	0.85	1.85	1.95	2.66
MnO	0.19	0.09	0.03	0.02	0.01	0.04	0.04	0.06
MgO	2.05	1.26	0.33	0.57	0.10	0.44	0.55	0.79
CaO	4.51	2.40	1.30	1.45	0.84	1.33	1.46	1.72
Na ₂ O	4.58	3.90	4.18	2.81	2.56	3.72	3.67	3.58
K ₂ O	1.73	4.07	4.69	5.78	7.32	5.02	4.99	5.35
P ₂ O ₅	0.09	0.29	0.05	0.13	0.08	0.08	0.10	0.15
S	0.11	b.d.l.	b.d.l.	b.d.l.	b.d.l.	b.d.l.	b.d.l.	b.d.l.
LOI (1000°C)	0.78	0.52	0.36	0.49	0.32	0.34	0.54	0.56
Total	99.51	99.17	99.21	99.1	98.96	99.23	99.59	99.04
<i>Trace elements (ppm)</i>								
Sc	16	b.d.l.	b.d.l.	b.d.l.	b.d.l.	b.d.l.	b.d.l.	b.d.l.
V	75	14	18	24	19	24	26	39
Cr	48	12	28	15	14	12	19	19
Co	30	36	51	17	17	31	29	29
Ni	13	b.d.l.	b.d.l.	b.d.l.	b.d.l.	b.d.l.	b.d.l.	6
Zn	77	58	42	48	8	60	55	82
Ga	20	22	25	22	14	29	27	35
Rb	65	305	171	165	223	197	228	235
Sr	197	117	340	304	334	762	728	820
Y	114	14	11	20	13	20	16	24
Zr	61	130	136	235	53	211	208	298
Nb	29	15	11	15	b.d.l.	14	15	19
Mo	b.d.l.	b.d.l.	b.d.l.	b.d.l.	b.d.l.	b.d.l.	b.d.l.	b.d.l.
Sn	b.d.l.	b.d.l.	b.d.l.	b.d.l.	b.d.l.	b.d.l.	b.d.l.	b.d.l.
Ba	182	632	1285	1358	1327	1652	1601	1904
Pb	15	45	39	41	34	40	46	37
Th	13	31	13	41	b.d.l.	54	39	48
U	b.d.l.	9	b.d.l.	b.d.l.	b.d.l.	b.d.l.	b.d.l.	b.d.l.
<i>CIPW norm</i>								
Quartz	21.62	23.96	26.54	28.86	28.46	27.99	27.64	23.24
Corundum	0.00	0.29	0.52	1.10	0.25	0.22	0.39	0.29
Orthoclase	10.22	24.05	27.72	34.16	43.26	29.67	29.49	31.62
Albite	38.75	33.00	35.37	23.78	21.66	31.48	31.05	30.29
Anorthite	14.96	10.01	6.12	6.34	3.65	6.08	6.59	7.55
Diopside	4.74	0.00	0.00	0.00	0.00	0.00	0.00	0.00
Hypersthene	2.91	3.14	0.82	1.42	0.25	1.10	1.37	1.97
Ilmenite	0.41	0.19	0.06	0.04	0.02	0.09	0.09	0.13
Apatite	0.21	0.67	0.12	0.30	0.19	0.19	0.23	0.35
Hematite	4.28	3.17	1.40	2.27	0.85	1.85	1.95	2.66
Titanite	0.53	0.00	0.00	0.00	0.00	0.00	0.00	0.00
Rutile	0.00	0.27	0.18	0.34	0.06	0.24	0.25	0.38
Total	98.63	98.75	98.85	98.61	98.64	98.89	99.05	98.48
Solidification Index	29.87	17.73	11.24	11.78	7.26	11.16	12.10	12.92
Differentiation Index	70.59	81.01	89.63	86.80	93.38	89.13	88.18	85.15
Color Index	12.34	6.50	2.29	3.73	1.12	3.03	3.41	4.76
Agpaitic Index	0.63	0.73	0.81	0.76	0.88	0.83	0.80	0.79
Mg#	79.15	75.90	65.13	66.55	48.25	65.33	69.09	70.18

Table A.3.1: Major and trace element data (continued).

* Sample containing amphibole minerals

Rock type	Deformed biotite granite								
Sample	MD-1	ND-1	LE-1	NG-1a	NO-28*	BNF-24*	BA-31*	TK-3*	TK-2*
<i>Major elements (wt %)</i>									
SiO ₂	70.49	73.55	60.29	62.4	54.49	58.24	64.97	66.6	58.07
TiO ₂	0.32	0.22	1.48	1.35	1.09	1.96	0.59	0.53	1.31
Al ₂ O ₃	14.7	14.00	15.2	15.16	21.12	15.5	16.29	15.93	15.37
Fe ₂ O ₃	2.04	1.46	6.67	6.12	5.44	7.79	3.92	3.57	8.75
MnO	0.06	0.03	0.08	0.08	0.06	0.11	0.08	0.08	0.20
MgO	0.48	0.30	2.08	1.91	1.94	2.66	1.32	1.24	3.14
CaO	1.50	0.95	3.52	3.32	5.46	4.85	3.15	2.98	4.60
Na ₂ O	4.05	3.68	3.63	3.42	5.55	3.55	4.12	4.19	4.08
K ₂ O	5.20	5.47	4.43	4.71	2.27	2.85	4.00	4.01	2.51
P ₂ O ₅	0.08	0.06	0.71	0.64	0.34	0.90	0.20	0.18	0.43
S	b.d.l.	b.d.l.	b.d.l.	b.d.l.	0.36	b.d.l.	b.d.l.	b.d.l.	b.d.l.
LOI (1000°C)	0.43	0.33	0.51	0.51	1.26	0.67	0.46	0.53	0.65
Total	99.35	100.5	98.6	99.62	99.38	99.08	99.1	99.84	99.11
<i>Trace elements (ppm)</i>									
Sc	b.d.l.	14	20	15	b.d.l.	16	b.d.l.	11	30
V	22	18	81	82	98	162	69	58	146
Cr	12	15	50	39	18	24	15	13	27
Co	26	26	19	32	33	28	25	34	31
Ni	b.d.l.	b.d.l.	20	17	17	16	6	5	10
Zn	49	31	137	126	67	142	108	58	147
Ga	17	30	34	25	26	25	23	22	22
Rb	188	233	232	253	168	222	122	138	149
Sr	174	371	594	557	873	590	485	387	354
Y	53	15	35	33	43	28	37	24	53
Zr	184	187	688	633	825	319	220	208	441
Nb	19	11	45	43	40	29	14	13	24
Mo	b.d.l.	b.d.l.	b.d.l.	b.d.l.	6	b.d.l.	b.d.l.	b.d.l.	b.d.l.
Sn	b.d.l.	b.d.l.	b.d.l.	b.d.l.	b.d.l.	b.d.l.	b.d.l.	16	18
Ba	587	964	1735	1555	490	915	1099	958	372
Pb	38	42	36	44	27	13	20	33	22
Th	37	43	49	49	29	22	10	19	21
U	7	b.d.l.	b.d.l.	b.d.l.	8	b.d.l.	b.d.l.	8	b.d.l.
<i>CIPW norm</i>									
Quartz	23.40	28.90	13.74	16.37	0.00	14.92	17.58	19.33	12.23
Corundum	0.00	0.44	0.00	0.00	0.42	0.00	0.00	0.00	0.00
Orthoclase	30.73	32.33	26.18	27.83	13.41	16.84	23.64	23.70	14.83
Albite	34.27	31.14	30.72	28.94	46.96	30.04	34.86	35.45	34.52
Anorthite	6.57	4.32	12.10	12.10	24.87	17.94	14.14	12.81	16.21
Diopside	0.00	0.00	0.00	0.00	0.00	0.00	0.00	0.00	0.02
Hypersthene	1.20	0.75	5.18	4.76	4.45	6.63	3.29	3.09	7.81
Ilmenite	0.13	0.06	0.17	0.17	0.13	0.24	0.17	0.17	0.43
Apatite	0.19	0.14	1.65	1.48	0.79	2.09	0.46	0.42	1.00
Hematite	2.04	1.46	6.67	6.12	5.44	7.79	3.92	3.57	8.75
Titanite	0.24		0.52	0.13	0.00	0.17	0.13	0.56	2.66
Rutile	0.15	0.19	1.18	1.21	1.02	1.77	0.45	0.21	0.00
Total	98.92	99.72	98.09	99.11	97.50	98.41	98.64	99.31	98.46
Solidification Index	11.73	8.22	19.29	18.90	29.17	25.47	20.74	20.20	23.07
Differentiation Index	88.40	92.36	70.63	73.14	60.38	61.80	76.08	78.48	61.58
Color Index	3.36	2.27	12.02	11.05	10.29	14.65	7.38	6.83	17.01
Agpaitic Index	0.84	0.86	0.71	0.71	0.55	0.58	0.68	0.71	0.61
Mg#	65.09	61.95	71.19	71.21	73.86	73.02	72.74	73.35	73.98

Table A.3.1: Major and trace element data (continued).

* Sample containing amphibole minerals

Rock type	Deformed biotite granitoid								
Sample	BFS-4	NG-1	NG-3	BNF-8	BNF-3	BNF-6	BNF-10	BFS-7	BNF-4
<i>Major elements (wt %)</i>									
SiO ₂	63.92	63.10	62.79	68.21	63.41	72.14	64.33	61.03	58.48
TiO ₂	0.80	0.85	0.86	0.36	0.40	0.33	0.61	0.72	1.31
Al ₂ O ₃	14.56	14.66	14.44	15.06	17.49	13.74	15.39	16.60	14.42
Fe ₂ O ₃	4.85	5.00	5.52	3.51	4.14	2.34	5.53	5.79	10.46
MnO	0.09	0.10	0.11	0.06	0.08	0.03	0.09	0.10	0.14
MgO	1.86	1.91	1.99	1.30	0.48	0.39	1.99	2.41	1.11
CaO	3.05	3.44	3.61	2.81	2.11	1.16	3.70	4.59	3.94
Na ₂ O	3.54	3.66	3.72	3.22	5.13	3.63	3.60	4.71	3.79
K ₂ O	4.70	5.17	4.77	3.84	5.80	5.19	2.75	2.57	3.75
P ₂ O ₅	0.39	0.39	0.39	0.12	0.09	0.06	0.23	0.23	0.54
S	b.d.l.	b.d.l.	b.d.l.	b.d.l.	b.d.l.	b.d.l.	b.d.l.	b.d.l.	0.43
LOI (1000°C)	0.57	0.34	0.61	0.68	0.56	0.39	0.57	0.59	0.66
Total	98.33	98.62	98.81	99.17	99.69	99.4	98.79	99.34	99.03
<i>Trace elements (ppm)</i>									
Sc	13	24	18	b.d.l.	b.d.l.	b.d.l.	b.d.l.	b.d.l.	14
V	77	78	85	46	21	12	72	115	33
Cr	37	34	35	29	11	11	34	24	17
Co	20	33	25	22	30	34	34	29	26
Ni	15	23	13	6	b.d.l.	b.d.l.	21	10	b.d.l.
Zn	103	102	109	72	65	40	89	75	113
Ga	18	29	24	27	27	18	20	23	24
Rb	168	137	134	131	73	87	136	101	79
Sr	1414	1531	1525	393	187	150	730	605	315
Y	35	41	42	13	4	24	28	20	69
Zr	403	411	438	105	354	388	233	179	703
Nb	21	26	28	9	40	24	14	9	48
Mo	b.d.l.	b.d.l.	6	b.d.l.	9	b.d.l.	b.d.l.	b.d.l.	7
Sn	b.d.l.	b.d.l.	b.d.l.	b.d.l.	b.d.l.	b.d.l.	b.d.l.	b.d.l.	b.d.l.
Ba	2983	3229	2944	1082	761	631	2095	941	1517
Pb	31	45	48	25	19	15	24	27	10
Th	17	23	25	6	7	29	12	15	9
U	b.d.l.	6	b.d.l.						
<i>CIPW norm</i>									
Quartz	17.70	14.25	14.75	27.16	6.89	28.26	22.62	12.03	14.54
Corundum	0.00	0.00	0.00	0.78	0.00	0.18	0.31	0.00	0.00
Orthoclase	27.78	30.55	28.19	22.69	34.28	30.67	16.25	15.19	22.16
Albite	29.95	30.97	31.48	27.25	43.41	30.72	30.46	39.85	32.07
Anorthite	9.96	8.30	8.61	13.16	7.57	5.36	16.85	16.56	11.26
Diopside	0.15	2.85	3.26	0.00	0.96	0.00	0.00	2.02	0.59
Hypersthene	4.56	3.44	3.45	3.24	0.75	0.97	4.96	5.07	2.49
Ilmenite	0.19	0.21	0.24	0.13	0.17	0.06	0.19	0.21	0.30
Apatite	0.90	0.90	0.90	0.28	0.21	0.14	0.53	0.53	1.25
Hematite									
Titanite	1.71	1.81	1.81	0.00	0.76	0.00	0.00	1.49	2.83
Rutile	0.00	0.00	0.00	0.29	0.00	0.30	0.51	0.00	0.00
Total	92.91	93.29	92.69	94.98	94.99	96.67	92.69	92.97	87.48
Solidification Index	18.90	19.92	20.49	21.00	12.28	9.42	23.75	25.99	17.96
Differentiation Index	75.43	75.77	74.42	77.10	84.57	89.65	69.33	67.08	68.77
Color Index	9.76	11.50	12.47	6.88	6.02	3.38	10.68	13.09	13.84
Agpaitic Index	0.75	0.79	0.78	0.63	0.84	0.84	0.58	0.63	0.71
Mg#	75.24	75.17	74.07	74.59	47.88	56.91	74.04	76.74	45.68

Table A.3.1: Major and trace element data (continued).

* Sample containing amphibole minerals

Rock type Sample	Deformed biotite granitoid		Mega feldspar granitoid					
	ND-2*	NN-1*	BM-1	HO-1	KE-1	DML-1a	DML-2	KO-12
<i>Major elements (wt %)</i>								
SiO ₂	65.34	62.71	70.42	72.5	71.27	73.81	71.1	70.68
TiO ₂	0.68	0.68	0.32	0.34	0.35	0.29	0.4	0.27
Al ₂ O ₃	14.27	16.76	15.04	13.72	14.17	12.81	13.97	15.05
Fe ₂ O ₃	4.21	4.56	1.97	2.50	2.62	2.28	3.25	2.00
MnO	0.09	0.06	0.03	0.03	0.04	0.03	0.04	0.04
MgO	1.51	1.29	0.58	0.39	0.41	0.31	0.38	0.47
CaO	2.78	3.12	1.51	1.55	1.47	1.21	1.39	1.95
Na ₂ O	3.65	3.54	3.78	3.04	3.14	2.78	3.02	3.92
K ₂ O	5.11	5.67	4.90	4.93	5.11	5.24	5.37	4.11
P ₂ O ₅	0.32	0.24	0.11	0.10	0.11	0.07	0.12	0.11
S	b.d.l.	b.d.l.	b.d.l.	b.d.l.	b.d.l.	b.d.l.	b.d.l.	b.d.l.
LOI (1000°C)	0.35	0.47	0.48	0.27	0.47	0.35	0.41	0.47
Total	98.31	99.1	99.14	99.37	99.16	99.18	99.45	99.07
<i>Trace elements (ppm)</i>								
Sc	b.d.l.	15	b.d.l.	b.d.l.	b.d.l.	b.d.l.	b.d.l.	b.d.l.
V	64	61	29	19	18	11	20	17
Cr	26	16	12	15	20	13	13	16
Co	30	28	32	25	20	36	28	20
Ni	13	6	b.d.l.	b.d.l.	b.d.l.	b.d.l.	5	7
Zn	91	65	52	62	73	47	68	64
Ga	29	26	22	24	27	24	26	25
Rb	172	199	211	179	204	192	204	200
Sr	1295	529	428	196	169	143	156	222
Y	34	28	15	16	16	17	18	23
Zr	360	505	178	221	211	209	268	168
Nb	21	24	12	14	15	17	16	13
Mo	b.d.l.	b.d.l.	b.d.l.	b.d.l.	b.d.l.	b.d.l.	b.d.l.	b.d.l.
Sn	b.d.l.	b.d.l.	b.d.l.	b.d.l.	b.d.l.	b.d.l.	b.d.l.	b.d.l.
Ba	2765	1455	1171	731	756	477	622	621
Pb	50	49	41	29	32	27	26	38
Th	32	26	19	23	24	27	25	22
U	9	b.d.l.	b.d.l.	b.d.l.	b.d.l.	b.d.l.	b.d.l.	b.d.l.
<i>CIPW norm</i>								
Quartz	18.16	12.66	25.89	32.33	30.00	34.73	29.78	27.58
Corundum	0.00	0.00	1.04	0.80	1.06	0.53	0.95	0.87
Orthoclase	30.20	33.51	28.96	29.13	30.20	30.97	31.73	24.29
Albite	30.89	29.95	31.99	25.72	26.57	23.52	25.55	33.17
Anorthite	7.46	13.09	6.77	7.04	6.57	5.55	6.11	8.96
Diopside	1.74	0.00	0.00	0.00	0.00	0.00	0.00	0.00
Hypersthene	2.96	3.21	1.44	0.97	1.02	0.77	0.95	1.17
Ilmenite	0.19	0.13	0.06	0.06	0.09	0.06	0.09	0.09
Apatite	0.74	0.56	0.25	0.23	0.25	0.16	0.28	0.25
Hematite			1.97	2.50	2.62	2.28	3.25	2.00
Titanite	1.42	0.58	0.00	0.00	0.00	0.00	0.00	0.00
Rutile	0.00	0.38	0.29	0.31	0.30	0.26	0.35	0.22
Total	93.76	94.07	96.69	96.60	96.07	96.55	95.79	96.60
Solidification Index	17.65	18.47	12.42	12.90	11.91	10.51	10.67	16.28
Differentiation Index	79.25	76.13	86.83	87.19	86.77	89.22	87.06	85.04
Color Index	9.10	7.90	3.48	3.54	3.73	3.12	4.28	3.26
Agpaitic Index	0.81	0.71	0.77	0.75	0.75	0.80	0.77	0.72
Mg#	73.97	69.15	70.00	55.28	55.36	51.86	48.09	65.06

Table A.3.1: Major and trace element data (continued).

Rock type	Mega feldspar granitoid				
Sample	TS-1	TS-2	BN-1	BN-2	TE-6
<i>Major elements (wt %)</i>					
SiO ₂	71.65	72.94	69.32	70.4	73.74
TiO ₂	0.39	0.26	0.46	0.43	0.37
Al ₂ O ₃	14.10	13.57	15.08	14.37	12.45
Fe ₂ O ₃	2.34	2.05	2.52	2.48	3.07
MnO	0.04	0.03	0.04	0.04	0.05
MgO	0.54	0.31	0.61	0.61	0.83
CaO	1.40	1.46	1.57	1.55	1.86
Na ₂ O	3.30	3.59	3.34	3.36	3.38
K ₂ O	5.42	4.33	5.98	5.35	3.04
P ₂ O ₅	0.14	0.07	0.17	0.15	b.d.l.
S	b.d.l.	b.d.l.	b.d.l.	b.d.l.	b.d.l.
LOI (1000°C)	0.39	0.28	0.38	0.38	0.28
Total	99.71	98.89	99.47	99.14	99.07
<i>Trace elements (ppm)</i>					
Sc	b.d.l.	b.d.l.	b.d.l.	17	b.d.l.
V	26	20	38	32	50
Cr	12	12	15	13	28
Co	25	42	33	23	43
Ni	b.d.l.	b.d.l.	b.d.l.	b.d.l.	12
Zn	60	57	62	64	45
Ga	21	23	26	22	20
Rb	286	235	302	249	97
Sr	185	172	273	250	220
Y	19	12	14	13	20
Zr	246	160	230	248	270
Nb	21	22	17	15	8
Mo	b.d.l.	b.d.l.	b.d.l.	b.d.l.	b.d.l.
Sn	b.d.l.	b.d.l.	b.d.l.	17	b.d.l.
Ba	763	543	1049	880	929
Pb	38	46	36	36	23
Th	68	41	38	63	59
U	b.d.l.	10	b.d.l.	11	7
<i>CIPW norm</i>					
Quartz(Q)	28.30	32.09	23.21	26.57	37.22
Corundum(C)	0.59	0.49	0.66	0.59	0.22
Orthoclase(Or)	32.03	25.59	35.34	31.62	17.97
Albite(Ab)	27.92	30.38	28.26	28.43	28.60
Anorthite(An)	6.03	6.79	6.68	6.71	9.23
Diopside(Di)	0.00	0.00	0.00	0.00	0.00
Hypersthene(Hy)	1.35	0.77	1.52	1.52	2.07
Ilmenite(II)	0.09	0.06	0.09	0.09	0.11
Apatite(Ap)	0.32	0.16	0.39	0.35	0.00
Hematite(Hm)	2.34	2.05	2.52	2.48	3.07
Titanite(Tn)	0.00	0.00	0.00	0.00	0.00
Rutile(Ru)	0.34	0.23	0.41	0.38	0.31
Total	96.98	96.56	96.57	96.26	95.72
Solidification Index	11.24	12.77	11.71	12.17	16.39
Differentiation Index	88.26	88.06	86.81	86.62	83.79
Color Index	3.77	2.89	4.12	4.08	5.24
Agpaitic Index	0.80	0.78	0.79	0.79	0.71
Mg#	64.65	54.51	65.73	66.09	68.18

Table A.3.1: Major and trace element data (continued).

Rock type	Two-mica granitoid								
Sample	BM-3	BM-4	BM-5	BP-1	BAN-6	BF-1	BF-2	TA-9	NO-30
<i>Major elements (wt %)</i>									
SiO ₂	74.55	74.51	73.22	73.59	72.38	72.2	73.13	73.69	71.33
TiO ₂	0.07	0.06	0.11	0.18	0.21	0.25	0.21	0.18	0.31
Al ₂ O ₃	14.25	14.09	14.65	14.11	14.49	14.26	14.3	14.26	14.42
Fe ₂ O ₃ *	0.96	0.69	1.44	1.22	1.54	1.61	1.33	1.34	1.97
MnO	0.02	0.01	0.04	0.02	0.03	0.02	0.02	0.06	0.02
MgO	0.13	0.09	0.2	0.22	0.23	0.29	0.25	0.24	0.37
CaO	0.49	0.54	0.37	0.92	0.89	1.13	1.08	0.74	1.17
Na ₂ O	3.82	4.08	3.29	3.28	3.17	3.45	3.44	3.4	3.09
K ₂ O	4.52	4.56	5.2	5.42	5.51	5.35	5.15	4.56	5.88
P ₂ O ₅	0.03	0.03	0.04	0.07	0.15	0.08	0.06	0.1	0.14
S	b.d.l.	b.d.l.	b.d.l.	b.d.l.	b.d.l.	b.d.l.	b.d.l.	b.d.l.	b.d.l.
LOI (1000°C)	0.59	0.42	1.02	0.42	0.72	0.37	0.49	0.79	0.45
Total	99.43	99.08	99.58	99.45	99.32	99.01	99.46	99.36	99.15
<i>Trace elements (ppm)</i>									
Sc	b.d.l.	b.d.l.	b.d.l.	b.d.l.	b.d.l.	12	b.d.l.	b.d.l.	b.d.l.
V	b.d.l.	b.d.l.	14	14	13	12	15	12	19
Cr	26	16	b.d.l.	12	b.d.l.	14	13	13	13
Co	26	22	33	36	26	36	29	19	23
Ni	b.d.l.	b.d.l.	b.d.l.	b.d.l.	b.d.l.	b.d.l.	b.d.l.	b.d.l.	b.d.l.
Zn	14	10	41	58	80	74	63	62	64
Ga	31	26	34	22	27	27	24	35	20
Rb	283	264	334	305	353	335	305	470	318
Sr	46	55	48	117	113	126	135	97	126
Y	24	14	14	14	14	15	14	12	23
Zr	61	45	43	130	145	178	149	125	237
Nb	24	20	29	15	24	20	14	20	23
Mo	b.d.l.	b.d.l.	b.d.l.	b.d.l.	b.d.l.	b.d.l.	b.d.l.	b.d.l.	b.d.l.
Sn	b.d.l.	b.d.l.	b.d.l.	b.d.l.	b.d.l.	b.d.l.	b.d.l.	17	b.d.l.
Ba	142	174	178	632	634	683	690	485	621
Pb	47	50	52	45	33	40	41	24	29
Th	5	6	5	31	37	48	41	24	89
U	b.d.l.	b.d.l.	b.d.l.	9	7	b.d.l.	12	5	6
<i>CIPW norm</i>									
Quartz	33.87	32.12	33.20	31.67	31.03	29.03	30.89	34.80	28.19
Corundum	2.25	1.53	3.03	1.34	2.05	0.93	1.25	2.62	1.18
Orthoclase	26.71	26.95	30.73	32.03	32.56	31.62	30.43	26.95	34.75
Albite	32.32	34.52	27.84	27.75	26.82	29.19	29.11	28.77	26.15
Anorthite	2.24	2.48	1.57	4.11	3.44	5.08	4.97	3.02	4.89
Diopside	0.00	0.00	0.00	0.00	0.00	0.00	0.00	0.00	0.00
Hypersthene	0.32	0.22	0.50	0.55	0.57	0.72	0.62	0.60	0.92
Ilmenite	0.04	0.02	0.09	0.04	0.06	0.04	0.04	0.13	0.04
Apatite	0.07	0.07	0.09	0.16	0.35	0.19	0.14	0.23	0.32
Hematite	0.96	0.69	1.44	1.22	1.54	1.61	1.33	1.34	1.97
Titanite	0.00	0.00	0.00	0.00	0.00	0.00	0.00	0.00	0.00
Rutile	0.05	0.05	0.06	0.16	0.18	0.23	0.19	0.11	0.29
Total	98.84	98.66	98.56	99.03	98.60	98.64	98.97	98.57	98.70
Solidification Index	5.01	5.47	3.59	8.49	8.01	9.79	9.82	7.37	9.66
Differentiation Index	92.91	93.59	91.77	91.45	90.41	89.84	90.44	90.52	89.08
Color Index	1.33	0.94	2.02	1.81	2.18	2.38	2.00	2.07	2.93
Agpaitic Index	0.78	0.83	0.75	0.80	0.77	0.80	0.79	0.74	0.79
Mg#	51.76	50.83	52.39	58.83	54.20	58.80	59.83	58.67	59.81

Table A.3.2: Rare earth element and some trace element data – LA-ICPMS analyses (continued).

$$(Eu/Eu^*)_N = Eu_N \times (Sm_N \times Gd_N)^{-0.5}$$

Rock type Sample	Biotite granitoid				
	NG-7	BG-1	BL-9	PA-2	BD-1
<i>Trace elements (ppm)</i>					
Sc	2.54	10.40	18.30	1.73	2.46
Cr	8.22	7.88	119.00	7.68	6.82
Ni	5.11	6.00	39.80	5.38	5.02
Nb	9.69	22.80	33.30	4.41	15.20
Mo	0.71	2.74	1.89	1.00	3.16
Hf	4.04	9.05	10.80	4.60	9.12
Ta	1.01	2.37	2.04	0.32	1.81
<i>REE (ppm)</i>					
Sn	0.86	2.58	4.31	0.97	2.42
La	40.90	71.80	93.50	51.00	111.00
Ce	48.10	133.00	177.00	75.20	191.00
Pr	6.60	17.00	22.50	7.55	22.60
Nd	22.80	68.40	95.60	25.20	82.40
Sm	3.44	14.20	18.10	3.30	12.80
Eu	1.07	1.54	4.00	0.83	2.40
Gd	2.63	12.40	13.00	2.05	8.17
Tb	0.30	1.93	1.52	0.23	0.98
Dy	1.68	12.50	7.97	1.19	5.07
Ho	0.35	2.43	1.33	0.23	0.88
Er	0.92	6.89	3.35	0.67	2.38
Tm	0.13	0.99	0.46	0.10	0.34
Yb	0.88	6.33	3.02	0.81	2.22
Lu	0.13	0.83	0.43	0.14	0.33
Σ REE (ppm)	129.92	350.24	441.78	168.50	442.57
$(La/Lu)_N$	32.41	8.97	22.68	37.81	34.81
LREE ($La/Sm)_N$	7.42	3.16	3.23	9.65	5.42
HREE ($Gd/Lu)_N$	2.48	1.84	3.75	1.81	3.05
$(Eu/Eu^*)_N$	1.08	0.35	0.79	0.97	0.72

Table A.3.2: Rare earth element and some trace element data – LA-ICPMS analyses (continued).

$$(Eu/Eu^*)_N = Eu_N \times (Sm_N \times Gd_N)^{-0.5}$$

Rock type Sample	Deformed biotite granitoid				
	TK-3	NN-1	BFS-7	BFS-1	ND-1
<i>Trace elements (ppm)</i>					
Sc	8.82	9.30	14.60	3.03	2.16
Cr	10.40	16.00	22.00	15.80	9.15
Ni	7.00	8.65	13.10	6.94	6.05
Nb	14.60	27.00	12.20	11.60	12.30
Mo	1.42	1.80	1.73	1.20	1.31
Hf	6.91	14.30	5.36	4.16	6.73
Ta	1.06	2.39	0.79	1.09	1.36
<i>REE (ppm)</i>					
Sn	2.08	2.87	3.95	1.43	1.46
La	57.50	111.00	44.80	44.20	75.00
Ce	86.20	188.00	70.70	65.50	104.00
Pr	9.30	20.80	8.13	6.78	12.80
Nd	34.70	76.40	31.70	24.00	45.30
Sm	6.07	11.80	5.86	3.94	6.66
Eu	1.37	2.19	1.42	0.87	1.06
Gd	4.81	8.04	4.67	2.58	3.97
Tb	0.67	1.02	0.62	0.31	0.45
Dy	4.26	5.91	3.77	1.58	2.38
Ho	0.83	1.07	0.71	0.27	0.42
Er	2.38	2.96	2.16	0.69	1.06
Tm	0.37	0.41	0.30	0.09	0.17
Yb	2.55	2.89	2.20	0.59	1.24
Lu	0.41	0.43	0.32	0.09	0.19
Σ REE (ppm)	211.42	432.92	177.36	151.48	254.70
$(La/Lu)_N$	14.56	26.86	14.67	52.13	42.08
LREE ($La/Sm)_N$	5.92	5.87	4.77	7.01	7.03
HREE ($Gd/Lu)_N$	1.45	2.32	1.82	3.62	2.65
$(Eu/Eu^*)_N$	0.77	0.69	0.83	0.83	0.63

Table A.3.2: Rare earth element and some trace element data – LA-ICPMS analyses (continued).

$$(Eu/Eu^*)_N = Eu_N \times (Sm_N \times Gd_N)^{-0.5}$$

Rock type Sample	Mega feldspar granitoid				
	TS-1	KO-12	DML-1a	KE-1a	BN-2a
<i>Trace elements (ppm)</i>					
Sc	4.98	4.61	3.78	4.63	5.24
Cr	11.80	10.80	6.95	10.50	12.40
Ni	7.27	7.18	4.76	6.28	6.99
Nb	27.00	14.30	18.80	18.40	21.20
Mo	1.44	1.61	1.06	0.96	0.74
Hf	8.66	5.62	6.81	6.92	9.48
Ta	1.79	0.81	1.94	1.10	1.44
<i>REE (ppm)</i>					
Sn	3.62	3.11	2.49	3.65	2.97
La	107.00	68.50	110.00	70.10	67.10
Ce	183.00	111.00	180.00	126.00	110.00
Pr	20.70	14.10	20.60	13.50	12.40
Nd	75.10	54.30	74.00	49.30	44.00
Sm	12.00	9.69	11.00	8.31	6.43
Eu	1.38	1.41	1.27	1.19	1.25
Gd	7.41	7.08	6.96	5.61	3.84
Tb	0.81	0.84	0.76	0.63	0.44
Dy	3.97	4.23	3.71	3.21	2.26
Ho	0.63	0.75	0.60	0.55	0.38
Er	1.51	1.95	1.57	1.39	1.09
Tm	0.21	0.26	0.21	0.19	0.16
Yb	1.37	1.78	1.26	1.22	1.04
Lu	0.21	0.27	0.20	0.18	0.17
Σ REE (ppm)	415.30	276.15	412.13	281.38	250.56
$(La/Lu)_N$	54.18	26.63	57.38	40.88	42.21
LREE ($La/Sm)_N$	5.57	4.41	6.24	5.27	6.52
HREE ($Gd/Lu)_N$	4.47	3.28	4.32	3.90	2.88
$(Eu/Eu^*)_N$	0.45	0.52	0.44	0.53	0.77

Table A.3.2: Rare earth element and some trace element data – LA-ICPMS analyses (continued).

$$(Eu/Eu^*)_N = Eu_N \times (Sm_N \times Gd_N)^{-0.5}$$

Rock type Sample	Two-mica granitoid				
	BP-1	BAN-6	BM-4	BM-5	TA-9
<i>Trace elements (ppm)</i>					
Sc	2.62	3.57	5.27	8.11	2.85
Cr	6.54	8.11	6.63	6.07	8.55
Ni	4.70	4.96	3.19	4.48	5.30
Nb	15.70	28.30	22.10	33.30	25.70
Mo	0.65	2.94	0.67	0.68	1.16
Hf	4.43	4.97	1.83	1.68	4.35
Ta	1.53	3.36	3.42	3.66	3.51
<i>REE (ppm)</i>					
Sn	4.05	4.71	2.95	8.26	11.40
La	52.70	67.30	12.70	14.60	52.70
Ce	92.60	120.00	22.40	21.10	91.70
Pr	10.30	13.30	2.21	1.98	10.10
Nd	36.70	47.70	8.24	7.15	35.80
Sm	6.58	8.32	2.38	1.91	6.30
Eu	0.71	0.70	0.23	0.17	0.57
Gd	4.17	5.20	2.45	1.92	4.03
Tb	0.43	0.60	0.43	0.35	0.45
Dy	1.87	2.91	2.76	2.12	2.05
Ho	0.29	0.46	0.46	0.37	0.32
Er	0.71	1.19	1.26	1.04	0.77
Tm	0.10	0.18	0.19	0.15	0.10
Yb	0.64	1.16	1.29	1.06	0.72
Lu	0.09	0.16	0.18	0.16	0.10
Σ REE (ppm)	207.88	269.18	57.18	54.07	205.70
$(La/Lu)_N$	58.82	43.93	7.32	9.59	53.63
LREE ($La/Sm)_N$	5.00	5.05	3.33	4.77	5.22
HREE ($Gd/Lu)_N$	5.54	4.04	1.68	1.50	4.88
$(Eu/Eu^*)_N$	0.41	0.32	0.29	0.27	0.35

A.4 Whole-rock Rb–Sr and Sm–Nd isotope geochemistry

Table A.4.1: Whole-rock Rb–Sr isotope data

Sample	Rb (ppm)	Sr (ppm)	$^{87}\text{Rb}/^{86}\text{Sr}$	$^{87}\text{Sr}/^{86}\text{Sr}$	$\pm 2\sigma_m$	$^{87}\text{Sr}/^{86}\text{Sr}$ (600Ma)	$f_{\text{Rb/Sr}}$	ϵSr (0)	ϵSr (600 Ma)
<i>Biotite granitoid</i>									
BL-8	168	221	2.2030	0.724573	± 0.000014	0.705723	26	285	27
BG-1	160	244	1.8999	0.721906	± 0.000012	0.705650	22	247	26
BLF-5 *	359	1425	0.7293	0.712818	± 0.000013	0.707309	8	118	49
BLF-6G *	173	504	0.9938	0.715032	± 0.000013	0.707524	11	149	52
BLF-1 *	173	297	1.6880	0.720932	± 0.000013	0.708180	20	233	61
BLF-2 *	137	1191	0.3323	0.710045	± 0.000012	0.707534	3	79	52
BLF-3 *	182	1491	0.3538	0.710197	± 0.000013	0.707524	3	81	52
BLF-4 *	158	1395	0.3276	0.710017	± 0.000013	0.707542	3	78	52
<i>Mega feldspar granitoid</i>									
BM-1	211	428	1.4281	0.720083	± 0.000014	0.707864	17	221	58
HO-1	179	196	2.6480	0.729843	± 0.000013	0.707185	31	360	48
KE-1	204	169	3.5026	0.737504	± 0.000014	0.707534	42	468	53
DML-1	194	142	3.9652	0.739780	± 0.000014	0.705853	48	501	29
DML-2	204	156	3.7948	0.738152	± 0.000014	0.705683	46	478	27
KO-12	200	222	2.6115	0.727273	± 0.000011	0.704928	31	323	16
BN-1a	302	273	3.2088	0.733791	± 0.000014	0.706336	38	416	36
BN-1b	266	296	2.6057	0.730174	± 0.000014	0.707878	31	364	58
BN-2b	256	250	2.9699	0.732747	± 0.000012	0.707335	35	401	50
TS-1	286	185	4.4899	0.746750	± 0.000017	0.708333	54	600	65
TS-2	235	172	3.9665	0.742528	± 0.000013	0.708589	48	540	68
<i>Two-mica granitoid</i>									
BF-2	305	135	6.5726	0.764009	± 0.000012	0.707771	80	845	57
BAN-6	353	113	9.1071	0.785585	± 0.000012	0.707661	111	1151	55
BM-4	264	55	14.0607	0.835105	± 0.000014	0.714796	171	1854	156
BM-5	334	48	20.5017	0.895309	± 0.000017	0.719888	250	2708	229
TA-9	470	97	14.1943	0.835665	± 0.000024	0.714213	173	1862	148

(1) $f_{\text{Rb/Sr}} = (\text{Sr}^{87}/\text{Sr}^{86})_{\text{s}} / (\text{Sr}^{87}/\text{Sr}^{86})_{\text{UR}} - 1$, where s = samples, $(\text{Sr}^{87}/\text{Sr}^{86})_{\text{UR}} = 0.7045$ and $(\text{Rb}^{87}/\text{Rb}^{86})_{\text{UR}} = 0.0816$ (Faure, 1986)

(2) Samples with asterisk (*) are from Nzolang (2005).

Table A.4.2: Whole-rock Sm–Nd isotope data

Sample	Sm (ppm)	Nd (ppm)	$^{147}\text{Sm}/^{144}\text{Nd}$	$^{143}\text{Nd}/^{144}\text{Nd}$	$\pm 2\sigma_m$	$^{143}\text{Nd}/^{144}\text{Nd}$ (600 Ma)	$f_{\text{Sm/Nd}}$	$\epsilon_{\text{Nd}}(0)$	ϵ_{Nd} (600 Ma)	T_{DM} (Ga)
<i>Biotite granitoid</i>										
BL-8	10.50	52.72	0.120433	0.512347	± 0.000011	0.511873	-0.39	-5.7	0.2	1.31
BG-1	11.09	53.03	0.126487	0.512357	± 0.000014	0.511860	-0.36	-5.5	-0.1	1.39
BLF-5 *	12.23	71.32	0.103754	0.512016	± 0.000013	0.511656	-0.47	-12.1	-5.9	1.57
BLF-6G *	13.81	80.10	0.104208	0.512065	± 0.000021	0.511703	-0.47	-11.2	-4.9	1.51
BLF-1 *	8.21	42.20	0.117679	0.512280	± 0.000012	0.511871	-0.40	-7.0	-1.6	1.38
BLF-2 *	21.75	130.33	0.100898	0.511994	± 0.000012	0.511644	-0.49	-12.6	-6.1	1.56
BLF-3 *	22.40	126.72	0.106892	0.512034	± 0.000010	0.511663	-0.46	-11.8	-5.7	1.59
BLF-4 *	22.58	134.22	0.101714	0.511986	± 0.000010	0.511633	-0.48	-12.7	-6.3	1.58
<i>Mega feldspar granitoid</i>										
BM-1	5.74	36.39	0.095387	0.511720	± 0.000012	0.511345	-0.52	-17.9	-10.2	1.84
HO-1	7.14	42.05	0.102675	0.511889	± 0.000014	0.511485	-0.48	-14.6	-7.4	1.73
KE-1	6.60	38.68	0.103223	0.511898	± 0.000011	0.511492	-0.48	-14.4	-7.3	1.72
DML-1	9.10	59.21	0.092965	0.511925	± 0.000011	0.511559	-0.53	-13.9	-6.0	1.54
DML-2	9.80	64.66	0.091609	0.511940	± 0.000010	0.511580	-0.53	-13.6	-5.6	1.51
KO-12	8.43	46.51	0.109600	0.511882	± 0.000009	0.511451	-0.44	-14.8	-8.1	1.85
BN-1a	7.65	50.52	0.091548	0.511694	± 0.000013	0.511334	-0.53	-18.4	-10.4	1.81
BN-1b	6.88	39.27	0.105850	0.511690	± 0.000014	0.511274	-0.46	-18.5	-11.6	2.06
BN-2b	5.02	34.62	0.087594	0.511652	± 0.000012	0.511308	-0.55	-19.2	-10.9	1.81
TS-1	9.65	59.88	0.097389	0.511628	± 0.000024	0.511245	-0.50	-19.7	-12.1	1.99
TS-2	3.91	22.54	0.104908	0.511674	± 0.000012	0.511262	-0.47	-18.8	-11.8	2.06
<i>Two-mica granitoid</i>										
BF-2	7.76	46.34	0.101277	0.511617	± 0.000013	0.511219	-0.49	-19.9	-12.6	2.07
BAN-6	7.06	40.20	0.106886	0.511571	± 0.000018	0.511151	-0.46	-20.8	-14.0	2.25
BM-4	2.03	6.83	0.179500	0.512033	± 0.000013	0.511327	-0.09	-11.8	-10.5	4.93
BM-5	1.65	6.18	0.161891	0.511995	± 0.000011	0.511358	-0.18	-12.5	-9.9	3.38
TA-9	5.79	32.78	0.106821	0.511603	± 0.000012	0.511183	-0.46	-20.2	-13.3	2.20

(1) $f_{\text{Sm/Nd}} = (\text{Sm}^{147}/\text{Nd}^{144})_s / (\text{Sm}^{147}/\text{Nd}^{144})_{\text{CHUR}} - 1$, where s = sample, $(\text{Nd}^{143}/\text{Nd}^{144})_{\text{CHUR}} = 0.512638$ and $(\text{Sm}^{147}/\text{Nd}^{144})_{\text{CHUR}} = 0.1967$ (Faure, 1986)

(2) Samples with asterisk (*) are from Nzolang, 2005.

A.5 Microthermometric fluid inclusion data

Table A.5.1: Non-aqueous volatiles-rich mixed fluid inclusions.

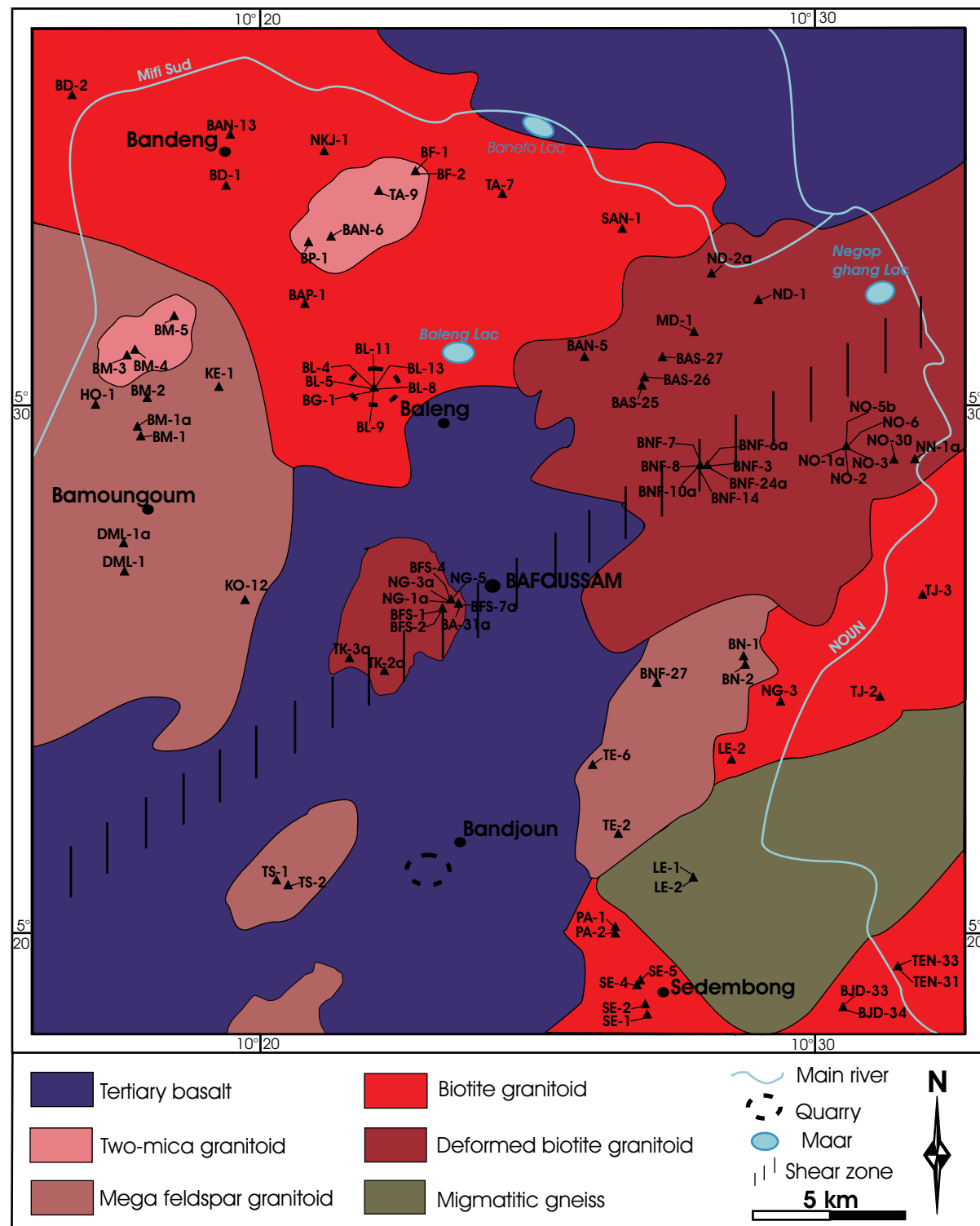
N°	Size (long axis: μm)	F	Number of phases	Tm CO_2 ($^{\circ}\text{C}$)	Tm cla ($^{\circ}\text{C}$)	Th CO_2 ($^{\circ}\text{C}$)/Mode	Th total ($^{\circ}\text{C}$)/Mode	CH ₄ (mole %)	Salinity (equiv. wt. %)
1	29	0.4	3	-56.9	9.8	17.5 → L	174.0 → V	-	0.41
2	25.2	0.1	3	-57	-	8.7 → L	197.0 → V	1.1	-
3	24.8	0.4	2	-56.9	-	8.0 → L	200.0 → V	-	-
4	43.5	0.3	2	-57	-	29.9 → V	186.0 → V	-	-
5	21.7	0.1	2	-56.9	-	7.7 → L	186.0 → V	-	-
6	42	0.1	2	-56.8	-	29.7 → L	-	-	-
7	17.5	0.2	3	-56.8	5.8	19.3 → L	225.1 → V	-	7.81
8	21	0.05	2	-57	-	14.6 → V	255.1 → V	-	-
9	17.5	0.1	2	-56.7	-	14.8 → V	224.7 → V	-	7.97
10	35	0.3	3	-57.2	-	-	-	-	-
11	14.5	0.1	3	-58.1	-	20.6 → L	-	7.5	-
12	13.2	0.05	3	-57.8	-	5.2 → L	-	-	-
13	32.7	0.4	3	-57.6	5.7	18.7 → L	259.6 → V	5	10.12
14	12.9	0.3	3	-56.9	5.3	22.2 → L	361.8 → V	-	8.61
15	28.6	0	1	-57.5	5.4	10.8 → V	-	10	-
16	24.3	0.2	3	-57.8	-	20.2 → L	239.6 → V	6.1	-
18	20.2	0.2	3	-57.5	5.1	16.1 → V	293.7 → V	8.5	10.59
19	23.1	0.1	3	-57.4	5.6	21.0 → L	256.0 → V	4.1	9.92
20	28	0.1	3	-56.6	4.4	26.4 → L	293.7 → V	-	9.99
21	24.5	0.1	3	-57.7	5.5	6.9 → V	297.0 → V	13.5	-
22	11.5	0.3	3	-56.9	7.5	5.1 → L	-	-	-
23	11.5	0.05	3	-57.8	-	9.7 → L	-	5.5	-
24	10.8	0.5	3	-56.6	-	14.2 → L	-	-	-
25	23	0.1	3	-56.7	-	10.2 → L	210 → V	-	-

Table A.5.2: Aqueous-rich mixed fluid inclusions.

N°	Size (long axis: µm)	F	Number of phases	Tm CO ₂ (°C)	Te (°C)	Tm cla (°C)	Th CO ₂ (°C)/Mode	Th _{total} (°C)/Mode	CH ₄ (mole %)	Salinity (equiv. wt. %)
1	29.0	0.70	2	-56.9	-	-	26.0 → L	-	-	-
2	14.5	0.85	2	-56.9	-	-	6.6 → L	-	-	-
3	13.8	0.80	2	-56.7	-39.1	7.0	23.2 → L	195 → L	-	5.77
4	14.0	0.85	2	-56.7	-	-	37.8 → L	-	-	-
5	13.5	0.80	2	-57.7	-	-	20.2 → L		9.0	-
6	35.0	0.80	2	-56.7	-26.7	4.6	14.6 → L	228.5 → V	-	9.64
7	31.5	0.60	3	-56.7	-	5.6	17.8 → L	246.0 → V	-	8.13
8	14.5	0.60	3	-57.1	-	5.8	12.8 → L	250.0 → V	-	7.81

Table A.5.3: Pure aqueous fluid inclusions.

N°	Size (long axis: µm)	F	Number of phases	Te (°C)	Tm ice (°C)	Tm cla (°C)	Th CO ₂ (°C)/Mode	Th _{total} (°C)/Mode	CH ₄ (mole %)	Salinity (equiv. wt. %)
1	23.8	0.90	2	-25.6	-7.6	-	13.8 → L	-	-	-
2	35.0	0.95	2	-34.2	-1.2	-	-	152.0 → L	-	2.07
3	34.5	1.00	1	-32.1	-0.5	-	-	-	-	0.88
4	17.5	1.00	2	-34.5	-2.1	-	-	150.0 → L	-	3.55
5	24.5	1.00	2	-30.7	-5.4	-	-	145.0 → L	-	8.41
6	24.5	1.00	2	-34.7	-3.7	-	-	143.8 → L	-	6.01
7	17.5	1.00	2	-31.1	-5.0	-	-	145.2 → L	-	7.86
8	14.0	1.00	2	-32.6	-4.4	-	-	145.0 → L	-	7.02
9	17.5	1.00	2	-30.5	-4.3	-	-	148.5 → L	-	6.88



Sample locations map of the Bafoussam area

Merline Laure Djouka-Fonkwé

Institut für Mineralogie

Am Hubland

97074 Würzburg

Erklärung

Hiermit erkläre ich ehrenwörtlich, dass ich die vorgelegte Dissertation selbstständig angefertigt habe und dass ich keine weiteren als die angegebenen Quellen und Hilfsmittel benutzt habe.

Würzburg, dem 15. Juni 2005

Lebenslauf

Merline Laure Djouka-Fonkwé

Institut für Mineralogie

Am Hubland

97074 Würzburg

Geburtsdatum: 03.04.1973

Geburtsort: Nkongsamba, Kamerun

Familienstand: ledig

Schulischer Werdegang

09/1984–07/1992 Gymnasium Ntui und Bafoussam, Kamerun
07/1992 Abitur

Studium

10/1992–09/1997 Studium der Geologie an der Universität Jaunde I, Kamerun
09/1997 "Bachelor" in Studiengang Geologie
10/1997–09/1999 Studium der Vulkanologie an der Universität Jaunde I
Diplomarbeit im Studiengang Vulkanologie über das Thema "Etude volcanologique et pétrographique du secteur de Mangoum (Région de Foumbot Ouest-Cameroun)."
09/1999 "Master" im Studiengang Vulkanologie
10/1999–09/2000 Promotionvorstudium der Vulkanologie an der Universität Jaunde I
Bericht der Promotionvorstudium über das Thema "Les dynamismes eruptifs"
09/2000 Abschluss 1. Jahr Promotionvorstudium
10/2001–03/2002 Sprachkurs in Goethe-Institut in Freiburg
Seit 04/2002 Promotionstudium am Mineralogischen Institut der Universität Würzburg

Tätigkeit als wissenschaftlicher Angestellter

10/2000–07/2001 Wissenschaftlicher Angestellter am Wissenschaftlichen Facultät, Universität Jaunde I; Betreuung der Übungen zur Lehrveranstaltung "Mikroskopie der gesteinsbildenden Minerale"